



4D evolution of the Sadiola-Yatela gold district, Kédougou-Kénieba inlier, West Africa

QUENTIN MASUREL
B.Sc., M.Sc.



Centre for Exploration Targeting
ARC Centre for Core to Crust Fluid Systems (CCFS)
School of Earth and Environment
The University of Western Australia

This thesis is presented for the degree of Doctor of Philosophy

October 2015

Supervisors:

Dr. Nicolas Thébaud (coordinator)

Dr. John Miller

Dr. Stanislav Ulrich

A vous Maman, Papa, Manon, Arthur

“Happiness is only real when shared”

(Christopher Johnson McCandless, *Into the wild*)

Abstract

The Paleoproterozoic belts of West Africa are the fastest-growing gold production in the world. The Kédougou-Kénieba inlier (KKI) represents the westernmost exposure of Paleoproterozoic crust in the West African Craton, with outcrops in western Mali and eastern Senegal. The KKI is an emerging world-class gold province (>40 Moz, cumulative past production and resources), threatening the premier position of Ghana in West African gold production. The inlier hosts a number of world-class gold mining districts that are located along regional-scale shear zones. Recent discoveries in the inlier have triggered a real need for understanding the controls on gold mineral system location and ore shoot geometry in order to improve Brownfield and Greenfield exploration strategies. Through a multiscale and multidisciplinary approach including structural geology, petrography, geochemistry and geochronology, this work presents the first integrated study of gold mineralisation in the world-class Sadiola-Yatela district.

Deposit-scale investigations indicate that gold deposits of the Sadiola-Yatela district are primarily hosted by impure metacarbonates and, to a lesser extent, detrital metasedimentary rocks (e.g., wacke, arenite, siltstone, and argillite) and Eburnean granitoids. The presence of carbonate host rocks is very rare compared to gold mineralisation in typical granite-greenstone belts of the West African Craton. Country rocks have undergone polycyclic deformation, which included early fold-and-thrust tectonics (D_1 , D_2) followed by transcurrent tectonics accommodating oblique convergence (D_3 , D_4). The gold deposits of the district share a similar structural setting and gold relative timing.

District-scale work indicates that orogenic gold mineralisation occurred during D_3 , after the cessation of region-wide compressional deformation. Hydrothermal fluid circulation was coeval with sinistral displacement along the Senegal-Mali Shear Zone and local steep NNE-trending shears connected to structural traps in the Kofi basin. The D_2 and D_3 events represent a transpressional deformation continuum that was associated with voluminous calc-alkaline magmatism. This deformation continuum marks the principal imprint of the Eburnean orogeny (ca. 2115-2060 Ma) in the district. Eburnean granitoids exposed in the district display a temporal evolution from ca. 2115-2080 Ma

metaluminous plutons (e.g., diorite, hornblende-biotite-granodiorite) to ca 2080-2060 Ma peraluminous biotite-monzogranites.

The tectonic, magmatic, metamorphic and hydrothermal alteration history of the gold deposits in the district is comparable to that of other world-class orogenic gold deposits in the KKI. Despite the commonalities, gold mineralisation in the Sadiola-Yatela district exhibits three distinct styles defined on the basis of contrasted ore and alteration paragenesis. The three gold mineralisation styles are typified by the Sadiola Hill-style Au-As-Sb mineralisation, the Alamoutala-style Au-Cu mineralisation, and the Yatela-style auriferous residuum. The metal enrichment association and geothermometric estimates from ore and alteration paragenesis at Sadiola Hill are compatible with those of mesozonal Au-As-Te (6-12 km, 300°-475°C) to near-epizonal Au-Sb (\leq 6 km, 150°-300°C) orogenic gold deposits worldwide. The Alamoutala deposit represents two distinct hydrothermal systems in which a magnetite-bearing skarn developed locally surrounding syn-kinematic quartz-feldspar-porphyry stocks, and was overprinted by district-wide orogenic gold mineralisation. The Yatela gold deposit formed by residual and supergene gold enrichment of a low grade Birimian carbonate-hosted gold occurrence. We propose that the atypical carbonate nature of the host rocks represents a critical factor explaining the observed variability in gold mineralisation at both the deposit- and camp-scale.

Table of contents

Chapter I. Introduction	1
1. Preamble and knowledge gaps.....	1
2. Aims of the thesis.....	6
3. Methodology	6
3.1. Fieldwork and geological sampling.....	6
3.1.1. <i>Geological mapping</i>	6
3.1.2. <i>Diamond drill core logging</i>	7
3.1.3. <i>Geological sampling</i>	7
3.2. Analytical techniques.....	8
3.2.1. <i>Optical microscopy</i>	8
3.2.2. <i>Scanning Electron Microscopy</i>	8
3.2.3. <i>Electron Probe Microanalyser</i>	8
3.2.4. <i>Whole-rock geochemistry</i>	10
3.2.5. <i>U-Pb Geochronology</i>	10
3.2.6. <i>Laser Ablation - Inductively Coupled Plasma Mass Spectrometry</i>	10
4. Structure of the thesis	11
5. Justification of thesis format and authorship.....	12
6. Supporting references.....	15
6.1. Short scientific communication	15
6.2. Peer-reviewed abstracts	15
7. Summary declaration	16
8. References	16

Chapter II. Sadiola Hill: a world-class carbonate-hosted gold deposit in Mali, West Africa.....	21
1. Abstract.....	21
2. Introduction.....	22
3. Regional geology.....	23
4. Mining background	26
5. Materials and methods	28
5.1. Pit mapping, 3D modeling, logging and sampling	28
5.2. Petrographic study	28
5.3. Arsenopyrite geothermometry	29
5.4. LA-ICPMS on sulfides	29
6. Deposit geology	30
6.1. Sedimentary rocks	31
6.2. Intrusions and relationship to metasedimentary rocks	33
6.3. Structural setting and geometry	35
6.4. Deposit-scale gold distribution	38
6.5. Ore styles and textures.....	40
6.6. Hydrothermal alteration.....	43
6.7. Ore mineralogy	48
7. Discussion.....	53
7.1. Integration of the Sadiola Hill deposit with regional geology and tectonics	53
7.2. Physico-chemical conditions of the ore-forming fluid and potential controls on Au-Sb co-precipitation	56

7.3. Towards a genetic model.....	59
8. Conclusions	60
9. Acknowledgments	62
10. References	62
11. Supplementary material	71
11.1. Representative chemical composition of syn-mineralization stage hydrothermal tourmalines at Sadiola Hill.	
11.2. Representative analyses of ore minerals.	
11.3. Representative analyses of gold phases.	
11.4. Representative EPMA analyses of Stage I arsenopyrite crystals.	
11.5. Representative LA-ICPMS analyses of Stage I arsenopyrites and pyrites.	
11.6. Representative EPMA analyses of buffered arsenopyrite crystals used for geothermometry.	

Chapter III. The Alamoutala carbonate-hosted gold deposit, Kédougou-Kénieba inlier, West Africa.....	83
1. Abstract.....	83
2. Introduction	84
3. Geological setting	85
3.1. Regional geology	85
3.2. Local geology	89
4. Alamoutala exploration and mining history.....	91
5. Materials and methods	91

5.1.	Pit mapping, logging, sampling and 3D modeling	91
5.2.	Petrography and mineral chemistry	92
5.3.	Whole-rock geochemical analyses	93
5.4.	Geochronology	93
6.	Deposit geology	95
6.1.	Sedimentary rocks and intrusions	95
6.2.	Intrusion geochemistry	98
6.3.	Geochronology	100
6.4.	Contact metamorphism.....	101
6.5.	Structural setting and geometry	105
6.6.	Deposit-scale gold distribution	108
6.7.	Ore-related hydrothermal alteration	110
6.8.	Ore mineralogy	113
7.	Discussion.....	117
7.1.	Towards a genetic model for the Alamoutala gold deposit	117
7.2.	Integration of the Alamoutala deposit with regional geology and tectonics	
	118	
8.	Conclusions	119
9.	Acknowledgments	120
10.	References	120
11.	Supplementary material	126
11.1.	Lithogeochemistry data for igneous rocks of the Alamoutala open pit.	

11.2. Sensitive high resolution ion microprobe (SHRIMP) analytical results for the Alamoutala quartz-feldspar-porphyry.

11.3. Representative electron probe micro-analyses of pyroxene in endoskarn.

Chapter IV. The Yatela gold deposit in Mali, West Africa: the final product of a long-lived history of hydrothermal alteration and weathering.....131

1. Abstract.....	131
2. Introduction	132
3. Background.....	133
3.1. Regional geology	133
3.2. Local geology	136
3.3. The Yatela gold resource	138
4. Methodology	139
4.1. Pit mapping, drill core logging, sampling and 3D modelling.....	139
4.2. Petrography and mineral chemistry	139
4.3. Host rocks	140
4.4. Structural framework	142
4.5. Primary gold distribution	144
4.6. Hydrothermal alteration.....	146
4.7. Primary ore mineralogy	150
4.8. Karst infill stratigraphy.....	152
4.9. Secondary gold distribution.....	155

5. Discussion.....	156
5.1. Integration with regional geology and tectonics.....	156
5.2. Towards a genetic model	157
6. Conclusions.....	161
7. Acknowledgements	161
8. References.....	162
9. Supplementary material.....	168
9.1. Representative chemical composition of syn-mineralisation hydrothermal tourmalines at Yatela.	

Chapter V. The tectono-magmatic evolution of the Kédougou-Kénieba inlier, West Africa: new insights from igneous rock geochemistry and U-Pb geochronology in the Sadiola-Yatela region171

1. Abstract.....	171
2. Introduction.....	172
3. Geological setting of the Kédougou-Kénieba inlier	173
3.1. Magmatic activity	174
3.2. Sedimentary basins	177
3.3. Tectonics.....	178
3.4. Metamorphism.....	181
3.5. Post-Birimian dolerite dykes	181
4. Methodology	181
4.1. Geological mapping and sampling	181

4.2.	Petrography and whole-rock geochemistry	182
4.3.	U-Pb geochronology	183
5.	Results	184
5.1.	Lithostratigraphy.....	184
5.2.	Structural framework	186
5.3.	Geochronology	190
5.3.1.	<i>Pre- to syn-D_{1s} magmatism</i>	190
5.3.2.	<i>Syn-D_{2s} magmatism.....</i>	193
5.3.3.	<i>Syn-D_{3s} magmatism.....</i>	200
5.4.	Whole rock geochemistry	203
5.4.1.	<i>Major elements.....</i>	203
5.4.2.	<i>Trace elements</i>	205
6.	Discussion.....	209
6.1.	Geological framework for the Sadiola-Yatela region.....	209
6.1.1.	<i>Structural evolution.....</i>	209
6.1.2.	<i>Magmatic evolution.....</i>	209
6.2.	Integration with regional geology and tectonics.....	210
6.3.	Implications for the geodynamic evolution of the KKI.....	213
6.4.	Comparison with other Birimian terranes and diachroneity of geological development	216
7.	Acknowledgments	217
8.	References	217

Chapter VI. Conclusions.....	227
1. Key research outcomes	227
1.1. Lithostratigraphy	227
1.2. Deformation.....	228
1.3. Metamorphism.....	229
1.4. Magmatism	229
1.5. Gold mineralisation	230
1.6. Hydrothermal alteration.....	230
2. Implications for exploration.....	233
3. Future work	234
3.1. Source of fluids and metals.....	234
3.2. Timing of regional orogenic gold mineralisation	234
3.3. Metamorphic data	235
3.4. Lu-Hf isotopic studies	235
4. References	235
Electronic Appendices.....	239

Acknowledgements

What an amazing journey! I came to Australia with pre-conceived ideas about the people and lifestyle (e.g., crocodile Dundee, sun and pristine beaches, deadly animals, the bush) and I have not been disappointed. I guess I can say that I have been “living the dream”.

First, I would like to thank my supervisors Nicolas Thébaud, John Miller and Stanislav Ulrich, for supporting me during these past 3.5 years. Nicolas has been a great and supportive supervisor. He has given me the freedom to pursue various projects while conveying insightful ideas to me. He has spent a considerable amount of time going through my manuscripts and always provided constructive comments. Nicolas has also been a source of inspiration in the field and as a young research scientist. John put his faith in me despite my disturbing structural geology skills at the start of my PhD project. I had the pleasure to spend weeks with him in the field and we always came back with some memorable stories about remote West Africa. I hope that I can be as skilled and energetic in the field as John and to someday be able to command an audience and network in conferences as well as he can. Stanislav supervised me for one year before he moved to AngloGold Ashanti. I thank him for guidance in the field and for staying involved and making his scientific expertise available despite his new responsibilities. Also, I thank Cam McCuaig for giving me the opportunity to join the Centre for Exploration Targeting and work on that challenging and exciting project in West Africa.

AngloGold Ashanti Ltd. and IAMGOLD Corporation are gratefully acknowledged for their financial support. AMIRA International and the industry sponsors are also gratefully acknowledged for their support of the WAXI project (P934A). Thanks to Tom Gell for his enthusiasm for the study and his comprehensiveness in releasing scientific communications. Thanks to Alex Mason-Apps and Marian Skwarnecki for their constructive discussions. Thank you to Ockert Terblanche for his geophysical magic and his energy on a squash court. Thank you to SEMOS managers Geoffrey Gushee, Heinrich Eybers, Hlabangana Sitshengiso, Paul Herron, and Samuel Tessougue for their good advices and assistance with field work logistics. My deepest thanks go to my Malian geologist friends Daouda Traoré, Cheick

Sanogo, Fousseyni Samake, Monzon Traoré, Yakouba Koné, and Timothé Sogoba, for their warm welcome and making every fieldwork period great.

I acknowledge the Australian Microscopy and Microanalysis Research Facility at the Centre for Microscopy, Characterisation and Analysis; a facility funded by the University of Western Australia, the state, and Commonwealth governments. I especially thank Dr. Janet Muhling and Malcolm Roberts for their excellent scientific assistance on the electron microprobe. I also acknowledge the John de Laeter Centre of Excellence for Mass Spectrometry at Curtin University in Western Australia. Hao Gao and Cristina Talavera are thanked for their tireless assistance on the mystical SHRIMP II. Noreen Evans and Bradley McDonald from Curtin University, Olivier Bruguier from Geosciences Montpellier, and Didier Béziat from Geosciences Environment Toulouse, are thanked for their expertise in the collection and interpretation of LA-ICPMS data.

Outside the academic world, I wholeheartedly thank my mom Pascale, my dad Vincent, my sister Manon, and my brother Arthur. My parents have always provided unconditional love and inspiration. They passed me on values such as determination and curiosity, made me who I am. My sister and brother have always been instrumental in me taking time off and not saving any money out of my PhD scholarship. I consider myself very lucky that I could spend wonderful times with them 15000 km away from home visiting unique places such as Shark Bay, Exmouth, Kalbarri, Karijini, Cairns... (many more sites to list here but it would affect my credibility). Also, I need no words to thank the best person out there, my partner Margaux Le-Vaillant. In an ocean of great times working on my PhD project, there were times where I was irritable and depressed but Margaux has always been my true and great supporter. She is my love and my best friend, and I feel that we both learned how to live life to the fullest. To my friends Erik Cornelisse and Owen Perry, thank you for having me live the dream and reach a fluent level in Aussie slang. The irony has me settling down in Perth for 2 more years while you move back to Adelaide and Melbourne respectively. Keep up living the outdoor life (e.g., kitesurf, surf) and may we meet again soon! To my beach volley-ball partner Thierry Caron, thanks for the great atmosphere on court and showing me that losing is fun. To my international friends at CET, Erwann Lebrun (fun and proactive friend always enthusiastic for going out), Francois Voute (great roommate and all-rounder guy that can play guitar and kite surf), James Davis (resourceful field geologist aka “MacGyver” and devoted beer drinker), Luis Parra (friday balcony beer chief executive

officer), Denis Fougerouse (aka the corridor walker, always keen to make conversation), Stephane Roudaut (aka the table tennis master), and Yoram Teitler (aka the mad fisherman), my time as a PhD student would have been dull if it wasn't for the great social atmosphere prone to valuable distraction.

Chapter I. Introduction

1. Preamble and knowledge gaps

Paleoproterozoic (i.e. Birimian) volcano-plutonic belts and sedimentary basins of West Africa not only provide a complete record of crustal growth but also host a number of world-class gold deposits (Abouchami et al., 1990; Boher et al., 1992). To date, a large number of studies have focused on the Baoulé-Mossi domain, which covers portions of Burkina Faso, Côte d'Ivoire, Ghana, Guinea and Mali (Fig. 1). Gold deposits of various types have been recognised in these Birimian belts and include orogenic gold (e.g., Ashanti, Allibone et al., 2002a, b), intrusion-related gold (e.g., Morila, McFarlane et al., 2011; Hammond et al., 2011), Cu-Au porphyry (e.g., Gaoua, public data from AMIRA International West African Initiative final report, 2013), and paleoplacer (e.g., Tarkwa, Pigois et al., 2003). Detailed deposit-scale studies, which integrated structural-metamorphic-hydrothermal data with high precision isotopic dating, have also shown evidence for distinct gold mineralisation pulses (e.g., 2191–2158 Ma gold at Wassa, Parra-Avila, in press; 2105 ± 2 Ma gold at Ashanti, Oberthür et al., 1998; 2063 ± 9 Ma gold at Damang, Pigois et al., 2003). Nevertheless, the vast majority of world-class gold deposits in the Baoulé-Mossi domain belong to the orogenic class (e.g., Groves et al., 1998; Goldfarb et al., 2001; Groves et al., 2003; Goldfarb et al., 2005) and have been related to geological processes associated with the Eburnean orogeny dated between 2115 and 2060 Ma (e.g., Feybesse et al., 2006; Lawrence et al., 2013; Fougerouse et al., in press; Lebrun et al., in press). A number of studies have been carried out elsewhere, in the Archean Kénéma-Man domain and the Kédougou-Kénieba inlier (Fig. 1), but have been limited by disjointed political and geographic landscapes, volatile social context, and the recent Ebola outbreak.

The KKI represents the westernmost exposure (~ 22000 km 2) of Birimian crust in the West African Craton and has received increased attention from both the industry and academia as it represents an emerging world-class gold province. The geology of the inlier consists of two linear volcano-plutonic belts (Mako and Falémé) and

intervening sedimentary basins (Dialé-Daléma and Kofi) (Fig. 2). It differs from other Birimian granite-greenstone belts by the abundance of carbonates, with thick sequences in the Dialé-Daléma and Kofi Series representing the most extensive carbonate exposure in the Birimian of West Africa (Bosse et al., 1996; Bering et al., 1998). The structural architecture of the inlier is marked by two regional-scale tectonic discontinuities, respectively the Senegal-Mali Shear Zone and Main Transcurrent Zone. A number of world-class mining districts are located along these highly prospective lineaments and include Loulo-Gounkoto (~14 Moz), Sadiola-Yatela (~12 Moz), and Sabodala-Massawa (~12 Moz) (Fig. 2). Recent discoveries in the inlier include the Fekola gold deposit (3.72 Moz probable mineral reserves, B2Gold press release, July 2015) and the Petowal gold deposit (mineral resource of 1.35 Moz contained Au, public data from ToroGold website, 2015). Recent research in the KKI has highlighted the spatial association between calc-alkaline Eburnean plutons, gold mineralisation, and local iron skarn mineralisation, suggesting the potential role of a complex fluid history in the development of major gold deposits (e.g., Loulo, Lawrence et al., 2013a, b; Massawa, Treloar et al., 2014; Falémé, Lambert-Smith, 2014).

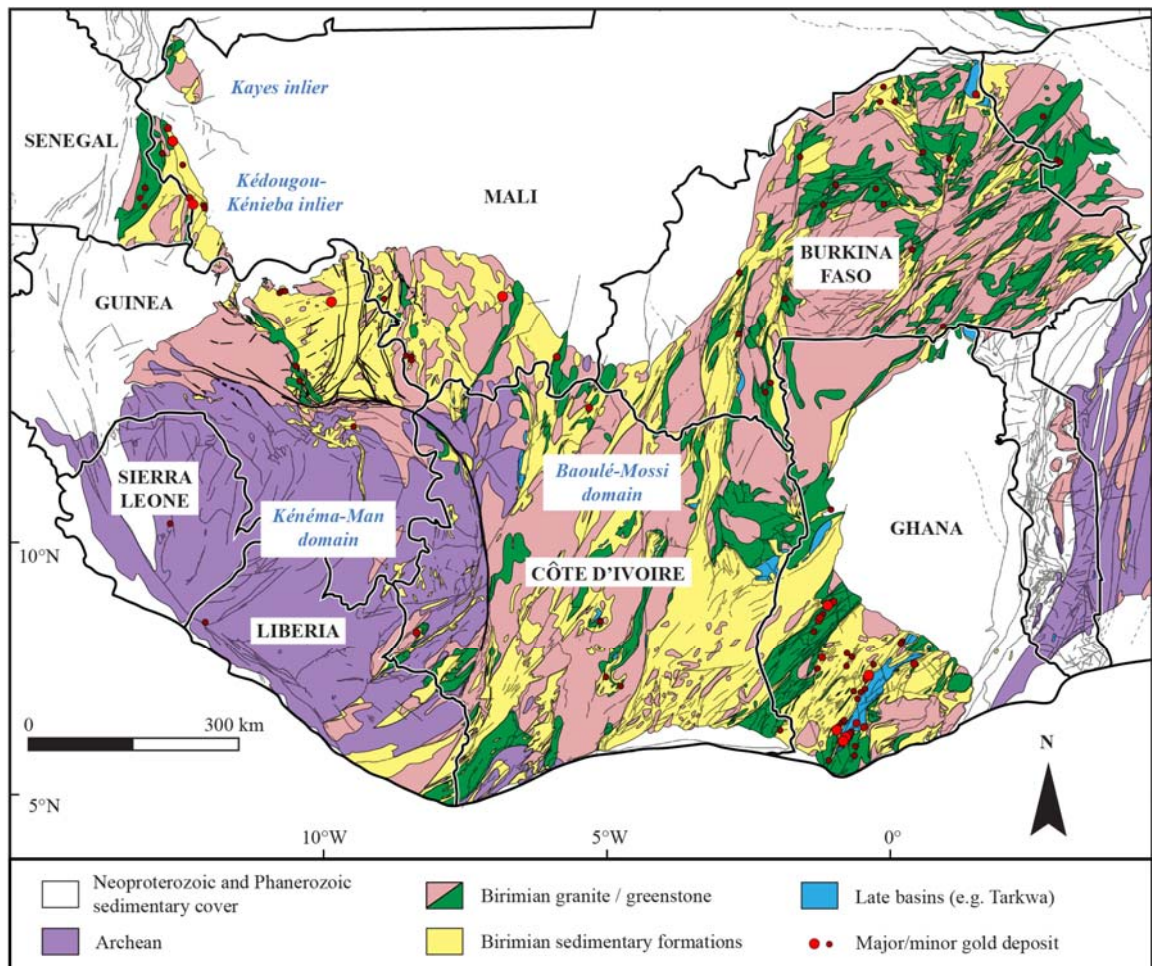


Figure 1. Geological map of the West African Craton (modified after Milési et al., 2004 SIGAfrique map, Lebrun et al., in press).

The Sadiola-Yatela gold district is located in the Malian northeastern part of the inlier (Fig. 3). The region displays widespread evidence of ancient and recent artisanal mining, with written records of mining dating back more than 250 years (public data from IAMGold website, 2015). The bulk of gold mineralisation in the district is hosted by carbonates, which is atypical for orogenic gold deposits worldwide (e.g., Goldfarb et al., 2005). Gold deposits of the district have been studied by geological consultants and during a 2-years-long one-on-one project involving researchers from the University of Witwatersrand in South Africa. The considered studies identified distinct styles of gold deposits on the basis of differing geological characteristics. As of 2012, however, the apparent variability in mineralisation styles led to contrasted interpretations that remained to be effectively integrated with knowledge of the camp-scale to regional context. The concept of this study was to understand the underpinning factors that allow integration of the observed variability in gold mineralisation (e.g., structural setting, host rocks, ore and alteration paragenesis) at both the deposit- and camp-scale into a single coherent framework of value to exploration. This multi-scale and multi-disciplinary study relied on the use of the mineral system approach, whereby gold deposits are viewed as local expressions of orogen- to lithospheric-scale processes (e.g., Bierlein et al., 2006; McCuaig et al., 2010; McCuaig and Hronsky, 2014). The results of this study were aimed directly at aiding Brownfield and Greenfield exploration strategies.

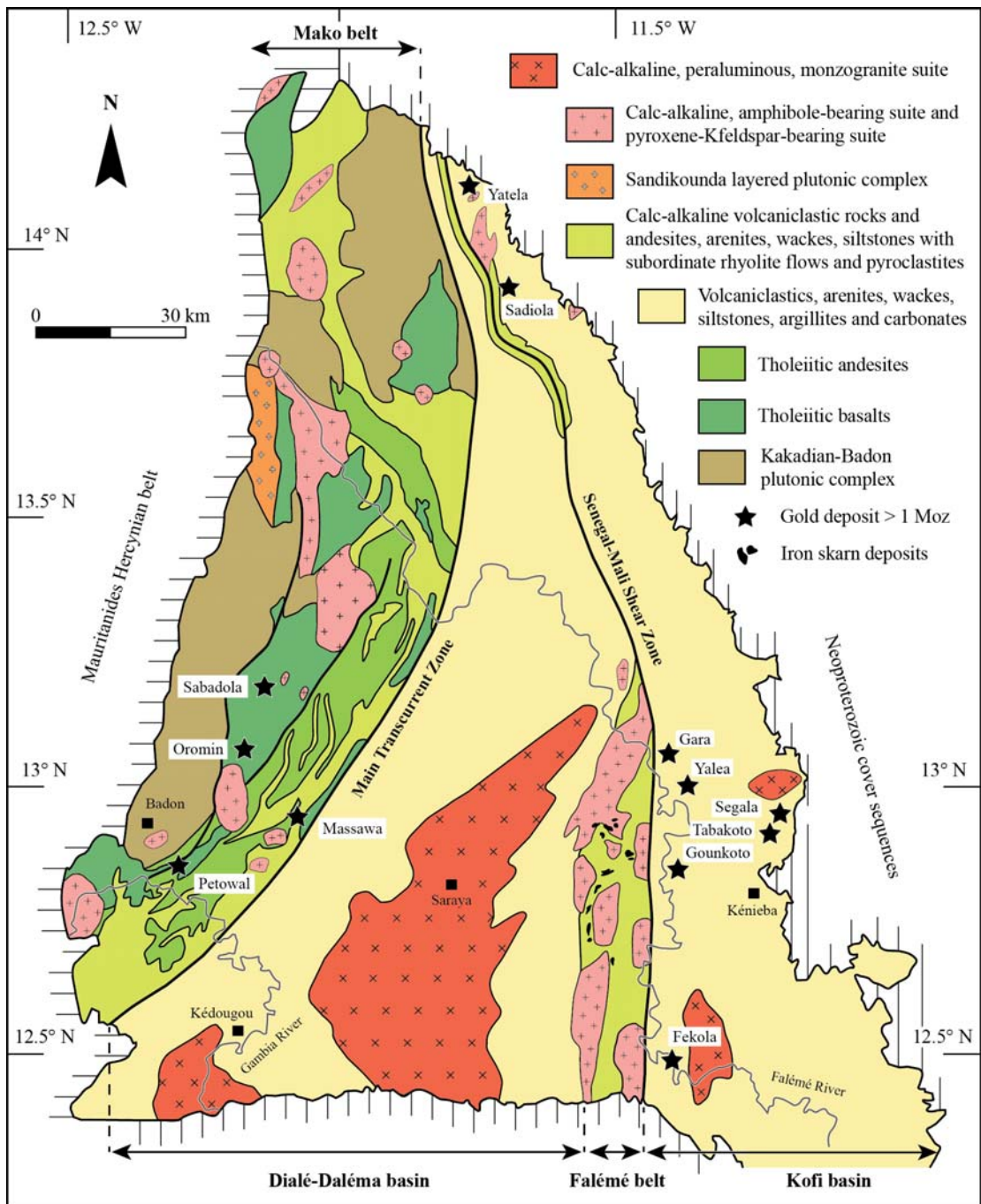


Figure 2. Geologic map of the Kédougou-Kéniéba inlier (1:250,000 scale, modified after Gueye et al., 2007; Lawrence et al., 2013a). Inset map shows the geologic setting of the West African Craton (modified after Boher et al., 1992). The Falémé River forms the international border with Senegal to the west and Mali to the east and north.

2. Aims of the thesis

Based on the knowledge gaps identified in the Sadiola-Yatela gold district, the principal objectives of this study have been to:

- Clarify the geological and structural setting of the deposits;
- Establish an ore and alteration paragenetic sequence integrated with the structural-metamorphic evolution for each deposit;
- Identify the metal enrichment associations of the deposits in order to provide a geochemical footprint to gold mineralisation;
- Characterise the structural evolution of the district by integrating field mapping data with geophysical data-sets;
- Frame the tectonic, magmatic, metamorphic and hydrothermal alteration history of the gold deposits in time with the help of focused U-Pb geochronology;
- Develop an integrated model for the control on location and ore geometry within the Sadiola-Yatela region at the ore shoot, ore body, and district scale.

3. Methodology

This section provides a summary of each method used in the course of the research. Detailed procedures and descriptions of the various analytical methods are provided in each chapter.

3.1. Fieldwork and geological sampling

3.1.1. Geological mapping

The terrain in the Sadiola-Yatela region is flat at an average elevation of 125 m above the sea level. The region is characterized by a thick subtropical weathering profile that has obscured much of the surface geology. Geological mapping was conducted over 12 weeks. It covered all gold deposits of the Sadiola-Yatela mining district (Sadiola

Hill, Tambali, Yatela, Alamoutala, KW18, FE3-North, FE3-South, and FE4) and a representative coverage of the surface outcrops in the region. Systematic face mapping was done on most accessible ramps of the open pits with a particular emphasis on the relationship between deformation, magmatism, hydrothermal alteration and gold mineralisation. 3D geological modelling was performed ahead of the field investigation using Leapfrog® Mining and refined with advancing mapping. The trends of ore shoots in the orebodies were evaluated using three-dimensional rendering of grade control and exploration drill-hole assay data. In addition to the open pit mapping exercise, five regional mapping transects were undertaken using of a rugged tablet containing geophysical data such as magnetics and radiometrics under ArcGIS. Two transects were undertaken across the Senegal-Mali Shear Zone from East to West and two transects investigated sedimentary rocks of the Kofi basin all the way to the escarpment of Neoproterozoic cover.

3.1.2. Diamond drill core logging

Drill core logging was conducted over 4 weeks and included spatially representative diamond drill holes from individual gold deposits (i.e. Sadiola Hill, Tambali, Yatela, Alamoutala, KW18, FE3-North, FE3-South, and FE4). Structural measurements were collected using a rocket launcher device and/or using α - β angles protractors.

3.1.3. Geological sampling

On the basis of the field observations, 215 samples were collected from outcrop in the open pits and diamond drill core. These rock samples were chosen to represent the main structural, lithological, and mineralogical variations observed in the deposits. In addition, 62 samples were collected from outcrops in the field for whole rock geochemistry and petrographic characterisation.

3.2. Analytical techniques

3.2.1. Optical microscopy

A total of 277 polished thin sections were prepared at the University of Western Australia (UWA) and at Vancouver Petrographics Ltd. The database included 62 polished thin sections from regional outcrops, 60 from Sadiola Hill, 58 from Alamoutala, 41 from Yatela, 10 from FE3-FE4, and 14 from KW18. Transmitted and reflected light optical microscopy was used to investigate rock types, alteration textures and intensities, ore mineralogy, and strain fabrics in magmatic and sedimentary rocks of the region. Such study took place at the Centre for Exploration Targeting (UWA) and enabled prioritisation of samples for higher resolution microscopy.

3.2.2. Scanning Electron Microscopy

Backscattered electron (BSE) imaging and mineral chemistry analyses were obtained using a Tescan Vega3 XM SEM equipped with an Oxford instrument X-ACT energy dispersive detector (EDS) at the Centre for Microscopy, Characterisation and Analysis (UWA). The analytical software used to collect semi-quantitative micro-analyses was the Oxford Instruments® INCA analytical suite.

3.2.3. Electron Probe Microanalyser

A JEOL JXA-8530F hyperprobe (EPMA) fitted with 5 wavelength-dispersive spectrometers was used to collect quantitative data on silicates and ore minerals at the Centre for Microscopy, Characterisation and Analysis (UWA). The analytical software used to collect quantitative data was the Probe softwares® Probe for EPMA. Multi-elemental X-ray mapping of minerals was carried out by WD spectrometry. Mineral mapping results were processed off-line with the CalcImage® software.

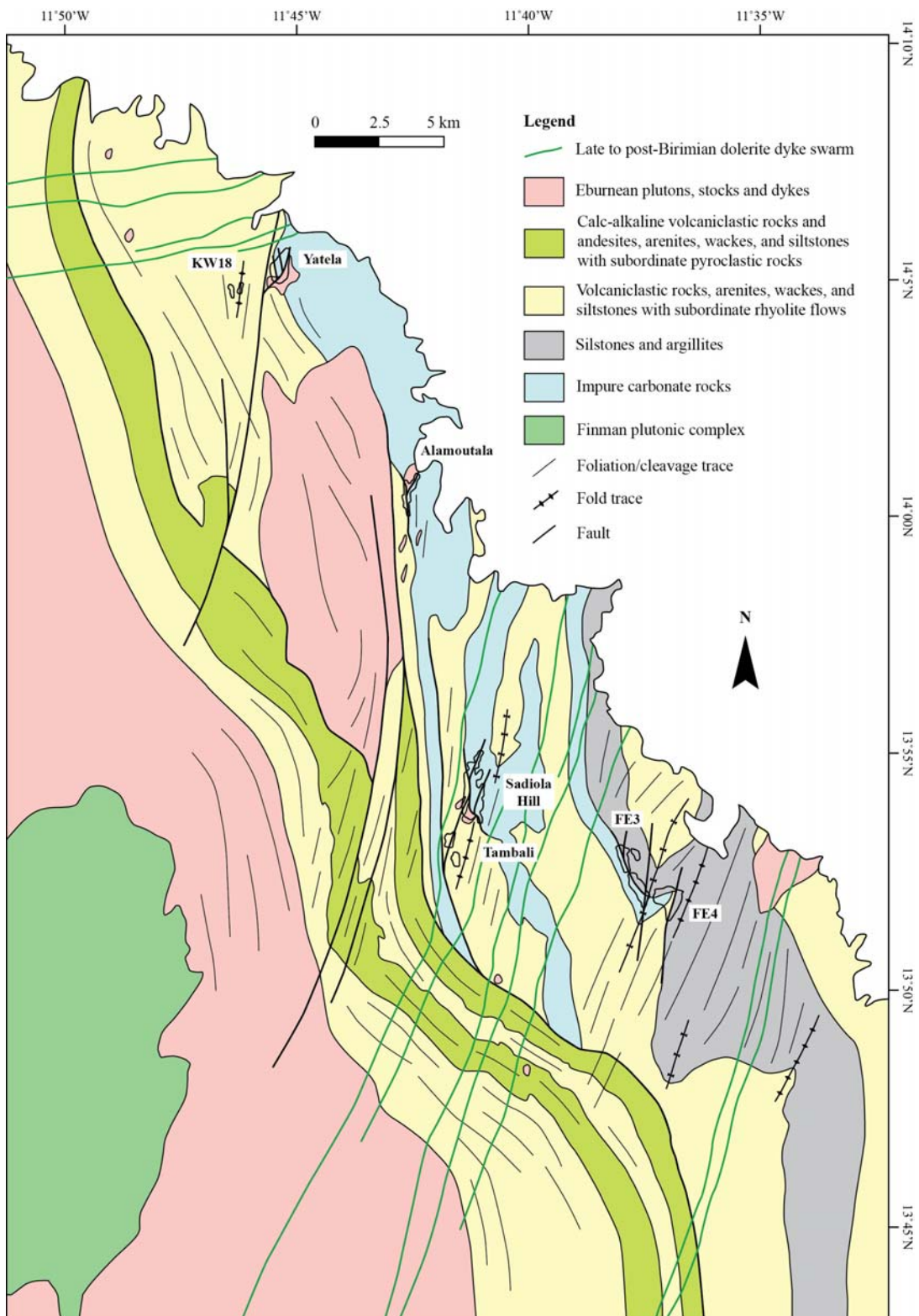


Figure 3. Geology of the Sadiola-Yatela region based on field investigation by the authors and interpretation of SEMOS geophysical data sets.

3.2.4. Whole-rock geochemistry

Least-altered samples of representative igneous rocks in the Sadiola-Yatela region were analysed for major and trace elements at the Intertek Genalysis Laboratory in Perth. Major elements were measured by XRF spectrometry. REE, HFSE and trace elements (e.g., Ba, Cr, Cs, Ga, Rb, Sc, Sn, Sr, U, V, W) were analysed by inductively coupled plasma mass spectrometry (ICP-MS) and inductively coupled plasma optical emission spectrometry (ICP-OES). The Geological Survey of Western Australia Bunbury basalt and Kerba granite standards were analysed during each session to monitor accuracy and instrument stability.

3.2.5. U-Pb Geochronology

U–Pb analyses on magmatic zircons were performed using the sensitive high-resolution ion microprobe (SHRIMP II) at the John de Laeter Centre of Excellence for Mass Spectrometry in Curtin University (Western Australia) using standard operating procedures similar to those described by Compston et al. (1984) and Wingate and Kirkland (2013). Data reduction was carried out using the softwares SQUID and ISOPLOT (Ludwig, 2003, 2009).

3.2.6. Laser Ablation - Inductively Coupled Plasma Mass Spectrometry

In situ trace element concentrations in sulphides were determined by LA-ICPMS at the Géosciences Montpellier laboratories (France). Analyses were performed using a Geolas (Microlas) Excimer ArF automated platform housing a 193 nm Compex 102 nanosecond laser from LambdaPhysik, coupled with a high-resolution ThermoFinnigan (ELEMENT XR) ICP-MS. Trace element concentrations were calculated following the procedure in Longerich et al. (1996), using Laflamme-Po-726 (Sylvester et al., 2005) and MASS-1 (Wilson et al., 2002) as external calibrators, and taking ^{57}Fe as the internal calibrator. Raw data were processed using the WaveMetrics® Igor Pro analytical suite and the GLITTER software package.

4. Structure of the thesis

This thesis is presented as a series of four manuscripts tied together by an introduction (chapter I) and a conclusion chapter (chapter VI). Such design follows the University of Western Australia regulations outlined in the Postgraduate Research and Scholarship handbook. Each manuscript is designed as a self-standing publication that includes background information on regional geology and consequently, minor overlap is to be expected between the chapters/manuscripts. At the time of submission of this thesis (i.e. October 2015), two manuscripts (chapters II and III) have been accepted for publication in the Economic Geology Special Issue about the West African Craton. The third manuscript (chapter IV) has been accepted for publication in the Journal of African Earth Sciences. The last manuscript (chapter V) will be sent to Precambrian Research following submission of this thesis.

The first manuscript (chapter II) presents the geology, tectonic setting, hydrothermal alteration, and ore mineralogy of the world-class Sadiola Hill carbonate-hosted gold deposit. The documented results are integrated with available data on other gold deposits in the Kédougou-Kénieba inlier to form the basis of a metallogenic model.

The second manuscript (chapter III) presents the geology, tectonic setting, contact metamorphism, absolute timing and whole rock geochemistry of the local intrusive stocks, hydrothermal alteration, and ore mineralogy of the Alamoutala gold deposit. The results are used to discuss the possible links between local magnetite skarn formation and regional orogenic gold mineralisation in the Kédougou-Kénieba inlier.

The third chapter (chapter IV) focuses on the Yatela gold deposit, which is unique with respect to mineralisation types encountered in West Africa because the gold resource is hosted by a gold-rich dissolution residue derived from an underlying low-grade, sub-economic Birimian occurrence.

The fourth manuscript (chapter V) provides a regional synthesis. It aims (i) to document for the first time the petrographical-geochemical characteristics and absolute timing of

representative igneous rocks in the Sadiola-Yatela region and (ii) to place them into a regional geological framework with respect to polycyclic deformation and gold mineralisation. The results are used to discuss the tectono-magmatic evolution of the Kédougou-Kénieba inlier and geodynamic implications.

The four manuscripts form sections of a coherent study on 4D evolution of the Sadiola-Yatela gold system by integrating the structural, metamorphic and alteration history of the gold deposits. This study can be regarded as a multi-scale approach and zooms out from the deposit scale (chapter II-III-IV) to the district scale (chapter V).

The conclusion (chapter VI) summarises the key messages of this thesis and their implication for exploration targeting. The chapter also includes a discussion on possibilities for future work.

Electronic Appendices are attached to this thesis. Appendix A corresponds to a co-authored manuscript (candidate as fourth co-author) accepted for publication in the Journal of African Earth Sciences. Electronic appendices B, C, D, and E are related to the fourth manuscript (chapter V). Appendix B contains whole rock geochemistry data for representative igneous rocks from the Sadiola-Yatela region. Appendix C contains U-Pb geochronology data for selected igneous rocks from the Sadiola-Yatela region. Individual geochronology reports are provided in Appendix D. Appendix E presents outcrop, hand specimen and petrographic descriptions for representative igneous rocks from the Sadiola-Yatela region.

5. Justification of thesis format and authorship

A number of collaborators from different institutions worldwide contributed to this PhD study. The candidate confirms that each manuscript has been read and approved by all named co-authors and that no other persons who satisfied the criteria of authorship are not listed. The contributions made by the PhD candidate and each co-author are as follow.

Chapter II: the manuscript is first authored by the candidate Quentin Masurel and co-authored by Nicolas Thébaud, John Miller, Stanislav Ulrich, Kim A.A., Hein, Greg Cameron, Didier Beziat, Olivier Bruguier, and James A. Davis. The candidate was the main scientific investigator and is responsible for writing the manuscript. Nicolas Thébaud, John Miller and Stanislav Ulrich spent time with the candidate in the field and contributed to structural data collection. The considered co-authors also provided insightful reviews that helped frame the manuscript into the suitable high standard for Economic Geology. Greg Cameron and Kim A.A. Hein communicated deposit-scale field observations and provided excellent scientific feedback on the presented data. Didier Beziat and Olivier Bruguier provided their expertise for the collection and interpretation of LA-ICPMS data on sulphides. James A. Davis provided editorial comments for the manuscript.

Chapter III: the manuscript is first authored by the candidate Quentin Masurel and co-authored by Nicolas Thébaud, John Miller, Stanislav Ulrich, Malcolm P. Roberts, and Didier Béziat. The candidate was the main scientific investigator and is responsible for writing the manuscript. Nicolas Thébaud, John Miller and Stanislav Ulrich spent time with the candidate in the field and helped gather geological observations. Nicolas Thébaud and John Miller also provided insightful reviews that helped frame the manuscript into the suitable high standard for Economic Geology. Malcolm Roberts assisted with data collection using the electron probe microanalyser on garnet, pyroxene and magnetite. Malcolm Roberts also helped with data processing and provided insights on skarn mineralogy. Didier Béziat provided editorial comments and feedback on data interpretation.

Chapter IV: the manuscript is first authored by the candidate Quentin Masurel and co-authored by John Miller, Kim A.A. Hein, Eric Hanssen, Nicolas Thébaud, Stanislav Ulrich, Jean Kaisin, and Samuel Tessougue. The candidate was the main scientific investigator and is responsible for writing the manuscript. John Miller spent time with the candidate in the field and contributed to structural data collection. John Miller also assisted in building a three-dimensional geological model of the deposit under Leapfrog®. Kim A.A. Hein communicated deposit-scale field observations and provided scientific feedback on the presented data. Eric Hanssen is responsible for

drafting the geological cross-section of the Yatela deposit and contributed to the descriptions of the karst infill stratigraphy. Eric Hanssen was critical in establishing the genetic link between primary gold mineralisation and the auriferous residuum at Yatela. Nicolas Thébaud, Stanislav Ulrich, Jean Kaisin, and Samuel Tessougue provided scientific reviews and constructive comments for the manuscript.

Chapter IV: the manuscript is first authored by the candidate Quentin Masurel and co-authored by Nicolas Thébaud, John Miller, Stanislav Ulrich. The candidate was the main scientific investigator and is responsible for writing the manuscript. Nicolas Thébaud, John Miller and Stanislav Ulrich spent time with the candidate in the field and contributed to structural data collection. U-Pb geochronology work (zircon mount making, imaging and SHRIMP data collection) was undertaken by the candidate under the supervision of Nicolas Thébaud. John Miller provided re-processed geophysical data used as a base for the making of district-scale geological map. John Miller also contributed to the interpretation of the structural evolution of the Sadiola-Yatela district. Stanislav Ulrich provided a comprehensive appraisal of the study and constructive scientific reviews.

Electronic Appendix A: the manuscript entitled “The Yatela gold deposit: 2 billion years in the making” has recently been accepted for publication in the Journal of African Earth Sciences. It is first authored by Kim A.A. Hein and co-authored by Irvin R. Matsheka, Olivier Bruguier, the candidate Quentin Masurel, Delphine Bosch, Caby Renaud, and Patrick Monié. The candidate is responsible for writing the U-Pb geochronology section on the Yatela feldspathic wacke and diorite, and associated analytical procedures. The candidate also provided feedback and constructive reviews for the manuscript.

6. Supporting references

In addition to the manuscripts intended for publication listed above, the PhD candidate has written a number of abstracts printed in international conference volumes and two short papers for the Mineral Atlas Monograph of the West African Craton to be published in Ore Geology Reviews in 2016.

6.1. Short scientific communication

Masurel, Q., Thébaud, N., Miller, J., Ulrich, S., Hein, K.A.A., accepted with minor revisions. The world-class Sadiola Hill gold deposit in Mali, West Africa. Ore Geology Reviews.

Masurel, Q., Thébaud, N., Miller, J., Ulrich, S., Hein, K.A.A., accepted with minor revisions. The Alamoutala carbonated-hosted gold deposit in Mali, West Africa. Ore Geology Reviews.

6.2. Peer-reviewed abstracts

Masurel, Q., Miller, J., Thébaud, N., McCuaig, T.C., Ulrich, S., 2013, Structural setting and mineralisation of the carbonate-hosted Sadiola gold deposit, Mali, West Africa. SGA-12th biennial meeting, “Mineral deposits research for a high-tech world”, Uppsala, Sweden, August 12-15.

Masurel, Q., Thébaud, N., Miller, J., Ulrich, S., 2014, Tectono-stratigraphic evolution of the Sadiola gold camp, Mali, West Africa: defining the framework of a world-class gold province. Australian Earth Sciences Convention, Newcastle, NSW, Australia, July 7-10.

Masurel, Q., Thébaud, N., Miller, J., Ulrich, S., Terblanche, O., 2014, The world-class Sadiola gold camp, Mali, West Africa: evidence for contrasted styles of carbonate-

hosted gold mineralisation within an orogenic gold province. Gold14@Kalgoorlie International Symposium, Kalgoorlie, WA, Australia, October 8-10.

Masurel, Q., Thébaud, N., Miller, J., Ulrich, S., 2014, Tectonics, magma generation, and gold endowment: A study of the mineralization styles in the Sadiola gold camp, Mali, West Africa. SEG 2014, “Building Exploration Capability for the 21st Century”, Keystone, Colorado, USA, September 27-30.

Masurel, Q., Thébaud, N., Miller, J., Ulrich, S., Hein, K.A.A., 2015, The geology and mineralogy of the Sadiola-Yatela gold camp, Mali, West Africa: contrasted mineralisation styles derived from a dynamic hydrothermal system in the late Eburnean and post-Birimian karstification-weathering processes. SGA-13th biennial meeting, “Mineral resources in a sustainable world”, Nancy, France, August 24-27.

7. Summary declaration

I declare that I am responsible for all portions of this thesis, except for collaborative work as acknowledged above. I have not presented any material included in this thesis for a degree at any other university.

8. References

- Abouchami, W., Boher, M., Michard, A. and Albarede, F., 1990, A major 2.1 Ga event of mafic magmatism in West Africa: an early stage of crustal accretion: Journal of Geophysical Research, v. 95, p. 17605-17629.
- Allibone, A.H., McCuaig, T.C., Harris, D., Etheridge, M.A., Munroe, S., Byrne, D., Amanor, J., and Gyapong, W., 2002a, Structural controls on gold mineralization at the Ashanti gold deposit, Obuasi, Ghana: Society of Economic Geologists Special Publication, v. 9, p. 65–93.
- Allibone, A.H., Teasdale, J., Cameron, G., Etheridge, M.A., Uttley, P., Soboh, A., Appiah-Kubi, J., Adanu, A., Arthur, R., Mamphrey, J., Odoom, B., Zuta, J., Tsikata, A., Patave, F., Famiyeh, S., and Lamb, E., 2002b, Timing and structural

- controls on gold mineralization at the Bogoso gold mine, Ghana, West Africa: Economic Geology, v. 97, p. 949–969.
- AMIRA International P934A West African Exploration Initiative – Stage II, Final Report, Appendix, p. 463-498.
- Bering, D., Brinckmann, J., Camara, N., Diawara, M., Gast, L., and Kieita, S., 1998, Evaluation de l'inventaire des ressources minérales de Guinée: Hannover, Bundesanstalt für Geowissenschaften und Rohstoffe, 109 p.
- Bierlein, F.P., Groves, D.I., Goldfarb, R.J., and Dubé, B., 2006, Lithospheric controls on the formation of provinces hosting giant orogenic gold deposits: Mineralium Deposita, v. 40, p. 874-886.
- Boher, M., Abouchami, W., Michard, A., Albarede, F., and Arndt, N.T., 1992, Crustal Growth in West Africa at 2.1 Ga: Journal of Geophysical Research, v. 97, p. 345-369.
- Bosse, H.R., Gwosdz, W., Lorenz, W., Markwich, H., Roth, W., and Wolff, F., 1996, Limestone and dolomite resources of Africa: Geologisches Jahrbuch, D102, 3-532.
- B2Gold, 2015, Press release, B2Gold announces filling of thecnical report on the Fekola project. Accessed in 2015 on website <http://www.b2gold.com>.
- Feybesse, J.L., Billa, M., Guerrot, C., Duguey, E., Lescuyer, J.L., Milesi, J.P., and Bouchot, V., 2006, The paleoproterozoic Ghanaian province: Geodynamic model and ore controls, including regional stress modeling: Precambrian Research, v. 149, p. 149-196.
- Fougerouse, D., Micklethwaite, S., Ulrich, S., Miller, J., Godel, B., Adams, D. T. and McCuaig, T. C., in press, Evidence for two stages of mineralization in West Africa's largest gold deposit: Obuasi, Ghana: Economic Geology.
- Goldfarb, R.J., Baker, T., Dubé, B., Groves, D.I., Hart, C.J.R., and Gosselin, P., 2005, Distribution, character, and genesis of gold deposits in metamorphic terranes: Economic Geology 100th Anniversary Volume, p. 407–450.
- Goldfarb, R.J., Groves, D.I., and Gardoll, S., 2001, Orogenic gold and geologic time: a global synthesis: Ore Geology Reviews, v. 18, p. 1-75.
- Groves, D.I., Goldfarb, R.J., Robert, F., and Hart, C.J.R., 2003, Gold Deposits in Metamorphic Belts: Overview of Current Understanding Outstanding Problems, Future Research, and Exploration Significance: Economic Geology, v. 98, p. 1-29.

- Groves, D.I., Goldfarb, R.J., Gebre-Mariam, M., Hagemann, S.G., and Robert, F., 1998, Orogenic gold deposits: A proposed classification in the context of their crustal distribution and relationship to other gold deposit types: *Ore Geology Reviews*, v. 13, p. 7-27.
- Hammond, N., Robb, L., Foya, S., and Ishiyama, D., 2011, Mineralogical, fluid inclusion and stable isotope characteristics of Birimian orogenic gold mineralization at the Morila Mine, Mali, West Africa: *Economic Geolog*, v. 39, p. 218-229.
- IAMGold, 2015, public data from <http://www.iamgold.com/Operations/Operating-Mines/Yatela-GoldMine>.
- Lambert-Smith, J., 2014, The geology, structure and metallogenesis of the world class Loulo-Bambadji Au district in Mali and Senegal, West Africa: Ph.D. Thesis, Kingston University London, U.K., 346 p.
- Lawrence, D.M., Treloar, P.J., Rankin, A.H., Harbidge, P., and Holliday, J., 2013a, The Geology and Mineralogy of the Loulo Mining District, Mali, West Africa: Evidence for Two Distinct Styles of Orogenic Gold Mineralization: *Economic Geology*, v. 108, p. 199-227.
- Lawrence, D.M., Treloar, P. J., Rankin, A.H., Boyce, A., and Harbidge, P., 2013b, A Fluid Inclusion and Stable Isotope Study at the Loulo Mining District, Mali, West Africa: Implications for Multifluid Sources in the Generation of Orogenic Gold Deposits: *Economic Geology*, v. 108, p. 229-257.
- Lebrun, E., Miller, J., Thébaud, N., Ulrich, S., McCuaig, T.C., in press, Structural controls on an orogenic gold system: the world-class Siguiri gold district, Siguiri basin, Guinea, West Africa: *Economic Geology*.
- Lebrun, E., Thébaud, N., Miller, J., Ulrich, S., Bourget, J. and Terblanche, O., in press, Geochronology and lithostratigraphy of the Siguiri district: implications for gold mineralisation in the Siguiri Basin (Guinea, West Africa): *Precambrian Research*.
- McFarlane, C. R. M., Mavrogenes, J., Lentz, D., King, K., Allibone, A., and Holcombe, R., 2011, Geology and Intrusion-Related Affinity of the Morila Gold Mine, Southeast Mali: *Economic Geology*, v. 106, p. 727-750.
- McCuaig, T.C., and Hronsky, J.M.A., 2014, The Mineral System Concept: The Key to Exploration Targeting: *Society of Economic Geologists Special Publication*, v. 18, p. 153-175.

- McCuaig, T.C., Beresford, S., and Hronsky, J.M.A., 2010, Translating the mineral systems approach into an effective exploration targeting system: Ore Geology Reviews, v. 38, p. 128-138.
- Milési, J.P., Feybesse, J.L., Pinna, P., Deschamps, Y., Kampunzu, H., Muhongo, S., Lescuyer, J.L., Le Goff, E., Delor, C., and Billa, M., 2004, Geological map of Africa 1:10,000,000, SIGAfrique project: 20th Conference of African Geology, BRGM, Orléans, France, p. 2-7.
- Oberthür, T., Vetter, U., Davis, D.W., and Amanor, J.A., 1998, Age constraints on gold mineralization and Paleoproterozoic crustal evolution in the Ashanti belt of southern Ghana: Precambrian Research, v. 89, p. 129-143.
- Parra-Avila, L.A., Bourassa, Y., Miller, J., Perrouty, S., Fiorentini, M., and McCuaig, T.C., in press, Age constrains of the Wassa and Benso mesothermal gold deposits, Ashanti belt, Ghana, West Africa: Journal of African Earth Sciences.
- Pigois, J.P., Groves, D.I., Fletcher, I.R., McNaughton, N.J., and Snee, L.W., 2003, Age constraints on Tarkwaian paleoplacer and lode-gold formation in the Tarkwa-Damang district, SW Ghana: Mineralium Deposita, v. 38, p. 695-714.
- ToroGold, 2015, Mako project Definitive Feasibility Study overview. Accessed in 2015 on website <http://www.torogold.com/en/projects/>

Chapter II. Sadiola Hill: a world-class carbonate-hosted gold deposit in Mali, West Africa.

Quentin Masurel^{1*}, Nicolas Thébaud¹, John Miller¹, Stanislav Ulrich², Kim A. A. Hein³, Greg Cameron⁴, Didier Béziat⁵, Olivier Bruguier⁶, James A. Davis¹

¹Centre for Exploration Targeting, The University of Western Australia, 35 Stirling Highway, Crawley, WA, Australia.

²AngloGold Ashanti Australia Limited, Asset Development - Brownfields, 44 St. Georges Terrace, Perth, WA, Australia.

³University of the Witwatersrand, Johannesburg, South Africa.

⁴Cameron and Associates Pty. Ltd., Perth, WA, Australia.

⁵Laboratoire Géosciences Environment Toulouse, UMR-CNRS 5563, Université Paul Sabatier, France.

⁶Geosciences Montpellier, UMR-CNRS 5543, Université de Montpellier, France.

*Corresponding author: qmasurel@hotmail.com

Keywords: Kédougou-Kénieba inlier, Sadiola, carbonate-hosted gold, Eburnean orogeny, Au-As-Sb metal signature.

1. Abstract

The ~8 Moz Sadiola Hill gold deposit is located in the Kédougou-Kénieba inlier, a window of deformed ca. 2200-2050 Ma rocks that outcrops in eastern Senegal and western Mali. The geology of the inlier differs from other Paleoproterozoic granite-greenstone belts and sedimentary basins by the abundance of carbonate rocks. The Sadiola Hill gold deposit occurs within 3 km of the Senegal-Mali Shear Zone and country rocks in the region have undergone polycyclic deformation. The lithostratigraphy of the open pit consists of impure limestones overlain by younger sequences of detrital sedimentary rocks, which include arenite, wacke, and siltstone. The sedimentary rocks have been subjected to regional greenschist-facies metamorphism and have been intruded by multiple generations of syn-kinematic, calc-alkaline stocks and dikes. The bulk of the ore is hosted within a N-S- to NNW-trending, 10- to 50-m-wide, brittle-ductile dilational shear zone defined as the Sadiola Fracture

Zone. Gold lodes also occur along an array of steep NNE-trending shears. Geometric and kinematic analyses indicate that the ore-hosting structures were undergoing sinistral displacement at the time of mineralization, locally defined as the D_{3s} NNW-SSE shortening event. Hydrothermal alteration is polyphase and includes an early high temperature calc-silicate phase (i.e., porphyroblastic growth of actinolite-tremolite) followed by a potassic phase (i.e., biotite-calcite-quartz \pm K-feldspar-tourmaline-actinolite) that was synchronous with ore mineral deposition. Paragenetic studies reveal a multistage ore development that includes an As-rich sulfide stage, followed by an Au-Sb stage. The ore is associated with a metal enrichment suite of Au-As-Sb \pm Cu-Fe-W-Mo-Ag-Bi-Zn-Pb-Te. The Sadiola Hill deposit shares a similar relative timing and structural setting to that of other world-class orogenic gold systems in the West African Craton (e.g. Ashanti, Loulo), with gold deposition occurring during a period of transcurrent tectonics soon after the cessation of region-wide contractional deformation. The high temperature ore and alteration paragenesis at Sadiola Hill is atypical of gold mineralization in the craton and indicates that the late Eburnean tectono-magmatic activity between ca. 2090 and 2070 Ma played an important role in the dynamics of hydrothermal fluid circulation along the Senegal-Mali Shear Zone.

2. Introduction

The Paleoproterozoic terranes of the West African Craton host a number of world-class gold deposits that are related to orogenic processes associated with the ca. 2120-2060 Ma Eburnean orogeny (Milési et al., 1992; Oberthür et al., 1998; Goldfarb et al., 2001; Feybesse et al., 2006; McFarlane et al., 2011; Lawrence et al., 2013a; Treloar et al., 2014; Fougerousse et al., this volume; Lebrun et al., this volume). Within the Kédougou-Kénieba inlier (KKI), the Sadiola and Loulo gold districts contain some of the largest gold endowments in west Africa outside of the Ashanti belt in Ghana. Gold deposits in the inlier are hosted by a wide range of host rocks including mafic volcanics, detrital sedimentary rocks, and carbonates. Host rocks have been subjected to regional greenschist-facies metamorphism and have undergone polycyclic deformation. Gold mineralization in the KKI is interpreted to result from protracted hydrothermal fluid circulation along regional-scale lineaments, which include the Senegal-Mali Shear Zone

(SMSZ) and the Main Transcurrent Zone (MTZ), and along local NNE-trending structures during late-Eburnean tectono-thermal activity between ca. 2090 and 2070 Ma (Schwartz and Melcher, 2004; Lawrence et al., 2013a; Treloar et al., 2014). Despite gold deposits in the KKI sharing a similar relative timing and structural setting, gold mineralization occurs in a variety of styles including epizonal orogenic Au-As-Sb mineralization at Massawa (~3.6 Moz) (Treloar et al., 2014), As-rich orogenic gold mineralization at Yalea (~6.3 Moz), and polymetallic Fe-B-rich orogenic gold mineralization at Gara (~3.1 Moz) (Lawrence et al., 2013a, b). These gold deposits have developed synchronously with the generation of large melt volumes, leading to the possibility of a genetic connection.

Recent studies by Lawrence et al. (2013a, b) and Treloar et al. (2014) have suggested the diversity in mineralization styles and ore paragenesis in the KKI resulted from hydrothermal systems that sourced fluids and metals from both metamorphic and magmatic reservoirs. Such diversity appears to be largely controlled by the distance of the deposits from the regional-scale lineaments and late Eburnean syn-kinematic intrusions. Yalea-style deposits occur along brittle-ductile shears as far as 8 km from the SMSZ and share characteristics typical of Birimian gold mineralization in the Ashanti belt of Ghana. In contrast, a magmatic hydrothermal influence has been suggested for the Gara deposit, which occurs within 2 km of the SMSZ, and shows possible links between gold mineralization and magnetite skarn development in the region (e.g., Falémé iron district). The shear-hosted Massawa deposit occurs within 3 km of the MTZ and is related to a magmatic fluid derived from syn-kinematic quartz-feldspar-porphyry sills. The goal of this contribution is to summarize the geology, tectonic setting, hydrothermal alteration, and ore mineralogy of the Sadiola Hill gold deposit in an attempt to clarify its genesis. The results are then integrated with available data on other world-class gold deposits in the KKI to form the basis of a metallogenetic model.

3. Regional geology

The Sadiola Hill gold deposit is located along the NNE margin of the KKI, which crops out in eastern Senegal and western Mali. This inlier, which consists of a window of deformed Paleoproterozoic terranes, represents the westernmost exposure of

the ca. 2200–2050 Ma Birimian Supergroup of the West African Craton. The KKI is bounded on its western margin by the Hercynian Mauritanides (Villeneuve, 2008) and is unconformably overlain by flat-lying Neoproterozoic sandstones of the Taoudeni intracratonic basin on all other sides (Villeneuve and Cornée, 1994) (inset, Fig. 1). The geology of the KKI can be divided into two volcano-plutonic belts and two sedimentary basins based on the location of two regional-scale lineaments, the MTZ and the SMSZ (Fig. 1). Bassot (1987) defined the Mako belt to the west of the MTZ and the Dialé-Daléma basin to the east. The Falémé belt is recognized as a distinct entity from the Dialé-Daléma basin (Hirdes and Davis, 2002; Lawrence, 2010) and is bordered to the east by the SMSZ. The Kofi basin, as first defined by Klöckner Industrie (1989), is situated east of the SMSZ. The Dialé-Daléma and Kofi sedimentary basins contain the most extensive occurrence of carbonate rocks in the Birimian (Bessoles, 1977).

The Mako belt (Fig. 1) consists of tholeiitic basalts and calc-alkaline andesitic lavas intercalated with minor immature sedimentary and volcaniclastic rocks (Hirdes and Davis, 2002; Dioh et al., 2006; Gueye et al., 2008). The volcanic assemblage has been dated between 2160 ± 16 Ma (Boher et al., 1992; Sm-Nd on whole rock andesite) and 2197 ± 13 Ma (Dia, 1988; Sm-Nd on whole rock basalt). The Mako crustal rocks are intruded by a group of variably deformed syn-tectonic plutons, such as the Tinkoto and Mamakono granodiorites, respectively dated at 2074 ± 9 Ma and 2076 ± 3 Ma (Bassot and Caen-Vachette, 1984; Dia et al., 1997; Hirdes and Davis, 2002; Gueye et al., 2007; U-Pb zircon). Geochemical and isotopic studies of the volcanic package and intrusions from the Mako belt suggest a volcanic arc setting (Dia et al., 1997; Dioh et al., 2006; Pawlig et al., 2006).

The Dialé-Daléma basin (Fig. 1) consists of thick sequences of wackes, arenites, conglomerates, siltstones, and argillites that are intercalated with carbonates, volcaniclastics, andesite lavas, and rhyolitic pyroclastites (Bassot, 1997; Hirdes and Davis, 2002). Conglomerates of the Dialé-Daléma basin host boulders of carbonate from the lower units of the series and pebbles sourced from the Mako belt (Bassot, 1997). Detrital zircons from a quartz wacke in the Dialé-Daléma basin indicate a uniform age of 2165 ± 1 Ma (Hirdes and Davis, 2002; Pb-Pb zircon) for the source material. Rocks of the Dialé-Daléma Series are intruded by the peraluminous, K-rich Saraya granite, which has been dated at 2079 ± 2 Ma (Hirdes and Davis, 2002; U-Pb zircon).

The Falémé belt (Fig. 1) consists of calc-alkaline volcaniclastic rocks, wackes, chert, manganiferous shale, minor andesitic lavas, and local rhyolite flows (Ndiaye et al., 1997; Hirdes and Davis 2002; Lawrence, 2010). The Falémé belt has been intruded by numerous syn-tectonic, belt-type, calc-alkaline granitoids (Ndiaye et al., 1997; Hirdes and Davis, 2002) such as the Boto tonalite dated at 2082 ± 1 Ma and the Boboti granodiorite dated at 2080 ± 1 Ma (Hirdes and Davis, 2002; Pb-Pb zircon). The plutons are spatially and genetically associated with iron skarns of the Falémé district (Schwartz and Melcher, 2004).

The Kofi basin, which is host to the Sadiola Hill deposit, consists of a sequence of carbonates, wackes, arenites, siltstones, and calcareous clastic rocks (Fig. 1) (Lawrence et al., 2013a). Detrital zircons in the Loulo area have been dated between 2156 ± 10 Ma and 2125 ± 8 Ma (Calvez et al., 1990; Pb-Pb zircon). The peraluminous Gamaye leucogranite that intruded the Kofi sediments has been dated at 2045 ± 27 Ma (Bassot and Caen-Vachette, 1984; Rb-Sr on whole rock).

Birimian rocks of the KKI have undergone polycyclic deformation. Early phases of fold-and-thrust tectonics (D_1 - D_2) linked to initial accretion are followed by a period of transcurrent tectonics (D_3 - D_4) (Ledru et al., 1991; Milési et al., 1992; Dabo and Aïfa, 2010, 2011; Diene et al., 2012; Lawrence et al., 2013a; Treloar et al., 2014). A similar polyphase character has been reported in other Birimian terranes of West Africa (e.g., in Ivory Coast, Pouclet et al., 2006; Vidal et al., 2009; in Burkina Faso, Hein, 2010; in Guinea, Lahondère et al., 2002; in southern Mali, McFarlane et al., 2011; in southern Ghana, Feybesse et al., 2006; in Burkina Faso, Baratoux et al., 2011). The SMSZ and MTZ have been interpreted to represent major transpressional faults initiated during D_2 (Lawrence et al., 2013a). The D_3 event is associated with fluid flow and sinistral displacement along the regional-scale lineaments, voluminous calc-alkaline magmatism, and gold mineralization between ca. 2090 and 2070 Ma (Pons et al., 1992; Hirdes and Davis, 2002; Gueye et al., 2007, 2008; McFarlane et al., 2011; Lawrence et al., 2013a; Treloar et al., 2014). The major shear zones acted as the main conduits for hydrothermal fluids in the region, with gold deposits located along lower order N-S splays (e.g., Yalea Shear) and steep NNE-trending sinistral shears that formed during the D_3 deformation (Lawrence et al., 2013a). The D_4 event is associated with a late dextral reactivation between ca. 2070 and 2050 Ma (Dabo and Aïfa, 2011). Available metamorphic data for the KKI point to peak metamorphism under regional greenschist-facies conditions

(Debat et al., 1984; Liégeois et al., 1991; Dia et al., 1997). Hornblende-hornfels contact aureoles have locally been observed surrounding Eburnean granitoids (Debat et al., 1984; Pawlig et al., 2006).

4. Mining background

The Sadiola Hill deposit and satellite occurrences are mined by the Société des Mines d'Or du Mali (SEMODS), a joint venture between AngloGold Ashanti Limited, IAMGold Corporation, and the government of Mali. The region displays widespread evidence of ancient and recent artisanal mining, and written records of mining date back more than 300 years (public data from IAMGOLD website). However, the development of the Sadiola Hill mine began in 1992 and was based on proven and probable reserves amounting to 49.2 Mt of oxide and partly oxidized ore at an average grade of 2.86 g/t Au, representing approximately 4.5 Moz (141 t) of contained gold to an average depth of 140 m (Boshoff et al., 1998). The first gold bar was poured in 1996. Mining ceased in 2011, but evaluation and feasibility studies of the deeper sulfide orebody are in progress, considering new open pit mining and a pushback of the existing pit. As of December 31, 2012, the Sadiola Hill sulfide orebody recorded proven and probable reserves of 3.853 Moz at 1.78 g/t (AngloGold Ashanti Ltd. 2012 mineral resource and ore reserve report).

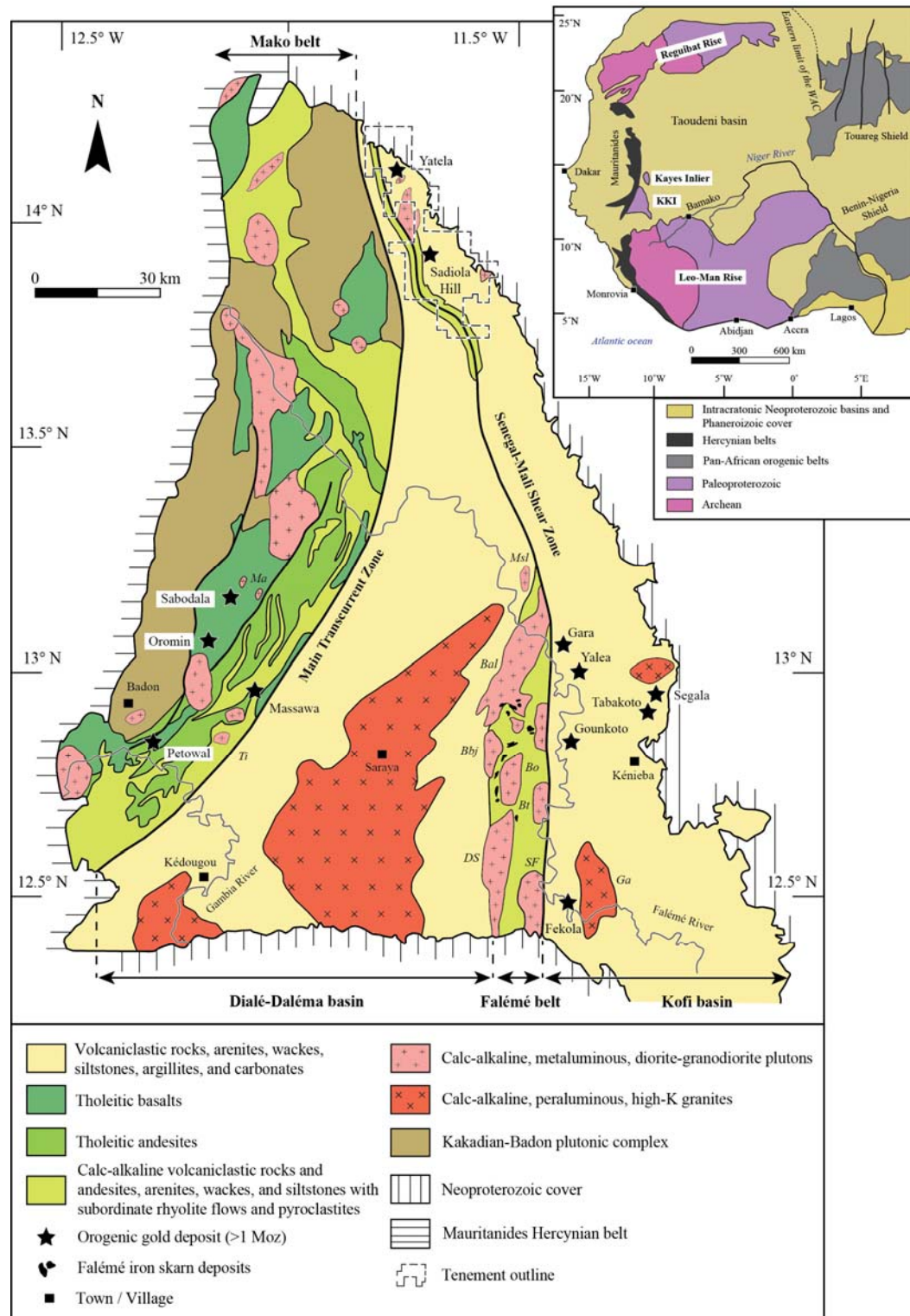


Figure 1. Geologic map of the Birimian Kédougou-Kéniéba inlier (1:250,000 scale, modified after Gueye et al., 2007; Lawrence et al., 2013a). Inset map shows the geologic setting of the West African Craton (modified after Boher et al., 1992). The Falémé River forms the international border with Senegal to the west and Mali to the east and north. Abbreviations refer to plutons mentioned in the text: Bal = Balangouma tonalite, Bo = Boboti granodiorite, Ga = Gamaye granite, Ma = Mamakono granodiorite, SF = South Falémé pluton, Ti = Tinkoto granodiorite.

5. Materials and methods

5.1. Pit mapping, 3D modeling, logging and sampling

Systematic face mapping was completed on all accessible ramps of the mine at the Sadiola Hill deposit. Detailed section logging was undertaken and included 10 diamond drill holes chosen to represent the main structural, lithological, and mineralogical variations observed in the deposit. Petrographic data reported in this paper largely come from drill core samples and, to a lesser extent, from oriented blocks sampled directly in the field. All structural readings are given in true north coordinates. Planar features were reported in strike/dip/quadrant and linear data as plunge and azimuth. In this paper, the “s” subscript indicates that the considered structural event is only valid for the Sadiola district, which may differ from regional structural compilations reported for the West African Craton. The trends of ore shoots in and surrounding the orebody were evaluated using Leapfrog® three-dimensional rendering of the assay data, which combined grade control and exploration.

5.2. Petrographic study

More than 100 samples were collected from diamond drill core and directly in the Sadiola Hill pit. The considered suite of samples included country rocks with various alteration types and intensities, and all ore types. Approximately 100 polished thin-sections were prepared at the University of Western Australia (UWA) and at Vancouver Petrographics Ltd. These were studied using optical microscopy at the Centre for Exploration Targeting at UWA, and scanning electron microscopy and electron microprobe at the Centre for Microscopy, Characterisation and Analysis at UWA. Backscattered electron (BSE) imaging and mineral chemistry analyses were obtained using a Tescan Vega3 XM (SEM) equipped with an Oxford instrument X-ACT energy dispersive spectrometer (EDS) and JEOL JXA-8530F Hyperprobe fitted with five wavelength-dispersive spectrometers (EPMA). Quantitative microanalyses were performed using internal proprietary standards. The analytical software used to collect semi-quantitative micro-analytical data was the Oxford Instruments® INCA

analytical suite on the Tescan Vega 3. Operating parameters for the SEM-EDS include an accelerating voltage of 20 kV, a working distance of 15 mm, a beam current of 1.5 nA, and a detector process time of 4 s. Operating conditions for WD analysis were an accelerating voltage of 20 kV, a beam current of 40 nA, and a counting time of 40 s on peak for sulfides. Mean atomic number background and ZAF corrections were used throughout. The algorithm utilized was that of Armstrong (1988).

5.3. Arsenopyrite geothermometry

Despite being an empirical thermometer, and therefore not fully quantitative, arsenopyrite geothermometry can be used to estimate the temperature of mineralization (Kretschmar and Scott, 1976; Sharp et al., 1985). Quantitative in-situ microanalyses of 20 selected arsenopyrite crystals were performed with a field emission electron microprobe JXA-8530F (EPMA) using internal standard databases. Analytical data are provided in the supplementary material. The lack of optical and chemical zoning of analyzed crystals, the assumption of equilibrium with pyrite-pyrrhotite, and the low content (< 1 wt.%) of combined minor elements along with the suitable Fe content allow for the use of the arsenopyrite geothermometer (Kretschmar and Scott, 1976; Sharp et al., 1985). Crystallization temperatures were determined using the f_{S_2} -buffered arsenopyrite-pyrite-pyrrhotite equilibrium.

5.4. LA-ICPMS on sulfides

A refractory ore component has recently been indentified at the Massawa orogenic gold deposit (Treloar et al., 2014). Multistage ore development included a low-grade (<10 g/t) and high-tonnage As-rich sulfide stage, followed by a high-grade (>10 g/t) and low-tonnage Au-Sb stage. Approximatively 75-90 % of the first stage gold is refractory in nature and occurs as solid solution gold in the crystal lattice of disseminated arsenopyrite and pyrite (Treloar et al., 2014). Laser ablation work was undertaken for the Sadiola Hill deposit following the identification of a similar ore paragenetic sequence to that reported for Massawa. The results were used to assess the potential for a refractory gold ore component and provide insights into the chemical

conditions of the ore-forming fluid. In situ trace element concentrations of arsenopyrite and pyrite grains were determined by laser ablation inductively-coupled plasma mass spectrometry (LA-ICP-MS) at Géosciences Montpellier (France). A total of 44 analyses were collected on four mineralized samples chosen for their mineralogical and micro-textural characteristics. Analyses were performed using a Geolas (Microlas) Excimer ArF automated platform housing a 193 nm Compex 102 nanosecond laser from LambdaPhysik, coupled with a single collector, high-resolution ThermoFinnigan (ELEMENT XR) ICP-MS. Ablation experiments were conducted in an ablation cell of ~30 cm³ in a He atmosphere (0.6 lmin⁻¹). The helium gas stream and particles from the sample were then mixed with Ar (1 lmin⁻¹) before entering the plasma. The laser was fired using a fluence of 12 J/cm² at a frequency of 5 Hz and using a spot size of 51 µm. Trace element concentrations were calculated following the procedure in Longerich et al. (1996), using Laflamme-Po-726 (Sylvester et al., 2005) and MASS-1 (Wilson et al., 2002) as external calibrators, and taking ⁵⁷Fe as the internal calibrator. Raw data were processed using the GLITTER software package (e.g. Velásquez et al., 2014). The following isotopes were monitored: ²⁹Si, ³¹P, ³³S, ³⁴S, ⁴³Ca, ⁴⁷Ti, ⁵¹V, ⁵⁵Mn, ⁵⁷Fe, ⁵⁹Co, ⁶⁰Ni, ⁶⁵Cu, ⁶⁶Zn, ⁷⁵As, ⁸²Se, ⁸⁵Rb, ⁸⁸Sr, ⁹⁰Zr, ⁹⁵Mo, ¹⁰³Rh, ¹⁰⁵Pd, ¹⁰⁶Pd, ¹⁰⁷Ag, ¹¹¹Cd, ¹¹⁸Sn, ¹²¹Sb, ¹²⁵Te, ¹³⁷Ba, ¹³⁹La, ¹⁸²W, ¹⁹⁵Pt, ¹⁹⁷Au, ²⁰⁵Tl, ²⁰⁸Pb, and ²⁰⁹Bi. Trace element data, achieved detection limits, and 1σ errors are provided in the supplementary material.

6. Deposit geology

The Sadiola Hill deposit is located approximately 425 km northwest of the Mali capital Bamako, near the border with Senegal. The terrain surrounding the Sadiola Hill gold mine is flat at an average elevation of 125 m above the sea level. The region is characterized by a thick subtropical weathering profile that has obscured much of the surface geology. Nevertheless, the first-order geological features that characterize the Sadiola Hill gold deposit are outlined below. Host rocks in the Sadiola area have undergone regional greenschist facies metamorphism. For the purpose of clarity, the prefix “meta” will be omitted in the following section.

6.1. Sedimentary rocks

The geology of the Kofi basin in the Sadiola Hill deposit area consists of impure carbonates, wackes, and arenites to the west, progressing to siltstones and argillites towards the east. The structural mapping of the open pit and surrounding outcrops provides evidence for complex folding and stacking of the original strata during the Eburnean orogeny (Fig. 2). Based on pit mapping and core logging, the lithostratigraphy of the Sadiola Hill deposit consists of impure carbonates overlain by younger detrital sedimentary rocks (Fig. 3). The contact between the two rock types is faulted and represented by the N-S- to NNW-trending Sadiola Fracture Zone. Impure limestones (>250 m thick) crop out on the eastern walls of the pit and are interlayered with minor dolomitic horizons. The limestone is well-bedded and characterized by abundant thin (0.2-2 cm) argillaceous-silty interbeds. The impure limestones have recrystallized as silty marbles adjacent to the Sadiola Fracture Zone and, to a lesser extent, along the steep NNE-trending faults. Detrital sedimentary rocks crop out on the western walls of the pit and are dominated by feldspathic wacke, and arkosic arenite with discrete decimeter-scale beds (Fig. 3). Minor siltstone and shale interbeds occur within these coarser-grained packages and are best observed close to the contact with the basal carbonate unit. Well-preserved way-up indicators, such as fining-upwards sequences and rare cross-beds in sandstone, indicate upright beds with a younging direction to the west.

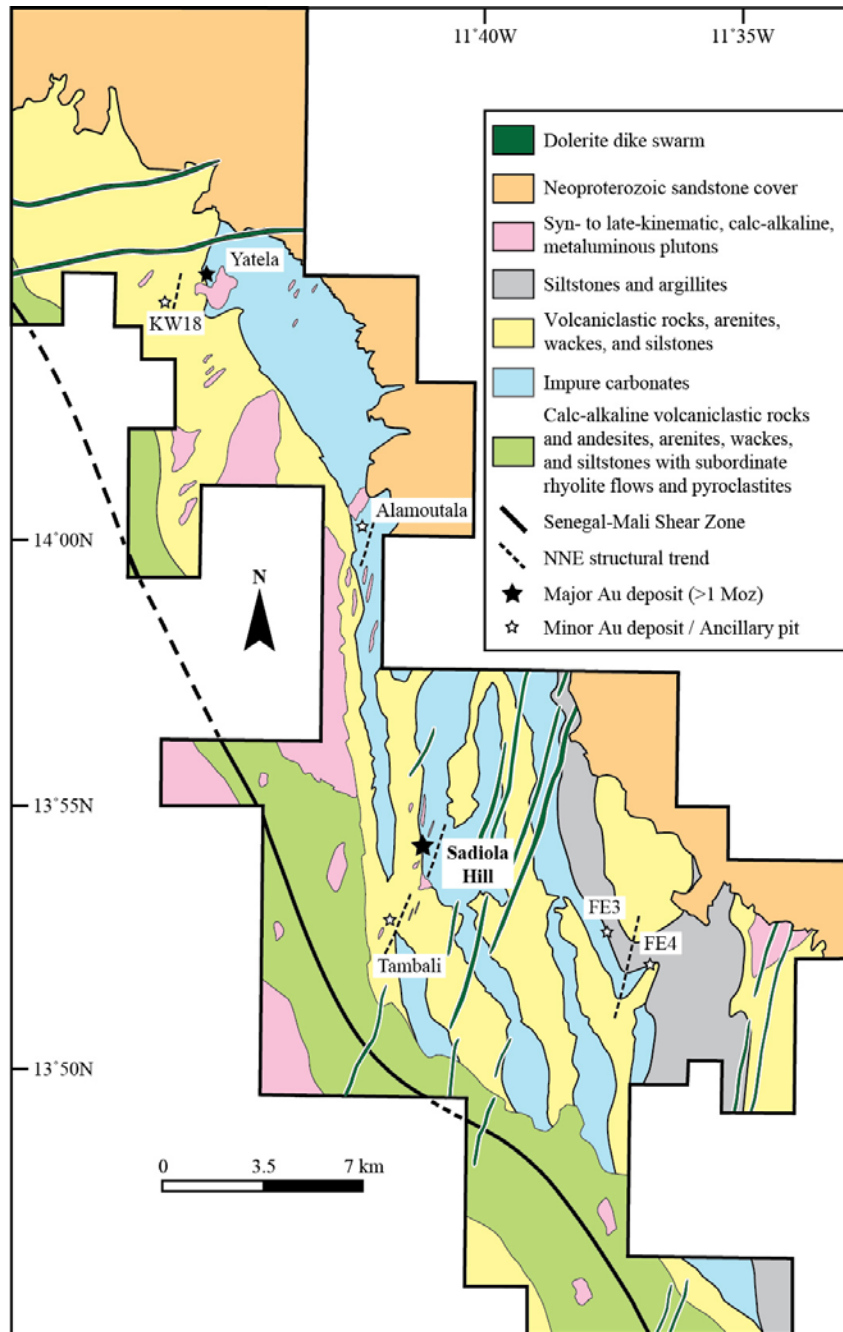


Figure 2. Geology of the Sadiola-Yatela mining and exploration permit based on SEMOS regional map (2014) and field investigation by the authors (scale 1:35,000).

6.2. Intrusions and relationship to metasedimentary rocks

Numerous syn-tectonic granitoids have intruded the sedimentary rocks of the Kofi basin to the east of the SMSZ (Fig. 2). Chemical and detrital sedimentary rocks exposed in the Sadiola Hill open pit are intruded by three successive generations of intrusion, namely early diorite, quartz-feldspar porphyry, and late diorite. All intrusive rocks were affected by the late sinistral shearing.

Diorite stocks, and discontinuous dikes and sills were emplaced parallel to sub-parallel to bedding at the lithostratigraphic contact between carbonate and sandstone units (Fig. 3). The least-altered samples from this suite indicate that the rock is largely composed of plagioclase grains (>80 % modal vol.), which are fine-grained (< 2 mm in size). Magmatic green hornblende is common (5-10 % modal vol.), whereas quartz remains a minor phase (<10 % modal vol.). In drill-core, the main early diorite body to the south of the Sadiola Hill open pit is locally bordered by zones of contact-metasomatized country rocks. Garnet-rich mineral assemblages are observed in the proximal aureole (0-2 m) in silty-marble, whereas pyroxene-rich assemblages tend to dominate further away from the intrusive contact (2-5 m). Retrograde alteration of the garnet-pyroxene exoskarns to a lower temperature hydrous silicate assemblage is minor and characterized by epidote-clinozoisite, calcite, hornblende, quartz, and chlorite, with minor to traces of pyrite and magnetite.

The second generation of intrusions, the quartz-feldspar porphyries, consists of sub-vertical NNE-trending felsic dikes and stocks (Fig. 3). The dikes are generally 1-2 m wide and are spatially associated with NNE-trending faults. These dikes crosscut the first generation diorite bodies, impure carbonates, and detrital sedimentary rocks. Their texture is quartz-feldspar-phyric and their mineralogy is consistent with that of a granite. In thin section, the least-altered samples exhibit sub-rounded sparse quartz (5-10 % modal vol.) and euhedral prismatic feldspar phenocrysts (5-10 % modal vol., plagioclases ≈ K-feldspars) set in a fine-grained (<0.1 mm) to very fine-grained (<0.05 mm) equant quartz-feldspathic groundmass (80-90 % modal volume). The dikes are associated with narrow zones (<1.5 m) of hydraulic fracturing and silicification of country rocks and may contain partially digested greywacke xenoliths.

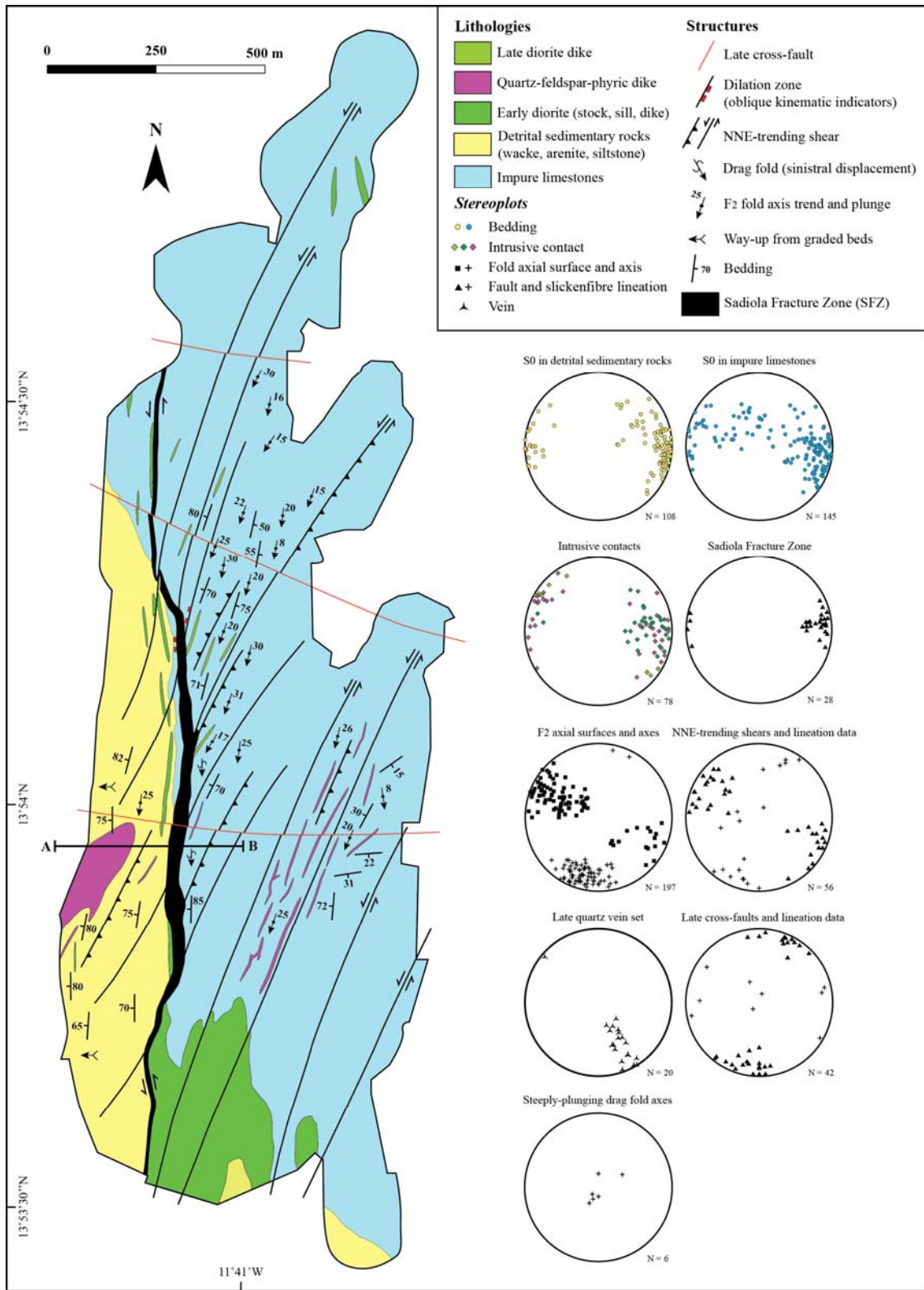


Figure 3. Geological map of the Sadiola Hill main pit and associated structural data. *Equal area stereonets, lower hemisphere convention.

A distinct set of NNE- to NE-trending late diorite dikes (<2 m wide) was identified in the pit (Fig. 3). Although no direct crosscutting relationships could be observed at Sadiola Hill, these dikes crosscut the quartz-feldspar-phyric felsic dikes at the Tambali ancillary pits, which are situated 2 km southwest of the Sadiola Hill deposit (See Fig. 2).

6.3. Structural setting and geometry

The broad structure of the Sadiola Hill open pit is dominated by the N-S to NNW-trending Sadiola Fracture Zone and an array of NNE-trending shears (Fig. 3). Evidence for a complex and polyphase ductile to brittle progressive deformation was recorded in both open pit and diamond drill core. The nomenclature used in this chapter refers to local deformation only.

Ductile deformation (D_{1s} and D_{2s}): The earliest structural component consists of recumbent to sheath folds (F_1) with associated low-angle thrusts (Fig. 4A). Such folding in impure limestones is associated with the development of a weak cleavage (S_1) that is sub-parallel to bedding and a gently NNW-plunging lineation (L_1). This episode of deformation remains unconstrained due to poor exposure and penetrative reworking during later deformation.

The Sadiola Fracture Zone strikes NNW to N-S. It dips moderately to the west and turns to sub-vertical at depth (Fig. 3, 4B). It ranges in thickness from 10-50 m and consists of an anastomosing network of fractures and shears. The associated pinch-and-swell geometry extends both along strike and down dip. Discrete left-hand flexures are marked by shifts in the hangingwall - footwall contact along its strike.

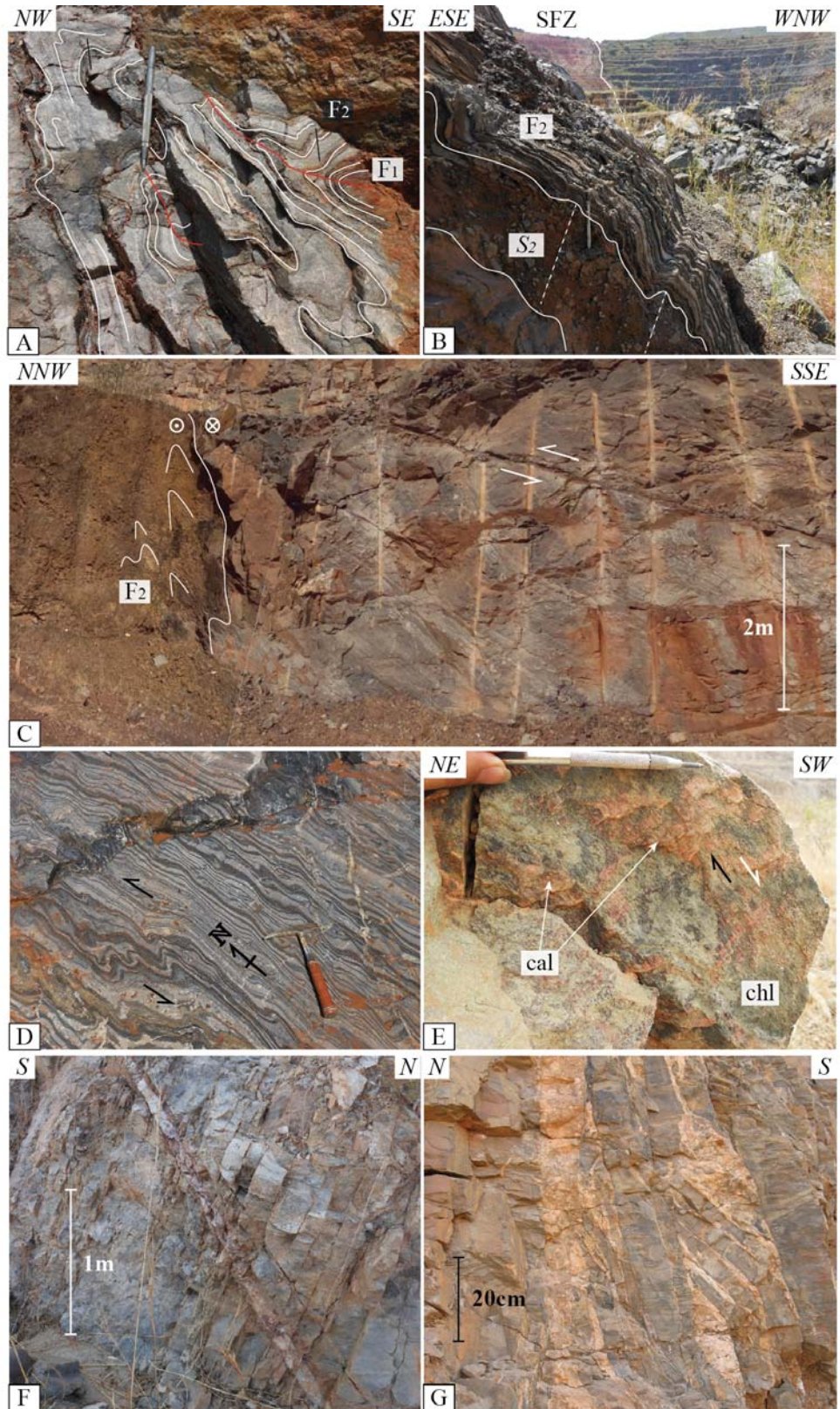
An S_2 fabric oblique to the Sadiola Fracture Zone is associated with refolding (F_2) of F_1 , resulting in a fold interference pattern (Fig. 4A). The F_2 folds are disharmonic with upright to inclined fold hinges. Fold axes plunge gently (15-30°) to the SSW and are associated with a 020°/75E axial-planar cleavage indicative of WNW fold-vergence (Fig. 3, 4B). A number of NNE-trending thrusts and high-angle reverse faults are closely associated with these F_2 folds (Fig. 3, 4C). Quartz-feldspar-phyric dikes are spatially associated with these faults and intrude axial-planar to F_2 folds. Steeply-plunging parasitic folds occur in transposed impure limestones that are located <50 m

from the Sadiola Fracture Zone. They are distinct from typical F₂ folds and exhibit an S-shaped asymmetry indicative of a component of sinistral displacement along the main structure (Fig. 3, 4D). A drag pattern of the F₂ folds into the main structure was also mapped in the open pit and correlates with F₂ folds re-orienting along a N-S axis.

Brittle deformation (D_{3s}): A brittle overprint was recorded in outcrop and drill core and is associated with sinistral reactivation of the NNE-trending high-angle structures and the Sadiola Fracture Zone as well as sinistral slip along S₂ planar fabric (D_{3s}) (Fig. 3, 4C). Importantly, a few NNE-trending fault planes in direct proximity to or within the Sadiola Fracture Zone display oblique slickenfibres indicating sinistral-normal displacement (Fig. 3, 4E). This episode of deformation is linked to the bulk of mineralization on the basis of field relationships and micro-textural observations.

Late brittle deformation (D_{4s} and D_{5s}): Following D_{3s}, a set of late barren extensional quartz veins (<30 cm wide) was preferentially developed in greywackes and quartz-feldspar-phyric dikes (Fig. 3, 4F). The general orientation of these veins is 240°/65°NW. These veins trend at an angle to S₂ and transect F₂ folds. A late generation of WNW-trending sub-vertical brittle faults crosscuts all previously described structures (Fig. 3, 4G). These faults range from 10 cm to over 10 m wide and contain fault gouge and clasts of country rocks. Slickenfibres kinematic indicators measured in the pit indicate an oblique dextral-normal displacement.

Figure 4. Sadiola Hill structural context: A) Interference pattern resulting from refolding of recumbent F₁ by upright F₂ folds. B) Typical field observation of F₂ folding in impure limestones looking down stretching lineation. The Sadiola Fracture Zone (SFZ) is indicated to provide additional structural context. C) Bench view in the central part of the pit illustrating the relationship between F₂ folds, thrusts and high-angle sinistral shears. D) Steeply north-plunging parasitic folds in transposed impure limestones located <50 m east off the Sadiola Fracture Zone. The S-shaped fold asymmetry indicates sinistral movement along the main shear. E) NNE-trending fault wall in proximity to the Sadiola Fracture Zone displays slickenfibres indicating oblique sinistral-normal movement. White arrow indicates apparent movement of missing block. Slickenfibres consist in calcite and chlorite (after biotite?) together with rusty sulfides (e.g., pyrite). F) NE-trending extensional quartz vein cutting across greywacke. G) Late cross-fault; fault breccia consists of impure limestone clasts and dolomite infill.



6.4. Deposit-scale gold distribution

Leapfrog® was used to produce a three-dimensional rendering of the assay data (combined grade control and exploration) in order to better visualize and evaluate trends both within and surrounding the Sadiola deposit orebody. The bulk of the ore is hosted within the brittle-ductile Sadiola Fracture Zone and footwall impure carbonates (Fig. 5). Mineralization also occurs along the array of NNE-trending shears, although gold grade decreases with increasing distance from the Sadiola Fracture Zone (Fig. 5). A minor part of the ore is hosted by detrital sedimentary rocks, quartz-feldspar-porphries, and diorites within the Sadiola Fracture Zone and along the NNE-trending shears. The bulk of the ore is concentrated in the southern half of the pit and correlates with an approximately 45° south-dipping high-grade ore shoot identified on a longitudinal section (Fig. 5). Numerous 20° to 25° south-dipping high-grade ore shoots are also indicated on the surface of the Sadiola Fracture Zone (Fig. 5). Finally, the 3D model shows that some of these high-grade ore shoots coincide with a left-hand (anticlockwise) flexure of the Sadiola Fracture Zone (See Fig. 3).

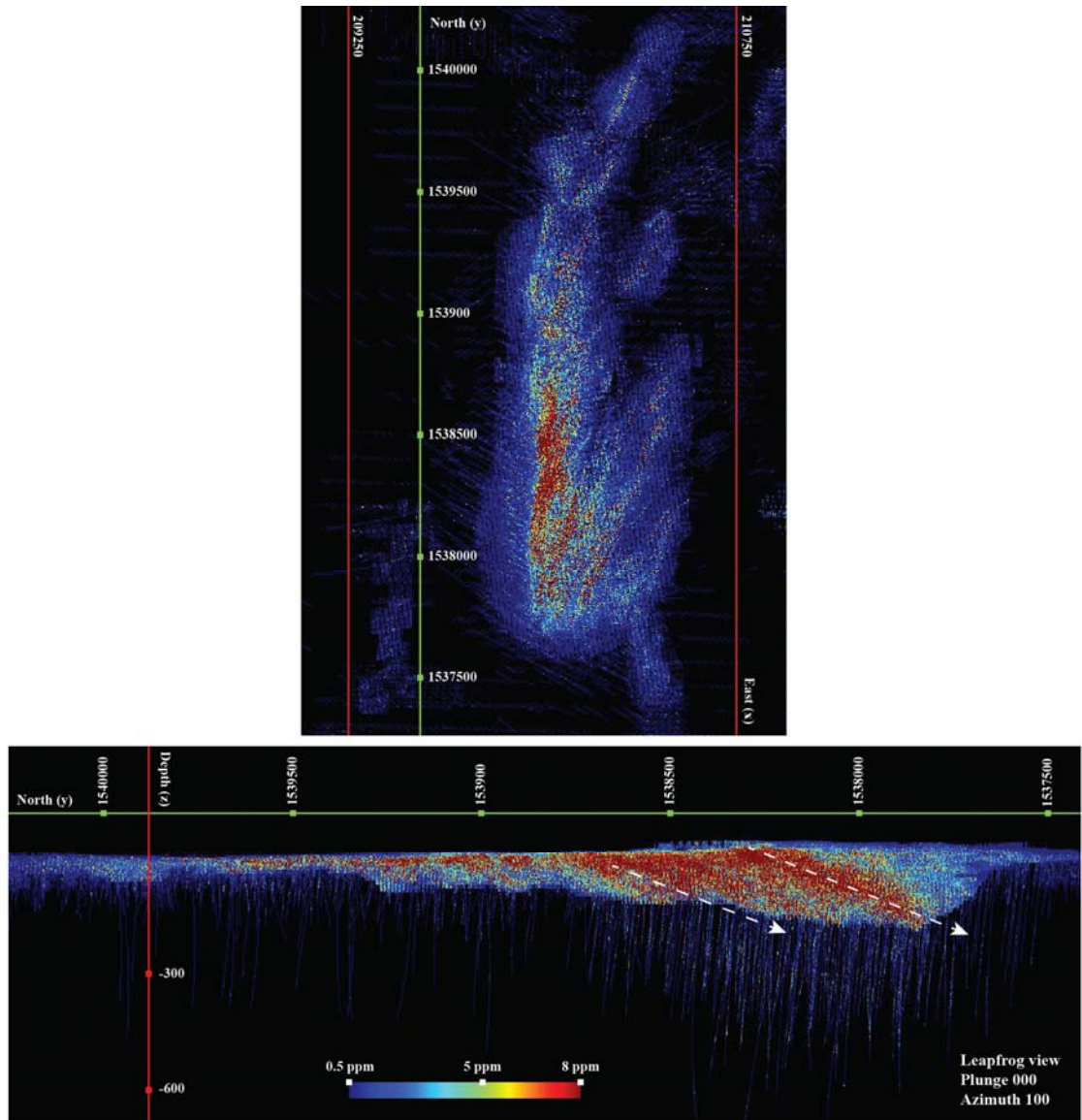


Figure 5. Leapfrog® scenes illustrate structural controls on ore shoot geometry. Data includes combined grade control and exploration assay data. Color-scaled assay value bar is equivalent for both scenes. Note the high grades map out the NNE-trending shears and the Sadiola Fracture Zone in plan view. Also note that south-plunging high grade ore shoots are identified in the longitudinal section.

6.5. Ore styles and textures

Mineralization may be associated with sulfides aligned along the shear fabric in host rocks and with disseminated sulfides in hydrothermal-tectonic breccias, which together define about 50% of the ore. Ore minerals are quite diverse, but their volumetric proportions are typically low in each rock type, ranging from approximately 0.5-3 % sulfides. On the basis of diamond core logging, fabrics displaying a greater degree of deformation correlate with higher sulfide and gold abundances. About 25% of the ore occurs in the form of fine-grained disseminated sulfides in footwall impure limestones, where the distribution of sulfides is controlled by the abundance of argillaceous-silty laminae. Another 20% of the ore is present as biotite-calcite-tourmaline-quartz veins, with sulfides largely confined to the vein walls. Scattered and variably-oriented sulfide veinlets and stringers comprise the remaining 5 % of the ore. A range of ductile to brittle ore textures is observed at the Sadiola Hill deposit. Brittle textures are well-developed in the steeply-dipping segments of the Sadiola Fracture Zone, whereas ductile textures are best-observed in the moderately-dipping segments (Fig. 6). The bedding angular relationship that is observed in cross-section between footwall impure limestones and hangingwall detrital sedimentary rocks corresponds with the change in dip of the Sadiola Fracture Zone at depth (Fig. 6).

Ductile textures are best-observed in the diorite dikes within the Sadiola Fracture Zone, where fine-grained sulfides are consistently aligned parallel to the shear fabric (Fig. 7A). Sheared greywackes in the hangingwall of the Sadiola Fracture Zone exhibit a well-defined fabric marked by sulfides, and by lenses and augen-shaped pods of quartz reflecting deformation of early quartz veins (Fig. 7B). Gold grades in the ductile part of the Sadiola Fracture Zone are commonly >10 g/t. Ductile textures are also observed along the NNE-trending shears in deformed quartz-feldspar-phyric dikes. The dikes exhibit a distinct foliation marked by arsenopyrite crystals and are associated with strong stretching. Quartz porphyroclasts are strained and polycrystalline, whereas feldspar porphyroclasts, more resistant to deformation, exhibit strain shadows. Shear sense indicators in oriented thin sections, such as strain shadow, mica fish, and sigma-shaped porphyroclasts, are compatible with sinistral shearing along S_2 .

Brittle textures are best-observed in deep footwall impure limestones within the Sadiola Fracture Zone (Fig. 7C-D). They consist of randomly oriented dolomite veinlets-stockworks, patchy biotite, and crackle breccias commonly sealed by sulfides. These hydrothermal-tectonic breccias are responsible for wide zones of low to medium grade mineralization that average 1 to 3 g/t Au.

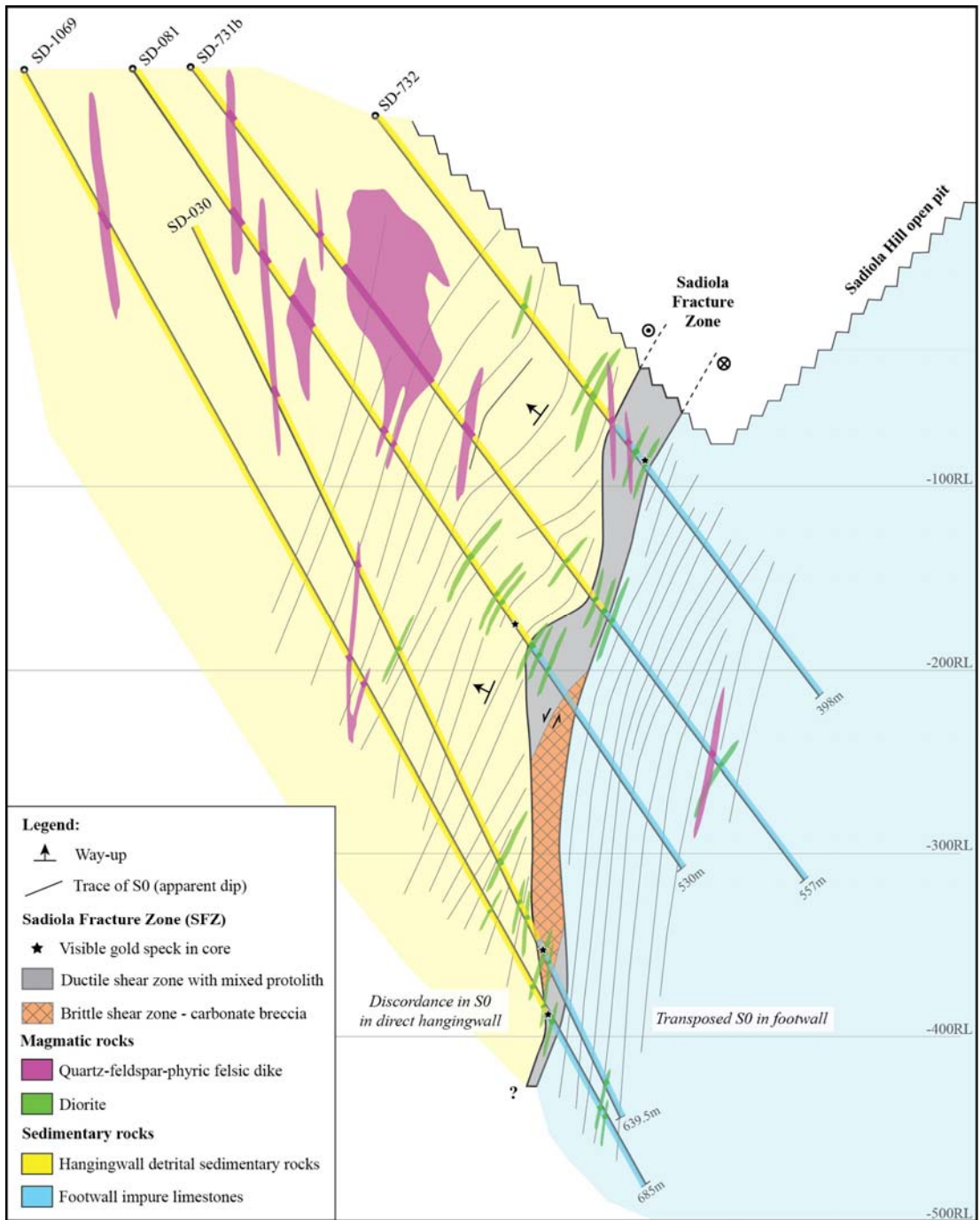


Figure 6. Cross-section through the southern portion of the deposit showing the geometry of the Sadiola Fracture Zone and deep ore body (scale 1:2700). The main structure ranges in thickness from 10 to over 50 m and consists of an anastomosing network of brittle fracture and ductile shear. Interpretative notes illustrate the Sadiola Hill model whereby sinistral shearing associated with a normal component of movement results in enhanced dilation on steeper segments of the fault.

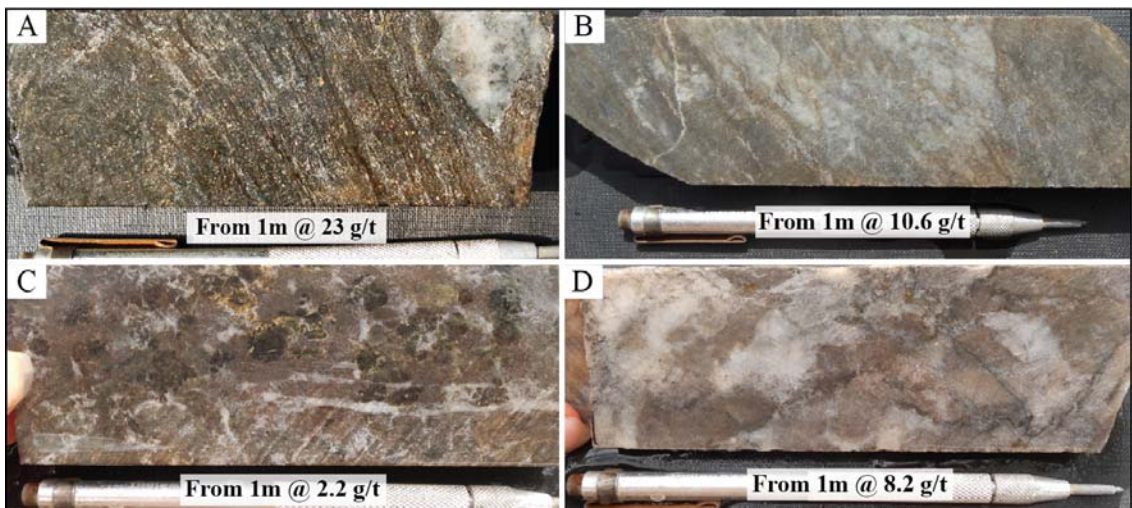


Figure 7. Mineralization styles and ore textures in drill core. A) Sheared diorite within the Sadiola Fracture Zone. Up to 3% pyrrhotite and arsenopyrite crystals are aligned parallel to the shear fabric marked by biotite and calcite. B) Sheared hangingwall greywacke that exhibits a well-defined fabric marked by biotite and sulfides, and by lenses and augen-shaped pods of quartz reflecting deformation of early quartz veins. C) Calc-silicate-bearing limestone breccia. The actinolite-tremolite dark green clots are overprinted by the potassic alteration assemblage. Pyrite is mantling the retrograde-altered clots. D) Typical carbonate breccia. The rock is strongly altered with patchy dolomite and biotite. Fine-grained pyrrhotite and arsenopyrite crystals occur disseminated and as thin stringers.

6.6. Hydrothermal alteration

Based on diagnostic textural and mineralogical features, a polyphase hydrothermal alteration history has been identified at Sadiola Hill. An early high-temperature phase is recorded by the porphyroblastic growth of actinolite-tremolite. In drill core, this alteration phase is characterised by dark green clots and box-shaped spots, millimetric to centimetric in size (≤ 1 cm). Actinolite-tremolite porphyroblasts are locally strongly developed within the Sadiola Fracture Zone and to a lesser extent along the NNE-trending faults (Fig. 8A). This assemblage has been observed in silty-argillaceous interbeds in limestones, in greywackes and as rare occurrences in the early diorite. Such clots are superimposed on the bedding-parallel foliation in footwall impure limestones, but are stretched along the shear fabric within the Sadiola Fracture Zone. Deep drilling has not indicated zoning surrounding any of the intrusions, but it does show a strong correlation between the early alteration assemblage and the Sadiola Fracture Zone and NNE-trending shears. Zones altered with actinolite-tremolite clots have been identified up to 200 m away from the Sadiola Fracture Zone in footwall

impure limestones and up to 100 m away in less reactive hangingwall detrital sedimentary rocks. The early alteration phase is overprinted by a syn-mineralization potassic alteration stage at the Sadiola Hill deposit (Fig. 8A-C). Arsenopyrite, pyrrhotite, pyrite, native gold, aurostibite, and a wide range of accessory minerals are texturally associated with minerals precipitated during this phase. The assemblage is dominated by biotite-(phlogopite), calcite-dolomite, and quartz, with minor tourmaline, actinolite-tremolite, muscovite, and K-feldspar, and accessory titanite, rutile, apatite, and fluorite. Despite the early calc-silicate and the potassic mineral assemblages being locally spatially associated and exhibiting gradual to sharp alteration fronts with the country rocks, economic gold grades are only located in areas where the potassic alteration is present.

Biotite marks the fabric in host rocks within the Sadiola Fracture Zone and along the NNE-trending shears (Fig. 8D). The potassic alteration halo in country rocks occurs in the form of pervasive biotite and extends beyond the extent of the current open pit. Biotite minerals are also developed along axial-planar fabric associated with F₂ folds (Fig. 8E), associated with calcite and muscovite as patchy replacement of the tremolite-actinolite clots, present as veins with calcite-quartz-tourmaline-sulfides and in surrounding wall-rocks of such veins, and as disseminations in the argillaceous-silty interbeds in footwall limestones. The type of mica in the alteration assemblages is, at least in part, lithologically-controlled. Within the basal impure carbonates, phlogopite is dominant over biotite. Muscovite is preferentially developed instead of biotite in the quartz-feldspar-phyric dikes and commonly occurs in strain shadows with quartz (Fig. 8F).

In addition to calcite in the veins, carbonate alteration occurs in a 15-75 m wide zone in the greywackes of the immediate hangingwall to the Sadiola Fracture Zone. Texturally-referred to as “calcite eye bands”, this alteration texture is defined by rounded clots of calcite locally stretched along the foliation. The disseminated carbonate spots change to intense pervasive carbonate flooding of the greywackes within the Sadiola Fracture Zone.

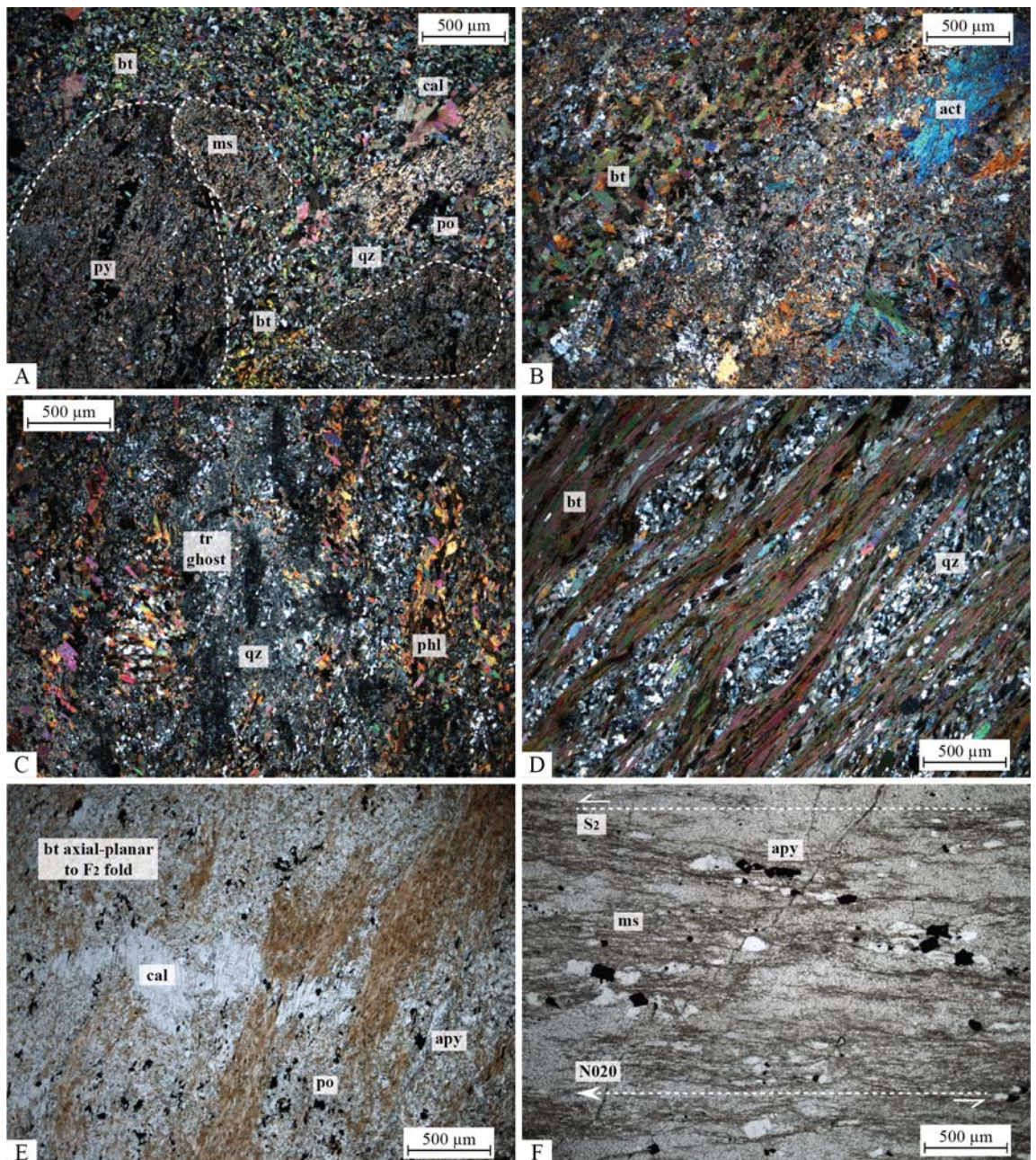


Figure 8. Representative micrographs of ore-related hydrothermal alteration. A) Calc-silicate-bearing impure metalimestone. Relict Ca-amphibole clots are retrograde-altered by a muscovite-biotite-calcite-sulfides mineral assemblage. B) Biotite-sulfides mark the foliation and overprint an earlier alteration stage characterized by the porphyroblastic growth of fibrous actinolite. C) Phlogopite marks the spaced cleavage in dolomitic host rock and overprints abundant ghost tremolite fibres. D) Biotite flakes mark the spaced cleavage and are stretched along it in sheared metadiorite. E) Biotite-sulfides occur axial-planar to an early calcite vein folded by F_2 . F) Muscovite is closely associated with arsenopyrite crystals in sheared quartz-feldspar-phyric dike. Arsenopyrite crystals exhibit asymmetrical quartz-muscovite strain shadows, which indicate a sinistral shear sense along the S_2 cleavage. The section was cut perpendicular to foliation and parallel to lineation.

Tourmaline is structurally-controlled and occurs as a euhedral, rod- and heart-shaped accessory mineral (up to 2%). Tourmaline is observed in quartz-calcite-biotite veins and in narrow selvages of such veins, as acicular masses and heart-shaped mineral sections along shear fabric in the Sadiola Fracture Zone, and as part of the alteration envelope surrounding the NNE-trending shears. Tourmaline grains either display no chemical zoning or a core-and-rim texture (Fig. 9A-B). Two styles of occurrence have been studied under electron microprobe: (a) tourmaline grains orientated parallel to the shear fabric in impure carbonate and (b) tourmaline crystals on the selvages of quartz-calcite-biotite veins. Electron probe micro-analyses (supplementary material) show that these tourmalines dominantly belong to the alkali group and the schorl-dravite series, similarly to that identified in the Loulo district (Fig. 9C-D). Zoned tourmalines from the veins display a chemical zoning pattern that features a core-to-rim decrease in Al and Mg and an increase in Fe and Ca. They also plot along the oxydravite-povondraite compositional trend (meta-evaporite tie line) (Fig. 9D).

A final stage of hydrothermal alteration recognized at Sadiola Hill is associated with normal displacement of the reactivated ore-hosting structures and formation of numerous chlorite-calcite-pyrite veins. Based on textural relationships, these veins post-date the potassic alteration stage and, by implication, the main mineralization phase.

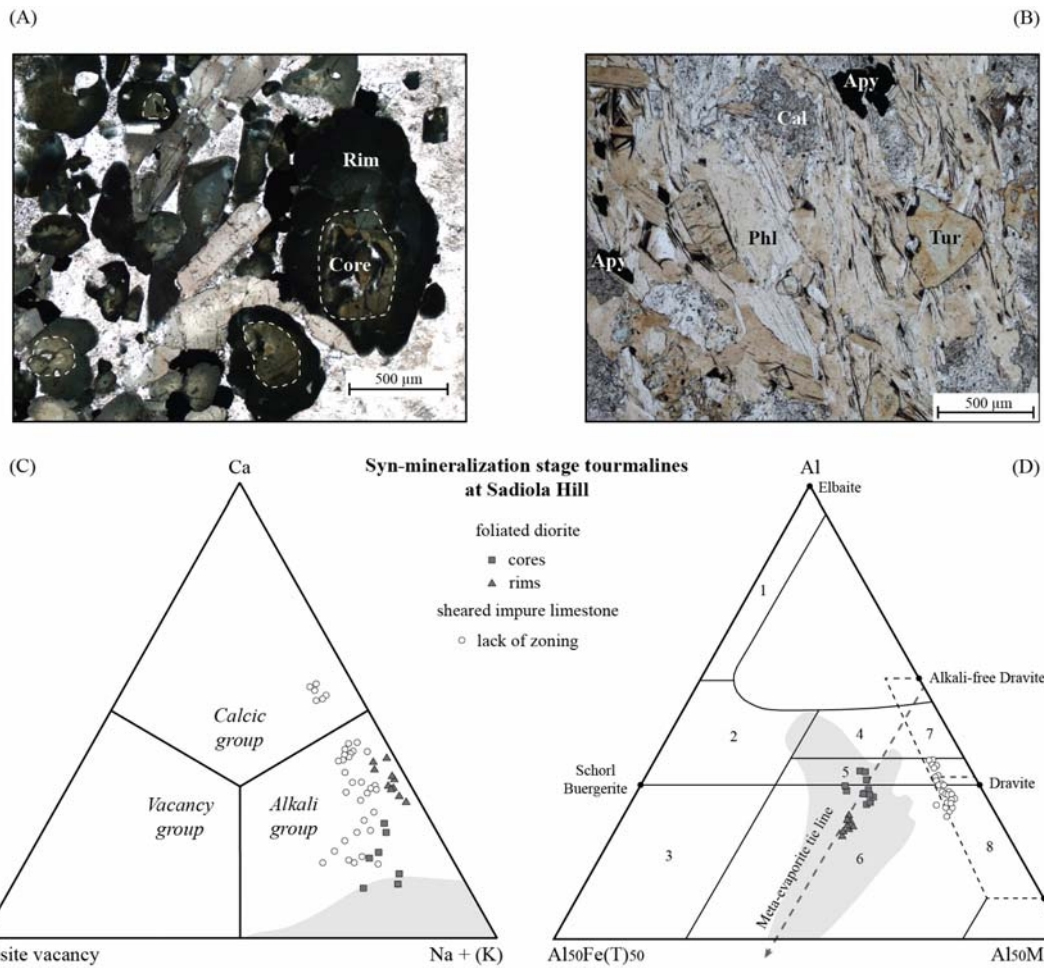


Figure 9. A) Micrograph of zoned hydrothermal tourmalines in a quartz-calcite-biotite vein in diorite. **B)** Hydrothermal tourmalines in sheared impure limestone. **C-D)** Representative chemical composition of syn-mineralization stage hydrothermal tourmalines were analysed by electron probe and the stoichiometry calculated using the Winclastour software (Yavuz et al., 2006). Ternary plots show the classification of tourmalines at Sadiola Hill deposit. Shaded areas show the composition of multistage hydrothermal tourmaline from the Loulo deposits (Yalea North, Gara, P-129, P-64 and Gouunkoto; modified from Lawrence et al., 2013a). Classification based on the X-site occupancy, using the Ca-X-site vacancy-Na + (K) diagram of Hawthorne and Henry (1999). Classification based on Y- and Z-site occupancy, using the Al-Fe-Mg ternary diagram of Henry and Guidotti (1985). Labeled fields: 1. Li-rich granitoid pegmatites and aplites. 2. Li-poor granitoids pegmatites and aplites. 3. Fe³⁺-rich quartz-tourmaline rocks (altered granitoids). 4. Metapelites and metapsammites with Al-saturating phase. 5. Metapelites and metapsammites lacking Al-saturating phase. 6. Fe³⁺-rich quartz-tourmaline rocks, calc-silicate rocks and metapelites. 7. Low Ca meta-ultramafic rocks and Cr-V-rich metasedimentary rocks. 8. Metacarbonates and metapyroxenites. *Meta-evaporite tie line after Henry et al., 2008.

6.7. Ore mineralogy

Ore minerals are texturally associated with silicate minerals precipitated during the potassic alteration phase. The metal enrichment association of the primary ore typically comprises As-Au-Sb and minor W-Mo-Ag-Bi-Cu-Zn-Pb-Te. Studies of ore mineralogy suggest a multistage ore paragenesis consisting of an early As-rich sulfide stage (Stage I), followed by an Au-Sb stage (Stage II). Both ore stages overlap with the potassic alteration event. A summary of the ore and alteration paragenesis is presented in Figure 10. Chemical compositions of representative ore minerals and gold are given in the supplementary material.

Stage I produced a sulfide assemblage characterized by arsenopyrite + pyrrhotite ± pyrite, chalcopyrite, and native gold (Fig. 11A). Arsenopyrite is the dominant sulfide phase and is mostly present as fine-grained euhedral to subhedral, prismatic to acicular grains (~ 10-100 µm) and crystal aggregates (up to 250 µm). It occurs as single crystals, intergrown with euhedral to subhedral pyrrhotite (~ 10-150 µm) and/or subhedral pyrite (~ 5-125 µm). Minor ore phases include fine-grained chalcopyrite (~ 2-75 µm), scheelite, and molybdenite. Scheelite is preferentially deposited in limestones suggesting a dependence on host rock composition and reactivity. Molybdenite is present in trace amounts as needles and subhedral crystal aggregates, up to 300 µm in length, and enclosed in scheelite and pyrite.

Gold associated with stage I accounts for a minor part of the recovered gold (~20 % of the ore) and occurs as fine inclusions (~1 µm) enclosed in arsenopyrite crystals, as grains (~1-10 µm) nucleated on sulfide margins, or as fine-grained blebs (15< µm) within the gangue closely associated with the sulfides (Fig. 11B). The LA-ICPMS technique indicates that gold is preferentially concentrated in arsenopyrite between 0.126 - 23.7 ppm with a mean of 3.02 ppm. Gold concentration in pyrite is insignificant (mean of 0.15 ppm). The sub-microscopic gold is heterogeneously distributed within individual arsenopyrite crystals. Antimony is also concentrated in arsenopyrite at a mean of 1368 ppm, with variations reflected by patchy compositional zoning on a scale of tens of microns to 1 µm. Variations in Ni, Co, Bi, and Se concentrations of arsenopyrite hosted in impure limestone versus in quartz-feldspar-phyric dikes indicate a lithological control on trace element content of arsenopyrite. Chemical compositions

of selected arsenopyrite grains ($>45\text{ }\mu\text{m}$ in size, no zoning) buffered by pyrrhotite and/or pyrite ($n = 20$) and determined by electron microprobe vary from 30.06 to 31.63 atomic % As. Using the $f_{\text{S}2}$ -buffered arsenopyrite-pyrite-pyrrhotite equilibrium, this compositional range suggests crystallization temperatures greater than 300°C (i.e. between 300°C and 410°C) for stage I arsenopyrite crystals, with an average crystallization temperature of 350°C (30.78 atomic % As).

Stage II is characterized by the abundance of antimony sulfosalts and the assemblage pyrrhotite + berthierite + tetrahedrite + stibnite \pm native gold and aurostibite (Fig. 11C). Fine-grained berthierite ($\sim 2\text{-}75\text{ }\mu\text{m}$) was observed attached to the margins of arsenopyrite and pyrrhotite, enclosing arsenopyrite/pyrite/pyrrhotite, and as rare inclusion in pyrrhotite/pyrite. Stibnite is closely associated with berthierite, but typically appears late in the paragenetic sequence. Tetrahedrite ($\sim 15\text{-}25\text{ }\mu\text{m}$, up to 250 μm) was observed on the margins of arsenopyrite-pyrrhotite-pyrite or as intergrain space infill. Chemical analyses give tetrahedrite₉₀₋₁₀₀tennantite₀₋₁₀ compositions (Cu-Sb-rich end member in the solid-solution series), although intermediate compositions with tennantite (Cu-As-rich end member) were measured. Analyzed tetrahedrite grains may contain up to 5 wt% Ag and 6 wt% Zn. Accessory sphalerite occurs as intergrowths with pyrrhotite and contains acicular arsenopyrite inclusions. Accessory antimony sulfosalts of Pb and Ni (e.g. gudmundite, ullmannite, jamesonite) deposited very late in the paragenetic sequence.

Gold associated with stage II accounts for the bulk of the recovered gold (~80 % of the ore). It occurs as free native gold blebs ($\sim 5\text{-}25\text{ }\mu\text{m}$) within the gangue closely associated with Sb sulfosalts (Fig. 11D), as polygonal grains ($\sim 1\text{-}10\text{ }\mu\text{m}$) attached to the margins of tetrahedrite crystals, as aurostibite (AuSb_2) ($\sim 5\text{-}20\text{ }\mu\text{m}$) at sharp crystal faces with and/or mantling native gold blebs (Fig. 11E), as late infill and locally remobilized particles in micro-fissures in arsenopyrite crystals (Fig. 11F), and as rare maldonite crystals (Au_2Bi) ($\sim 25\text{ }\mu\text{m}$) intergrown with chalcopyrite crystals.

A suite of minerals generally observed near the oxide-fresh transition zone formed by weathering of the hypogene ore and include native antimony, marcasite, hematite, and gudmundite. Pyrrhotite is replaced by a porous or skeletal intergrowth of pyrite and marcassite. Native antimony is observed as rare anhedral particles infilling microcracks in arsenopyrite. Pyrrhotite and berthierite also display rare embayments and digitations filled by native antimony suggesting breakdown or replacement reactions. Gudmundite is associated with apparent breakdown textures after pyrrhotite, berthierite, and tetrahedrite.

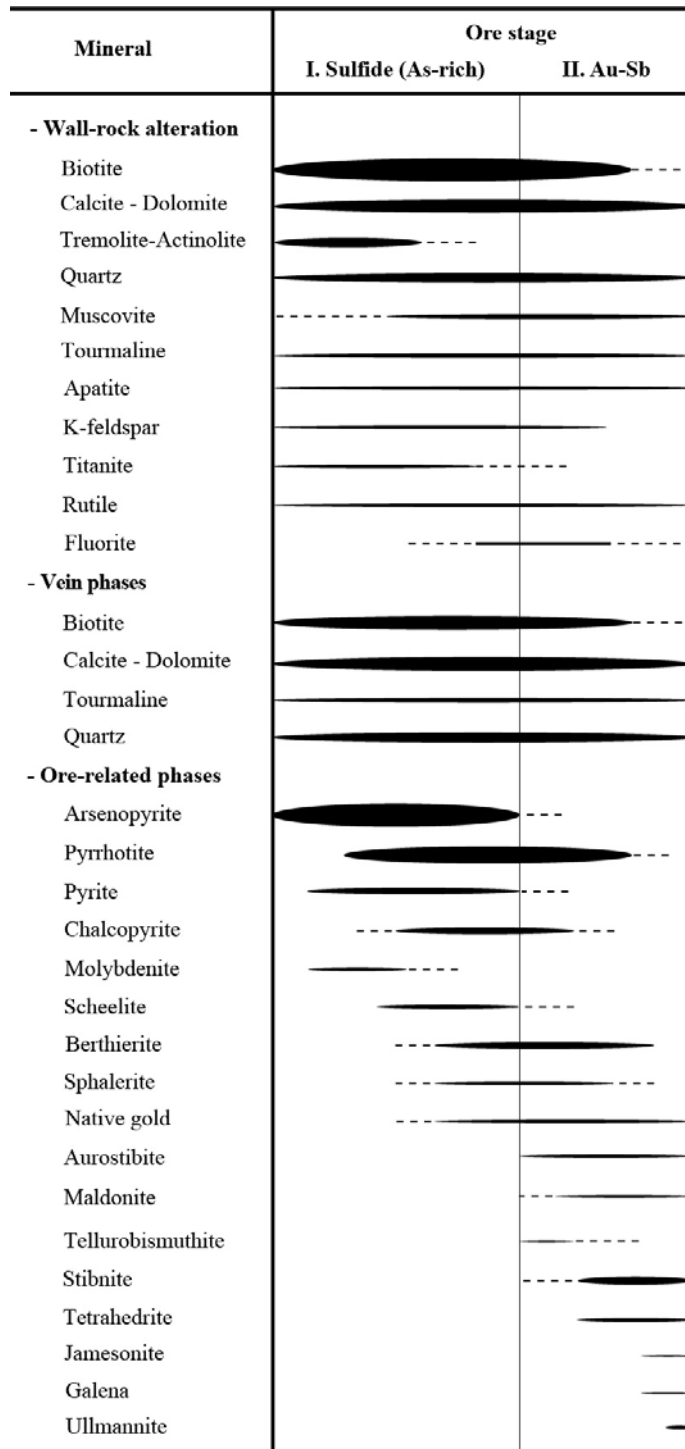


Figure 10. Ore and alteration paragenetic sequence chart for Sadiola Hill. The ore-related phases correspond to both the dominant disseminated style and minor veining styles of mineralization (both styles formed contemporaneously). Berthierite = FeSb_2S_4 ; Tetrahedrite = $(\text{Cu},\text{Fe})_{12}\text{Sb}_4\text{S}_{13}$; Aurostibite = AuSb_2 ; Stibnite = Sb_2S_3 ; Ullmannite = NiSbS ; Jamesonite = $\text{Pb}_4\text{FeSb}_6\text{S}_{14}$; Maldonite = Au_2Bi ; Tellurobismuthite (Bi_2Te_3).

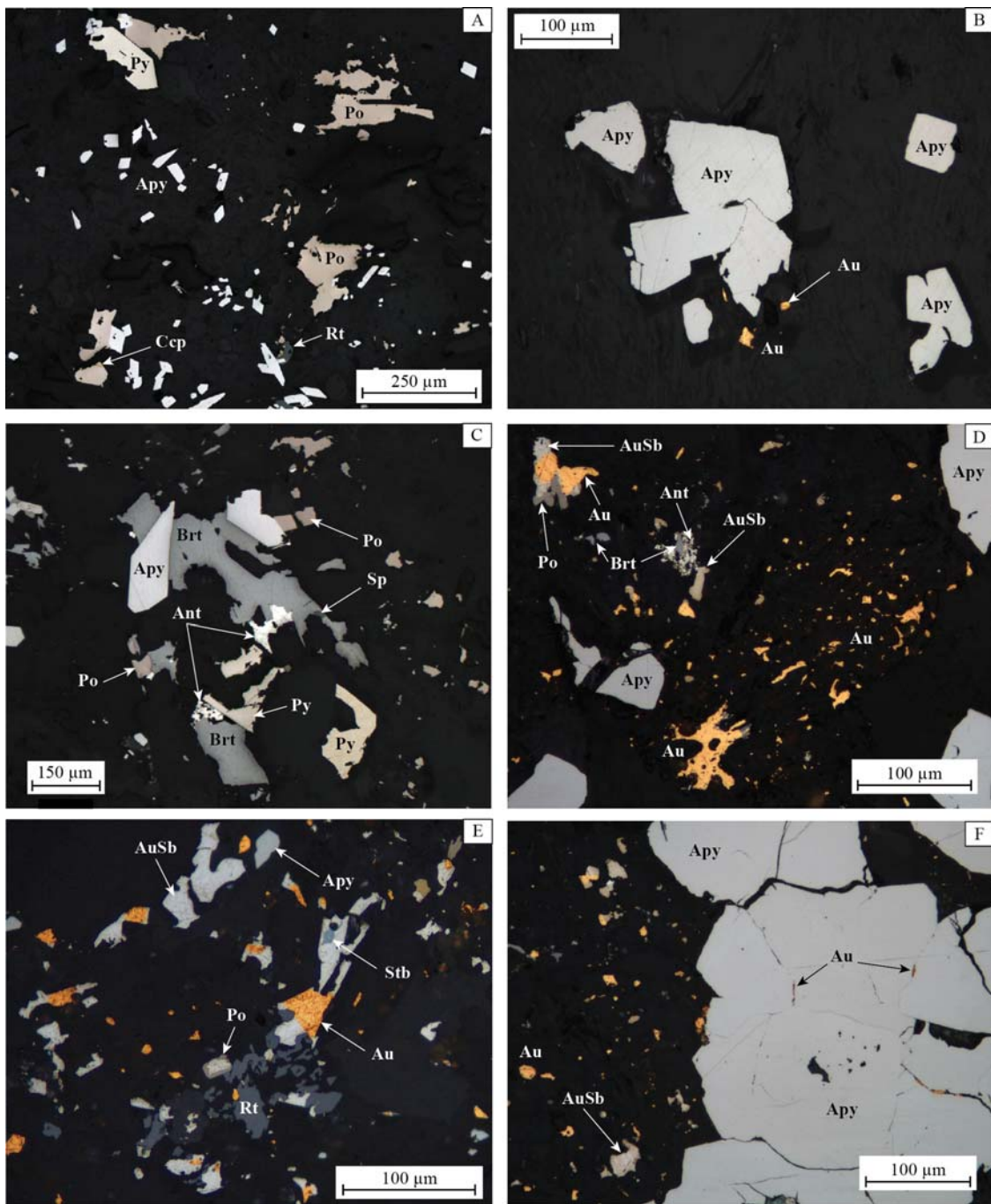


Figure 11. Reflected light images of ore-related phases at Sadiola Hill. A) Typical early sulfide assemblage consists of euhedral prismatic to acicular arsenopyrite, subhedral pyrrhotite, minor pyrite and traces chalcopyrite. B) Free gold grains within the gangue closely associated with the early sulfide mineral assemblage. C) Early sulfide mineral assemblage overprinted by berthierite. Berthierite is mantling a pyrrhotite crystal and also occurs as filling inter-arsenopyrite grains. Embayments in berthierite are filled by native antimony. D) Native gold, aurostibite and berthierite are closely associated with arsenopyrite and pyrrhotite. E) Aurostibite occurs as disseminated crystals, intergrown at sharp crystal faces with native gold or mantling the latter. F) Native gold particles in micro-fissures in arsenopyrite.

7. Discussion

7.1. Integration of the Sadiola Hill deposit with regional geology and tectonics

In this section, the local deformation history identified at Sadiola Hill is compared to the prolonged tectono-magmatic history recorded in other Paleoproterozoic greenstone belts of the West African Craton. At least two phases of folding have affected the country rocks in the Sadiola Hill deposit area. Little is known about the kinematics of the earliest local deformation phase (D_{1s}), but fold geometry and associated lineation data are consistent with NE-SW-directed shortening. At the regional scale, D_{1s} is compatible with an early deformation event (D_1) recorded in southern Mali (Liégeois et al., 1991; McFarlane et al., 2011). The development of NNE-trending upright folds and penetrative axial-planar cleavage (S_2) are correlated with the D_{2s} deformation event. Fold and fault geometries, and kinematic indicators are consistent with NW-SE-directed shortening. At the regional scale, D_{2s} is compatible with a period of fold-and-thrust tectonics correlated with a region-wide compressive event (D_2) (in Ivory Coast, Pouclet et al., 2006; Vidal et al., 2009; in Burkina Faso, Hein, 2010; in Guinea, Lahondère et al., 2002; in Mali, Liégeois et al., 1991; Milési et al., 1992; Dabo and Aïfa, 2010; McFarlane et al., 2011; Diene et al., 2012; Lawrence et al., 2013a; Treloar et al., 2014). In southern Mali, inversion of the Birimian host sequence is constrained to $2103 \pm 14 - 2094 \pm 4$ Ma (Amstrong, 2003; McFarlane et al., 2011). The D_{3s} event marks a switch from dominantly pure shear (folding and reverse faulting with minor strike-slip displacement during D_{2s}) to a simple-shear (strike-slip faulting) system (Fig. 12). Fault geometries and kinematic indicators are consistent with NNW-SSE-directed shortening. At the regional scale, D_{3s} is compatible with a period of transcurrent tectonics (D_3) that is coeval with local intrusion of ca. 2090 to 2070 Ma metaluminous, hornblende-biotite-bearing diorite-granodiorite and peraluminous, K-rich granite plutons (Milési et al., 1992; Egal et al., 2002; Schwartz and Melcher, 2004; Gueye et al., 2008; Hirde and Davis, 2002; Lawrence et al. 2013a; Lambert-Smith, 2014). The bulk of the mineralization is constrained to have taken place during D_{3s} at Sadiola Hill. The similarity in relative timing and structural setting between the KKI

and southern Ghana suggests that gold mineralization within the Birimian terranes of West Africa occurred over a protracted interval between ca. 2100 to 2070 Ma, during a period of transcurrent tectonics, soon after the cessation of regional-scale contractional deformation (e.g., in the Ashanti belt of Ghana, Allibone et al., 2002a, b; in southern Mali, Olson et al., 1992; McFarlane et al., 2011; in the KKI, Lawrence et al., 2013a; Treloar et al., 2014). At Morila, orogenic gold mineralization has been dated at 2074 ± 14 Ma (McFarlane et al., 2011: U-Pb on hydrothermal titanite). The structural evolution from early fold-and-thrust tectonics to strike-slip tectonics has been described in other orogenic belts (e.g. Vassallo and Wilson, 2002; Clegg and Holdsworth, 2005; Ulrich et al., 2011) and is typically associated with gold-forming events. At Sadiola Hill, the Sadiola Fracture Zone was the dominant structure active during mineralization and has therefore focused the greatest amount of dilation and permeability. The main ore shoots plunge 45°S, indicating that mineralization resulted from the sinistral-normal linkage between the Sadiola Fracture Zone and the NNE-trending shears (Fig. 12). Within the KKI, NW-SE shortening in a transpressive regime has similarly been proposed for the Kolia-Boboti sedimentary basin (Dabo and Aïfa, 2010; Diene et al., 2012) and in a transtensional regime for the Loulo district (Lawrence et al., 2013a). Vein geometry and kinematic indicators associated with the steep NE-trending barren quartz veins ($240^\circ/65^\circ\text{NW}$) present at Sadiola Hill are consistent with a late phase of NW-SE extension (D_{4s}). These veins post-date mineralization. The last local deformation event (D_{5s}) is associated with the formation of WNW-trending sub-vertical brittle cross-faults (Fig. 12). Similar late E-W faults have been reported at the Yalea deposit in the Loulo district (Lawrence et al., 2013a). The integration of D_{4s} and D_{5s} into the regional tectonic framework remains unclear at this stage.

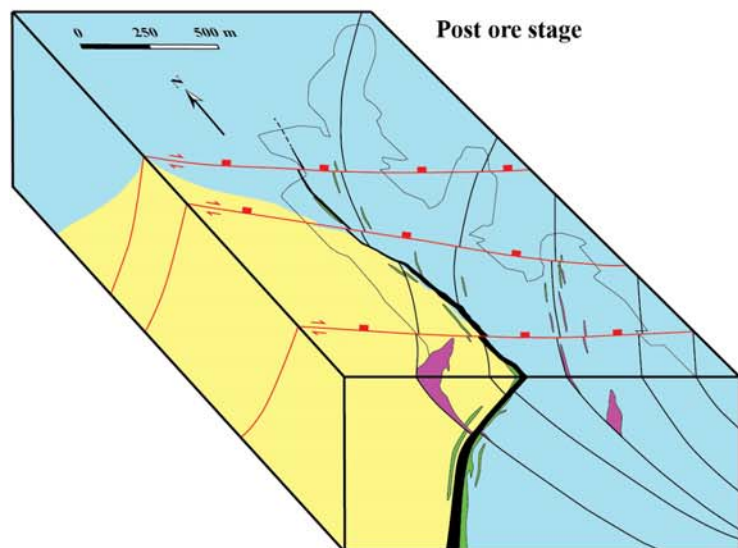
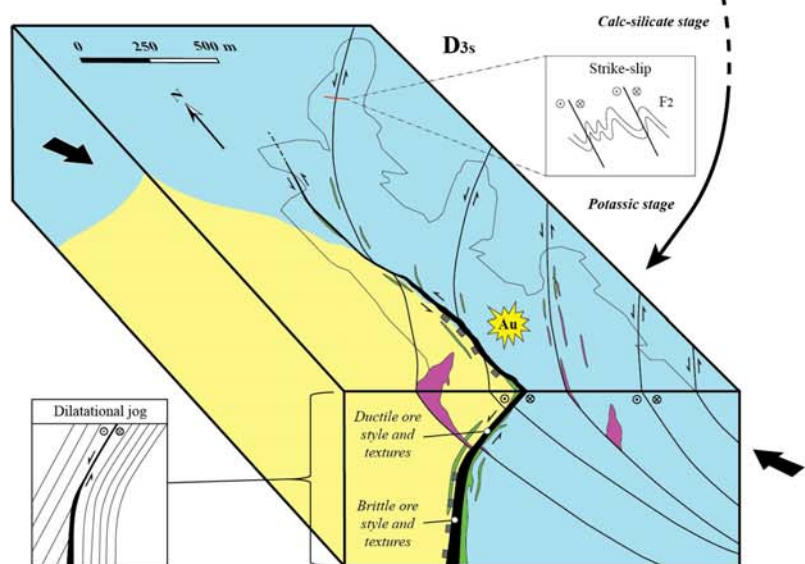
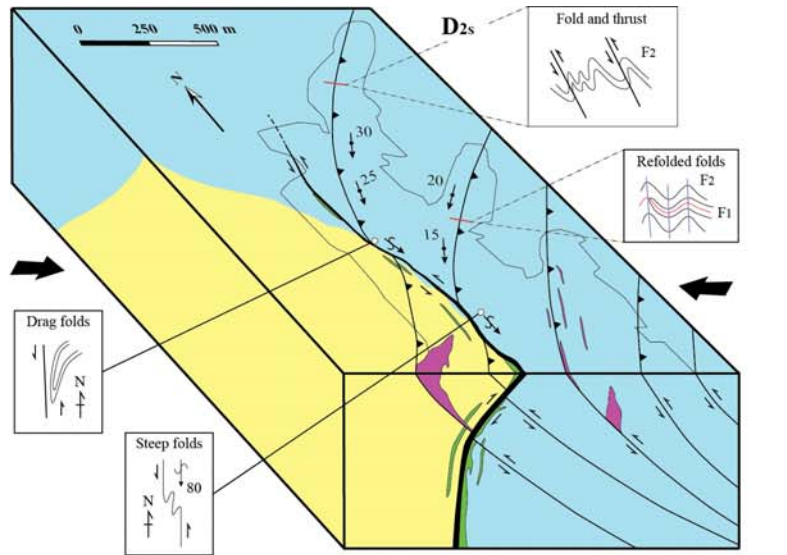


Figure 12. Schematic bloc diagram succession of most important local deformation events as recorded in the recent field study. D_{2s} is associated with the formation of a fold and thrust belt and the syn-tectonic emplacement of the quartz-feldspar-phyric dikes. F_2 folds orientation, fault geometries and kinematic indicators are consistent with NW-SE-oriented shortening. D_{3s} marks a switch from inverse tectonics to a strike-slip dominated system under NNW-SSE shortening. D_{3s} also marks a transition from the ductile regime to brittle conditions. It is characterized by sinistral movement along both the Sadiola Fracture Zone and the NNE-trending shears, synchronous with the potassic hydrothermal alteration stage and gold mineralization. The latest recorded event is associated with the formation of WNW-trending sub-vertical brittle cross-faults that offset mineralization trends.

7.2. Physico-chemical conditions of the ore-forming fluid and potential controls on Au-Sb co-precipitation

The principal parameters that are generally assumed to control ore mineral solubility, other than the activities of the aqueous metallic species, are temperature (T), pressure (P), oxygen fugacity (f_{O_2}), pH and the total sulphur activity (Σa_s) (Williams-Jones and Normand, 1997). Gold saturation and precipitation at Sadiola Hill is interpreted to have occurred predominantly in response to decompression during brittle-ductile failure and sulfidation reactions during fluid - wall-rock interaction. The extensive brecciation recorded over the best-mineralized drill core intersects illustrates the enhanced and cumulative dilation that has developed along the vertical and left-hand flexures of the Sadiola Fracture Zone. The rheological contrasts within the host lithologies, the variations in strain along the main shear (dilation vs. shearing), the occurrence of locally over-pressured fluid migration, and host rock reactivity may have further favored brecciation. The coexistence of arsenopyrite, pyrrhotite, and pyrite in ore Stage I indicates relatively reducing conditions and suggests that H_2S and/or HS^- ligands were responsible for transport of gold in the ore fluids (Shenberger and Barnes, 1989; Benning and Seward, 1996; Williams-Jones et al., 2009). The predominance of pyrrhotite and arsenopyrite over pyrite within the Stage I ore mineral assemblage reflects low sulfur activities (Thorne et al., 2008). Gold concentrations in the lattice of Stage I arsenopyrite crystals are too low to have an economic potential but anomalous concentrations in antimony (i.e. mean of 1368 ppm) reflect an early saturation of the fluid with that element. The precipitation of berthierite followed by the deposition of stibnite in the paragenetic sequence is best-explained through cooling of the

hydrothermal system from Stage I to Stage II (e.g., Barton, 1971; Barton and Skinner, 1979; Williams-Jones and Normand, 1997). The Au-Sb-rich stage II is characterized by the formation of aurostibite and native gold. Favorable chemical conditions for aurostibite formation are from weakly acidic to alkaline conditions and a low sulfur reducing environment (Nekrasov, 1996). The maximum possible temperature for formation of the gold + aurostibite mineral assemblage is 360°C (Hansen and Anderko, 1958). On the basis of combined field relationships, mineralogical and micro-textural data, and arsenopyrite geothermometry, the multistage ore development is interpreted to reflect the cooling continuum of a high temperature (>400°C) reduced hydrothermal fluid rather than contrasting mineralization styles developing at distinct crustal levels and times. Stage I and Stage II ore mineral assemblages are constrained on $\log f_{O_2}/f_{S_2} - T$ diagrams (Fig. 13A, B) in order to illustrate the evolution of the ore-forming fluid during mineralization.

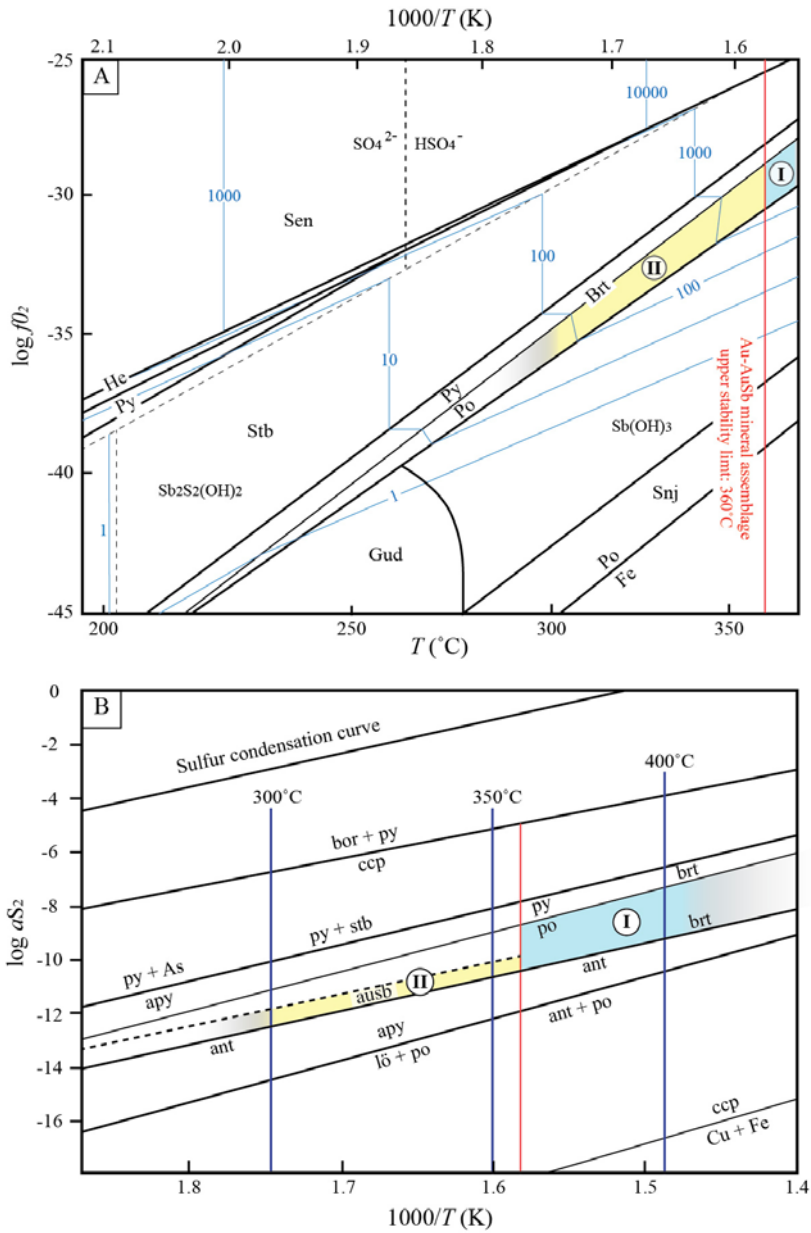


Figure 13. A) $\log f_{O_2} - 10^3/T$ (K) diagram at neutral pH and $\Sigma a_s = 0.01$ showing stability relationships in the system Fe-Sb-S-O and contours of antimony mineral solubility in ppm (light blue lines) (after Williams-Jones and Normand, 1997). The predominant species of Sb is $Sb(OH)_3$, but at intermediate f_{O_2} and temperatures between 185 and 280°C, the predominant species is $Sb_2S_2(OH)_2$. The heavy dashed lines show the predominance boundaries of species in the system H-S-O. B) $\log a_{S_2} - 10^3/T$ (K) diagram (after Thorne et al., 2008; thermodynamic fields defined using equations from Barton and Skinner, 1979) showing phase equilibrium constraints at Sadiola Hill. On both diagrams: upper stability limit of gold + aurostibite (red line i.e. 360°C); (I) Stage I typical mineral assemblage: po + apy ± py; (II) Stage II typical mineral assemblage: po + brt + au + ausb ± stb ± tetr. Mineral abbreviations: ant - native antimony, ausb - aurostibite, brt - berthierite, ccp - chalcopyrite, gud - gudmundite, he - hematite, lö - löellingite, po - pyrrhotite, py - pyrite, sen - senarmontite, snj - seinajokite, stb - stibnite, tetr - tetrahedrite.

7.3. Towards a genetic model...

The Sadiola Hill deposit shares a number of characteristics typical of orogenic gold deposits worldwide (Mikucki and Ridley, 1993; Groves et al., 1998; McCuaig and Kerrich, 1998; Ridley and Diamond, 2000; Bierlein and Maher, 2001; Goldfarb et al., 2001; Groves et al., 2003; Bierlein et al., 2006) including a late-orogenic relative timing, strong regional (i.e., Senegal-Mali Shear Zone) and local structural controls (i.e., Sadiola Fracture Zone and NNE-trending shear array) on ore location and geometry, and a pronounced Au-As-Sb metal enrichment association. The metal enrichment association and geothermometric estimates from ore and alteration paragenesis are compatible with mesozonal Au-As-Te (6-12 km, 300°-475°C) to near-epizonal Au-Sb (\leq 6 km, 150°-300°C) conditions in terms of crustal level based on the proposed classification of orogenic gold deposits by Groves et al. (1998). However, the high temperature ore and alteration paragenesis at Sadiola Hill is in thermal disequilibrium with host rocks at regional greenschist-facies conditions, which is atypical for that class of deposit. Such geological feature alone is not diagnostic of a magmatic fluid source because it can reflect the interaction of a fluid from any source with reactive country rocks at a temperature high enough to form stable actinolite and biotite (Ridley and Diamond, 2000; Meinert et al., 2005). Obolensky et al. (2009) suggested that the physico-chemical parameters of ore-forming fluids associated with Au-As-Sb deposits indicate deep circulation of hydrothermal solutions, which make them in disequilibrium with country rocks at the ore deposition level. The late orogenic switch from fold-and-thrust tectonics to strike-slip tectonics along the Senegal-Mali Shear Zone most likely promoted high fluid flow and the arrival of magmatic fluids with minor heat loss at upper crustal levels, which is consistent with the occurrence of voluminous calc-alkaline magmatism at ca. 2090-2070 Ma. The high temperature ore and alteration paragenesis is therefore suggested to represent a transient thermal effect associated with syn-kinematic igneous activity at the time of mineralization. Based on this study and recent research by Lawrence et al. (2013a, b) and Treloar et al. (2014), a deposit classification for major gold mines in the KKI is proposed in Table 1. A potential analogue to the Sadiola Hill deposit is the Massawa gold deposit in the Senegalese part of the KKI. Nevertheless, the source of fluids and metals for the Sadiola

Hill hydrothermal system remains uncertain. Indeed, although a magmatic source is indicated at Massawa (Treloar et al., 2014) and may be proposed for Sadiola Hill, gold deposits of the Kweke district in the Archean Midlands greenstone belt of Zimbabwe are associated with low salinity, mixed aqueous-carbonic fluid inclusions and stable isotope data indicating a homogeneous metamorphic or mixed metamorphic and/or magmatic fluid source for both the Au-As and the Au-Sb mineralization stages (Buchholz et al., 2007).

8. Conclusions

The presented field and mineralogical data suggest that the Sadiola Hill carbonate-hosted Au-As-Sb mineralization formed during a period of sinistral tectonics (i.e. D_{3s} NNW-SSE shortening) that was coeval with calc-alkaline magmatic activity between ca. 2090 and 2070 Ma. The Senegal-Mali Shear Zone acted as the main conduit for hydrothermal fluids in the Sadiola camp. The sinistral reactivation of early accretionary structures, and their linkage with belt-discordant NNE-trending shears, appears to be a critical factor controlling ore deposit location and ore shoot geometry. Paragenetic studies reveal a multistage ore development comprising an early As-rich sulfide stage, followed by an Au-Sb stage. The similar gold relative timing and structural setting in the KKI and southern Ghana (e.g., Ashanti, Loulo, Massawa, Sadiola Hill) suggests that gold mineralization within the Birimian terranes of West Africa occurred over a protracted period of transcurrent tectonics, soon after the cessation of regional-scale contractional deformation. Despite the uncertainty regarding the source of fluids and metals for the Sadiola Hill hydrothermal system, the late-Eburnean tectono-magmatic activity reflects a transient geodynamic process that may have been critical for orogenic gold mineralization in the region.

Table 1. Deposit classification for major gold mines in the Kédougou-Kéniéba inlier

Deposit style	Gara	Yalea	Massawa	Sadiola Hill
Structural controls	Senegal-Mali Shear Zone and sinistral NNE-trending shears	Senegal-Mali Shear Zone, N-S Yalea Shear, and sinistral NNE-trending shears	Main Transcurrent Zone and sinistral NE-trending shears	Senegal-Mali Shear Zone, N-S to NW-trending Sadiola Fracture Zone, and sinistral NNE-trending shears
Ore mineralogy	Ankerite-quartz vein-hosted, breccia-hosted, and disseminated sulfides along shears	Quartz vein-hosted, quartz-carbonate vein-hosted, and disseminated sulfides along shears	1. lower-grade (average <10 g/t) and high tonnage, disseminated arsenopyrite-pyrite along shears 2. higher-grade (>10 g/t, maximum of 1500 g/t), lower-tonnage, quartz-stibnite-Au veins	Disseminated sulfides along shears, hydrothermal-tectonic breccia-hosted, biotite-calcite-tourmaline-quartz vein-hosted
Mineralization styles				
Major sulfides	Pyrite	Arsenian pyrite and arsenopyrite	Asenian pyrite, pyrrhotite and pyrite	
Minor-trace ore minerals	Chalcopyrite + gersdorffite + pentlandite + arsenopyrite + tennantite + cobaltite + clausenthalite + galena + sphalerite + molybdenite + scheelite + magnetite + Ni-bearing phases + monazite and traces of xenotime	Pyrrhotite + chalcopyrite + tennantite ± tetrahedrite ± galena ± jamesonite ± bournonite ± magnetite ± traces of xenotime	Tetrahedrite + berthierite + stibnite + chalcopyrite ± molybdenite + scheelite ± sphalerite + jamesonite ± galena ± ullmannite ± tellurobisulfite ± apatite ± rutile ± traces of magnetite	
Metal association	Fe-Cu-Ni-REE-P-W-Ag ± Co-Pb-Se-Zn-Mo	Asenian pyrite and arsenopyrite	Asenian pyrite, pyrrhotite and pyrite	
Gold sites	95% of the gold particles exist as subbedrial to anhedral inclusions (2–70 µm) in pyrite; individual grains situated along deformation cracks in pyrite or as distributed remobilized particles within micro-discrete gold veinlets infilling micro-fractures; and as particles located on pyrite margins within pressure shadows or along fracture terminations. The remaining rarely as free gold in chlorite-sericitic alteration gold (5%) occurs in close proximity to sulfide grains.	Pyrite + gersdorffite + pentlandite + arsenopyrite + tennantite + cobaltite + clausenthalite + galena + sphalerite + molybdenite + scheelite + magnetite + Ni-bearing phases + monazite and traces of xenotime	1. Tetrahedrite + stibnite ± sphalerite ± galena ± Ni-Co sulfosilicate + gersdorffite ± apatite + monazite ± traces of xenotime 2. Stibnite ± sphalerite ± tetrahedrite ± zinkerite ± chalcostibite ± robinsonite ± jamesonite ± roshchinitie ± pyrite ± arsenopyrite	Tetrahedrite + berthierite + stibnite + chalcopyrite ± molybdenite + scheelite ± sphalerite + jamesonite ± galena ± ullmannite ± tellurobisulfite ± apatite ± rutile ± traces of magnetite
		Fe-As-Cu-Au-Ag ± Pb-Sb-W	Au-As-Sb ± Cu-Fe-W-Mo-Ag-Bi-Zn-Pb-Te	
		Gold temporally associated with numerous stages of sulfide I. Gold occurs as fine inclusions (1 µm) in sulfides; as grains growth. Gold occurs as included grains; as small, randomly arsenopyritic and 27 ppm in pyrite. Native gold occurs as fine inclusions in sulfides; along micro-fissures; and free within the gangue.	Gold occurs as fine inclusions (1 µm) in sulfides; as grains (1–10 µm) nucleated on sulfide margins; as blebs (<30 µm) within the gangue closely associated with the sulfides and Sb-sulfosilicates; as aurostibite (5–20 µm) at sharp crystal faces with and/or mantling native gold blebs; and as late infill and locally remobilized particles in micro-fissures in sulfides.	
Gold fineness	Ag-poor (980–998, mainly >990)	Ag-rich (920–990, mean of 950)	Ag-poor, coarse (250 mm to 2 mm) in vein	Ag-poor (850–970)
Alteration	Tourmalinization (1) and abitisation (2)	Phyllite (1) and silica-carbonate ± albite (2)	Silica-carbonate (1) and silica (2)	Calc-silicate (1) and potassic (2)
Alteration types	1. Tourmaline + quartz + ankerite + siderite ± rhodochrosite ± biotite ± chlorite 2. Ankerite + quartz ± albite ± hematite	1. Sericitic + chlorite + quartz 2. Ankerite + quartz ± albite ± hematite	1. Quartz + ankerite ± dolomite 2. Quartz	1. Porphyroblastic actinolite-tremolite 2. Biotite + calcite + quartz ± actinolite-tremolite ± muscovite ± tourmaline ± K-feldspar
Fluid inclusion types	1. Hypersaline (40–50 wt% total dissolved solids), high T (>400°C), multiphase H ₂ O-rich CO ₂ -NaCl-FeCl ₃ inclusions 2. Mixed salinity (5–21 wt% NaCl equivalent) CO ₂ -rich H ₂ O-NaCl inclusions 3. CO ₂ ± Na ± CH ₄ inclusions	1. Low salinity (<10 wt % NaCl equivalent), H ₂ O-NaCl inclusions 2. CO ₂ -N ₂ ± CH ₄ inclusions	1. CO ₂ -CH ₄ inclusions 2. Low salinity (<6 wt % NaCl equivalent), H ₂ O-NaCl inclusions	
Stable isotopes	δ ₃₄ S signatures from 11.5 to 15.5‰ (N = 11; mean of 13.6 ± 1.3‰) in pyrite	δ ₃₄ S values between 5.8 and 9.6‰ (N = 10; mean of 7.5 ± 1.2‰) in arsenopyrite-pyrite	δ ₃₄ S sulfide values of between 0 and 4.1‰ and δH ₂ O values of 5.5 to 10.9‰ for all stages of mineralization	
	δ ₁₃ C range from –14.4 to –8.6‰ (N = 9; mean of –11.7 ± 1.9‰) in mineralized vein carbonates	δ ₁₃ C signatures of –21.7 to –15.8‰ (N = 6; mean of –2.8‰) in mineralized vein and alteration ankerites	δ ₁₃ C values of –16.2 to 17.2‰ (N = 10; mean of 16.7 ± 0.5‰) for stage I δ ₁₃ C values of 15.9 to 17.0‰ (N = 5; mean of 16.4 ± 0.5‰) for stage II	
P-T conditions	311°C to 447°C minimum pressures of 1.4 to 2.2 kbars	270°C to 340°C 1.4 to 1.8 kbar	220°C to 315°C 1 to 1.65 kbar	
Source of fluids and metals	Fluid mixing - dominantly metamorphic with a magmatic influence	Metamorphic	Magmatic	?
References	Lawrence et al., 2013a, b	Treloar et al., 2014	This study	

9. Acknowledgments

This study forms part of a PhD project, which began in February 2012 at the Centre for Exploration Targeting, UWA. SEMOS, a joint venture between AngloGold Ashanti, IAMGOLD and the Malian government, is gratefully acknowledged for its financial support. Many thanks to T. Gell (AGA), A. Mason-Apps (AGA), O. Terblanche (AGA) and M. Skwarnecki (AGA) for their enthusiasm for the study and their constructive discussions. Our special thanks are extended to D. Traoré, C.O. Sanogo, F. Samake, M. Traoré , Y.S. Kone, and to SEMOS managers G. Gushee, H. Eybers, H. Sitshengiso, P. Herron, and S. Tessougue who assisted with field work studies and logistics. The authors acknowledge the Australian Microscopy and Microanalysis Research Facility at the Centre for Microscopy, Characterisation and Analysis (UWA). Dr. Janet Muhling is thanked for her excellent scientific assistance on the electron microprobe. Richard Goldfarb, Christopher McFarlane and David Lawrence are thanked for their comprehensive appraisal of the study and constructive reviews.

10. References

- Allibone, A.H., McCuaig, T.C., Harris, D., Etheridge, M.A., Munroe, S., Byrne, D., Amanor, J., and Gyapong, W., 2002a, Structural controls on gold mineralization at the Ashanti gold deposit, Obuasi, Ghana: Society of Economic Geologists Special Publication 9, p. 65–93.
- Allibone, A.H., Teasdale, J., Cameron, G., Etheridge, M.A., Uttlev, P., Soboh, A., Appiah-Kubi, J., Adanu, A., Arthur, R., Mamphey, J., Odoom, B., Zuta, J., Tsikata, A., Patave, F., Famiyeh, S., and Lamb, E., 2002b, Timing and structural controls on gold mineralization at the Bogoso gold mine, Ghana, West Africa: Economic Geology, v. 97, p. 949–969.
- AngloGold Ashanti, 2012, AGA Mineral Resource and Ore Reserve Report. Accessed in 2015 from <http://www.agareports.com/12/>, p. 87-92.
- Armstrong, J.T., 1988, Quantitative analysis of silicates and oxide minerals: Comparison of Monte-Carlo, ZAF and Phi-Rho-Z procedures: Microbeam Analysis, v. 23, p. 239-246.

- Armstrong, R.A., 2003, A Geochronological Investigation of the Morila gold mine, Mali: Canberra, Australian National University, Research School of Earth Sciences, Precise Radiogenic Isotope Services (PRISE), 25 p.
- Baratoux, L., Metelka, V., Naba, S., Jessell, M.W., Grégoire, M., and Ganne, J., 2011, Juvenile Paleoproterozoic crust evolution during the Eburnean orogeny (ca. 2.2–2.0 Ga), western Burkina Faso: *Precambrian Research*, v. 191, p. 18-45.
- Barton, P.B., 1971, The Fe-Sb-S system: *Economic Geology*, v. 66, p. 121-132.
- Barton, P.B., and Skinner, B. J., 1979, Sulfide Mineral Stabilities, in Barnes, H.L., ed., *Geochemistry of Hydrothermal Ore Deposits*, 2d ed., New York, Wiley, p. 278-403.
- Bassot, J. P., 1987, Le complexe volcano-plutonique calco-alcalin de la rivière Daléma (Est Sénégal): discussion de sa signification géodynamique dans le cadre de l'orogénie eburnéenne (Protérozoïque inférieur): *Journal of African Earth Sciences*, v. 6, p. 505-519.
- Bassot, J. P., 1997, Albitisations dans le Paléoprotérozoïque de l'Est sénégal: relations avec les minéralisations ferrifères de la rive gauche de la Falémé: *Journal of African Earth Sciences*, v. 25, p. 353-367.
- Bassot, J. P., and Caen-Vachette, M., 1984, Données géochronologiques et géochimiques nouvelles sur les granitoïdes de l'Est du Sénégal: Implications sur l'histoire géologique du Birimien de cette région, in Klerkx, J., and Michot, J., eds., *African Geology*: Belgium, Tervuren, p. 196-209.
- Benning, L.G., and Seward, T.M., 1996, Hydrosulphide complexing of Au (I) in hydrothermal solutions from 150-400°C and 500-1500 bar: *Geochimica et Cosmochimica Acta*, v. 60, p. 1849-1871.
- Bessoles, B., 1977, Géologie de l'Afrique, le craton ouest-africain. Mémoire BRGM 88.
- Bierlein, F.P., Groves, D.I., Goldfarb, R.J., and Dubé, B., 2006, Lithospheric controls on the formation of provinces hosting giant orogenic gold deposits: *Mineralium Deposita*, v. 40, p. 874-886.
- Bierlein, F.P., and Maher, S., 2001, Orogenic disseminated gold in phanerozoic fold belts — examples from Victoria, Australia and elsewhere: *Ore Geology Reviews*, v. 18, p. 113-148.
- Boher, M., Abouchami, W., Michard, A., Albarede, F., and Arndt, N. T., 1992, Crustal Growth in West Africa at 2.1 Ga: *Journal of Geophysical Research*, v. 97, p. 345-369.

- Boshoff, F., Hanssen, E., Hill, J.V., Jones, D., Kaisin, J., Traore, S., and Voet, H.W., 1998, The Sadiola Hill mine: a lower Proterozoic gold deposit in the Kenieba window, Mali, West Africa. Unpublished internal report to the Société d'Exploitation des Mines d'Or de Sadiola S.A. (SEMOS), 6 p.
- Buchholz, P., Oberthür, T., Lüders, V., and Wilkinson, J., 2007, Multistage Au-As-Sb Mineralization and Crustal-Scale Fluid Evolution in the Kwekwe District, Midlands Greenstone Belt, Zimbabwe: A Combined Geochemical, Mineralogical, Stable Isotope, and Fluid Inclusion Study: Economic Geology, v. 102, p. 347-378.
- Calvez, J.Y., Feybesse, J.L., Ledru, P., and Milesi, J.P., 1990. Géochronologie du Proterozoïque inférieur du craton ouest africain (méthode d'évaporation directe de zircons isolés): Conference proceedings - 13^e Réunion des Sciences de la Terre, Grenoble, France; *in* Milési, J.P., Feybesse, J.L., Ledru, P., Domanget, A., Quedraogo, M.F., Marcoux, E., Prost, A., Vinchon, C., Sylvain, J.P., Johan, V., Tegyey, M., Calvez, J.Y., and Lagny, P., 1989, Les minéralisations aurifères de l'Afrique de l'Ouest et leurs relations avec l'évolution lithostructurale au Protérozoïque inférieur: Chronique de la Recherche Minière, v. 497, p. 3-98.
- Clegg, P. and Holdsworth, R.E., 2005, Complex deformation as a result of strain partitioning in transpression zones: an example from the Leinster Terrane, SE Ireland: Journal of the Geological Society, London, v. 162, p. 187–202.
- Dabo, M., and Aïfa, T., 2011, Late Eburnean deformation in the Kolia-Boboti sedimentary basin, Kédougou-Kéniéba Inlier, Senegal: Journal of African Earth Sciences, v. 60, p. 106-116.
- Dabo, M., and Aïfa, T., 2010, Structural styles and tectonic evolution of the Kolia-Boboti sedimentary Basin, Kédougou-Kéniéba inlier, eastern Senegal: Comptes Rendus Geoscience, v. 342, p. 796-805.
- Debat, P., Diallo, D.P., Ngom, P.M., Rollet, M., and Seyler, M., 1984, La série de Mako dans ses parties centrale et méridionale (Sénégal Oriental, Afrique de l'ouest). Précisions sur l'évolution de la série volcanosédimentaire et données géochimiques préliminaires sur les formations magmatiques post-tectoniques: Journal of African Earth Sciences, v. 2, p. 71-79.
- Dia, A., 1988, Caractères et signification des complexes magmatiques et métamorphiques du secteur de Sandikounda-Laminia (Nord de la boutonnière de Kédougou, Est du

- Sénégal): un modèle géodynamique du Birimien de l'Afrique de l'Ouest: Unpublished Ph.D. thesis, Sénégal, Université de Dakar, 350 p.
- Dia, A., Van Schmus, W.R., and Kröner, A., 1997, Isotopic constraints on the age and formation of a Palaeoproterozoic volcanic arc complex in the Kedougou Inlier, eastern Senegal, West Africa: *Journal of African Earth Sciences*, v. 24, p. 197-213.
- Diene, M., Gueye, M., Diallo, D.P., and Dia, A., 2012, Structural Evolution of a Precambrian Segment: Example of the Paleoproterozoic Formations of the Mako Belt (Eastern Senegal, West Africa): *International Journal of Geosciences*, v. 03, p. 153-165.
- Diouf, E., Béziat, D., Debat, P., Grégoire, M., and Ngom, P.M., 2006, Diversity of the Palaeoproterozoic granitoids of the Kédougou inlier (eastern Sénégal): Petrographical and geochemical constraints: *Journal of African Earth Sciences*, v. 44, p. 351-371.
- Egal, E., Thiéblemont, D., Lahondère, D., Guerrot, C., Costea, C.A., Iliescu, D., Delor, C., Goujou, J.C., Lafon, J.M., Tegyey, M., Diaby, S., and Kolié, P., 2002, Late Eburnean granitization and tectonics along the western and northwestern margin of the Archean Kénéma – Man domain (Guinea, West African Craton): *Precambrian Research*, v. 117, p. 57-84.
- Feybesse, J.L., Billa, M., Guerrot, C., Duguey, E., Lescuyer, J.L., Milesi, J.P., and Bouchot, V., 2006, The paleoproterozoic Ghanaian province: Geodynamic model and ore controls, including regional stress modeling: *Precambrian Research*, v. 149, p. 149-196.
- Fougerouse, D., Micklethwaite, S., Ulrich, S., Miller, J., Godel, B., Adams, D., McCuaig, T.C., 2015, Evidence for two stages of mineralization in West Africa's largest gold deposit: Obuasi, Ghana: *Economic Geology*, this volume.
- Goldfarb, R.J., Groves, D.I., and Gardoll, S., 2001, Orogenic gold and geologic time: a global synthesis: *Ore Geology Reviews*, v. 18, p. 1-75.
- Groves, D.I., Goldfarb, R.J., Gebre-Mariam, M., Hagemann, S.G., and Robert, F., 1998, Orogenic gold deposits: A proposed classification in the context of their crustal distribution and relationship to other gold deposit types: *Ore Geology Reviews*, v. 13, p. 7-27.
- Groves, D.I., Goldfarb, R.J., Robert, F., and Hart, C.J.R., 2003, Gold Deposits in Metamorphic Belts: Overview of Current Understanding, Outstanding Problems, Future Research, and Exploration Significance: *Economic Geology*, v. 98, p. 1-29.
- Gueye, M., Ngom, P.M., Diène, M., Thiam, Y., Siegesmund, S., Wemmer, K., and Pawlig, S., 2008, Intrusive rocks and tectono-metamorphic evolution of the Mako

- Paleoproterozoic belt (Eastern Senegal, West Africa): Journal of African Earth Sciences, v. 50, p. 88-110.
- Gueye, M., Siegesmund, S., Wemmer, K., Pawlig, S., Drobe, M., Nolte, N., and Layer, P., 2007, New evidence for an early Birimian evolution in the West African Craton: An example from the Kédougou-Kéniéba inlier, southeast Senegal: South African Journal of Geology, v. 110, p. 511-534.
- Hansen, M., and Anderko, L., 1958, Sulfide Mineral Stabilitites, *in* Barnes, H.L., ed., Geochemistry of Hydrothermal Ore Deposits, 2d ed., New York, Wiley, p. 302-303.
- Hawthorne, F.C., and Henry, D.J., 1999, Classification of the minerals of the tourmaline group: European Journal of Mineralogy, v. 11, p. 201–215.
- Hein, K.A.A., 2010, Succession of structural events in the Goren greenstone belt (Burkina Faso): Implications for West African tectonics: Journal of African Earth Sciences, v. 56, p. 83-94.
- Henry, D.J., and Guidotti, C.V., 1985, Tourmaline as a petrogenetic indicator mineral- an example from the staurolite-grade metapelites of NW Maine: American Mineralogist, v. 70, p. 1–15.
- Hirdes, W., and Davis, D.W., 2002, U-Pb Geochronology of Paleoproterozoic Rocks in the Southern Part of the Kédougou-Kéniéba Inlier, Senegal, West Africa: Evidence for Diachronous Accretionary Development of the Eburnean Province: Precambrian Research, v. 118, p. 83-99.
- IAMGold, 2015, IAMGold Corporation Operations: Sadiola Gold Mine, Mali. Accessed from <http://www.Iamgold.com/English/Operations/Operating-Mines/SadiolaGoldMine/>
- Klöckner, I., 1989, Notice explicative de la carte géologique du Mali occidental, Direction Nationale de la Géologie et des Mines, Ministère de l'industrie, République du Mali.
- Kretschmar, U., and Scott, S.D., 1976, Phase relations involving arsenopyrite in the system Fe-As-S and their application: Canadian Mineralogist, v. 14, p. 364-386.
- Lahondère, D., Thiéblemont, D., Tegyey, M., Guerrot, C., and Diabate, B., 2002, First evidence of early Birimian (2.21 Ga) volcanic activity in Upper Guinea: The volcanics and associated rocks of the Niani suite: Journal of African Earth Sciences, v. 35, p. 417–431.
- Lambert-Smith, J., 2014, The geology, structure and metallogenesis of the world class Loulo-Bambadji Au district in Mali and Senegal, West Africa: Ph.D Thesis, Kingston University, London, 346 p.

- Lawrence, D.M., 2010, Characterization and evolution of Au mineralization in the Loulo mining district, western Mali: Unpublished Ph.D. thesis, London, Kingston University, 341 p.
- Lawrence, D.M., Treloar, P. J., Rankin, A.H., Boyce, A., and Harbidge, P., 2013b, A Fluid Inclusion and Stable Isotope Study at the Loulo Mining District, Mali, West Africa: Implications for Multifluid Sources in the Generation of Orogenic Gold Deposits: *Economic Geology*, v. 108, p. 229-257.
- Lawrence, D.M., Treloar, P.J., Rankin, A.H., Harbidge, P., and Holliday, J., 2013a, The Geology and Mineralogy of the Loulo Mining District, Mali, West Africa: Evidence for Two Distinct Styles of Orogenic Gold Mineralization: *Economic Geology*, v. 108, p. 199-227.
- Lebrun, E., Miller, J., Thébaud, N., Ulrich, S., and McCuaig, C., 2015, The world-class Siguiri gold district, Siguiri Basin, Guinea (West Africa): Stress switches within an orogenic gold system: *Economic geology*, this volume.
- Ledru, P., Pons, J., Milesi, J.P., Feybesse, J. L., and Johan, V., 1991, Transcurrent tectonics and polycyclic evolution in the Lower proterozoic of Senegal-Mali: Precambrian Research, v. 50, p. 337-354.
- Liégeois, J.P., Claessens, W., Camara, D., and Klerkx, J., 1991, Short-lived Eburnian orogeny in southern Mali. *Geology, tectonics, U-Pb and Rb-Sr geochronology: Precambrian Research*, v. 50, p. 111-136.
- Longerich, H.P., Jackson, S.E., Günther, D., 1996, Laser ablation inductively coupled plasma mass spectrometric transient signal data acquisition and analyte concentration calculation: *Journal of Analytical Atomic Spectrometry*, v.11, p. 899-904.
- McCuaig, T.C., and Kerrich, R., 1998, P-T-t-deformation-fluid characteristics of lode gold deposits: evidence from alteration systematics: *Ore Geology Reviews*, v. 12, p. 381-453.
- McFarlane, C.R.M., Mavrogenes, J., Lentz, D., King, K., Allibone, A., and Holcombe, R., 2011, Geology and Intrusion-Related Affinity of the Morila Gold Mine, Southeast Mali: *Economic Geology*, v. 106, p. 727-750.
- Meinert, L. D., Dipple, G.M., and Nicolescu, S., 2005, World Skarn Deposits: *Economic Geology*, 100th Anniversary Volume, p. 299-336.

- Mikucki, E.J., and Ridley, J.R., 1993, The hydrothermal fluid of Archæan lode-gold deposits at different metamorphic grades: compositional constraints from ore and wallrock alteration assemblages: *Mineralium Deposita*, v. 28, p. 469-481.
- Milési, J.P., Ledru, P., Feybesse, J.L., Dommange, A., and Marcoux, E., 1992, Early Proterozoic ore deposits and tectonics of the Birimian orogenic belt, West Africa: *Precambrian Research*, v. 58, p. 305-344.
- Ndiaye, P.M., Dia, A., Vialette, Y., Diallo, D.P., Ngom, P.M., Sylla, M., Wade, S., and Dioh, E., 1997, Données pétrographiques, géochimiques et géochronologiques nouvelles sur les granitoïdes du Paléoprotérozoïque du Supergroupe de Dialé-Daléma (Sénégal Oriental): Implications pétrogénétiques et géodynamiques: *Journal of African Earth Sciences*, v. 25, p. 193-208.
- Nekrasov, I.Y., 1996, *Geochemistry, Mineralogy and Genesis of Gold Deposits*, CRC Press, A.A. Balkema Publishers, Brookfield, USA, p. 141-180.
- Oberthür, T., Vetter, U., Davis, D.W., and Amanor, J.A., 1998, Age constraints on gold mineralization and Paleoproterozoic crustal evolution in the Ashanti belt of southern Ghana: *Precambrian Research*, v. 89, p. 129-143.
- Obolensky, A.A., Gushchina, L. V., Borisenko, A. S., Borovikov, A.A., and Nevol'ko, P.A., 2009, Computer thermodynamic modeling of the transport and deposition of Sb and Au during the formation of Au-Sb deposits: *Russian Geology and Geophysics*, v. 50, p. 950-965.
- Olson, S.F., Diakité, K., Ott, L., Guindo, A., Ford, C.R.B., Winer, N., Hanssen, E., Lay, N., Bradley, R., and Pohl, D., 1992, Regional Setting, Structure, and Descriptive Geology of the Middle Proterozoic Syama Gold Deposit, Mali, West Africa: *Economic Geology*, v. 87, p. 310-331.
- Pawlig, S., Gueye, M., Klischies, R., Schwarz, S., Wemmer, K., and Siegesmund, S., 2006, Geochemical and Sr-Nd isotopic data on the Birimian of the Kedougou-Kenieba Inlier (Eastern Senegal): Implications on the Palaeoproterozoic evolution of the West African Craton: *South African Journal of Geology*, v. 109, p. 411-427.
- Pons, J., Oudin, C., and Valero, J., 1992, Kinematics of large syn-orogenic intrusions: example of the Lower Proterozoic Saraya batholith (Eastern Senegal): *Geologische Rundschau*, v. 81, p. 473-486.
- Pouclet, A., Doumbia, S., and Vidal, M., 2006, Geodynamic setting of the Birimian volcanism in central Ivory Coast (western Africa) and its place in the Palaeoproterozoic

- evolution of the Man Shield: Bulletin de la Société Géologique de France, v. 177, p. 105-121.
- Ridley, J.R., and Diamond, L.W., 2000, Fluid Chemistry of Orogenic Lode Gold Deposits and Implications for Genetic Models: SEG Reviews, v. 2000, p. 141-162.
- Schwartz, M. O., and Melcher, F., 2004, The Falémé Iron District, Senegal: Economic Geology, v. 99, p. 917-939.
- Sharp, Z.D., Essene, E.J., and Kelly, W.C., 1985, A re-examination of the arsenopyrite geothermometer: pressure considerations and applications to natural assemblages: Canadian Mineralogist, v. 23, p. 517-534.
- Shenberger, D.M., and Barnes, H.L., 1989, Solubility of gold in aqueous sulphide solutions from 150° to 350°C: Geochimica et Cosmochimica Acta, v. 53, p. 269–278.
- Sylvester, P.J., Cabri, L.J., Tubrett, M.N., McMahon, G., Laflamme, J.H.G., and Peregoedova, A., 2005, Synthesis and evaluation of a fused pyrrhotite standard reference material for platinum group elements and gold analysis by laser ablation ICPMS, *in* Törmänen, T.O., and Alapieti, T.T., eds., 10th International Platinum Symposium: Oulu, Geological Survey of Finland, Extended Abstracts, p. 16-20.
- Thorne, K.G., Lentz, D.R., Hoy, D., Fyffe, L.R., and Cabri, L.J., 2008, Characteristics of Mineralization at the Main Zone of the Clarence Stream Gold Deposit, Southwestern New Brunswick, Canada: Evidence for an Intrusion-Related Gold System in the Northern Appalachian Orogen: Exploration and Mining Geology, v. 17, p. 13-49.
- Treloar, P.J., Lawrence, D.M., Senghor, D., Boyce, A., and Harbidge, P., 2014, The Massawa gold deposit, Eastern Senegal, West Africa: an orogenic gold deposit sourced from magmatically derived fluids?: Geological Society, London, Special Publications, v. 393, p. 135-160.
- Ulrich, S., Konopásek, J., Jeřábek, P., and Tajčmanová, L., 2011, Transposition of structures in the Neoproterozoic Kaoko Belt (NW Namibia) and their absolute timing: International Journal of Earth Sciences, v. 100, p. 415–429.
- Vassallo, J.J., Wilson, C.J.L., 2002, Paleoproterozoic regional-scale non-coaxial deformation: an example from eastern Eyre Peninsula, South Australia: Journal of Structural Geology, v. 24, p. 1-24.
- Velásquez, G., Béziat, D., Salvi, S., Siebenaller, L., Borisova, A.Y., Pokrovski, G.S., and De Parseval, P., 2014, Formation and deofrmation of pyrite and implications for gold

mineralization in the El Callao district, Venezuela: Economic Geology, v. 109, p. 457-486.

Vidal, M., Gumiaux, C., Cagnard, F., Pouclet, A., Ouattara, G., and Pichon, M., 2009, Evolution of a Paleoproterozoic “weak type” orogeny in the West African Craton (Ivory Coast): Tectonophysics, v. 477, p. 145-159.

Villeneuve, M., 2008, Review of the orogenic belts on the western side of the West African Craton: the Bassarides, Rokelides and Mauritanides, *in* Ennih, N., and Liégeois, J.P., eds., The boundaries of the West African Craton: Geological Society of London Special Publication 297, p. 169-201.

Villeneuve, M., and Cornée, J.J., 1994, Structure, evolution and palaeogeography of the West African craton and bordering belts during the Neoproterozoic: Precambrian Research, v. 69, p. 307-326.

Williams-Jones, A.E., Bowell, R.J., and Migdisov, A.A., 2009, Gold in Solution: Elements, v. 5, p. 281-287.

Williams-Jones, A.E., and Normand, C., 1997, Controls of Mineral Parageneses in the System Fe-Sb-S-O: Economic Geology, v. 92, p. 308-324.

Wilson, S.A., Ridley, W.I., and Koenig, A.E., 2002, Development of sulfide calibration standards for the laser ablation inductively-coupled plasma mass spectrometry technique: Journal of Analytical Atomic Spectrometry, v. 16, p. 406-409.

Yavuz, F., Yavuz, V., and Sasmaz, A., 2006, WinClastour - a visual basic program for tourmaline formula calculation and classification: Computers & Geosciences, v. 32, p. 1156-1168.

11. Supplementary material

11.1. Representative chemical composition of syn-mineralization stage hydrothermal tourmalines at Sadiola Hill.

11.2. Representative analyses of ore minerals.

11.3. Representative analyses of gold phases.

11.4. Representative EPMA analyses of Stage I arsenopyrite crystals.

11.5. Representative LA-ICPMS analyses of Stage I arsenopyrites and pyrites.

11.6. Representative EPMA analyses of buffered arsenopyrite crystals used for geothermometry.

Representative chemical composition of syn-mineralization stage tourmalines at Sadiola Hill

	In selvage of quartz-carbonate vein in metadiorite																
	Core	Core	Core	Core	Core	Core	Core	Core	Core	Core	Core	Rim	Rim	Rim	Rim	Rim	
SiO ₂	35.23	35.25	35.16	35.19	35.04	35.24	35.52	35.28	35.57	35.21	35.35	34.99	34.88	34.99	34.59	34.83	34.85
TiO ₂	0.65	0.67	0.63	0.68	0.37	0.79	0.38	0.48	0.28	0.70	0.39	0.64	0.52	0.61	0.44	0.63	0.78
Al ₂ O ₃	29.82	29.49	30.05	29.80	30.35	29.63	31.46	30.85	31.54	30.13	30.37	27.90	28.38	27.65	28.27	28.49	28.34
FeO(T)	7.32	7.38	7.10	7.11	8.38	7.49	6.98	6.88	6.72	7.12	8.55	9.39	9.11	10.17	9.20	9.22	9.32
MnO	0.00	0.03	0.01	0.02	0.05	0.00	0.00	0.00	0.00	0.01	0.00	0.03	0.01	0.03	0.01	0.04	0.03
MgO	8.03	8.32	8.19	8.30	7.20	8.35	7.51	7.94	7.72	8.18	7.34	7.92	7.87	7.99	8.18	7.96	7.97
CaO	1.29	1.24	1.19	1.28	0.97	1.41	0.62	0.79	0.67	1.23	1.05	1.95	1.72	2.13	1.82	1.84	1.66
Na ₂ O	2.04	2.20	2.25	2.17	2.02	2.01	2.12	2.28	2.31	2.18	2.07	1.85	1.96	1.90	1.89	1.86	2.03
K ₂ O	0.01	0.01	0.01	0.01	0.01	0.01	0.01	0.01	0.01	0.01	0.01	0.03	0.03	0.04	0.03	0.03	0.03
H ₂ O*	3.48	3.52	3.52	3.42	3.50	3.41	3.48	3.49	3.52	3.46	3.50	3.49	3.52	3.50	3.52	3.53	3.53
B ₂ O ₃ *	10.33	10.34	10.36	10.35	10.29	10.37	10.43	10.39	10.46	10.38	10.37	10.20	10.21	10.20	10.23	10.21	10.23
Li ₂ O*	0.05	0.03	0.04	0.04	0.04	0.01	0.02	0.02	0.04	0.05	0.05	0.01	0.03	0.05	0.04	0.01	0.02
Total	98.25	98.45	98.49	98.46	98.13	98.82	98.44	98.38	98.80	98.73	99.01	98.36	98.27	98.82	98.57	98.87	98.03
Structural formula on the basis of 245 oxygens																	
B	3.00	3.00	3.00	3.00	3.00	3.00	3.00	3.00	3.00	3.00	3.00	3.00	3.00	3.00	3.00	3.00	3.00
Si(T)	5.93	5.93	5.90	5.91	5.92	5.90	5.91	5.90	5.92	5.90	5.96	5.92	5.94	5.94	5.89	5.90	5.93
Al(T)	0.07	0.07	0.10	0.09	0.08	0.10	0.09	0.08	0.08	0.09	0.04	0.06	0.06	0.06	0.11	0.10	0.07
Total(T)	6.00	6.00	6.00	6.00	6.00	6.00	6.00	6.00	6.00	6.00	6.00	6.00	6.00	6.00	6.00	6.00	6.00
A(Z)	5.84	5.77	5.84	5.81	5.96	5.76	6.00	5.98	6.00	5.84	5.92	5.56	5.61	5.50	5.60	5.58	5.51
Mg(Z)	0.16	0.23	0.16	0.19	0.04	0.25	0.00	0.02	0.00	0.16	0.08	0.44	0.39	0.51	0.40	0.42	0.49
Fe ³⁺ (Z)	0.00	0.00	0.00	0.00	0.00	0.00	0.00	0.00	0.00	0.00	0.00	0.00	0.00	0.00	0.00	0.00	0.00
Z Total	6.00	6.00	6.00	6.00	6.00	6.00	6.00	6.00	6.00	6.00	6.00	6.00	6.00	6.00	6.00	6.00	6.00
Al(Y)	0.00	0.00	0.00	0.00	0.00	0.00	0.10	0.00	0.00	0.00	0.00	0.00	0.00	0.00	0.00	0.00	0.00
Ti(Y)	0.08	0.08	0.08	0.09	0.05	0.10	0.05	0.06	0.04	0.09	0.05	0.08	0.10	0.07	0.08	0.06	0.07
Fe ³⁺ (Y)	0.00	0.00	0.00	0.00	0.00	0.00	0.00	0.00	0.00	0.00	0.00	0.00	0.00	0.00	0.00	0.00	0.00
Fe ²⁺ (Y)	1.03	1.04	1.00	1.00	1.18	1.05	0.97	0.96	0.93	1.00	1.20	1.34	1.30	1.36	1.31	1.38	1.31
Mg(Y)	1.86	1.86	1.89	1.89	1.77	1.84	1.87	1.96	1.91	1.88	1.75	1.57	1.61	1.52	1.61	1.59	1.54
Li(Y)	0.03	0.02	0.03	0.03	0.00	0.01	0.01	0.01	0.03	0.00	0.01	0.00	0.00	0.00	0.00	0.00	0.00
Y Total	3.00	3.00	3.00	3.01	3.00	3.00	3.00	3.00	3.00	3.00	3.00	3.00	3.00	3.04	3.00	3.02	3.03
Ca(X)	0.23	0.22	0.21	0.23	0.18	0.25	0.11	0.14	0.12	0.22	0.19	0.36	0.31	0.39	0.33	0.34	0.30
Na(X)	0.67	0.72	0.73	0.71	0.66	0.65	0.68	0.74	0.75	0.71	0.67	0.61	0.65	0.63	0.65	0.61	0.67
X Total	0.90	0.94	0.94	0.94	0.84	0.91	0.80	0.88	0.87	0.93	0.86	0.97	0.97	0.95	0.96	0.97	0.98
X vacancy	0.10	0.06	0.06	0.06	0.16	0.09	0.20	0.12	0.13	0.07	0.14	0.03	0.05	0.04	0.04	0.03	0.02
Fe/(Fe+Mg)	0.34	0.33	0.33	0.34	0.34	0.34	0.33	0.33	0.33	0.33	0.40	0.40	0.39	0.42	0.39	0.39	0.37
Na/(Na+Ca)	0.74	0.76	0.77	0.76	0.72	0.79	0.72	0.86	0.84	0.76	0.78	0.63	0.67	0.59	0.65	0.69	0.64
Fe ²⁺ /(Fe ²⁺ +Fe ³⁺)	1.00	1.00	1.00	1.00	1.00	1.00	1.00	1.00	1.00	1.00	1.00	0.94	1.00	0.96	1.00	0.99	0.98
Mg/(Fe ²⁺ +Fe ³⁺)	1.96	2.01	2.06	2.08	1.53	1.99	1.92	2.06	2.05	2.05	1.53	1.50	1.40	1.54	1.58	1.54	1.54
Al/(Al+Fe+Mg)	0.66	0.65	0.66	0.67	0.65	0.69	0.67	0.69	0.66	0.66	0.63	0.62	0.63	0.62	0.63	0.62	0.62
Mg/(Mg+Al+Fe)	0.23	0.23	0.23	0.20	0.23	0.21	0.22	0.23	0.21	0.23	0.20	0.23	0.22	0.23	0.22	0.23	0.23
Ca/(Ca+Fe+Mg)	0.07	0.07	0.07	0.07	0.06	0.08	0.04	0.05	0.04	0.07	0.06	0.10	0.09	0.10	0.08	0.10	0.10
Σ cations	18.90	18.94	18.94	18.94	18.85	18.91	18.80	18.88	18.87	18.93	18.87	18.97	18.90	18.98	18.99	19.01	18.98

Representative chemical composition of syn-mineralization stage tourmalines at Sadiola Hill

	1	2	3	4	5	6	7	8	9	10	11	12	13	14	15	16	17	18
SiO ₂	36.08	36.31	36.75	36.26	35.92	36.47	36.22	36.05	35.99	36.43	36.70	36.43	36.13	36.33	35.73	36.06	36.53	
TiO ₂	1.18	0.94	0.27	0.76	1.25	0.43	0.59	1.01	0.93	1.11	0.87	0.22	0.87	1.16	0.79	1.04	0.71	0.27
Al ₂ O ₃	29.17	29.80	32.03	30.23	29.17	32.06	31.05	29.62	30.20	29.77	30.68	32.68	30.68	29.54	30.40	29.61	30.88	32.45
FeO(T)	2.77	2.24	2.05	2.22	2.81	2.28	2.31	2.46	2.24	2.65	2.19	2.10	2.28	2.61	2.25	2.59	2.27	2.28
MnO	0.00	0.03	0.01	0.00	0.01	0.00	0.01	0.02	0.00	0.00	0.02	0.00	0.00	0.00	0.00	0.00	0.00	0.00
MgO	11.25	11.22	10.06	11.32	11.03	10.05	10.77	11.18	11.22	11.12	11.25	9.97	11.12	11.05	11.14	11.39	11.22	10.10
CaO	3.14	2.36	1.10	2.45	3.02	1.22	2.11	3.09	2.36	3.00	2.48	1.00	2.37	2.97	2.34	3.17	2.24	0.96
Na ₂ O	1.13	1.56	1.85	1.56	1.24	1.88	1.65	1.17	1.61	1.24	1.62	1.98	1.72	1.21	1.61	1.15	1.56	2.02
K ₂ O	0.01	0.02	0.01	0.02	0.01	0.01	0.02	0.01	0.02	0.01	0.02	0.01	0.01	0.01	0.01	0.01	0.02	0.01
H ₂ O*	3.57	3.58	3.47	3.60	3.58	3.50	3.58	3.58	3.61	3.59	3.65	3.51	3.66	3.57	3.60	3.58	3.58	3.51
B ₂ O ₃ *	10.57	10.60	10.66	10.64	10.54	10.66	10.65	10.58	10.64	10.61	10.73	10.72	10.72	10.59	10.65	10.57	10.66	10.70
Li ₂ O ₂ *	0.20	0.18	0.14	0.16	0.23	0.14	0.16	0.22	0.17	0.20	0.19	0.13	0.20	0.23	0.17	0.11	0.09	0.09
Total	99.06	98.82	98.40	99.21	98.79	98.71	99.99	98.98	99.26	99.29	100.12	99.02	100.05	99.06	99.28	99.01	99.28	98.91
Structural formula on the basis of 24.5 oxygens																		
B	3.00	3.00	3.00	3.00	3.00	3.00	3.00	3.00	3.00	3.00	3.00	3.00	3.00	3.00	3.00	3.00	3.00	3.00
Si(T)	5.93	5.95	5.99	5.92	5.93	5.95	5.91	5.92	5.92	5.90	5.90	5.95	5.91	5.93	5.93	5.87	5.88	5.94
Al(T)	0.07	0.05	0.01	0.08	0.08	0.06	0.09	0.08	0.08	0.10	0.10	0.05	0.09	0.07	0.07	0.13	0.12	0.07
Total(T)	6.00	6.00	6.00	6.00	6.00	6.00	6.00	6.00	6.00	6.00	6.00	6.00	6.00	6.00	6.00	6.00	6.00	6.00
Al(Z)	5.58	5.71	6.00	5.74	5.60	6.00	5.89	5.65	5.73	5.65	5.76	6.00	5.77	5.65	5.78	5.61	5.81	6.00
Mg(Z)	0.42	0.29	0.00	0.26	0.40	0.00	0.11	0.35	0.27	0.35	0.24	0.00	0.23	0.35	0.23	0.39	0.19	0.00
Fe ³⁺ (Z)	0.00	0.00	0.00	0.00	0.00	0.00	0.00	0.00	0.00	0.00	0.00	0.00	0.00	0.00	0.00	0.00	0.00	0.00
Z Total	6.00	6.00	6.00	6.00	6.00	6.00	6.00	6.00	6.00	6.00	6.00	6.00	6.00	6.00	6.00	6.00	6.00	6.00
Al(Y)	0.00	0.00	0.15	0.00	0.00	0.11	0.00	0.00	0.00	0.00	0.00	0.20	0.00	0.00	0.00	0.00	0.00	0.15
Ti(Y)	0.15	0.12	0.03	0.09	0.16	0.05	0.07	0.13	0.12	0.14	0.11	0.03	0.11	0.14	0.10	0.13	0.09	0.03
Fe ³⁺ (Y)	0.00	0.00	0.00	0.00	0.00	0.00	0.00	0.00	0.00	0.00	0.00	0.00	0.00	0.00	0.00	0.00	0.00	0.00
Fe ²⁺ (Y)	0.38	0.31	0.28	0.30	0.39	0.31	0.32	0.34	0.31	0.36	0.30	0.29	0.31	0.36	0.31	0.36	0.31	0.31
Mg(Y)	2.34	2.46	2.45	2.50	2.31	2.44	2.51	2.39	2.47	2.37	2.41	2.46	2.41	2.35	2.48	2.40	2.54	2.45
Li(Y)	0.14	0.12	0.09	0.10	0.15	0.09	0.10	0.14	0.11	0.14	0.12	0.09	0.13	0.15	0.11	0.11	0.07	0.06
Y Total	3.00	3.00	3.00	3.00	3.00	3.00	3.00	3.00	3.00	3.00	3.00	3.00	3.00	3.00	3.00	3.00	3.00	3.00
Ca(X)	0.55	0.42	0.19	0.43	0.53	0.21	0.37	0.54	0.41	0.53	0.43	0.17	0.41	0.52	0.41	0.56	0.39	0.17
Na(X)	0.36	0.50	0.59	0.49	0.40	0.59	0.52	0.37	0.51	0.39	0.51	0.62	0.54	0.39	0.51	0.37	0.49	0.64
X Total	0.91	0.92	0.78	0.93	0.81	0.93	0.90	0.92	0.93	0.92	0.94	0.80	0.95	0.91	0.92	0.93	0.89	0.81
X vacancy	0.09	0.09	0.22	0.07	0.07	0.19	0.11	0.08	0.07	0.08	0.06	0.20	0.05	0.09	0.08	0.07	0.11	0.20
Fe/(Fe+Mg)	0.12	0.10	0.10	0.10	0.13	0.11	0.11	0.10	0.12	0.10	0.11	0.10	0.10	0.12	0.10	0.11	0.10	0.11
Na/(Na+Ca)	0.39	0.55	0.75	0.54	0.43	0.74	0.59	0.41	0.55	0.43	0.54	0.78	0.57	0.42	0.56	0.40	0.56	0.79
Fe ²⁺ /(Fe ²⁺ +Fe ³⁺)	1.00	1.00	1.00	1.00	1.00	1.00	1.00	1.00	1.00	1.00	1.00	1.00	1.00	1.00	1.00	1.00	1.00	1.00
Mg/(Fe ²⁺ +Fe ³⁺)	7.25	8.93	8.73	9.10	7.01	7.85	8.31	8.12	8.92	7.47	9.15	8.45	8.68	7.53	8.84	7.84	8.82	7.89
Al/(Al+Fe+Mg)	0.64	0.65	0.69	0.66	0.65	0.69	0.67	0.65	0.66	0.65	0.66	0.65	0.65	0.66	0.65	0.66	0.69	0.69
Mg/(Mg+Al+Fe)	0.31	0.28	0.31	0.31	0.27	0.29	0.31	0.31	0.31	0.31	0.31	0.27	0.30	0.31	0.31	0.31	0.30	0.27
Ca/(Ca+Fe+Mg)	0.15	0.12	0.07	0.12	0.15	0.07	0.11	0.15	0.12	0.15	0.13	0.06	0.12	0.15	0.12	0.15	0.11	0.06
Σ cations	18.91	18.92	18.78	18.93	18.81	18.90	18.92	18.93	18.92	18.94	18.90	18.92	18.91	18.92	18.93	18.89	18.89	18.81

Representative chemical composition of syn-mineralization stage tourmaline at Sadiola Hill

	Acicular masses and heart-shaped mineral sections along the shear fabric in impure metallimestone																		
	19	20	21	22	23	24	25	26	27	28	29	30	31	32	33	34	35	36	37
SiO ₂	35.82	36.26	35.95	36.33	35.99	36.24	36.35	36.17	36.30	36.01	35.95	36.17	36.20	36.17	36.43	36.39	36.04	36.22	35.61
TiO ₂	0.76	0.23	0.61	0.28	0.93	0.64	1.00	0.67	1.58	0.89	0.88	0.77	1.11	1.11	0.36	0.87	1.07	0.84	2.19
Al ₂ O ₃	30.50	32.55	31.44	32.60	30.38	29.91	30.90	30.18	30.98	28.57	31.29	30.83	30.97	30.16	32.56	30.84	30.12	30.01	28.87
FeO(T)	2.38	2.23	2.55	2.13	2.34	2.53	2.41	2.59	2.52	3.08	2.33	2.45	2.61	2.51	2.33	2.56	2.49	2.39	3.36
MnO	0.01	0.00	0.00	0.00	0.00	0.00	0.00	0.03	0.01	0.00	0.01	0.02	0.00	0.00	0.00	0.00	0.01	0.00	0.02
MgO	11.10	10.09	10.46	10.26	11.35	10.68	10.63	10.68	10.17	11.17	10.28	10.27	10.30	10.85	9.81	10.51	10.73	11.16	10.48
CaO	2.30	0.94	1.82	1.03	2.38	1.90	1.35	1.87	1.73	2.26	1.83	1.48	1.58	1.97	0.95	1.33	1.86	1.96	2.06
Na ₂ O	1.56	2.17	1.84	2.05	1.57	1.85	1.99	1.87	1.81	1.58	1.70	1.90	1.93	1.75	1.82	1.91	1.83	1.70	1.62
K ₂ O	0.02	0.01	0.02	0.00	0.01	0.02	0.03	0.03	0.03	0.02	0.03	0.02	0.03	0.03	0.01	0.03	0.03	0.01	0.01
H ₂ O*	3.57	3.58	3.53	3.59	3.58	3.54	3.59	3.59	3.59	3.55	3.55	3.54	3.53	3.56	3.57	3.44	3.52	3.57	3.52
B ₂ O ₃ *	10.59	10.67	10.63	10.70	10.64	10.55	10.61	10.58	10.59	10.51	10.60	10.57	10.60	10.60	10.66	10.62	10.56	10.58	10.48
Li ₂ O*	0.12	0.10	0.14	0.09	0.12	0.11	0.18	0.20	0.14	0.18	0.17	0.17	0.16	0.10	0.11	0.17	0.11	0.19	0.19
Total	98.71	98.79	99.06	99.01	99.29	98.44	98.55	98.75	98.55	98.63	98.29	98.73	98.90	98.47	98.68	98.49	98.56	98.39	
Structural formula on the basis of 24.5 oxygens																			
B	3.00	3.00	3.00	3.00	3.00	3.00	3.00	3.00	3.00	3.00	3.00	3.00	3.00	3.00	3.00	3.00	3.00	3.00	3.00
Si(T)	5.88	5.91	5.88	5.90	5.88	5.97	5.96	5.94	5.96	5.89	5.95	5.94	5.93	5.94	5.96	5.93	5.95	5.90	5.90
Al(T)	0.12	0.10	0.12	0.10	0.12	0.03	0.04	0.06	0.04	0.04	0.11	0.05	0.07	0.07	0.06	0.07	0.05	0.07	0.10
Total(T)	6.00	6.00	6.00	6.00	6.00	6.00	6.00	6.00	6.00	6.00	6.00	6.00	6.00	6.00	6.00	6.00	6.00	6.00	
Al(Z)	5.78	6.00	5.93	6.00	5.73	5.78	5.92	5.79	5.95	5.53	5.94	5.92	5.76	6.00	5.90	5.78	5.76	5.76	5.55
Mg(Z)	0.22	0.00	0.07	0.00	0.28	0.22	0.08	0.22	0.05	0.47	0.06	0.08	0.24	0.00	0.10	0.22	0.24	0.45	0.45
Fe ³⁺ (Z)	0.00	0.00	0.00	0.00	0.00	0.00	0.00	0.00	0.00	0.00	0.00	0.00	0.00	0.00	0.00	0.00	0.00	0.00	0.00
Z Total	6.00	6.00	6.00	6.00	6.00	6.00	6.00	6.00	6.00	6.00	6.00	6.00	6.00	6.00	6.00	6.00	6.00	6.00	
Al(Y)	0.00	0.15	0.00	0.14	0.00	0.00	0.00	0.00	0.00	0.00	0.00	0.00	0.00	0.00	0.19	0.00	0.00	0.00	0.00
Ti(Y)	0.09	0.03	0.08	0.04	0.11	0.12	0.08	0.12	0.08	0.20	0.11	0.11	0.10	0.14	0.04	0.11	0.13	0.10	0.27
Fe ³⁺ (Y)	0.00	0.00	0.00	0.00	0.00	0.00	0.00	0.00	0.00	0.00	0.00	0.00	0.00	0.00	0.00	0.00	0.00	0.00	0.00
Fe ²⁺ (Y)	0.33	0.30	0.35	0.29	0.32	0.35	0.33	0.36	0.35	0.43	0.32	0.34	0.36	0.34	0.32	0.35	0.34	0.33	0.47
Mg(Y)	2.50	2.45	2.48	2.48	2.49	2.40	2.52	2.40	2.44	2.45	2.44	2.44	2.44	2.41	2.38	2.47	2.41	2.49	2.14
Li(Y)	0.08	0.07	0.09	0.06	0.08	0.13	0.07	0.12	0.13	0.10	0.12	0.11	0.11	0.11	0.06	0.08	0.11	0.08	0.12
Y Total	3.00	3.00	3.00	3.00	3.00	3.00	3.00	3.00	3.00	3.00	3.00	3.00	3.00	3.00	3.00	3.00	3.00	3.00	
Ca(X)	0.40	0.16	0.32	0.18	0.42	0.34	0.24	0.33	0.30	0.40	0.32	0.26	0.28	0.35	0.17	0.23	0.33	0.37	
Na(X)	0.50	0.69	0.58	0.65	0.50	0.59	0.63	0.60	0.58	0.51	0.54	0.61	0.56	0.58	0.61	0.58	0.54	0.52	0.59
X Total	0.91	0.85	0.91	0.83	0.91	0.93	0.87	0.93	0.89	0.91	0.87	0.90	0.91	0.74	0.84	0.92	0.89	0.89	0.89
X Vacancy	0.09	0.15	0.09	0.17	0.09	0.07	0.13	0.07	0.11	0.09	0.13	0.10	0.09	0.26	0.16	0.08	0.11	0.11	
Fe/(Fe ²⁺ +Mg)	0.11	0.12	0.10	0.10	0.12	0.11	0.12	0.12	0.13	0.11	0.12	0.12	0.12	0.12	0.12	0.12	0.12	0.11	0.15
Na/(Na+Ca)	0.55	0.81	0.65	0.78	0.54	0.64	0.73	0.64	0.66	0.56	0.63	0.70	0.69	0.62	0.78	0.72	0.64	0.61	0.59
Fe ²⁺ /(Fe ²⁺ +Fe ³⁺)	1.00	1.00	1.00	1.00	1.00	1.00	1.00	1.00	1.00	1.00	1.00	1.00	1.00	1.00	1.00	1.00	1.00	1.00	1.00
Mg/(Fe ²⁺ +Fe ³⁺)	8.33	8.09	7.32	8.58	8.65	7.52	7.88	7.36	7.20	6.46	7.87	7.47	7.04	7.72	7.50	7.33	7.67	8.32	5.57
Al/(Al+Fe ²⁺ +Mg)	0.66	0.69	0.68	0.69	0.66	0.67	0.66	0.67	0.66	0.64	0.68	0.68	0.66	0.70	0.67	0.66	0.66	0.65	0.65
Mg/(Mg+Al+Fe)	0.30	0.27	0.29	0.28	0.31	0.30	0.29	0.30	0.28	0.32	0.28	0.29	0.30	0.27	0.29	0.30	0.31	0.30	0.30
Ca/(Ca+Fe+Mg)	0.12	0.06	0.10	0.06	0.12	0.10	0.08	0.10	0.10	0.11	0.10	0.08	0.09	0.10	0.06	0.07	0.10	0.10	0.11
Σ cations	18.91	18.85	18.91	18.83	18.93	18.87	18.93	18.87	18.91	18.87	18.93	18.87	18.91	18.91	18.84	18.92	18.89	18.89	18.89

Representative analyses of ore minerals

Ore Mineral	Wt %											Host	Method		
	Fe	As	Sb	S	Au	Ag	Cu	Pb	Ni	Zn	Bi	Total			
<i>Sb-bearing phases</i>															
Berthierite	13.07	-	57.5	29.92	-	-	-	-	-	-	-	100.49	GW	SEM-EDS	
Berthierite	12.62	-	57.61	29.31	-	-	-	-	-	-	-	99.54	GW	SEM-EDS	
Berthierite	13.27	-	57.43	29.38	-	-	-	-	-	-	-	100.08	GW	SEM-EDS	
Berthierite	12.69	-	58.25	29.88	-	-	-	-	-	-	-	100.83	GW	SEM-EDS	
Berthierite	12.71	-	57.45	29.51	-	-	-	-	-	-	-	99.68	Mly Lms	SEM-EDS	
Berthierite	13.19	-	57.09	29.54	-	-	-	-	-	-	-	99.81	Mly Lms	SEM-EDS	
Stibnite	-	-	72.16	27.6	-	-	-	-	-	-	-	99.76	GW	SEM-EDS	
Stibnite	-	-	71.06	28.03	-	-	-	-	-	-	-	99.09	Mly Lms	SEM-EDS	
Stibnite	0.17	b.d.l.	70.65	28.51	b.d.l.	b.d.l.	b.d.l.	n.a.	n.a.	b.d.l.	b.d.l.	99.33	GW	EPMA	
Jamesonite	2.56	-	35.75	21.54	-	-	-	39.33	-	-	-	99.16	GW	SEM-EDS	
Jamesonite	2.88	-	36.16	21.84	-	-	-	39.83	-	-	-	100.72	GW	SEM-EDS	
Jamesonite	2.79	-	36.04	21.24	-	-	-	39.91	-	-	-	99.98	GW	SEM-EDS	
Ullmannite	-	-	58.36	15.39	-	-	-	-	27.15	-	-	101.25	GW	SEM-EDS	
Ullmannite	-	-	58.17	15.19	-	-	-	-	26.06	-	-	99.42	GW	SEM-EDS	
Gudmundite	25.95	0.45	57.09	15.97	b.d.l.	b.d.l.	b.d.l.	n.a.	n.a.	b.d.l.	b.d.l.	99.46	GW	EPMA	
Gudmundite	26.37	0.51	56.31	15.72	b.d.l.	b.d.l.	b.d.l.	n.a.	n.a.	b.d.l.	b.d.l.	98.92	GW	EPMA	
Native Sb	-	-	99.82	-	-	-	-	-	-	-	-	99.82	GW	SEM-EDS	
Tetrahedrite	5.86	-	28.19	24.67	-	5.05	32.89	-	-	3.03	-	101.12	GW	SEM-EDS	
Tetrahedrite	6.77	-	26.66	24.85	-	5.29	32.87	-	-	2.78	-	99.22	GW	SEM-EDS	
Tetrahedrite	2.08	0.46	27.92	23.83	-	0.51	39.45	-	-	5.69	-	99.94	Mly Lms	SEM-EDS	
Tetrahedrite	1.19	0.69	27.57	25.27	b.d.l.	0.13	37.20	n.a.	n.a.	6.31	b.d.l.	98.37	Mly Lms	EPMA	
Tetrahedrite	1.46	1.71	26.01	25.47	b.d.l.	b.d.l.	37.69	n.a.	n.a.	5.96	b.d.l.	98.28	Mly Lms	EPMA	
Tetrahedrite	1.48	b.d.l.	28.51	25.59	b.d.l.	0.08	37.28	n.a.	n.a.	6.00	b.d.l.	98.95	Mly Lms	EPMA	
Tetr-Tenn	3.44	3.23	23.93	25.78	b.d.l.	0.13	38.03	n.a.	n.a.	4.08	b.d.l.	98.62	Mly Lms	EPMA	
Tetr-Tenn	1.95	3.82	23.51	25.73	b.d.l.	b.d.l.	37.89	n.a.	n.a.	5.88	b.d.l.	98.79	Mly Lms	EPMA	
Tenn-Tetr	3.27	12.84	11.11	25.76	-	-	42.41	-	-	4.62	-	100.00	Mly Lms	SEM-EDS	
<i>Bi-bearing phases</i>															
Native bismuth	b.d.l.	b.d.l.	b.d.l.	0.05	b.d.l.	b.d.l.	b.d.l.	n.a.	n.a.	b.d.l.	98.43	98.48	GW	EPMA	
Native bismuth	0.04	b.d.l.	b.d.l.	b.d.l.	b.d.l.	b.d.l.	b.d.l.	n.a.	n.a.	b.d.l.	98.68	98.73	GW	EPMA	
Horobetsuite	-	-	28.66	23.40	-	-	-	-	-	-	48.73	100.79	GW	SEM-EDS	
<i>Sulfide phases</i>															
Pyrite	45.88	0.29	b.d.l.	53.37	b.d.l.	b.d.l.	b.d.l.	n.a.	n.a.	b.d.l.	b.d.l.	99.54	GW	EPMA	
Pyrite	45.72	0.42	b.d.l.	53.98	b.d.l.	b.d.l.	b.d.l.	n.a.	n.a.	b.d.l.	b.d.l.	100.12	GW	EPMA	
Pyrite	45.62	b.d.l.	b.d.l.	53.84	b.d.l.	b.d.l.	b.d.l.	n.a.	n.a.	b.d.l.	b.d.l.	99.47	GW	EPMA	
Pyrite	45.15	1.20	b.d.l.	53.36	b.d.l.	b.d.l.	b.d.l.	n.a.	n.a.	b.d.l.	b.d.l.	99.70	Mly Lms	EPMA	
Pyrite	45.04	1.07	b.d.l.	53.14	b.d.l.	b.d.l.	b.d.l.	0.03	n.a.	n.a.	b.d.l.	b.d.l.	99.28	Mly Lms	EPMA
Pyrite	45.00	1.52	0.11	52.89	b.d.l.	b.d.l.	b.d.l.	0.18	n.a.	n.a.	b.d.l.	b.d.l.	99.70	Mly Lms	EPMA
Pyrhotite	58.34	1.23	b.d.l.	39.40	b.d.l.	b.d.l.	b.d.l.	n.a.	n.a.	b.d.l.	b.d.l.	98.98	Mly Lms	EPMA	
Pyrhotite	58.84	0.42	b.d.l.	39.40	b.d.l.	b.d.l.	b.d.l.	n.a.	n.a.	b.d.l.	b.d.l.	98.66	Mly Lms	EPMA	

Representative analyses of gold phases

Mineralogy	Ore stage	Wt %						Host	Method
		Au	Ag	Sb	Cu	Bi	Total		
Gold	I	97.85	2.16	-	-	-	100.01	GW	SEM-EDS
Gold	I	94.87	5.77	-	-	-	100.65	GW	SEM-EDS
Gold	I	100.86	-	-	-	-	100.86	GW	SEM-EDS
Gold	I	99.95	-	-	-	-	99.95	Mly Lms	SEM-EDS
Gold	I	99.55	-	-	-	-	99.55	Mly Lms	SEM-EDS
Gold	I	96.02	3.64	-	-	-	99.66	GW	SEM-EDS
Gold	I	99.13	1.48	-	-	-	100.61	GW	SEM-EDS
Gold	I	99.28	0.79	b.d.l.	0.04	b.d.l.	100.10	GW	EPMA
Gold	I	100.05	1.00	b.d.l.	0.04	b.d.l.	101.08	GW	EPMA
Gold	I	99.28	0.58	b.d.l.	0.03	b.d.l.	99.90	GW	EPMA
Gold	I	100.86	0.52	b.d.l.	b.d.l.	b.d.l.	101.41	GW	EPMA
Gold	I	99.34	1.31	b.d.l.	b.d.l.	b.d.l.	100.65	Mly Lms	EPMA
Gold	I	97.88	0.94	b.d.l.	0.04	b.d.l.	98.86	Mly Lms	EPMA
Gold	II	100.54	-	-	-	-	100.54	GW	SEM-EDS
Gold	II	99.06	-	-	-	-	99.06	Mly Lms	SEM-EDS
Gold	II	99.55	-	-	-	-	99.55	Mly Lms	SEM-EDS
Gold	II	99.4	-	-	-	-	99.4	Mly Lms	SEM-EDS
Gold	II	99.24	-	-	-	-	99.24	Mly Lms	SEM-EDS
Gold	II	100.61	-	-	-	-	100.61	Mly Lms	SEM-EDS
Gold	II	99.39	-	-	-	-	99.39	Mly Lms	SEM-EDS
Gold	II	99.44	-	-	-	-	99.44	Mly Lms	SEM-EDS
Gold	II	99.46	0.56	b.d.l.	b.d.l.	b.d.l.	100.02	GW	EPMA
Gold	II	99.76	0.63	b.d.l.	b.d.l.	b.d.l.	100.39	GW	EPMA
Gold	II	99.34	0.70	0.07	b.d.l.	b.d.l.	100.11	GW	EPMA
Gold	II	99.52	0.55	b.d.l.	b.d.l.	b.d.l.	100.08	GW	EPMA
Gold	II	100.33	0.51	b.d.l.	b.d.l.	b.d.l.	100.84	GW	EPMA
Gold	II	100.58	0.71	b.d.l.	b.d.l.	b.d.l.	101.40	GW	EPMA
Gold	II	99.89	1.17	b.d.l.	b.d.l.	b.d.l.	101.08	GW	EPMA
Gold	II	99.30	0.70	b.d.l.	0.05	b.d.l.	100.05	GW	EPMA
Gold	II	100.49	0.15	b.d.l.	b.d.l.	0.16	100.80	GW	EPMA
Gold	II	100.75	0.19	b.d.l.	b.d.l.	b.d.l.	100.94	GW	EPMA
Gold	II	100.20	0.23	b.d.l.	0.05	b.d.l.	100.47	GW	EPMA
Gold	II	100.09	0.65	b.d.l.	b.d.l.	b.d.l.	100.74	GW	EPMA
Gold	II	100.35	0.83	b.d.l.	b.d.l.	b.d.l.	101.18	GW	EPMA
Gold	II	99.28	1.06	b.d.l.	0.04	b.d.l.	100.41	GW	EPMA
Gold	II	100.05	0.52	b.d.l.	0.05	b.d.l.	100.62	GW	EPMA
Gold	II	99.26	1.31	b.d.l.	0.03	b.d.l.	100.82	Mly Lms	EPMA
Gold	II	99.73	0.71	b.d.l.	0.05	b.d.l.	100.50	Mly Lms	EPMA
Aurostibite	II	46.07	-	53.62	-	-	99.69	GW	SEM-EDS
Aurostibite	II	46.6	-	54.28	-	-	100.88	GW	SEM-EDS
Aurostibite	II	45.19	-	53.82	-	-	99.01	GW	SEM-EDS
Aurostibite	II	45.17	-	55.24	-	-	100.41	Mly Lms	SEM-EDS
Aurostibite	II	45.84	-	54.28	-	-	100.12	Mly Lms	SEM-EDS
Aurostibite	II	45.19	-	55.4	-	-	100.59	Mly Lms	SEM-EDS
Aurostibite	II	45.45	-	54.69	-	-	100.14	Mly Lms	SEM-EDS
Aurostibite	II	44.44	-	55.35	-	-	99.79	Mly Lms	SEM-EDS
Aurostibite	II	44.77	-	55.25	-	-	100.02	Mly Lms	SEM-EDS
Aurostibite	II	42.88	b.d.l.	57.07	b.d.l.	b.d.l.	99.95	GW	EPMA
Aurostibite	II	44.15	b.d.l.	56.56	b.d.l.	b.d.l.	100.70	Mly Lms	EPMA
Aurostibite	II	43.90	b.d.l.	56.77	b.d.l.	b.d.l.	100.67	Mly Lms	EPMA
Aurostibite	II	43.71	b.d.l.	57.16	b.d.l.	b.d.l.	100.88	Mly Lms	EPMA
Aurostibite	II	43.67	b.d.l.	56.73	b.d.l.	b.d.l.	100.40	Mly Lms	EPMA
Aurostibite	II	44.22	b.d.l.	56.38	b.d.l.	b.d.l.	100.60	Mly Lms	EPMA
Aurostibite	II	44.22	b.d.l.	56.38	b.d.l.	b.d.l.	100.60	Mly Lms	EPMA
Maldonite	II	66.63	b.d.l.	b.d.l.	b.d.l.	35.14	101.77	GW	EPMA
Maldonite	II	66.29	b.d.l.	b.d.l.	0.06	35.19	101.54	GW	EPMA

Representative EPMA analyses of stage I arsenopyrite crystals

Spot-ID	Host rock	Zoning	Fe wt%	S wt%	As wt%	Co ppm	Ni ppm	Au ppm	Sb ppm	Total
Sa124_1	QFP	-	34.53	20.83	44.86	b.d.l.	b.d.l.	b.d.l.	448.86	100.26
Sa124_2	QFP	-	34.43	20.81	44.91	b.d.l.	b.d.l.	b.d.l.	b.d.l.	100.14
Sa124_3	QFP	-	34.35	20.94	44.81	b.d.l.	b.d.l.	b.d.l.	393.75	100.14
Sa124_4	QFP	-	33.91	20.46	45.95	b.d.l.	b.d.l.	b.d.l.	b.d.l.	100.33
Sa124_5	QFP	-	33.78	20.49	45.21	b.d.l.	b.d.l.	b.d.l.	b.d.l.	99.48
Sa124_6	QFP	-	34.67	21.33	44.15	b.d.l.	b.d.l.	b.d.l.	311.35	100.18
Sa124_7	QFP	-	34.40	20.70	44.97	b.d.l.	b.d.l.	b.d.l.	b.d.l.	100.09
Sa124_8	QFP	-	34.31	20.67	45.58	b.d.l.	b.d.l.	b.d.l.	b.d.l.	100.58
Sa124_9	QFP	-	34.61	20.86	45.17	b.d.l.	b.d.l.	b.d.l.	419.18	100.70
Sa124_10	QFP	-	34.58	20.89	44.93	b.d.l.	b.d.l.	b.d.l.	305.77	100.44
Sa124_11	QFP	-	34.32	20.56	45.39	b.d.l.	b.d.l.	b.d.l.	b.d.l.	100.28
Sa124_12	QFP	-	34.21	20.46	45.56	b.d.l.	b.d.l.	b.d.l.	345.11	100.28
Sa124_13	QFP	-	34.53	20.44	45.51	b.d.l.	b.d.l.	b.d.l.	b.d.l.	100.50
Sa124_14l	QFP	lighter	34.11	19.41	46.86	b.d.l.	b.d.l.	b.d.l.	763.07	100.46
Sa124_14d	QFP	darker	34.53	20.61	45.13	b.d.l.	b.d.l.	b.d.l.	b.d.l.	100.27
Sa124_15l	QFP	lighter	34.04	19.60	46.59	b.d.l.	b.d.l.	b.d.l.	840.32	100.32
Sa124_15d	QFP	darker	34.71	21.28	44.26	b.d.l.	b.d.l.	b.d.l.	b.d.l.	100.27
Sa124_16l	QFP	lighter	33.81	19.60	46.88	b.d.l.	b.d.l.	b.d.l.	860.38	100.38
Sa124_16d	QFP	darker	34.57	21.76	43.47	b.d.l.	b.d.l.	b.d.l.	424.82	99.84
Sa124_17l	QFP	lighter	33.90	19.69	46.93	b.d.l.	b.d.l.	b.d.l.	1240.56	100.65
Sa124_17d	QFP	darker	34.53	21.03	44.93	b.d.l.	b.d.l.	b.d.l.	405.90	100.55
Sa124_18l	QFP	lighter	34.04	19.54	46.61	b.d.l.	b.d.l.	b.d.l.	1014.04	100.29
Sa124_18d	QFP	darker	34.28	20.61	45.43	b.d.l.	b.d.l.	b.d.l.	316.33	100.36
SD732-1	Lms	-	34.21	20.47	45.91	398.85	457.94	b.d.l.	535.23	100.728
SD732-2	Lms	-	34.43	20.32	45.95	202.03	309.43	b.d.l.	935.38	100.857
SD732-3	Lms	-	34.83	22.29	43.45	294.64	140.6	b.d.l.	b.d.l.	100.646
SD732-4	Lms	-	35.00	22.29	43.26	b.d.l.	273.83	b.d.l.	b.d.l.	100.582
SD732-5	Lms	-	33.94	20.27	45.79	617.2	781.39	b.d.l.	500.09	100.183
SD732-6	Lms	-	34.10	20.32	45.89	434.1	152.47	b.d.l.	738.85	100.446
SD732-9	Lms	-	34.19	20.30	46.48	b.d.l.	146.96	b.d.l.	979.96	101.195
SD732-7	Lms	-	34.48	21.28	44.56	b.d.l.	138.79	b.d.l.	b.d.l.	100.364
SD732-8	Lms	-	34.47	20.20	46.19	348.25	169.99	b.d.l.	603.84	100.992
SD732-9	Lms	-	34.21	20.21	45.69	326.57	273.5	b.d.l.	834.5	100.266
SD732-10	Lms	-	34.85	21.76	43.68	82.25	185.88	b.d.l.	b.d.l.	100.328
SD732-11	Lms	-	34.16	20.42	45.80	360.5	723.2	b.d.l.	530.62	100.543
SD732-12	Lms	-	34.16	20.27	46.12	572.48	226.59	b.d.l.	777.14	100.703
SD732-13	Lms	-	34.24	20.55	45.76	1357.7	838.51	b.d.l.	795.34	100.852
SD732-14	Lms	-	34.25	20.23	46.12	336.32	186.68	b.d.l.	619.12	100.719
SD732-15	Lms	-	33.84	20.27	46.29	394.55	886.67	b.d.l.	901.3	100.617
SD732-16l	Lms	lighter	34.09	20.30	45.75	492.3	159.67	b.d.l.	560.58	100.274
SD732-16d	Lms	darker	34.85	22.13	43.13	205.37	119.81	b.d.l.	b.d.l.	100.158
SD732-17l	Lms	lighter	34.14	20.24	45.88	393.9	295.22	b.d.l.	1129.87	100.452
SD732-17d	Lms	darker	34.57	21.58	43.73	130.95	b.d.l.	b.d.l.	b.d.l.	99.9183
SD732-18l	Lms	lighter	34.18	20.32	45.93	308.92	891.64	b.d.l.	891.42	100.641
SD732-18d	Lms	darker	34.29	21.11	44.70	705.03	146.97	b.d.l.	345.37	100.221
SD732-19l	Lms	lighter	33.85	20.07	46.12	b.d.l.	860.47	b.d.l.	2598.26	100.403
SD732-19d	Lms	darker	34.04	20.30	46.07	308.07	589.93	b.d.l.	732.07	100.575

Detection limits at standard operating conditions: Au 380 ppm, Sb 290 ppm, Ni 90 ppm, Co 82 ppm.

Representative LA-ICPMS analyses of stage 1 arsenopyrites and pyrites

Ore mineral / Host rock	Arsenopyrites in quartz-feldspar-phryic dike (Sa-124)														
	mr_21	mr_22	mr_23	mr_24	mr_25	mr_26	mr_27	mr_28	mr_29	mr_30	mr_31	mr_32	mr_33	mr_34	mr_35
Trace Element Concentrations (ppm)															
Co ⁹⁹	0.251	0.181	0.596	0.281	4.920	0.160	3.480	13.780	4.510	0.449	0.394	0.459	0.392	0.273	0.510
Ni ⁶⁰	b.d.l.	b.d.l.	b.d.l.	b.d.l.	b.d.l.	b.d.l.	b.d.l.	b.d.l.	b.d.l.	b.d.l.	b.d.l.	b.d.l.	b.d.l.	b.d.l.	b.d.l.
Cu ⁶⁵	b.d.l.	b.d.l.	b.d.l.	b.d.l.	b.d.l.	b.d.l.	b.d.l.	b.d.l.	b.d.l.	b.d.l.	b.d.l.	b.d.l.	b.d.l.	b.d.l.	b.d.l.
Zn ⁶⁶	b.d.l.	b.d.l.	b.d.l.	b.d.l.	b.d.l.	b.d.l.	b.d.l.	b.d.l.	b.d.l.	b.d.l.	b.d.l.	b.d.l.	b.d.l.	b.d.l.	0.920
As ⁷⁵															
Se ⁸²	178.590	96.850	130.800	96.920	173.020	217.040	127.240	79.220	41.740	33.220	39.850	174.950	87.860	70.490	120.850
Ag ¹⁰⁷	b.d.l.	b.d.l.	0.095	0.067	0.736	b.d.l.	0.467	2.390	0.611	0.067	0.122	0.059	0.407	b.d.l.	0.052
Cd ¹¹¹	0.490	0.470	0.820	0.590	0.640	0.730	0.430	0.670	0.750	0.530	0.540	0.760	0.440	0.440	0.360
Sb ¹²¹	352.510	319.050	1110.750	1546.290	665.220	253.250	1195.010	727.050	882.570	670.910	5886.290	644.660	961.460	2357.690	596.290
Tl ¹²⁵	4.630	1.120	8.030	2.850	6.600	3.480	7.100	2.620	2.370	2.450	12.570	7.020	4.180	3.390	4.550
Tl ²⁰⁵	0.011	0.004	b.d.l.	0.003	0.070	b.d.l.	0.269	0.465	0.179	0.007	0.010	0.003	0.005	0.007	0.002
Pb ²⁰⁸	0.167	0.486	0.522	0.260	0.920	0.199	7.880	43.150	13.220	0.064	1.410	0.347	2.710	0.481	0.121
Bi ²⁰⁹	0.797	0.418	1.200	0.666	18.530	0.734	5.710	6.400	6.430	0.522	2.140	1.660	7.500	20.280	0.639
Pt ¹⁹⁵	0.025	0.022	0.062	0.079	0.042	0.062	0.015	0.041	0.030	0.033	0.027	0.057	0.042	0.050	0.023
Au ¹⁹⁷	7.260	2.350	3.060	0.428	7.690	3.350	11.370	4.800	0.920	0.136	0.910	3.510	0.700	2.570	0.504
1 sigma error															
Co ⁶⁹	0.041	0.036	0.058	0.041	0.290	0.048	0.210	0.780	0.260	0.052	0.049	0.055	0.053	0.046	0.051
Ni ⁶⁰	0.950	0.900	1.120	0.930	0.980	1.740	1.180	1.280	0.850	1.030	1.110	1.150	1.160	1.010	0.960
Cu ⁶⁵	0.940	0.940	1.200	1.350	1.140	2.160	1.450	1.290	1.150	1.670	1.980	2.370	1.910	1.540	1.680
Zn ⁶⁶	0.420	0.410	0.500	0.420	0.430	0.540	0.590	0.490	0.420	0.560	0.590	0.600	0.590	0.560	0.510
As ⁷⁵															
Se ⁸²	18.430	10.180	13.680	10.190	17.860	22.380	13.360	8.420	4.740	4.280	4.760	18.110	9.410	7.630	12.570
Ag ¹⁰⁷	0.030	0.030	0.038	0.031	0.070	0.039	0.057	0.190	0.059	0.036	0.036	0.037	0.052	0.033	0.031
Cd ¹¹¹	0.160	0.150	0.230	0.170	0.180	0.210	0.220	0.140	0.190	0.210	0.160	0.170	0.220	0.140	0.120
Sb ¹²¹	22.960	20.780	72.330	100.690	43.320	16.500	77.820	47.350	57.470	43.690	383.250	41.980	62.610	153.510	38.830
Tl ¹²⁵	0.530	0.170	0.880	0.340	0.720	0.420	0.780	0.310	0.310	0.310	1.320	0.770	0.490	0.400	0.510
Tl ²⁰⁵	0.003	0.002	0.001	0.001	0.011	0.001	0.035	0.059	0.024	0.002	0.003	0.001	0.002	0.001	0.001
Pb ²⁰⁸	0.033	0.065	0.071	0.041	1.070	0.039	0.940	5.120	1.570	0.028	1.170	0.052	0.330	0.065	0.028
Bi ²⁰⁹	0.093	0.050	0.140	0.078	2.100	0.086	0.650	0.730	0.730	0.062	0.240	0.190	0.850	2.300	0.075
Pt ¹⁹⁵	0.010	0.009	0.016	0.015	0.011	0.016	0.012	0.011	0.010	0.012	0.011	0.016	0.015	0.014	0.012
Au ¹⁹⁷	1.020	0.330	0.430	0.064	1.080	0.470	1.590	0.670	0.130	0.024	0.130	0.490	0.100	0.360	0.074
Minimum detection limits (MDL, 99% confidence)															
Co ⁹⁹	0.054	0.052	0.065	0.056	0.056	0.071	0.072	0.055	0.053	0.067	0.065	0.070	0.072	0.066	0.060
Ni ⁶⁰	1.420	1.410	1.730	1.500	1.470	1.860	1.880	1.410	1.350	1.670	1.640	1.750	1.770	1.620	1.470
Cu ⁶⁵	1.440	1.480	1.870	1.690	1.650	2.180	2.250	1.750	1.700	2.140	2.090	2.210	2.240	2.020	1.820
Zn ⁶⁶	0.652	0.629	0.796	0.690	0.678	0.849	0.864	0.651	0.664	0.876	0.869	0.940	0.955	0.920	0.810
As ⁷⁵															
Se ⁸²	3.410	3.300	3.960	3.440	3.370	4.040	4.280	3.320	3.110	3.980	3.740	3.980	4.060	3.720	3.280
Ag ¹⁰⁷	0.047	0.047	0.056	0.048	0.048	0.061	0.061	0.046	0.045	0.056	0.054	0.058	0.059	0.053	0.049
Cd ¹¹¹	0.118	0.104	0.112	0.113	0.100	0.125	0.140	0.107	0.095	0.114	0.117	0.126	0.126	0.108	0.107
Sb ¹²¹	0.030	0.031	0.039	0.031	0.033	0.040	0.044	0.032	0.033	0.040	0.036	0.043	0.043	0.036	0.032
Tl ¹²⁵	0.095	0.072	0.079	0.073	0.073	0.080	0.072	0.054	0.068	0.071	0.048	0.087	0.103	0.074	0.066
Tl ²⁰⁵	0.002	0.001	0.001	0.001	0.001	0.002	0.001	0.001	0.001	0.001	0.001	0.001	0.001	0.001	0.001
Pb ²⁰⁸	0.037	0.036	0.041	0.037	0.035	0.042	0.045	0.035	0.042	0.040	0.041	0.043	0.040	0.040	0.036
Bi ²⁰⁹	0.004	0.005	0.004	0.002	0.003	0.005	0.003	0.003	0.003	0.004	0.004	0.004	0.004	0.004	0.003
Pt ¹⁹⁵	0.007	0.008	0.012	0.008	0.014	0.015	0.014	0.013	0.013	0.016	0.014	0.014	0.014	0.015	
Au ¹⁹⁷	0.009	0.008	0.011	0.008	0.009	0.010	0.009	0.007	0.006	0.011	0.006	0.009	0.009	0.007	0.006

Representative LA-ICPMS analyses of stage I arsenopyrites and pyrites															
Ore mineral / Host rock	mr_42	mr_43	mr_44	mr_45	mr_46	mr_47	mr_48	mr_49	mr_50	mr_51	mr_52	ma_1	ma_2	Pyrites in sheared greywacke (SD-022)	
Trace Element Concentrations (ppm)															
Cs99	204.340	307.040	461.640	298.400	458.660	464.180	517.890	486.590	512.230	428.900	450.630	10.330	365.060	11.310	
Ni60	270.560	204.640	499.810	279.660	488.270	236.940	463.250	339.070	138.860	162.790	340.070	477.380	183.810	437.490	
Cu65	b.d.l.	b.d.l.	b.d.l.	b.d.l.	b.d.l.	b.d.l.	b.d.l.	b.d.l.	b.d.l.	b.d.l.	b.d.l.	0.067	2.140	0.340	
Zn66	b.d.l.	b.d.l.	2.340	37.660	11.640	5.300	b.d.l.	b.d.l.	28.630	2.430	b.d.l.	0.600	0.419	0.336	
A575	Se82	28.720	22.310	31.050	27.150	24.500	25.900	23.070	24.640	23.300	25.570	24.060	b.d.l.	1.540	
Ag107	b.d.l.	b.d.l.	0.100	0.089	b.d.l.	b.d.l.	b.d.l.	b.d.l.	0.078	0.078	0.087	0.006	0.447	0.040	
Cd111	0.650	0.620	0.380	0.670	0.740	4.970	0.460	0.760	0.660	0.840	0.610	0.029	0.011	0.014	
Sb121	1408.180	803.210	1448.820	1405.790	1254.950	3476.540	1569.340	2185.250	1314.360	1342.350	1184.000	0.892	10.230	2.610	0.022
Tet25	7.300	7.430	8.500	7.170	8.460	7.430	8.360	8.070	6.730	8.020	8.740	b.d.l.	0.011	b.d.l.	
Tl265	0.012	0.002	0.050	0.030	0.014	b.d.l.	b.d.l.	0.002	0.014	0.083	0.002	0.009	0.005	0.009	
Ph208	0.065	6.330	4.650	7.750	0.251	0.712	b.d.l.	b.d.l.	7.280	0.195	0.790	0.196	4.640	1.600	
B1209	0.021	0.501	5.680	0.243	1.170	0.117	0.014	0.045	1.160	0.108	0.713	b.d.l.	0.005	0.004	
Pr195	0.026	0.030	0.057	0.042	0.031	0.026	0.038	0.045	0.039	0.034	0.037	b.d.l.	0.002	0.006	
Au197	0.126	0.450	0.760	1.940	0.142	0.383	0.155	0.154	23.700	0.319	0.800	b.d.l.	0.028	0.024	
1 sigma error															
Cs99	11.440	17.180	25.840	16.700	25.670	25.970	28.980	27.230	28.670	24.000	25.220	0.540	19.220	0.600	
Ni60	14.260	10.790	26.270	14.720	25.640	12.500	24.340	17.850	7.460	8.660	17.880	20.940	8.180	19.350	
Cu65	1.310	1.220	2.620	1.210	1.690	2.380	1.980	1.700	2.610	1.860	1.480	0.047	0.160	0.043	
Zn66	0.510	0.490	0.750	2.450	0.990	0.720	0.640	0.680	2.040	0.740	0.580	0.100	0.070	0.069	
A575	Se82	4.080	3.170	4.530	3.600	3.590	3.670	3.570	3.780	4.030	3.910	3.390	0.390	0.380	
Ag107	0.038	0.030	0.046	0.031	0.034	0.033	0.037	0.037	0.045	0.039	0.032	0.004	0.027	0.004	
Cd111	0.190	0.180	0.150	0.190	0.210	1.240	0.150	0.220	0.200	0.240	0.180	0.010	0.005	0.017	
Sb121	91.700	52.300	94.350	91.540	81.720	226.360	102.190	142.290	85.590	87.740	77.100	0.073	0.820	0.210	
Tet25	0.800	0.800	0.940	0.780	0.910	0.810	0.910	0.880	0.760	0.880	0.940	0.005	0.004	0.004	
Tl265	0.003	0.001	0.009	0.005	0.003	0.001	0.001	0.004	0.013	0.001	0.003	0.001	0.001	0.001	
Ph208	0.030	0.750	0.560	0.920	0.042	0.092	0.026	0.028	0.870	0.039	0.100	0.039	0.920	0.320	
B1209	0.005	0.059	0.650	0.030	0.130	0.016	0.004	0.008	0.140	0.015	0.083	0.001	0.001	0.001	
Pr195	0.012	0.011	0.017	0.015	0.014	0.012	0.015	0.016	0.017	0.015	0.013	0.001	0.001	0.002	
Au197	0.023	0.067	0.110	0.280	0.025	0.058	0.027	0.027	3.320	0.051	0.120	0.001	0.004	0.003	
Minimum detection limits (MDL, 99% confidence)															
Cs99	0.071	0.058	0.085	0.061	0.068	0.070	0.074	0.076	0.090	0.080	0.065	0.006	0.006	0.007	
Ni60	1.810	1.470	2.100	1.470	1.680	1.780	1.790	2.160	1.900	1.560	0.098	0.119	0.106	0.126	
Cu65	2.080	1.720	2.560	2.080	2.110	2.210	2.230	2.680	2.350	1.920	0.047	0.058	0.053	0.055	
Zn66	0.839	0.726	1.110	0.780	0.931	0.956	1.050	1.070	2.370	1.140	0.928	0.072	0.083	0.078	
A575	Se82	4.380	3.430	4.850	3.490	3.940	3.890	4.160	4.290	5.000	4.500	3.580	0.387	0.472	
Ag107	0.059	0.048	0.069	0.047	0.055	0.054	0.058	0.058	0.069	0.060	0.049	0.005	0.005	0.008	
Cd111	0.134	0.107	0.153	0.111	0.117	0.133	0.117	0.110	0.143	0.115	0.098	0.007	0.009	0.014	
Sb121	0.045	0.033	0.050	0.040	0.040	0.044	0.045	0.045	0.052	0.045	0.035	0.003	0.003	0.004	
Tet25	0.085	0.062	0.073	0.065	0.078	0.068	0.097	0.101	0.085	0.096	0.077	0.006	0.005	0.009	
Tl265	0.001	0.001	0.001	0.001	0.001	0.001	0.001	0.001	0.001	0.001	0.001	0.001	0.001	0.001	
Ph208	0.044	0.035	0.050	0.035	0.041	0.040	0.043	0.044	0.051	0.044	0.044	0.037	0.003	0.006	
B1209	0.005	0.006	0.004	0.005	0.006	0.005	0.005	0.006	0.004	0.004	0.002	0.002	0.002	0.001	
Pr195	0.013	0.012	0.013	0.018	0.015	0.017	0.017	0.017	0.020	0.016	0.014	0.001	0.001	0.004	
Au197	0.012	0.008	0.011	0.007	0.009	0.008	0.009	0.011	0.011	0.010	0.010	0.001	0.001	0.005	

Representative LA-ICPMS analyses of stage I arsenopyrites and pyrites

Ore mineral / Host rock	Pyrites in limestone breccia (SD-030)								
	ma_10	ma_11	ma_12	ma_13	ma_14	ma_15	ma_16	ma_17	ma_18
Trace Element Concentrations (ppm)									
Cs9	9.380	8.160	8.940	9.410	295.400	3.970	6.740	2.050	2.220
Ni60	665.100	928.170	998.510	1126.090	74.610	418.400	815.810	0.950	817.300
Cu65	0.220	136.830	232.060	0.920	b.d.l.	19.800	234.460	8.120	6.170
Zn66	0.800	0.730	0.850	1.180	0.311	0.620	1.100	0.740	0.380
As75	7.120	5.190	5.770	6.200	1150.740	56.030	14.430	3240.100	5.760
Se82	8.510	8.740	3.350	7.780	1.060	3.460	5.750	b.d.l.	5.490
Ag107	0.203	0.885	1.600	0.500	b.d.l.	0.437	0.579	0.140	0.554
Cd111	b.d.l.	b.d.l.	0.018	0.035	b.d.l.	0.044	0.015	0.018	b.d.l.
Sb121	4.870	10.710	2.720	1.810	b.d.l.	31.830	21.660	26.400	4.500
Te125	b.d.l.	0.053	b.d.l.	0.088	b.d.l.	0.037	b.d.l.	0.070	0.128
Tl205	b.d.l.	0.015	0.028	0.010	b.d.l.	0.122	0.089	0.353	0.009
Pb208	3.440	1.490	2.130	19.860	b.d.l.	2.550	2.500	29.300	0.900
Bi209	0.008	0.142	0.007	0.069	b.d.l.	0.066	0.051	0.055	0.040
Pt195	b.d.l.	0.002	b.d.l.	b.d.l.	0.002	b.d.l.	b.d.l.	b.d.l.	b.d.l.
Au197	0.015	0.024	0.029	0.005	b.d.l.	0.024	0.006	0.103	0.134
1 sigma error									
Cs9	0.540	0.470	0.520	0.560	17.760	0.240	0.420	0.130	0.140
Ni60	31.650	44.660	48.590	55.450	3.730	21.130	41.720	0.140	42.930
Cu65	0.060	10.630	18.290	0.098	0.061	1.640	19.650	0.700	0.540
Zn66	0.110	0.110	0.120	0.160	0.068	0.100	0.160	0.120	0.077
As75	0.940	0.690	0.780	0.850	159.290	7.870	2.060	467.990	0.850
Se82	1.590	1.660	0.700	1.520	0.370	0.760	1.200	0.330	1.190
Ag107	0.014	0.058	0.110	0.034	0.005	0.031	0.042	0.012	0.041
Cd111	0.007	0.008	0.009	0.012	0.008	0.014	0.009	0.011	0.009
Sb121	0.440	0.980	0.250	0.170	0.002	3.110	2.150	2.670	0.460
Te125	0.006	0.012	0.006	0.016	0.007	0.011	0.007	0.016	0.024
Tl205	0.001	0.002	0.003	0.001	0.001	0.013	0.010	0.039	0.001
Pb208	0.800	0.350	0.510	4.910	0.004	0.660	0.660	7.920	0.250
Bi209	0.001	0.013	0.001	0.007	0.001	0.007	0.005	0.006	0.005
Pt195	0.001	0.001	0.001	0.001	0.001	0.001	0.001	0.001	0.001
Au197	0.003	0.004	0.004	0.002	0.001	0.004	0.002	0.015	0.020
Minimum detection limits (MDL, 99% confidence)									
Cs9	0.007	0.008	0.007	0.007	0.007	0.008	0.007	0.008	0.008
Ni60	0.177	0.186	0.172	0.182	0.192	0.210	0.186	0.210	0.214
Cu65	0.096	0.102	0.095	0.101	0.102	0.113	0.100	0.111	0.110
Zn66	0.095	0.093	0.085	0.085	0.087	0.091	0.079	0.085	0.088
As75	0.070	0.071	0.065	0.067	0.068	0.072	0.064	0.070	0.068
Se82	0.499	0.524	0.483	0.500	0.512	0.545	0.479	0.533	0.525
Ag107	0.008	0.008	0.008	0.008	0.008	0.009	0.008	0.009	0.009
Cd111	0.012	0.012	0.012	0.012	0.012	0.013	0.012	0.015	0.014
Sb121	0.003	0.003	0.003	0.003	0.003	0.004	0.003	0.004	0.004
Te125	0.009	0.007	0.010	0.009	0.012	0.011	0.010	0.011	0.012
Tl205	0.001	0.001	0.001	0.001	0.001	0.001	0.001	0.001	0.001
Pb208	0.005	0.006	0.005	0.006	0.006	0.007	0.006	0.007	0.007
Bi209	0.001	0.001	0.001	0.001	0.001	0.001	0.001	0.001	0.001
Pt195	0.001	0.000	0.001	0.001	0.001	0.001	0.001	0.001	0.001
Au197	0.001	0.002	0.001	0.002	0.002	0.002	0.002	0.002	0.002

Representative EPMA analyses of buffered arsenopyrite crystals used for geothermometry

Mineral	Fe	As	S	Wt %	Wt %					At % As	Host	Buffer
					Sb	Au	Ni	Co	Total			
Apy	34.91	43.69	20.57	b.d.l.	b.d.l.	0.04	99.25		31.51	GW	Po	
Apy	34.93	43.92	20.87	0.04	b.d.l.	0.05	99.81		31.46	GW	Py-Po	
Apy	35.17	43.48	21.06	0.09	b.d.l.	0.05	99.85		31.05	GW	Po	
Apy	34.86	43.68	20.69	b.d.l.	b.d.l.	0.04	99.30		31.45	GW	Po-Py	
Apy	35.22	43.31	21.28	0.06	b.d.l.	0.05	99.96		30.84	GW	Po-Py	
Apy	35.18	42.58	21.95	0.08	b.d.l.	0.05	99.88		30.15	GW	Py-Po	
Apy	35.13	43.04	21.15	b.d.l.	b.d.l.	0.05	99.40		30.81	GW	Po	
Apy	34.97	43.75	20.63	b.d.l.	b.d.l.	0.05	99.44		31.48	GW	Po	
Apy	34.73	43.96	20.68	0.05	b.d.l.	0.04	99.48		31.63	GW	Po	
Apy	34.94	42.47	21.53	b.d.l.	b.d.l.	0.04	0.15	99.16	30.35	GW	Po	
Apy	35.07	42.56	21.05	0.02	b.d.l.	0.04	0.10	98.85	30.62	GW	Po	
Apy	34.63	41.94	21.44	b.d.l.	b.d.l.	0.06	0.13	98.22	30.23	GW	Po	
Apy	34.99	42.91	21.15	b.d.l.	b.d.l.	0.17	99.25	30.76	Dio	Po		
Apy	35.24	42.50	21.80	b.d.l.	b.d.l.	0.02	0.11	99.68	30.16	Dio	Po	
Apy	34.71	43.01	21.06	0.14	b.d.l.	0.01	0.15	99.11	30.92	Dio	Po	
Apy	35.31	42.26	21.71	b.d.l.	b.d.l.	0.15	99.47	30.06	Dio	Py		
Apy	35.08	42.93	21.38	0.05	b.d.l.	0.14	99.60	30.62	Dio	Po		
Apy	35.21	43.27	21.13	b.d.	b.d.l.	0.01	0.15	99.82	30.88	Dio	Po	
Apy	34.90	43.25	21.19	0.02	b.d.l.	0.10	99.64	30.93	Dio	Po-Py		
Apy	35.41	42.36	21.63	0.11	b.d.l.	0.01	0.12	99.69	30.11	Dio	Po-Py	

Chapter III. The Alamoutala carbonate-hosted gold deposit, Kédougou-Kénieba inlier, West Africa.

Quentin Masurel^{1*}, Nicolas Thébaud¹, John Miller¹, Stanislav Ulrich², Malcolm Peter Roberts³, Didier Béziat⁴

¹Centre for Exploration Targeting, The University of Western Australia, 35 Stirling Highway, Crawley, WA, Australia.

²AngloGold Ashanti Australia Limited, Asset Development - Brownfields, 44 St. Georges Terrace, Perth, WA, Australia.

³Centre for Microscopy, Characterisation & Analysis, The University of Western Australia.

⁴Laboratoire Géosciences Environnement Toulouse, UMR-CNRS 5563, Université Paul Sabatier, France.

*Corresponding author: qmasurel@hotmail.com

Keywords: Yatela, carbonate-hosted gold, Eburnean orogeny, Kédougou-Kénieba inlier, West Africa.

1. Abstract

The Alamoutala gold deposit is located in the Kédougou-Kénieba inlier, a window of Paleoproterozoic rocks that outcrop in eastern Senegal and western Mali. The deposit is part of the ~3 Moz Au Yatela district and produced 308,400 oz Au between 2002 and 2012. Country rocks in the Alamoutala open pit consist of limestones, arenites, wackes, and siltstones. The sedimentary rocks have been subjected to polycyclic deformation and regional greenschist-facies metamorphism. Synkinematic, calc-alkaline, intermediate quartz-feldspar-porphyry stocks intruded the metasedimentary rock sequences at 2083 ± 7 Ma (U-Pb on zircon). Amphibolite-facies contact metamorphism of carbonate rocks resulted in the formation of a high T -low P magnetite-bearing skarn. Field relationships and micro-textural data, however, indicate that economic gold mineralization is shear-hosted and occurred during retrograde contact metamorphism. Geometric and kinematic analyses indicate that the ore-hosting structures were undergoing sinistral-reverse displacement at the time of mineralization. Ore minerals are synchronous with a potassic hydrothermal alteration assemblage

defined as biotite + calcite + pyrite \pm K-feldspar, actinolite-tremolite, quartz, muscovite, and tourmaline. Petrographic studies reveal that ore-related sulfides largely consist of pyrite with lesser pyrrhotite and chalcopyrite. The ore also contains accessory Ag-Sb-As-Hg-Bi-Te-Mo-W-Zn-Pb-Ni-Co-U-bearing mineral species. The Alamoutala deposit represents two distinct hydrothermal systems in which a locally-developed magnetite-bearing skarn was overprinted by a regional orogenic gold event in the late Eburnean.

2. Introduction

The Alamoutala deposit is situated within the Kédougou-Kénieba inlier (KKI), which represents the westernmost exposure (approx. 22000 km²) of Paleoproterozoic crust in the West African Craton (inset, Fig. 1). The KKI hosts numerous world-class gold districts, such as Loulo-Gounkoto (~14 Moz), Sadiola (~10 Moz), Yatela (~3 Moz), and Sabodala-Massawa (~8 Moz) (Fig. 1). Gold deposits in the inlier are hosted by a wide range of host rocks including mafic volcanic rocks, detrital sedimentary rocks, and carbonates. The relative timing and structural setting of gold deposits in the KKI indicate that the mineralizing episode occurred during a period of transcurrent deformation coeval with calc-alkaline magmatism between ca. 2090 and 2070 Ma, after the cessation of regional compressional deformation (Lawrence et al., 2013a; Treloar et al., 2014; Masurel et al., in press). The KKI also hosts iron skarn deposits of the Falémé district, which collectively represent the largest Birimian iron resource of West Africa (750 Mt ore reserves, ArcelorMittal 2007, press release) (Fig. 1). The iron skarns formed post-peak metamorphism at ca. 2080 Ma and are spatially and genetically associated with syn-kinematic plutons, such as the Balangouma monzodiorite and the Boboti clinopyroxene-hornblende-bearing granodiorite (Hirdes and Davis, 2002; Schwartz and Melcher, 2004; Lawrence et al., 2013a; Lambert-Smith, 2014). Recent research in the eastern part of the KKI has highlighted the spatial association between calc-alkaline Eburnean plutons, gold mineralization, and local iron skarn mineralization, suggesting the potential role of a complex fluid history in the development of major gold deposits (e.g., Loulo, Lawrence et al., 2013a,b). The Alamoutala carbonate-hosted gold deposit occurs within a magnetite-bearing contact-metamorphic aureole associated with syn-kinematic, calc-alkaline, intermediate quartz-feldspar-porphyry stocks (Fig. 1).

The deposit therefore provides an ideal setting to investigate field relationships between magnetite skarn formation and gold mineralization in the region. Although initial attempts to date the gold mineralization in-situ have failed, this study outlines the geology, tectonic setting, contact metamorphism, absolute timing, and whole rock geochemistry of the local intrusive stocks, hydrothermal alteration, and ore mineralogy in the area of the Alamoutala gold deposit. The primary conclusion is that the Alamoutala deposit represents a locally-developed magnetite-bearing skarn in the aureole to the quartz-feldspar-porphyry stocks that was overprinted by a regional orogenic gold event in the late Eburnean.

3. Geological setting

3.1. Regional geology

The geology of the KKI consists of two volcanic rock belts (Mako and Falémé) separated by wider sedimentary basins (Dialé-Daléma and Kofi) (Fig. 1). The crustal blocks are separated by two regional-scale lineaments, respectively the Main Transcurrent Zone (Ledru et al., 1991) and the Senegal-Mali Shear Zone (Bassot and Domanget, 1986) (Fig. 1). The Mako volcanic belt (Fig. 1) consists of tholeiitic basalts and calc-alkaline andesitic lavas intercalated with minor immature sedimentary and volcaniclastic rocks (Bassot, 1987; Hirdes and Davis, 2002; Dioh et al., 2006; Gueye et al., 2008). The volcanic assemblage has been dated between 2197 ± 13 Ma (Dia, 1988) and 2160 ± 16 Ma (Boher et al., 1992). Gneisses of the Kakadian-Badon basement have been dated between 2194 ± 4 and 2202 ± 6 Ma, and are interpreted to represent the deeper root of the Mako volcanic rocks (Dia et al., 1997, Pawlig et al., 2006; Gueye et al., 2007). The Mako bimodal volcanic rocks were intruded by the Sandikounda layered plutonic complex at 2158 ± 8 Ma (Dia et al., 1997). The latter complex largely consists of gabbro and hornblende-biotite-tonalite (Dioh et al., 2006). The Falémé volcano-sedimentary belt (Fig. 1) has only been recently recognized during exploration activities (Hirdes and Davis, 2002; Lawrence, 2010). It consists of calc-alkaline volcaniclastic rocks, chert, manganiferous shale, wackes, minor calc-alkaline andesitic lavas, and subordinate felsic flows (Hirdes and Davis, 2002; Dioh et al., 2006;

Gueye et al., 2008; Lawrence, 2010). Available geochronological data are limited to a rhyolite flow dated at 2099 ± 4 Ma (Hirdes and Davis, 2002), but indicate a late Birimian formation in relation to the Mako volcanic belt. Geochemical studies carried out on both the Mako and Falémé volcanic rocks are consistent with a volcanic arc setting (Dia et al., 1997; Schwartz and Melcher, 2004; Dioh et al., 2006; Pawlig et al., 2006). The Dialé-Daléma and Kofi sedimentary basins (Fig. 1) are composed of thick sequences of volcaniclastic rocks, arenites, wackes, siltstones, argillites, and carbonates, with subordinate andesitic lavas, rhyolite flows, and pyroclastites (Bassot, 1987; Hirdes and Davis, 2002). Available detrital zircon data from the region (Fig. 1) indicate ages from 2165 ± 1 Ma (Hirdes and Davis, 2002) down to 2093 ± 7 Ma (Boher et al., 1992), which suggests that the Dialé-Daléma and Kofi sequences represent rocks deposited in syn-deformational foreland basins. Rocks of the sedimentary basins and volcanic belts were intruded by different generations of syn-tectonic, calc-alkaline plutons during the Eburnean orogeny between ca. 2115 and 2070 Ma. These granitoids include metaluminous hornblende-biotite-bearing diorite to granodiorite (e.g., Mamakono, 2076 ± 3 Ma, Hirdes and Davis, 2002; Tinkoto, 2074 ± 5 Ma, Gueye et al., 2007), pyroxene-bearing granodiorite-tonalite (e.g., Boboti, 2080 ± 1 Ma, Hirdes and Davis, 2002), and peraluminous monzogranites (e.g., Saraya, 2079 ± 2 Ma, Hirdes and Davis, 2002) (Fig. 1). Available geochronological data suggest that the emplacement of most Eburnean granitoids took place within a short time span between ca. 2090 and 2070 Ma (Bassot and Caen-Vachette, 1984; Ndiaye et al., 1997; Hirdes and Davis, 2002; Gueye et al., 2007).

Country rocks in the KKI have undergone polycyclic deformation, which included early thrusting events responsible for crustal thickening (D_1 - D_2), followed by a period of transcurrent tectonics accommodating oblique convergence (D_3 - D_4) (Ledru et al., 1991; Milési et al., 1992; Gueye et al., 2008; Dabo and Aïfa, 2010, 2011; Diene et al., 2012; Lawrence et al., 2013a; Treloar et al., 2014; Masurel et al., in press). Little is known about the kinematics of the D_1 event due to penetrative reworking of the early fabric by later deformation. The D_2 and D_3 events correlate with the Eburnean orogeny and were undoubtedly responsible for the formation of map scale structures. The regional-scale shear zones are interpreted to have formed as sinistral transpressional faults during D_2 NW-SE shortening (Lawrence et al., 2013a; Treloar et al., 2014). The D_3 event marks a switch from a dominantly coaxial system to non-coaxial deformation. The bulk of the

gold deposit formation in the KKI occurred during D₃ NNW-SSE shortening, with hydrothermal fluid circulation along the sinistral regional-scale shear zones and steep NNE-trending shears connected to structural traps in the Kofi basin (Lawrence et al., 2013a; Treloar et al., 2014; Masurel et al., in press). The last deformation event, D₄, has been locally reported on the Senegalese side of the Falémé River and is correlated with the late dextral reactivation of the N-S-oriented to NNE-trending structural corridors during NE-SW-directed shortening (Dabo and Aïfa, 2011). Available metamorphic data for the KKI point to peak regional metamorphism under greenschist-facies conditions (Dia et al., 1997; Debat et al., 2003). Amphibolite-facies contact-metamorphic aureoles have locally been observed surrounding late-Eburnean granitoids (Debat et al., 1984; Pawlig et al., 2006). Mineral assemblages developed during regional metamorphism are overprinted by contact-metamorphic mineral assemblages (Schwartz and Melcher, 2004). Gold deposits in the region are unmetamorphosed (Lawrence et al., 2013a; Masurel et al., in press).

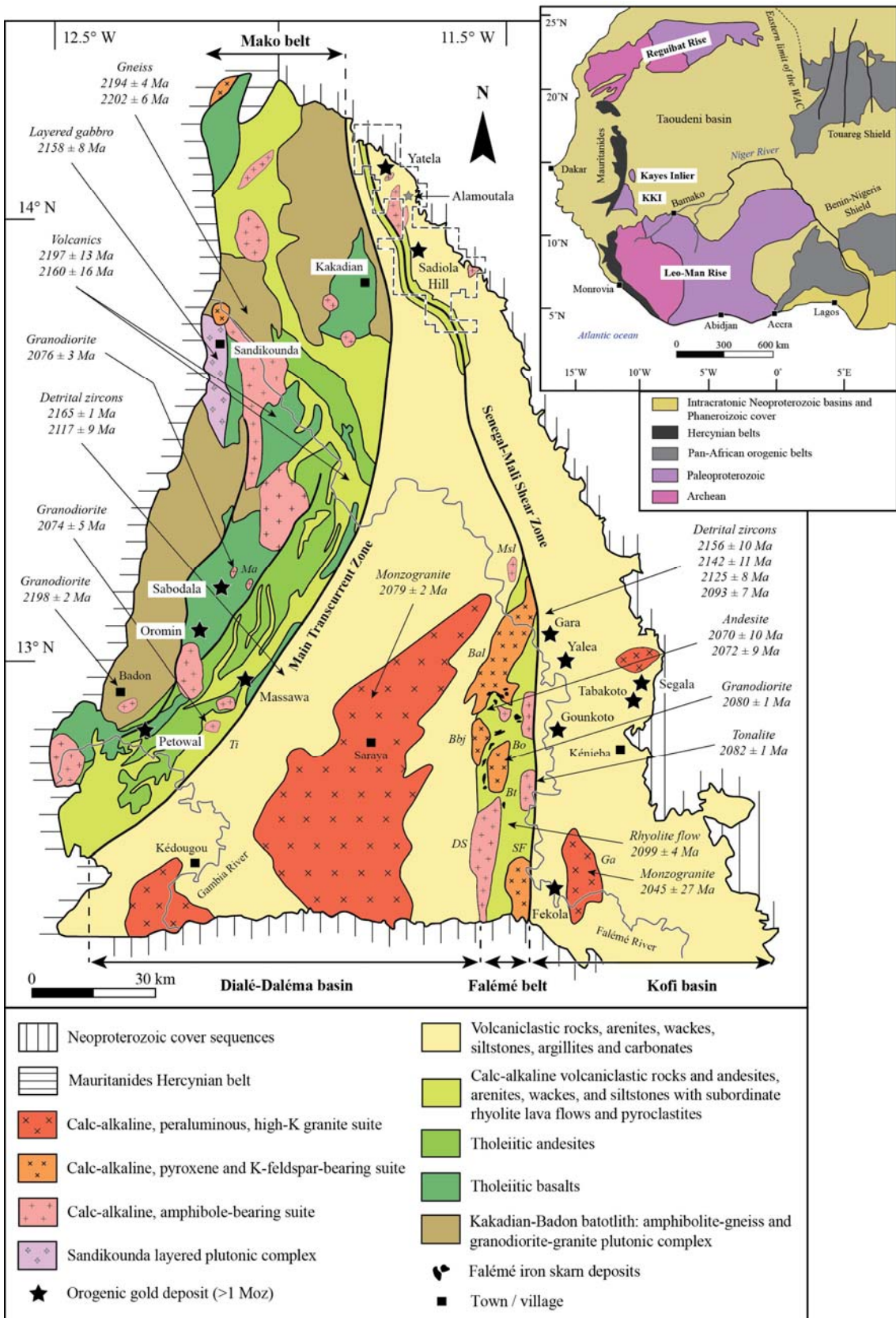


Figure 1. Geologic map of the Birimian Kédougou-Kéniéba inlier (1:250,000 scale, modified after Gueye et al., 2007; Lawrence et al., 2013a). Inset map shows the geologic setting of the West African craton (modified after Boher et al., 1992). The Falémé River forms the international border with Senegal to the west and Mali to the east and north. Abbreviations refer to plutons mentioned in the text: (Mako belt) Ma = Mamakono granodiorite, Ti = Tinkoto granodiorite, (Falémé belt) Bal = Balangouma tonalite, Bo = Boboti granodiorite, SF = South Falémé granodiorite, DS = Dar Salam granodiorite, Msl = Moussala granodiorite, Bbj = Bambadji granodiorite, Bt = Boto tonalite; (Kofi basin) Ga = Gamaye monzogranite. Geochronological data from Bassot and Caen-Vachette, 1984; Dia, 1988; Calvez et al., 1990; Boher et al., 1992; Dia et al., 1997; Hirdes and Davis, 2002; Gueye et al., 2007.

3.2. Local geology

The geology of the Kofi basin in the Yatela region consists of feldspathic wackes, arkosic arenites, and carbonates, with subordinate rhyolite flows, and pyroclastites to the west progressing to siltstones and argillites further east (Fig. 2). Thick sequences (>250 m) of carbonate rocks are exposed and consist of limestones locally interlayered with dolomitic horizons. The original lithostratigraphy consisted of carbonates overlain by younger sequences of detrital sedimentary rocks based on way-up indicators, such as fining-upwards sequences, scour-and-fill structures, and rare cross-bedding in sandstone. Chemical and detrital sedimentary rocks of the Kofi basin transition towards the west into a linear volcano-sedimentary belt that consists of calc-alkaline volcaniclastic rocks and porphyritic andesite flows. Sedimentary and volcanic rocks were intruded by different generations of syn-tectonic, calc-alkaline plutons forming circular to elliptical bodies of various sizes (Fig. 2). A large plutonic complex has been mapped in the field 2 km west of the Alamoutala deposit. The plutons range in composition from diorite and hornblende-biotite-granodiorite to K-rich biotite-granites. The Alamoutala deposit is located within the Kofi basin and occurs in the contact-metamorphic aureole to isolated intermediate quartz-feldspar-porphyry stocks. Country rocks in the Alamoutala deposit area have undergone regional greenschist-facies metamorphism. For the purpose of clarity, the prefix “meta” will be omitted in the following sections.

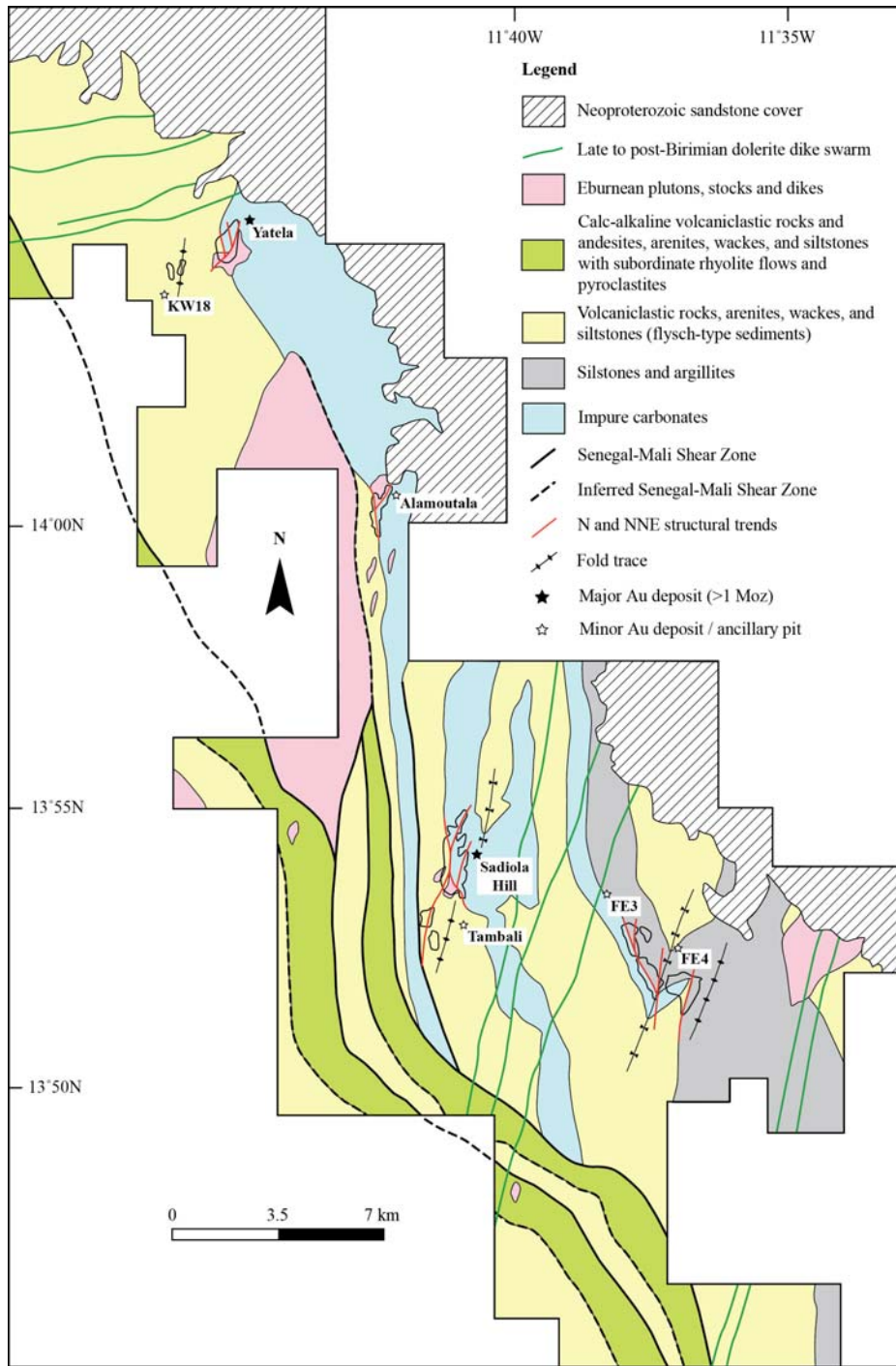


Figure 2. Geology of the Sadiola-Yatela district based on AngloGold Ashanti regional map (2014) and field investigation by the authors (scale 1:75,000).

4. Alamoutala exploration and mining history

The Alamoutala gold deposit is located in the Yatela mining district. The district displays widespread evidence of ancient and recent artisanal mining, with written records of mining dating back more than 250 years (public data from IAMGold website). A geochemical survey was conducted in 1994 over the Alamoutala and Yatela prospects, followed by trench sampling in 1996. Drill testing resulted in the discovery of a significant gold resource at Yatela and a minor one at Alamoutala. Disseminated magnetite is abundant in host rocks at Alamoutala but has never been of economic interest in contrast to the magnetite skarns of the Falémé district (see Fig. 1). In late 1997, IAMGOLD and Anglo American Corporation (now AngloGold Ashanti) signed an agreement to purchase the Yatela concession located 25 km north of the Sadiola Hill gold deposit. The Government of Mali issued an exploitation permit for the Yatela project in February 2000. The Alamoutala gold deposit has been operated by the Société des Mines d'Or du Mali (SEMODS), a joint venture between AngloGold Ashanti Limited, IAMGold Corporation and the government of Mali, until the mine was decommissioned in 2012. The total production of the Alamoutala gold deposit over its mine life was 308,400 oz Au at an average grade of 1.70 g/t (AngloGold Ashanti 2011 mineral resource and ore reserve report).

5. Materials and methods

5.1. Pit mapping, logging, sampling and 3D modeling

Systematic face mapping was done on all accessible ramps of the abandoned open –pit mine at the Alamoutala deposit. Detailed logging was undertaken and included four diamond drill holes chosen to include the main structural, lithological, and mineralogical variations observed in the deposit. A number of outcrops were also investigated surrounding the deposit to integrate pit observations into a regional framework. Petrographic data reported in this paper largely come from drill core samples and, to a lesser extent, from oriented blocks sampled directly in the field. All structural readings are given in true north coordinates. Planar features are given in

strike/dip/quadrant and linear data are given as plunge and azimuth. In this paper, the “y” subscript indicates that the considered structural event is only valid for the Yatela district, which may differ from regional structural compilations reported for the West African Craton. The trends of ore shoots in and surrounding the main orebody of the Alamoutala deposit were evaluated using Leapfrog® three-dimensional rendering of the assay data, which combined grade control and exploration.

5.2. Petrography and mineral chemistry

Approximately 50 polished thin sections were prepared at the University of Western Australia (UWA) and at Vancouver Petrographics Ltd. The selected suite of samples included country rocks with various alteration types and intensities, and all ore types. These were studied using optical microscopy at the Centre for Exploration Targeting (UWA), scanning electron microscopy and electron probe microanalysis at the Centre for Microscopy, Characterisation and Analysis (CMCA) at UWA. Backscattered electron (BSE) imaging and mineral chemical analyses were performed using a Tescan Vega3 XM (SEM) equipped with an Oxford instrument X-ACT energy dispersive detector and a JEOL JXA-8530F Hyperprobe fitted with 5 wavelength-dispersive spectrometers. Quantitative microanalyses were performed using proprietary standards. The analytical software used to collect semi-quantitative micro-analyses was the Oxford Instruments® INCA analytical suite on the Tescan Vega 3. Operating parameters for the SEM-EDS include an accelerating voltage of 20 kV, a working distance of 15 mm, a beam current of 1.5 nA and a detector process time of 4 s. Operating conditions for the wavelength-dispersive (WD) spectrometer were an accelerating voltage of 15 kV, a beam current of 20 nA and a counting time of 20 s on peak for silicates. Mean atomic number background and ZAF corrections were used throughout. The algorithm utilized was that of Armstrong (1988). The multi-elemental X-ray mapping of silicates was carried out by WD spectrometry using the same operating conditions for probe calibration detailed above in addition to a 80 nA beam current, 20 ms per pixel dwell time, and 2 x 2 μm pixel dimension. Mineral mapping results were processed off-line with the CalcImage® software.

5.3. Whole-rock geochemical analyses

Least-altered rock samples of the Alamoutala intermediate quartz-feldspar-porphyry stocks were obtained from wall rocks in the open pit and diamond drill core for geochemical characterization and comparison with those of the Falémé plutons. Approximately 1 kg of fresh, homogeneous rock was collected per sample. Rust stains were cleaned with abrasives and weathered surfaces were removed prior to crushing. Rock chips were pulverized using low chrome-steel vessels. Rock powders were mixed with lithium metaborate/tetraborate and prepared as fusion for lithogeochemistry package LITH/205X analysis at Intertek Genalysis Laboratories in Perth. Major elements were measured by X-ray fluorescence spectrometry (XRF). The rare earth elements (REE), high field strength elements (HFSE), and other trace elements (e.g., Ba, Cr, Cs, Ga, Rb, Sc, Sn, Sr, U, V, W) were analyzed by inductively coupled plasma mass spectrometry (ICP-MS) and inductively coupled plasma optical emission spectrometry (ICP-OES). Other metals were analyzed by the same techniques but prepared with multi-acid digestions, including hydrofluoric, nitric, perchloric, and hydrochloric acids in teflon tubes. Gold content was measured by fire-assay followed by ICP-MS. The Geological Survey of Western Australia Bunbury basalt and Kerba granite standards were analyzed during each session to monitor accuracy and instrument stability. The accuracy of the data was typically better than 3% for the major elements and trace elements were within 10% of reference values. Detail detection limits achieved for each analysis are provided in the supplementary material.

5.4. Geochronology

Intermediate quartz-feldspar-porphyry stocks that outcrop on walls of the Alamoutala open pit have been dated in order to compare the timing of magma emplacement and formation of the magnetite-bearing skarn aureole with those events in the Falémé iron district. Approximately 5 kg of rock was collected from outcrop for U-Pb geochronology. After cleaning and removal of weathered surfaces, the rock sample was processed at Geotrack Pty. Ltd. in Australia. The sample was crushed using a mechanical jaw crusher, and powdered using a ring mill. Heavy minerals were separated

using standard heavy liquids and magnetic procedures. Target zircons were handpicked from zircon concentrates and fractions for each sample and mounted in 25 mm epoxy-resin discs with chips of U/Pb zircon standard BR266 (559 Ma, 903 ppm U; Stern, 2001) and OGC1 (3465 Ma; Stern et al., 2009), and silicate glass NBS610 at the Minsep Laboratories in Denmark in Western Australia. Cathodoluminescence (CL) and backscattered electron (BSE) imaging on gold-coated mounts were performed using a Tescan Vega-3 scanned electron microscope at the CMCA of the UWA. The U-Pb analyses were performed using the sensitive high-resolution ion microprobe (SHRIMP II) at the John de Laeter Centre of Excellence for Mass Spectrometry, Curtin University (Western Australia) using standard operating procedures similar to those described by Compston et al. (1984) and Wingate and Kirkland (2013). Operating parameters include a 10 keV primary O^{2-} beam focussed to a \sim 20 μm diameter spot, a net primary ion current between 1.6 and 3.0 nA, and a secondary ion analyzer set to a mass of ≥ 5000 . Six data collection cycles (scans) were performed per analysis, and count times (per scan) were 10 s for the ^{204}Pb , ^{206}Pb , and ^{208}Pb mass peaks and background, and 30 s for the ^{207}Pb mass peak. Analyses of unknowns were referenced to multiple analyses of the BR266 / M257 primary standard for U/Pb calibration. Calibration and reproducibility uncertainties are included in the errors of $^{238}U/^{206}Pb$ ratios and age data listed in the supplementary material. Data reduction was carried out using the software SQUID v2.5 and ISOPLOT v3.0 (MS Excel add-ins by Ludwig, 2003, 2009). Corrections for common Pb were based on measured ^{204}Pb , assuming an average crustal composition appropriate to the age of the mineral (Stacey and Kramers, 1975). Analytical cut-offs were used in order to minimize the risk of including zircons with potentially disturbed U-Pb systematics during data interpretation. The U-Pb ages were only calculated from concordant to near-concordant grains (discordance between -3% and +10%). In addition, analyses that comprised more than 1% of non-radiogenic ^{206}Pb and yielded U concentrations greater than 1000 ppm were rejected. All age estimates are reported below with 95 % confidence and include propagated uncertainties in the standard calibrations. Raw data are listed in the supplementary material.

6. Deposit geology

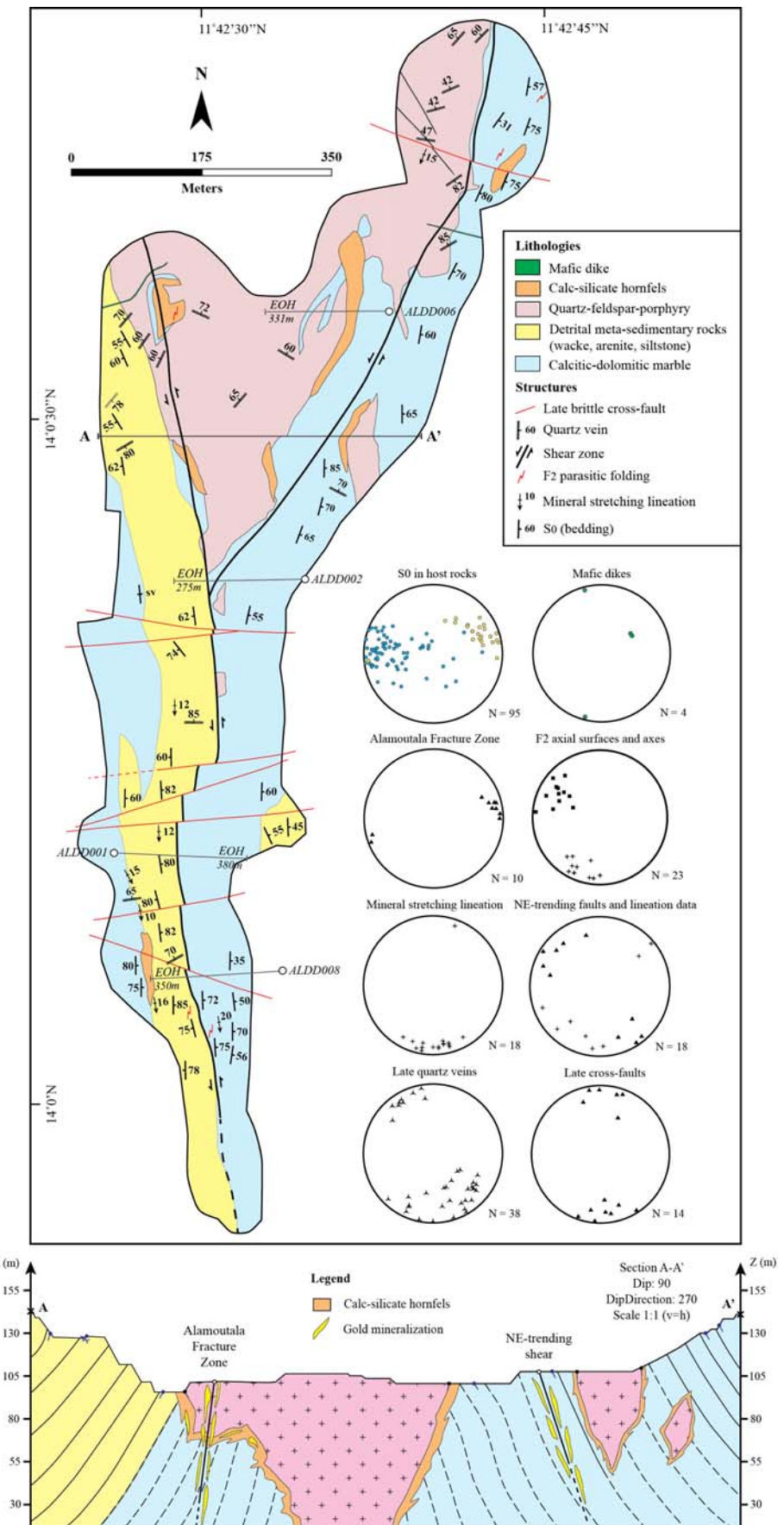
6.1. Sedimentary rocks and intrusions

Country rocks in the Alamoutala open pit consist of folded sequences of carbonates and detrital sedimentary rocks (Fig. 3). Limestones interlayered with minor dolomitic horizons outcrop on the eastern walls and are partially exposed on the western walls of the pit. The dominant carbonate facies is pure, although it is locally well-bedded and characterized by abundant thin (0.2 – 2 cm) argillaceous-silty interbeds. Clastic rock sequences are exposed on the western pit walls and consist of alternating sequences of quartz-feldspar to feldspathic wacke, moderately sorted arkosic arenite, and siltstone. Well-preserved way-up indicators, such as fining-upwards sequences and rare cross bedding in sandstone, indicate upright beds with a younging direction to the west. The main contact between the distinct rock types is faulted and is defined as the Alamoutala Fracture Zone.

The sedimentary rocks exposed in the Alamoutala open pit were intruded by three generations of intrusions that include intermediate quartz-feldspar-porphyry stocks and two distinct sets of mafic dikes (Fig. 3). Least-altered rock samples of the quartz-feldspar-porphyry stocks collected at different locations in the open pit show no significant mineralogical variations. The rocks are composed of up to 35% (modal vol.) phenocrysts (generally 1 mm up to 3 mm) set in a fine-grained (<0.1 mm) to very fine-grained (<0.05 mm) quartzo-feldspathic groundmass. Quartz phenocrysts (up to 10% modal vol.) are sub-rounded and exhibit rare corrosion gulf textures. Feldspar phenocrysts (up to 35% modal vol.) are euhedral prismatic and often exhibit oscillatory zoning. Minor magmatic biotite commonly shows sub-solidus exsolution of rutile and contains minute zircon inclusions with associated pleochroic haloes. Prismatic apatite is relatively abundant. Traces amounts of igneous magnetite occur disseminated in the groundmass. Parts of the epizonal pluton are hydrothermally altered and display evidence of sinistral-reverse shearing. A second generation of intrusion cuts both the sedimentary rock sequences and the quartz-feldspar-porphyry stock in the northeastern part of the pit. It consists of a set of approximately 1-m-wide, NW-trending, sub-vertical mafic dikes (Fig. 3). The grain size and mineralogy of these mafic dikes are compatible

with that of diorite. Although their absolute age of emplacement could not be determined due to very poor zircon yield, the dikes are hydrothermally altered and deformed by late shearing. The youngest generation of intrusive rocks consists of a set of 1.2-m-wide, ENE-trending, sub-vertical mafic dikes, which cuts all ore-hosting structures and is undeformed (Fig. 3).

Figure 3. Geological map of the Alamoutala open pit and associated cross-section A-A'. Structural data recorded during field mapping is presented as equal area stereonets using the lower hemisphere convention.



6.2. Intrusion geochemistry

Least-altered samples of the Alamoutala quartz-feldspar-porphyry suitable for igneous rock geochemistry characterization were defined on the basis of petrography (hydrothermal alteration minerals $\leq 3\%$) (Fig. 4A-B). The strong alteration and weathering of the mafic dikes has precluded accurate geochemical characterization. Major and trace element analyses of the Alamoutala quartz-feldspar-porphyry and mafic dikes are listed in the supplementary material. Major element chemistry for the Alamoutala quartz-feldspar-porphyry is consistent with that of granodiorite on a TAS diagram (Cox et al., 1979) (Fig. 4C), which supports the petrographic characterization. Similarly to Eburnean granitoids intruding rocks of the Falémé belt and Daléma-Kofi basins, the Alamoutala quartz-feldspar-porphyry belongs to the calc-alkaline series based on the AFM diagram by Irvine and Baragar (1971) (Fig. 4D). Least-altered samples of the Alamoutala quartz-feldspar-porphyry ($n=4$) range in SiO_2 content from 66.58 to 68.35 wt% with total alkalis ($\text{Na}_2\text{O} + \text{K}_2\text{O}$) ranging from 7.00 to 8.02 wt%. The $\text{Fe}_2\text{O}_3(\text{total})$ contents range from 1.67 to 1.91 wt% and igneous magnetite has been identified in these rocks in traces amounts ($\leq 1\%$). The TiO_2 content reaches a maximum content of 0.31 wt%, whereas Zr content shows no relative variation from 126 to 138 ppm. The quartz-feldspar-porphyry is metaluminous in character on the basis of its relatively low molar alkali ratio. Chondrite-normalized REE plots (Sun and McDonough, 1989) show fractionated REE patterns defined by a LREE enrichment and a relatively steep right-dipping curve towards the HREE; $[\text{La}/\text{Yb}]_N$ ratios range from 14.53 to 23.46 (Fig. 4E). The samples have Eu/Eu^* values between 0.86 and 0.96, and thus do not show marked Eu anomalies. Spider plots normalized to Primitive mantle (Sun and McDonough, 1989) show patterns enriched in highly incompatible trace elements, such as the light rare earth elements (LREE) and large-ion lithophile elements (LILE, e.g. Rb, Sr, Ba, U, Pb), but are depleted in Nb, Ti, and Th relative to neighboring REE (Fig. 4F). The HREE patterns are shallow dipping with uniform Dy/Yb ratios of 1.89 to 2.39.

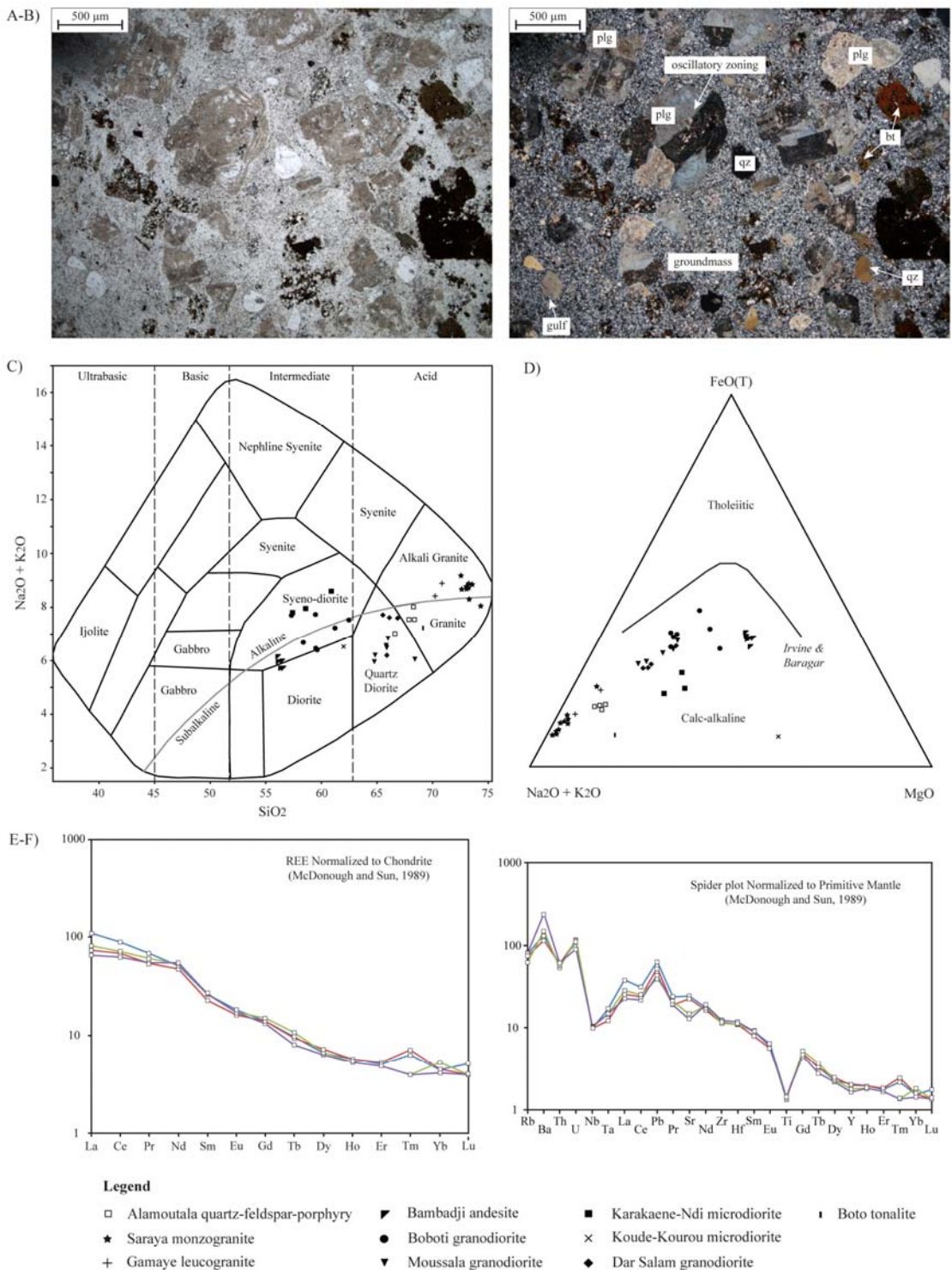


Figure 4. A-B) Representative micrographs of the least-altered Alamoutala quartz-feldspar porphyry in plane polarized light and crossed polars. **C)** Total alkalis vs. SiO_2 rock classification diagram from Cox et al. (1979). **D)** AFM diagram by Irvine and Baragar (1971). Data on the Falémé granitoids, the Saraya monzogranite, and the Gamaye leucogranite are shown for comparison (analyses included from Ndiaye et al., 1997; Schwartz and Melcher, 2004). **E)** REE spider plot normalized to chondrite values from Sun and McDonough (1989). **F)** Spider plot normalized to primitive mantle values from Sun and McDonough (1989).

6.3. Geochronology

The zircons isolated from the Alamoutala quartz-feldspar-porphyry are pale yellow to dark brown and black, generally between $40 \times 100 \mu\text{m}$ and $150 \times 350 \mu\text{m}$, and euhedral to subhedral prismatic. The vast majority of the grains exhibit strong oscillatory zoning, typical of igneous zircons (Fig. 5A). Zircons are extensively fractured; fluid and mineral inclusions are common. Eleven analyses of the standard BR266 and four analyses of OGC-1 were performed. One analysis of the BR266 standard was discarded because the spot hit a dark grain with micro-cracks and yielded an inaccurate age of $579 \text{ Ma} \pm 2$. Out of 10 primary standard analyses, the 1σ external spot to spot uncertainty was 0.74% and the calibration 1σ error of mean was 0.31%. Thirty-seven analyses were obtained from 35 zircons. Out of these 37 analyses, 20 were rejected on the basis of the defined cut-offs in order to keep only reliable data. Two additional analyses that yielded large errors on the $^{207}\text{Pb}/^{206}\text{Pb}$ age due to poor instrument sensitivity were also rejected. Rejected analyses are presented with the raw data and on the Tera-Wasserburg Concordia plot of all analyses (Fig. 5B). The 15 reliable analyses define a multi-component distribution ($n=2$) on a density probability plot (Fig. 5C). These 15 analyses can be assigned into two groups on the basis of their $^{207}\text{Pb}/^{206}\text{Pb}$ ratios (Fig. 5A-D). The four analyses assigned to Group I define a single population with a $^{207}\text{Pb}/^{206}\text{Pb}$ weighted mean date of $2134 \pm 12 \text{ Ma}$ (MSWD = 0.46, 2σ error) (Fig. 5D). Eleven analyses assigned to Group II define a single population that yield a weighted mean date of $2083 \pm 7 \text{ Ma}$ (MSWD = 1.4, 2σ error) (Fig. 5D). Both ages obtained by the weighted average method are within error of that obtained using Tera-Wasserburg U-Pb Concordia plots. The weighted mean date indicated by Group II is the best estimate for crystallization age of the Alamoutala quartz-feldspar-porphyry i.e. $2083 \pm 7 \text{ Ma}$. The older date indicated by Group I is interpreted to represent an inherited component of oscillatory zoned igneous zircons.

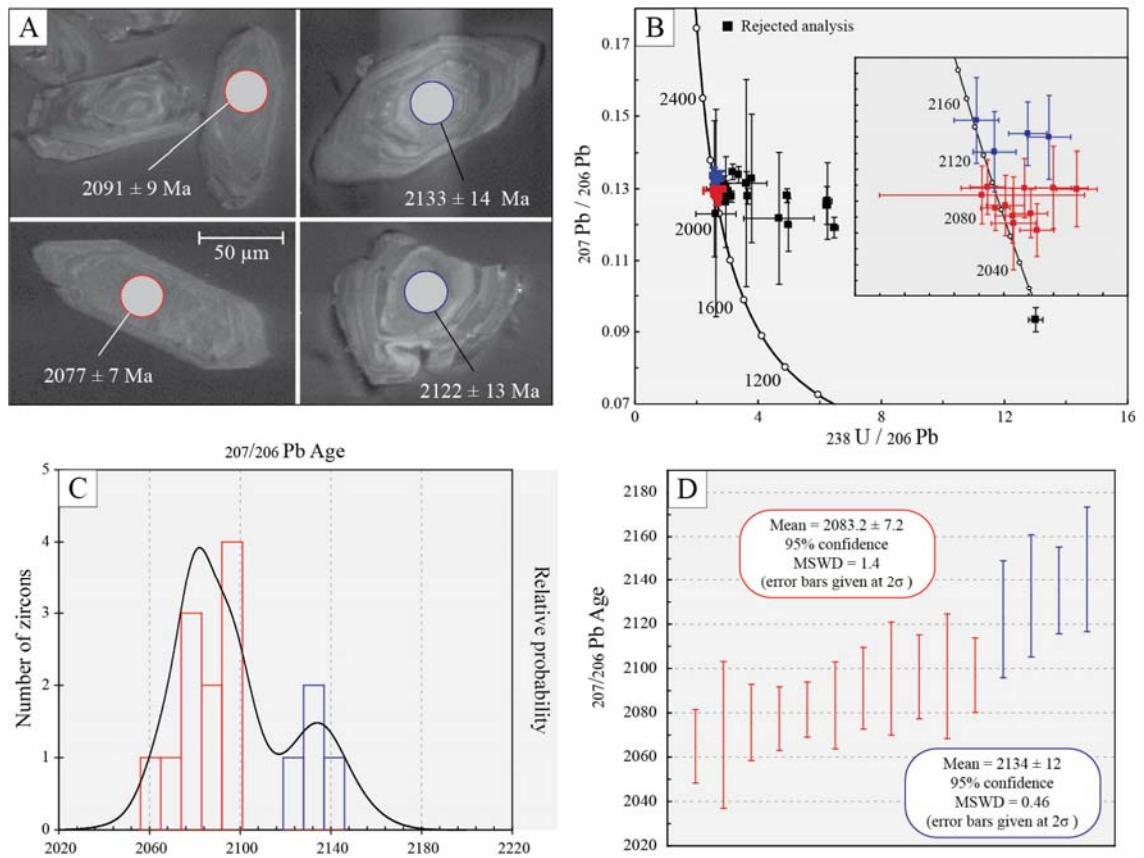


Figure 5. A) CL images that illustrate zircon morphology. B) Concordia plot (Tera-Wasserburg) showing all zircon analyses. See text for analysis rejection cut-offs. Inset provides a close-up view on near-concordant analyses. C) Probability density plot showing a mixed population component in the near-concordant zircon analyses. D) Weighted average plot of all near-concordant analyses illustrating the two U-Pb age groups.

6.4. Contact metamorphism

The Alamoutala quartz-feldspar-porphyry is locally bordered by contact metamorphic zones in country rocks. Amphibolite-facies contact-metamorphic assemblages overprint regional greenschist facies metamorphism of host rocks on the basis of textural relationships, which indicates that the peak of the regional metamorphism in the eastern part of the KKI occurred prior to 2083 ± 7 Ma. Early recrystallization of limestone was followed by the development of both exoskarns and endoskarns, which resulted in the destruction of all primary tectono-metamorphic texture in the host rocks (Fig. 6A). High temperature-low pressure prograde skarn assemblages are zoned and range from a proximal garnet-rich zone (0-5 m) (Fig. 6A-B) to an intermediate clinopyroxene-rich (5-10 m) (Fig. 6D), and distal actinolite/tremolite-

calcite-epidote-albite-rich zones further away from the intrusion (10-50 m) (Fig. 6E). Pockets of skarn-altered sedimentary rocks also occur locally throughout the opencast, suggesting flushing of the metasomatic fluids, and/or a complex intrusive stock geometry at depth. Reaction skarns formed after sandstone and siltstone consist of fine-grained siliceous and calc-silicate-hornfels whereas those formed after silty limestones consist of calc-silicate marble, reflecting a dependence on protolith composition. Exoskarns locally contain disseminated magnetite (up to 5%) and traces to minor amounts of pyrite (Fig. 6F-G).

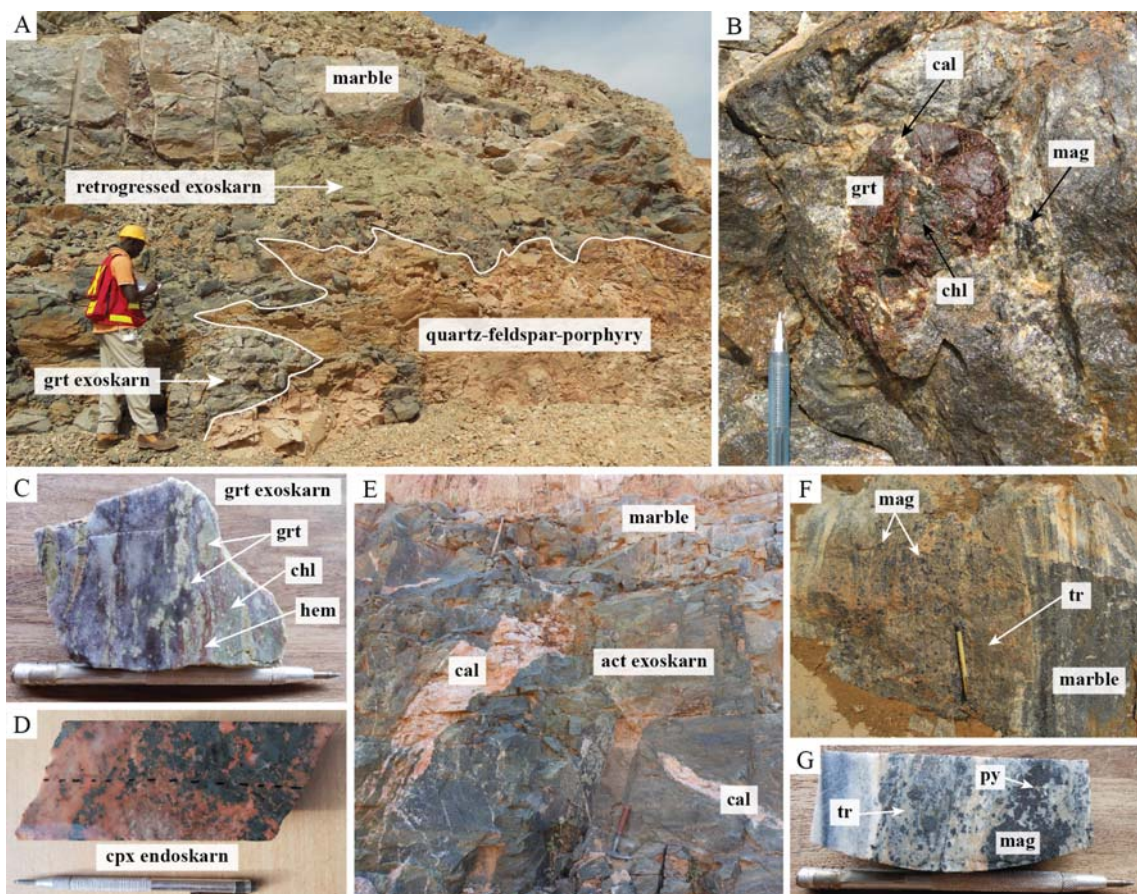


Figure 6. Field photographs illustrating contact metamorphism linked to emplacement of the Alamoutala quartz-feldspar-porphyry. A) Zoned skarn aureoles in marble. B) Megacrystic garnet in calc-silicate marble. C) Proximal garnet-rich exoskarn (after limestone). Granular garnets are stretched along the planar fabric and partially retrogressed to a mixture of chlorite, hematite and calcite. D) Clinopyroxene-epidote-bearing endoskarn. E) Pink calcite veins associated with the porphyroblastic growth of actinolite in marble. Traces of pyrite and magnetite occur disseminated in wall rocks of such veins. F) Tremolite-magnetite skarn lens in foliated marble. G) Tremolite-magnetite exoskarn in drill core.

At the micro-scale, garnets may exhibit complex oscillatory zoning reflecting the propagation of reactive fronts. Despite the wide range of internal textures, garnet composition essentially falls into the andradite-grossular series (Fig. 7A-F). Representative grains indicate essentially And₇₅Grs₂₅ compositions, although internal growth zones can reach intermediate And₅₀Grs₅₀ compositions. The composition of clinopyroxene in endoskarn varies between Hed₄₈₋₅₅Di₄₅₋₅₂Jo₁ in individual grains and between different grains (Fig. 8A-B). Retrogression of the garnet-pyroxene skarns occurs in the form of fine-grained granular epidote or as chlorite and calcite along grain boundaries, cleavage planes, and micro-fractures. Retrograde alteration of lower temperature amphibole-rich mineral assemblages is minor and characterized by clinozoisite, epidote, chlorite, calcite, and quartz.

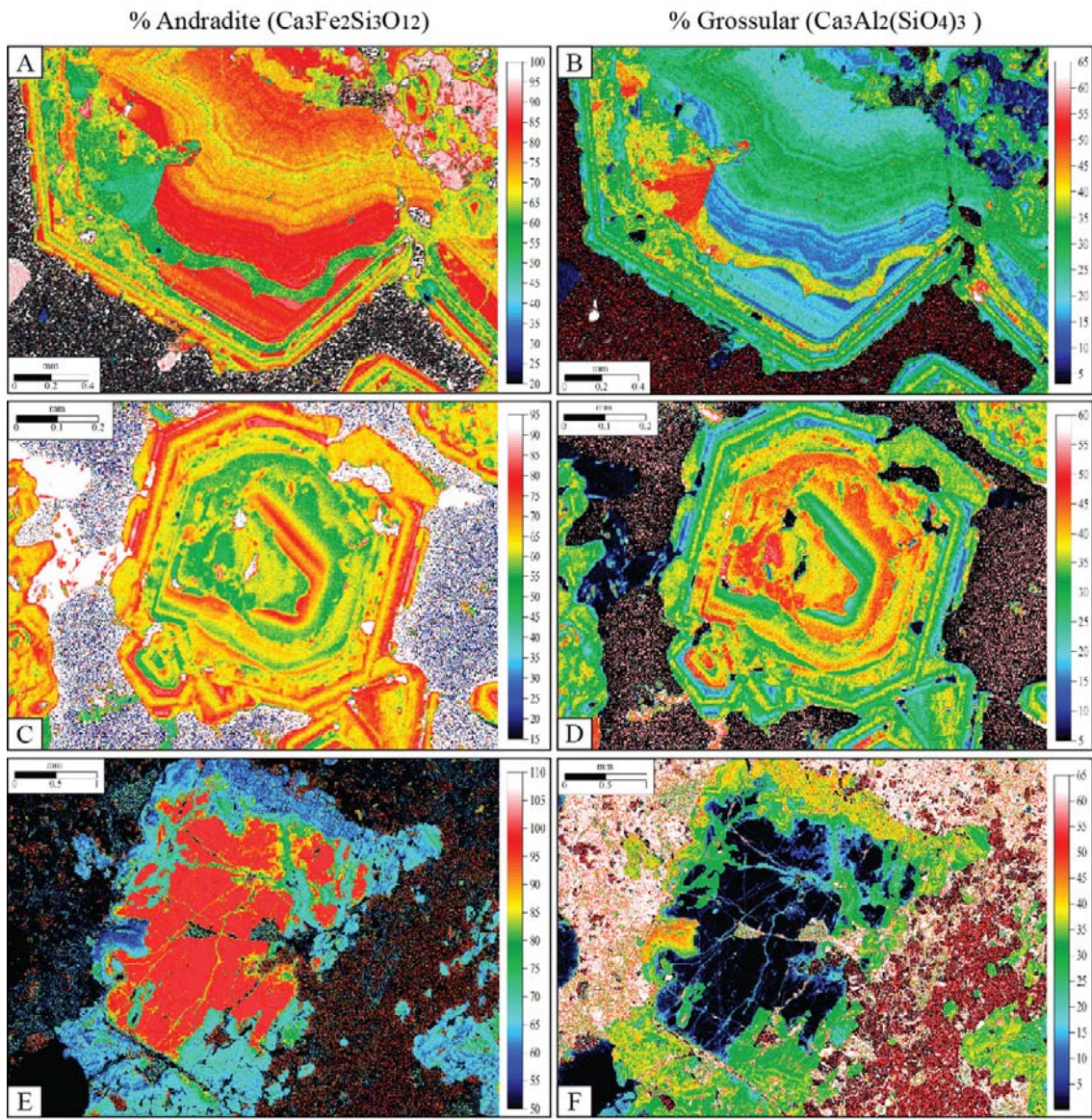


Figure 7. Electron probe end member garnet maps. Garnet composition at Alamoutala essentially falls into the andradite-grossular series. Maps A, C, and E show the % in andradite in selected garnets. In contrast, maps B, D, and F show the % in grossular. A-D) Oscillatory zoned garnet in exoskarn. The complex zoning reflects evolution of the fluid during progression of the reaction front. Potential syn-growth dissolution-reprecipitation features are observed. E-F) Garnet in endoskarn lacks complex zoning and typically is And₉₀₋₁₀₀Grs₀₋₁₀ in composition.

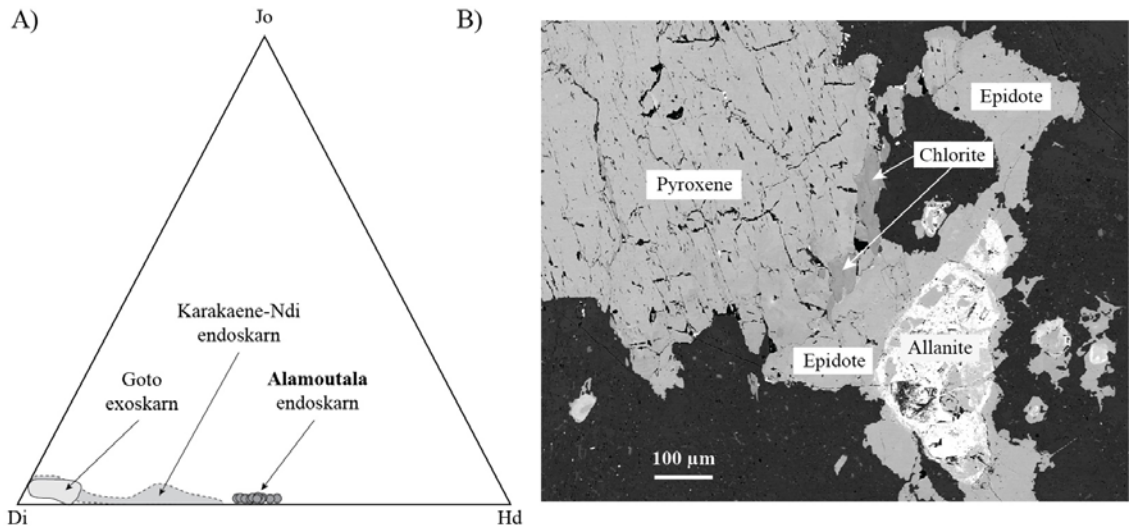


Figure 8. A) Representative chemical composition of pyroxenes analysed by electron probe. The stoichiometry was calculated using the WinPyrox software (Yavuz, 2013). $\text{MgCaSi}_2\text{O}_6\text{-FeCaSi}_2\text{O}_6\text{-CaMnSi}_2\text{O}_6$ plot (after Meinert, 1992) showing the compositional ranges of clinopyroxene in endoskarn at Alamoutala. Clinopyroxene is intermediate in composition and varies between $\text{Hed}_{48.55}\text{Di}_{45.52}\text{Jo}_{1}$ in individual grains and between different grains. Data for the Falémé contact metasomatic magnetite skarns is presented for comparison. Shaded areas show the compositional ranges of clinopyroxene in the Karakaene-Ndi endoskarn and Goto exoskarn (modified from Schwartz and Melcher, 2004). **B)** Photo micrograph of typical clinopyroxene in endoskarn. Clinopyroxene coexists with epidote, the latter growing over magmatic cores of allanite. Retrogression of the clinopyroxene is minor and marked by chlorite.

6.5. Structural setting and geometry

Ductile deformation (D_{1y} and D_{2y}): The thermal overprinting during emplacement of the Alamoutala quartz-feldspar-porphyry and skarn formation precludes accurate recording of any early structural component in the open pit. A steep planar fabric (S_1) now sub-parallel to bedding is associated with stacking of the sedimentary sequences in the open pit and surrounding outcrops (D_{1y}). The quartz-feldspar-porphyry stocks were emplaced post- D_{1y} because they cut the S_1 planar fabric.

A second planar fabric (S_2) is oblique to S_1 and is associated with upright to inclined disharmonic folds (F_2). Fold axes plunge gently (10-30°) to the SSW and are associated with a 035°/55SE axial-planar cleavage indicative of WNW fold-vergence (D_{2y}) (Fig. 3, 9A). The S_2 cleavage is refracted along the margins of the main porphyritic granodiorite stock. Importantly, garnet-pyroxene skarn assemblages are affected by F_2 folding (Fig. 3, 9B). Strong evidence for ductile deformation is also identified at the micro-scale. Under the microscope, less-deformed specimens of the

porphyritic granodiorite exhibit a mortar texture in which quartz and feldspar porphyroclasts are surrounded by a fine-grained groundmass. Strongly deformed specimens display strained quartz porphyroclasts and feldspar phenocrysts that exhibit strain shadows. Shear sense indicators such as asymmetrical strain shadow, mica fish, and sigma-shaped porphyroclasts are compatible with reverse displacement along S₂.

Brittle deformation (D_{3y}, D_{4y}, D_{5y}): A brittle overprint is recorded in outcrop and drill core. It is associated with sinistral reactivation of the Alamoutala Fracture Zone and NE-trending fault, as well as sinistral displacement along the S₂ planar fabric and reactivated bedding planes (D_{3y}) (Fig. 3, 9C). The Alamoutala Fracture Zone strikes NNW to N-S and dips steeply to the west. The fault developed at the lithostratigraphic contact in the south part of the pit and cuts the quartz-feldspar-porphyry on the northwestern walls of the pit. The fault is 1- to 7-m-wide and is associated with a discrete pinch-and-swell geometry that extends both along strike and down dip. Biotite-pyrite slickenfibers on fault walls of the Alamoutala Fracture Zone indicate oblique displacement, dominantly sinistral with a minor component of reverse displacement (Fig. 3, 9D).

Following D_{3s}, a set of barren quartz veins (<30-cm-wide) preferentially developed in the detrital sedimentary rocks and porphyritic granodiorite (D_{4y}) (Fig. 3, 9E). The general orientation of these veins is 215°/64°NW. These veins trend at an angle to S₂, and transect F₂ folds, the Alamoutala Fracture Zone and the NE-trending shear zone.

A late generation of E- to ENE-trending sub-vertical brittle faults crosscuts all previously described structures and veins (D_{5y}). These faults are 10-cm-to-1-m wide and contain fault gouge and clasts of host rocks (Fig. 3, 9F). Rare slickenfibers measured in the pit indicate dextral-(normal) displacement.

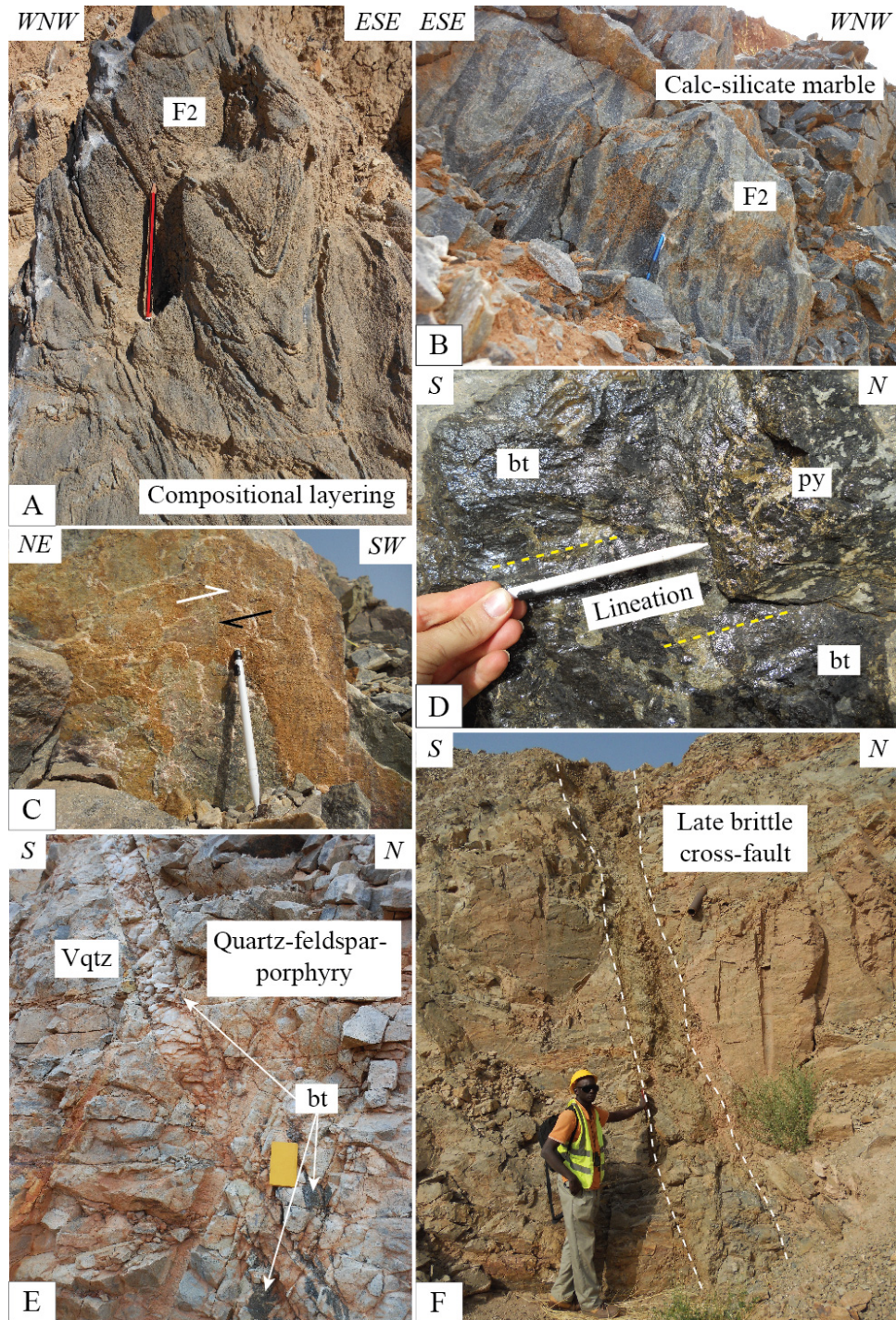


Figure 9. Alamoutala structural context from field photographs. A) Disharmonic F_2 folds in weathered silty-marble. Folding is highlighted by compositional layering. B) Folded calc-silicate marble which indicates F_2 folding post-dates prograde skarn formation. C) NE-trending fault wall in marble displays slickenfibers that indicate oblique sinistral-reverse movement. White arrow indicates apparent movement of missing block. Slickenfibers consist in calcite together with traces rusty pyrite. D) Fault wall on the Alamoutala Shear Zone that exhibit a sub-horizontal gently south-plunging lineation marked by biotite-pyrite. E) Typical field example of the late quartz vein set oriented $215^\circ/64^\circ\text{NW}$. F) Representative field photograph of a late brittle cross-fault.

6.6. Deposit-scale gold distribution

A multidisciplinary approach combining pit mapping, niche sampling, diamond drill core logging, and modeling under Leapfrog® was used to identify the setting of the gold resource because the Alamoutala orebody has been mined out. The bulk of the ore is hosted by the Alamoutala Fracture Zone and, to a lesser extent, by the steep NE-trending fault (Fig. 3, 10A-B). The Alamoutala Fracture Zone is discontinuous along its strike extensions. Gold mineralization is associated with sulfides aligned along the shear fabric in host rocks, and with disseminated sulfides in hydrothermal-tectonic breccias, which together define about 85% of the resource. Gold-bearing quartz veins are not common in the deposit. Ore minerals are quite diverse, but their volumetric proportions are typically low in each rock type, ranging from approximately 0.5-3 % sulfides. The shear-hosted mineralization is commonly associated with gold grades ranging from 2-10 g/t. Gold-related hydrothermal alteration mineral assemblages that occur in wall rocks to the Alamoutala Fracture Zone and NE-trending fault overprint contact-metamorphic mineral assemblages and are associated with solid-state deformation in the quartz-feldspar-porphyry. In addition to the shear-hosted mineralization, a minor, low-grade part of the gold mineralization (i.e. 1-2 g/t Au and less than 15% of the resource) locally presents as replacement-style orebodies correlated with pervasive biotite-pyrite lenses and bedding-parallel pyrite seams (Fig. 10C-D). Such ore zones have been observed along the intrusive contacts in low strain domains up to 15 m away from the Alamoutala Fracture Zone and NE-trending fault. Although textural relationships around the intrusive contact reflect a complex fluid history, these relationships indicate that the magnetite-bearing skarn aureole formed prior to these replacement-style orebodies. Also, the ore mineralogy within the shear zones is equivalent to that associated with these replacement-style orebodies, and thus the latter likely formed by lateral hydrothermal fluid flow surrounding the auriferous shear zones.

Leapfrog® was used to produce a three-dimensional rendering of the assay data (combined grade control and exploration) in order to better visualize and evaluate ore trends. Modeling indicates that gold mineralization was concentrated in low mean stress areas surrounding the intrusive stocks and in damage zones surrounding fault intersections (Fig. 11). Gold grades decrease with increasing distance from the quartz-

feldspar-porphyry stocks. The bulk of the ore in the central part of the open pit correlates with an approximately 35° south-dipping high grade ore shoot identified on a longitudinal section.

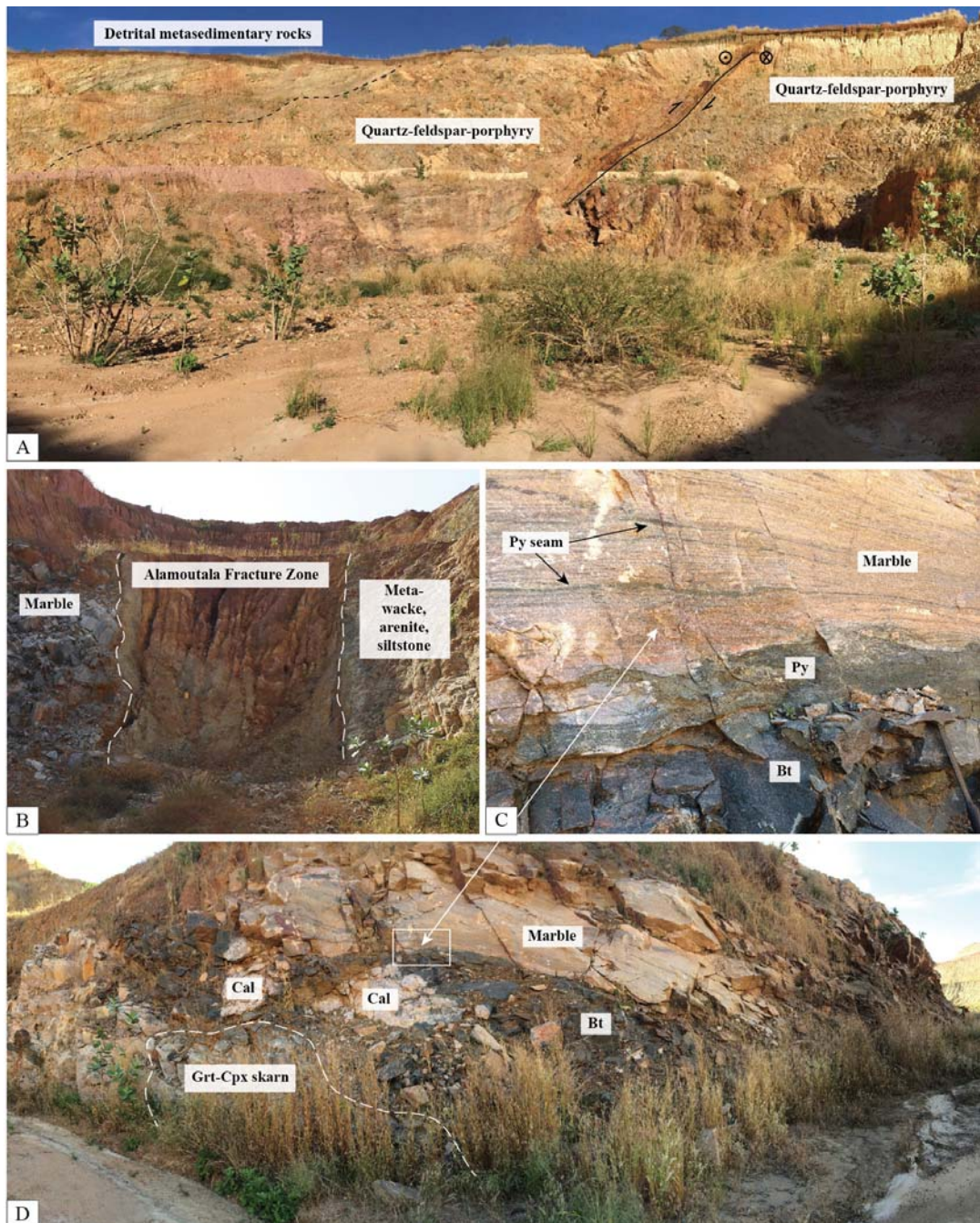


Figure 10. Representative field photographs illustrating controls on ore location and ore shoot geometry. A) Mineralized shear crosscutting the Alamoutala quartz-feldspar-porphyry in the northwestern end of the open pit. Benches are 5 m high. B) The Alamoutala Fracture Zone occupies the lithostratigraphic contact between detrital metasedimentary sequences and marbles at the southern end of the open pit. C-D) Replacement-style orebody.

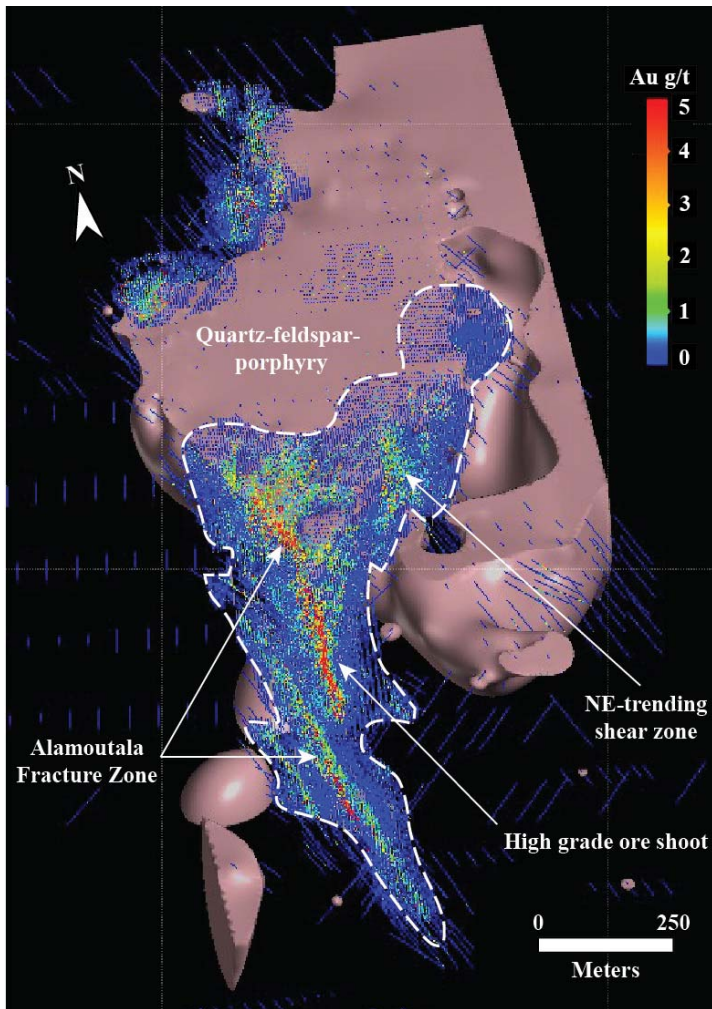


Figure 11. Leapfrog® scene that illustrates structural controls on ore shoot geometry. Data includes combined grade control and exploration assay data.

6.7. Ore-related hydrothermal alteration

Potassic hydrothermal alteration is ubiquitous in host rocks and synchronous with ore mineral deposition as determined from micro-textural relationships. The hydrothermal alteration assemblage is defined as biotite + calcite \pm muscovite \pm quartz \pm pyrite \pm tourmaline in the quartz-feldspar-porphyry (Fig. 12A-D) and biotite + calcite + pyrite \pm K-feldspar \pm actinolite-tremolite \pm quartz \pm tourmaline \pm pyrrhotite in marble (Fig. 12E-H). The pervasive biotite halo, surrounding the auriferous shear zones, in the country rocks extends beyond the extent of the current open pit.

Biotite and muscovite developed along the shear fabric mantling phenocrysts in the porphyry. Biotite preferentially developed in calcitic marble and marks a distinct foliation that overprints the porphyroblastic growth of garnet, clinopyroxene, and actinolite-tremolite. Phlogopite formed instead of biotite in the dolomitic marble horizons. Biotite also occurs as vein filling with variable amounts of quartz, calcite, K-feldspar, actinolite, and tourmaline and in altered wall rocks of such veins. Pinkish calcite veins with actinolite-tremolite in selvages are well developed in the pit. Calcite is best-observed in the quartz-feldspar-porphyry closely associated with disseminated biotite and/or as stringers with pyrite. Potassium-feldspar alteration occurs in the form of fine-grained poikiloblastic microcline and/or orthoclase intergrown with biotite, quartz, and calcite. The K-feldspar grains commonly contain minute inclusions of calcite and tourmaline. Tourmaline alteration is structurally-controlled and the mineral occurs in trace amounts to abundances of as much as 5 % of the rock. Tourmaline is observed as disseminated acicular masses and heart-shaped mineral sections along the shear fabric with biotite, calcite, muscovite, and sulfides; as filling in quartz micro-veins and narrow vein selvages; and as rod- and heart-shaped mineral sections intergrown with pyrite crystal aggregates.

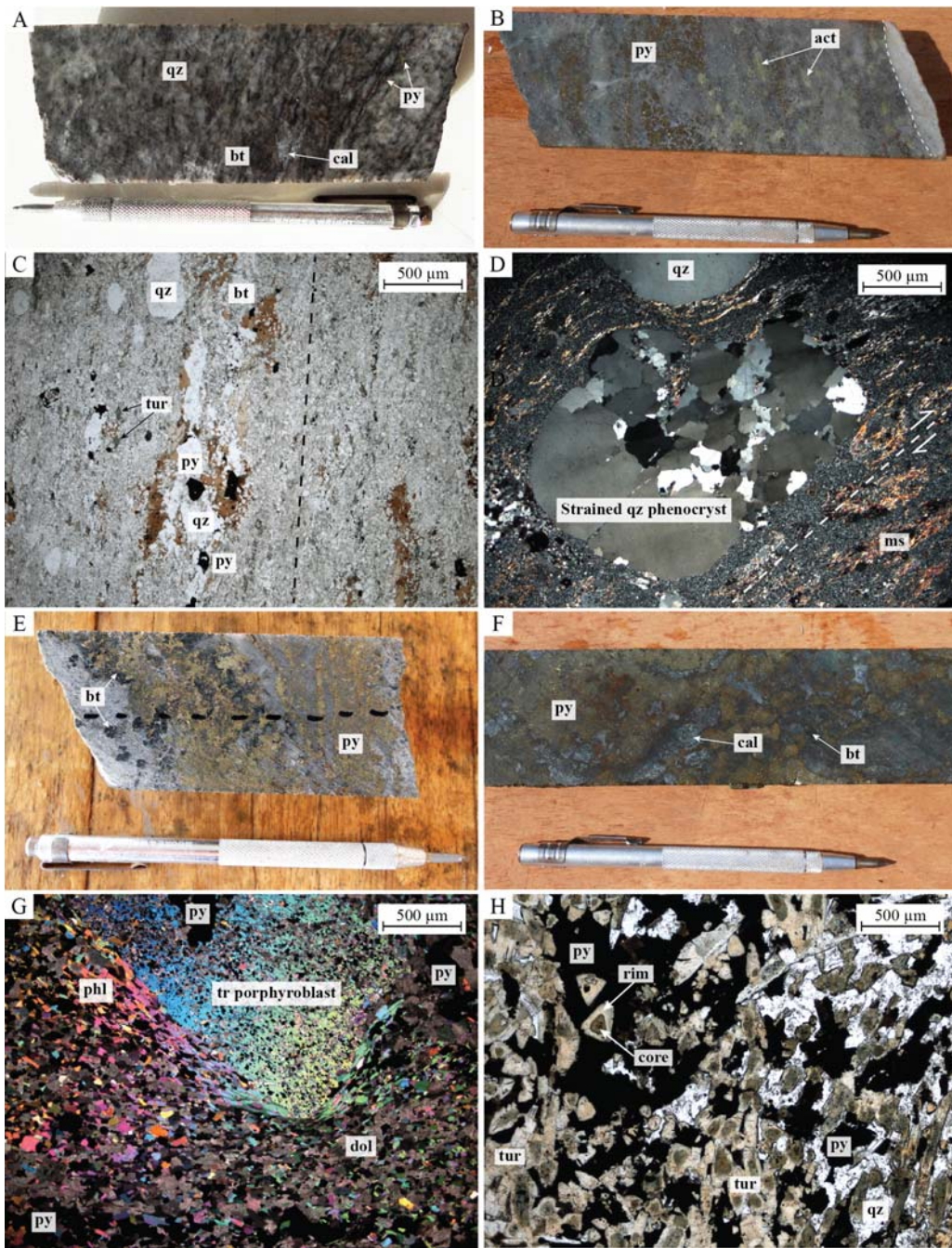


Figure 12. Drill core photographs and micrographs illustrating the potassic hydrothermal alteration assemblage in host rocks. A) Sheared quartz-feldspar-porphyry. The shear foliation is marked by biotite, calcite, quartz, and pyrite. B) Sheared quartz-feldspar-porphyry at contact with marble. Green actinolite flakes align along the fabric together with up to 5% pyrite. C) Feldspar phenocrysts are erased by sericitization while quartz phenocrysts are strained. Biotite, pyrite and accessory tourmaline align along the shear fabric. D) Muscovite alteration marks the S₂ planar fabric. Strained and assymetrical quartz phenocrysts indicate reverse displacement along the fabric. E) Foliated, sulfidic marble. The fabric is marked by pyrite, biotite and quartz. F) Massive pyrite ore after marble. G) A tremolite porphyroblast is overprinted by the syn-tectonic potassic assemblage in dolomitic marble. H) Zoned hydrothermal tourmalines closely associated with pyrite in marble.

6.8. Ore mineralogy

The shear-hosted ore largely consists of pyrite with lesser chalcopyrite and pyrrhotite. The ore also contains accessory Ag-Sb-As-Hg-Bi-Te-Mo-W-Zn-Pb-Ni-Co-U-bearing mineral species. A summary of the ore and alteration paragenesis at Alamoutala is presented in Figure 13 and explained in detail below.

Pyrite is the dominant sulfide phase at Alamoutala and occurs in numerous forms, including single euhedral to subhedral crystals (generally 50-250 μm), crystal aggregates (up to 1 cm), stringers, and massive pyrite (Fig. 14A). Pyrrhotite and chalcopyrite also are common ore phases. Pyrrhotite occurs as euhedral inclusions (2-10 μm) in pyrite and single crystals closely associated with, or intergrown with pyrite grains (Fig. 14A). Chalcopyrite occurs throughout the ore paragenesis. It is dominantly observed as single crystals (15-50 μm) infilling pyrite microfissures ($<15 \mu\text{m}$) or interstices between pyrite grains, and as overgrowths mantling on pyrite (Fig. 14A). A few minute chalcopyrite inclusions (2-10 μm) have been noted in pyrite.

The ore also includes a wide range of accessory minerals. Arsenopyrite is present in trace amounts as euhedral inclusions (2-20 μm) in pyrite and single fine-grained prismatic crystals (10-75 μm) closely associated with pyrite, although rarely observed intergrown (Fig. 14B). Apatite and rutile occur throughout the ore paragenesis. Monazite-(Ce) textural relationships suggest it formed syn- to post-pyrite crystallization. Tetrahedrite-tennantite crystals are syn- to post-pyrite formation and exhibit growth zoning from tetrahedrite₆₀₋₅₅tennantite₄₀₋₄₅ core (Cu-As-Sb-rich pole) to tetrahedrite₁₀₀ margins (Cu-Sb-rich pole). Traces of molybdenite, scheelite and coloradoite (HgTe) are found as fine-grained subhedral inclusions in pyrite. Traces of tellurobismuthite (Bi_2Te_3) and hessite (Ag_2Te) grains occur in pyrite microfractures that are often associated with tetrahedrite and chalcopyrite. Trace amounts of sphalerite and galena occur as subhedral to anhedral grains mantling pyrite and as infills in microfractures and interstices between pyrite crystals (Fig. 14B). Trace millerite (NiS) grains are enclosed by gersdorffite (NiAsS), which itself is observed mantling pyrite and chalcopyrite crystals. A suite of antimony-bearing minerals is also present in trace amounts and consistently deposited late in the paragenesis. The suite includes, in decreasing order of abundance, ullmannite (NiSbS), gudmundite (FeSbS), horobetsuite

$((\text{Bi},\text{Sb})_2\text{S}_3)$ and stibnite (Sb_2S_3). Rare uraninite (UO_2) and synchysite ($(\text{Ce},\text{La})\text{Ca}(\text{CO}_3)_2\text{F}$) grains exist as microscopic inclusions within pyrite or attached to its crystal edges.

The study of gold-bearing phases indicates that both native gold ($n=65\%$ modal volume) and electrum (i.e. gold content $>25\%$) ($n=35\%$ modal volume) particles are present in the ore and deposited as subhedral to anhedral inclusions and blebs ($1-12\ \mu\text{m}$) in pyrite (50%; G-I) (Fig. 14C); particles attached to pyrite-tetrahedrite-chalcopyrite crystal faces, often within pressure shadow or at fracture termination (35%; G-II) (Fig. 14D-E); and individual grains ($1-5\ \mu\text{m}$) situated along deformation cracks in pyrite and rarely in tetrahedrite (15%; G-III) (Fig. 14F). Micro-analyses of gold phases reveal electrum particles to contain 25 wt% Ag in average, whereas gold grains vary from native gold to particles containing up to 18 wt% Ag.

A suite of minerals generally observed near the oxide-fresh transition zone formed by weathering of the hypogene ore and include marcassite, hematite, malachite-azurite, and iron hydroxides, such as goethite and limonite. The oxide-fresh transition zone is also marked in marbles by abundant karst features, such as dissolution vugs and cavities.

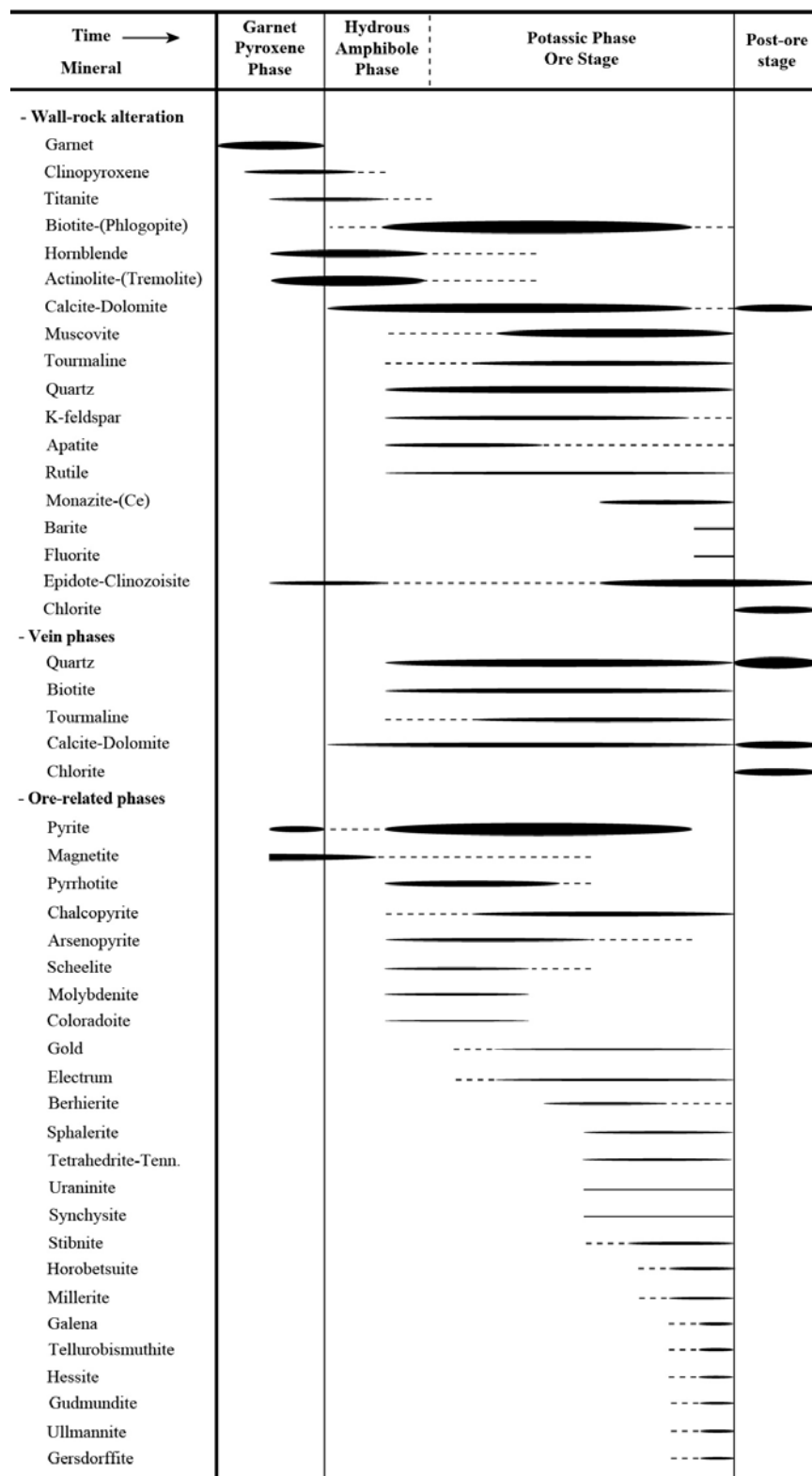


Figure 13. Ore and alteration paragenetic sequence chart for the Alamoutala gold deposit. Note: Tetrahedrite = $(\text{Cu}, \text{Fe})_{12}\text{Sb}_4\text{S}_{13}$; Tennantite = $(\text{Cu}, \text{Fe})_{12}\text{As}_4\text{S}_{13}$; Stibnite = Sb_2S_3 ; Gudmundite = FeSbS ; Berthierite = FeSb_2S_4 ; Millerite = NiS ; Ullmannite = NiSbS ; Tellurobismuthite (Bi_2Te_3); Coloradoite = HgTe ; Horobetsuite = $(\text{Bi}, \text{Sb})_2\text{S}_3$; Hessite = Ag_2Te ; Uraninite = UO_2 and Synchysite = $(\text{Ce}, \text{La})\text{Ca}(\text{CO}_3)_2\text{F}$.

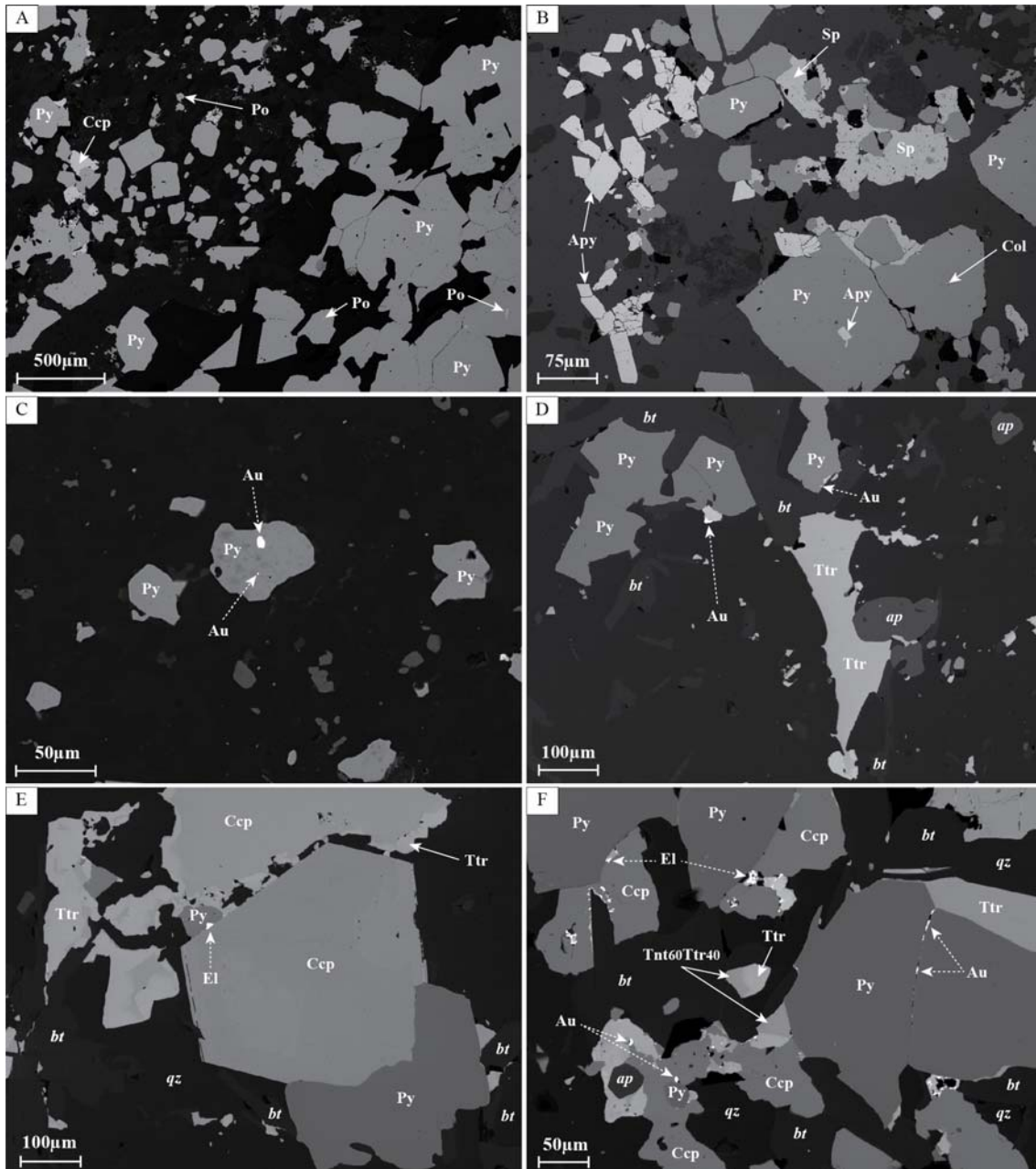


Figure 14. BSE images of the Alamoutala ore phases. A) Representative ore assemblage. B) Arsenopyrite is an accessory ore phase and deposited pre- to syn-pyrite. Sphalerite minerals formed late in the paragenetic sequence. C) Gold bleb (~1–5 µm) enclosed in pyrite (G-I). D–E) Gold and/or electrum particles attached to sulfide and tetrahedrite crystal faces (G-II). F) Gold particles along deformation cracks in pyrite (G-III).

7. Discussion

7.1. Towards a genetic model for the Alamoutala gold deposit

The geological setting of the Alamoutala gold deposit is analogous to that of magnetite skarns of the Falémé iron district as described in Schwartz and Melcher (2004). The mineralogy, whole rock geochemistry, and emplacement age of the Alamoutala quartz-feldspar-porphyry bodies are consistent with that of the Falémé plutons (e.g., Hirdes and Davis, 2002; Schwartz and Melcher, 2004). The silicate and oxide mineral association of endoskarn and exoskarn at Alamoutala indicates an overall oxidized magmatic-hydrothermal fluid (e.g., formation of Fe^{3+} -bearing andradite, relative abundance of magnetite, garnet >> pyroxene) and a shallow crustal level of emplacement (≤ 5 km) (e.g., Meinert, 2000; Meinert et al., 2005). The Alamoutala magnetite skarns, however, have never been of economic interest. The data presented in this study suggest that the Alamoutala deposit contains an early and locally-developed magnetite-bearing skarn that was overprinted by regional orogenic gold mineralization. This interpretation is supported by micro-textural evidence that indicates that the ore-forming process must have taken place, at least in part, after the solidification and cooling of the pluton because shearing generated mineralized proto-mylonite zones in the quartz-feldspar-porphyry stocks. Moreover, the bulk of the ore is shear-hosted and displays no vertical or lateral zonation of metals away from the intrusive contact as commonly observed in magmatic-hydrothermal systems (e.g., Au-skarn, Meinert et al., 2005; Cu-Au porphyry, Seedorff et al., 2005). It is likely that magmas, which exsolved a magmatic-hydrothermal fluid, and the regional gold-bearing fluids have utilized the same fault system at Alamoutala, although at different times. Ore fluids were most likely concentrated in low mean stress areas surrounding the quartz-feldspar-porphyry stocks and in damage zones surrounding fault intersections. Nevertheless, the difficulty in interpreting the Alamoutala deposit is to reconcile the thermal disequilibrium between country rocks at regional greenschist-facies conditions and the higher temperature of the ore-related hydrothermal alteration paragenesis with characteristics of orogenic gold deposits (e.g., Groves et al., 1998, 2003; Goldfarb et al., 2005). That thermal disequilibrium, however, is similar to data reported for the Sadiola Hill gold

deposit (Masurel et al., *in press*) and is suggested to represent a transient thermal effect associated with syn-kinematic igneous activity in the region at the time of mineralization (i.e. D_{3y}).

7.2. Integration of the Alamoutala deposit with regional geology and tectonics

At least two phases of folding have affected country rocks at the Alamoutala gold deposit. The D_{1y} early event may be correlated with the regional D₁ responsible for the formation of a NNW-trending structural corridor in Mali and associated WSW-ENE-directed shortening (public data from AMIRA International, West African Initiative final report, 2013). The D₁ deformation episode has been interpreted to have occurred between ca. 2160 and 2115 Ma (Ledru et al., 1991; Milési et al., 1992; Dabo and Aïfa, 2010, 2011; McFarlane et al., 2011; Diene et al., 2012; Gueye et al., 2008). At the regional scale D_{2y} is compatible with a period of fold-and-thrust tectonics correlated with a region-wide compressive event (D₂) (in Ivory Coast, Pouclet et al., 2006; Vidal et al., 2009; in Burkina Faso, Hein, 2010; in northern Guinea, Lahondère et al., 2002; in southern Mali, Liégeois et al., 1991; Milési et al., 1992; McFarlane et al., 2011; in the KKI, Dabo and Aïfa, 2010; Diene et al., 2012; Lawrence et al., 2013a; Treloar et al., 2014; Masurel et al., *in press*). The Senegal-Mali Shear Zone is inferred to have formed as a transpressional fault during D₂ deformation, coeval with development of the S₂ penetrative cleavage (Liégeois et al., 1991; Lawrence et al., 2013a). The Alamoutala quartz-feldspar-porphyry stocks emplaced in the upper crust syn-D_{2y} but were sheared subsequently during D_{3y}. The economic gold mineralization at Alamoutala formed during D_{3y} coeval with sinistral displacement along the Senegal-Mali Shear Zone and Alamoutala Fracture Zone. The similar relative timing and structural setting between the Alamoutala gold deposit and other deposits of the KKI (e.g., Loulo, Lawrence et al., 2013a; Massawa, Treloar et al., 2014; Sadiola Hill, Masurel et al., *in press*) suggest that gold mineralization in the region occurred during a period of transcurrent tectonics that outlasted emplacement of the Falémé-type granitoids, after the cessation of regional compressional deformation. The D_{2y} and D_{3y} events likely represent the local expression of regional deformation (D₂-D₃) associated with the Eburnean orogeny and were

undoubtedly responsible for the formation of map-scale structures. Syn-tectonic magmatic suites with arc-related geochemical signatures have been described to intrude the KKI volcano-sedimentary country rocks between ca. 2115 and 2070 Ma (Hirdes and Davis, 2002; Schwartz and Melcher, 2004; Pawlig et al., 2006; Gueye et al., 2007, 2008). The REE signature and calc-alkaline affinity of the Alamoutala quartz-feldspar-porphyry stocks are consistent with data reported for other Eburnean granitoids of the Falémé belt (e.g., Schwartz and Melcher, 2004; Dioh et al., 2006; Lambert-Smith, 2014) and suggests derivation from either a metasomatized mantle source with crustal contamination (e.g., Egal et al., 2002) or melting of an enriched lower-crustal garnet-amphibolite source (e.g., Doumbia et al., 1998; Pouclet et al., 2006). It is possible that the late Eburnean magmatic activity helped generate increased thermal gradients, which could have produced regional fluid systems capable of transporting gold (e.g., Oberthür et al., 1998). Additional geochronology and metamorphic data for the KKI will help to better understand the tectono-thermal evolution of the inlier.

8. Conclusions

Recent research in the eastern part of the KKI has highlighted the spatial association between calc-alkaline Eburnean plutons, gold mineralization, and local iron skarn mineralization, suggesting a complex fluid evolution in relation to the development of major gold deposits (e.g., Lawrence et al., 2013a, b). The emplacement of Eburnean quartz-feldspar-porphyry stocks in the Alamoutala deposit area resulted in the formation of a low P -high T magnetite-bearing skarn in a geological setting analogous to that of the Falémé iron skarns (e.g., Schwartz and Melcher, 2004). The gold mineralization is shear-hosted and occurred subsequently during a period of transcurrent tectonics, and thus overprints the contact-metamorphic mineral assemblages. The current study indicates that the magmatic episode occurred at 2083 ± 7 Ma, and thus regional orogenic gold mineralization is younger than this age.

9. Acknowledgments

This study forms part of a PhD project, which began in February 2012 at the Centre for Exploration Targeting, UWA. SEMOS, a joint venture between AngloGold Ashanti, IAMGOLD and the Malian government, is gratefully acknowledged for its financial support. Many thanks to T. Gell (AGA), A. Mason-Apps (AGA), O. Terblanche (AGA) and M. Skwarnecki (AGA) for their enthusiasm for the study and their constructive discussions. Special thanks are extended to D. Traoré, C.O. Sanogo, F. Samake, M. Traoré , Y.S. Kone, and to SEMOS managers G. Gushee, H. Eybers, H. Sitshengiso, P. Herron, and S. Tessougue who assisted with field work studies and logistics. The authors acknowledge the John de Laeter Centre of Excellence for Mass Spectrometry, Curtin University (WA) and Hao Gao for his excellent technical assistance on the SHRIMP. The authors acknowledge the Australian Microscopy & Microanalysis Research Facility at the Centre for Microscopy, Characterisation & Analysis (UWA), a facility funded by the University, State and Commonwealth Governments. Special thanks to Richard Goldfarb for his efforts and constructive reviews. Larry Meinert and Biswajit Mishra are also thanked for their comprehensive appraisal of the study.

10. References

- AMIRA International, 2013, P934A West African Exploration Initiative – Stage II Final Report Appendix, p. 446-536.
- AnglogGold Ashanti, 2011, AGA Mineral Resource and Ore Reserve Report. Accessed in 2015 from <http://www.agareports.com>.
- Arcelor Mittal, 2007, Press release, Arcelor Mittal signs agreement to develop iron ore mining in Senegal. Accessed in 2015 from <http://www.arcelormittal.com>.
- Armstrong, J.T., 1988, Quantitative analysis of silicates and oxide minerals: Comparison of Monte-Carlo, ZAF and Phi-Rho-Z procedures: Microbeam Analysis, v. 23, p. 239-246.
- Bassot, J.P., 1987, Le complexe volcano-plutonique calco-alcalin de la rivière Daléma (Est Sénégal): discussion de sa signification géodynamique dans le cadre de l'orogénie

- eburnéenne (Protérozoïque inférieur): Journal of African Earth Sciences, v. 6, p. 505-519.
- Bassot, J.P., and Dommange, A., 1986, Mise en évidence d'un accident majeur affectant le Protérozoïque inférieur des confins sénégalo-maliens: Comptes Rendus Géosciences, v. 302, p. 1101–1106.
- Bassot, J.P., and Caen-Vachette, M., 1984, Données géochronologiques et géochimiques nouvelles sur les granitoïdes de l'Est du Sénégal: Implications sur l'histoire géologique du Birimien de cette région, *in* Klerkx, J., and Michot, J., eds., African Geology: Belgium, Tervuren, p. 196-209.
- Boher, M., Abouchami, W., Michard, A., Albareda, F., and Arndt, N.T., 1992, Crustal Growth in West Africa at 2.1 Ga: Journal of Geophysical Research, v. 97, p. 345-369.
- Calvez, J.Y., Feybesse, J.L., Ledru, P., and Milesi, J.P., 1990, Géochronologie du Proterozoïque inférieur du craton ouest africain (méthode d'évaporation directe de zircons isolés) [abs]: 13^e Réunion des Sciences de la Terre, Grenoble, France, Conference proceedings; *in* Milési, J.P., Feybesse, J.L., Ledru, P., Dommange, A., Quedraogo, M.F., Marcoux, E., Prost, A., Vinchon, C., Sylvain, J.P., Johan, V., Tegyey, M., Calvez, J.Y., and Lagny, P., 1989, Les minéralisations aurifères de l'Afrique de l'Ouest et leurs relations avec l'évolution lithostructurale au Protérozoïque inférieur: Chronique de la Recherche Minière, v. 497, p. 3-98.
- Compston, W., Williams, I.S., and Meyer, C., 1984, U-Pb geochronology of zircons from lunar breccia 73217 using a sensitive high mass-resolution ion microprobe: Journal of Geophysical Research, v. 89, p. B252–B534.
- Cox, K.G., Bell, J.D., and Pankhurst, R.J., 1979, The interpretation of igneous rocks *in* Rollinson, H., Using Geochemical Data: evaluation, presentation and interpretation, p. 51-52.
- Dabo, M., and Aïfa, T., 2011, Late Eburnean deformation in the Kolia-Boboti sedimentary basin, Kédougou-Kéniéba Inlier, Senegal: Journal of African Earth Sciences, v. 60, p. 106-116.
- Dabo, M., and Aïfa, T., 2010, Structural styles and tectonic evolution of the Kolia-Boboti sedimentary Basin, Kédougou-Kéniéba inlier, eastern Senegal: Comptes Rendus Geoscience, v. 342, p. 796-805.
- Debat, P., Nikiéma, S., Mercier, A., Lombo, M., Béziat, D., Bourges, F., Roddaz, M., Salvi, S., Tollon, F., and Wenmenga, U., 2003, A new metamorphic constraint for the

- Eburnean orogeny from Palaeoproterozoic formations of the Man shield (Aribinda and Tampelga countries, Burkina Faso): Precambrian Research, v. 123, p. 47–65.
- Debat, P., Diallo, D.P., Ngom, P.M., Rollet, M., and Seyler, M., 1984, La série de Mako dans ses parties centrale et méridionale (Sénégal Oriental, Afrique de l'ouest). Précisions sur l'évolution de la série volcanosédimentaire et données géochimiques préliminaires sur les formations magmatiques post-tectoniques: Journal of African Earth Sciences, v. 2, p. 71-79.
- Dia, A., 1988, Caractères et signification des complexes magmatiques et métamorphiques du secteur de Sandikounda-Laminia (Nord de la boutonnière de Kédougou, Est du Sénégal): un modèle géodynamique du Birimien de l'Afrique de l'Ouest: Unpublished Ph.D. thesis, Sénégal, Université de Dakar, 350 p.
- Dia, A., Van Schmus, W.R., and Kröner, A., 1997, Isotopic constraints on the age and formation of a Palaeoproterozoic volcanic arc complex in the Kedougou Inlier, eastern Senegal, West Africa: Journal of African Earth Sciences, v. 24, p. 197-213.
- Diene, M., Gueye, M., Diallo, D.P., and Dia, A., 2012, Structural Evolution of a Precambrian Segment: Example of the Paleoproterozoic Formations of the Mako Belt (Eastern Senegal, West Africa): International Journal of Geosciences, v. 03, p. 153-165.
- Dioh, E., Béziat, D., Débat, P., Grégoire, M., and Ngom, P.M., 2006, Diversity of the Palaeoproterozoic granitoids of the Kédougou inlier (eastern Senegal): Petrographical and geochemical constraints: Journal of African Earth Sciences, v. 44, p. 351-371.
- Doumbia, S., Pouclet, A., Kouamelan, A., Peucat, J.J., Vidal, M., and Delor, C., 1998, Petrogenesis of juvenile-type Birimian (Paleoproterozoic) granitoids in Central Côte-d'Ivoire, West Africa: geochemistry and geochronology: Precambrian Research, v. 87, p. 33-63.
- Egal, E., Thiéblemont, D., Lahondère, D., Guerrot, C., Costea, C.A., Iliescu, D., Delor, C., Goujou, J.C., Lafon, J.M., Tegyey, M., Diaby, S., and Kolié, P., 2002, Late Eburnean granitization and tectonics along the western and northwestern margin of the Archean Kénéma-Man domain (Guinea, West African Craton): Precambrian Research, v. 117, p. 57-84.
- Goldfarb, R.J., Baker, T., Dubé, B., Groves, D.I., Hart, C.J.R., and Gosselin, P., 2005, Distribution, character, and genesis of gold deposits in metamorphic terranes: Economic Geology 100th Anniversary Volume, p. 407–450.

- Groves, D.I., Goldfarb, R.J., Gebre-Mariam, M., Hagemann, S.G., and Robert, F., 1998, Orogenic gold deposits: A proposed classification in the context of their crustal distribution and relationship to other gold deposit types: *Ore Geology Reviews*, v. 13, p. 7-27.
- Groves, D.I., Goldfarb, R.J., Robert, F., and Hart, C.J.R., 2003, Gold Deposits in Metamorphic Belts: Overview of Current Understanding, Outstanding Problems, Future Research, and Exploration Significance: *Economic Geology*, v. 98, p. 1-29.
- Gueye, M., Ngom, P.M., Diène, M., Thiam, Y., Siegesmund, S., Wemmer, K., and Pawlig, S., 2008, Intrusive rocks and tectono-metamorphic evolution of the Mako Paleoproterozoic belt (Eastern Senegal, West Africa): *Journal of African Earth Sciences*, v. 50, p. 88-110.
- Gueye, M., Siegesmund, S., Wemmer, K., Pawlig, S., Drobe, M., Nolte, N., and Layer, P., 2007, New evidences for an early Birimian evolution in the West African Craton: An example from the Kédougou-Kénieba inlier, southeast Senegal: *South African Journal of Geology*, v. 110, p. 511-534.
- Hein, K.A.A., 2010, Succession of structural events in the Goren greenstone belt (Burkina Faso): Implications for West African tectonics: *Journal of African Earth Sciences*, v. 56, p. 83-94.
- Hirdes, W., and Davis, D.W., 2002, U-Pb Geochronology of Paleoproterozoic Rocks in the Southern Part of the Kédougou-Kénieba Inlier, Senegal, West Africa: Evidence for Diachronous Accretionary Development of the Eburnean Province: *Precambrian Research*, v. 118, p. 83-99.
- IAMGold, 2015, public data from <http://www.iamgold.com/English/Operations/Operating-Mines/Yatela-GoldMine>.
- Irvine, T.N., and Baragar, W.R.A., 1971, a guide to the geochemical classification of the common volcanic rocks: *Canadian Journal of Earth Sciences*, v. 8, p. 523-548.
- Lahondère, D., Thiéblemont, D., Tegyey, M., Guerrot, C., and Diabate, B., 2002, First evidence of early Birimian (2.21 Ga) volcanic activity in Upper Guinea: The volcanics and associated rocks of the Niani suite: *Journal of African Earth Sciences*, v. 35, p. 417–431.
- Lambert-Smith, J., 2014, The geology, structure and metallogenesis of the world class Loulo-Bambadji Au district in Mali and Senegal, West Africa: Ph.D. Thesis, Kingston University, London, 346 p.

Lawrence, D. M., 2010, Characterization and evolution of Au mineralization in the Loulo mining district, western Mali: Unpublished Ph.D. thesis, London, Kingston University, 341 p.

Lawrence, D.M., Treloar, P.J., Rankin, A.H., Boyce, A., and Harbridge, P., 2013b, A Fluid Inclusion and Stable Isotope Study at the Loulo Mining District, Mali, West Africa: Implications for Multifluid Sources in the Generation of Orogenic Gold Deposits: *Economic Geology*, v. 108, p. 229-257.

Lawrence, D.M., Treloar, P.J., Rankin, A.H., Harbridge, P., and Holliday, J., 2013a, The Geology and Mineralogy of the Loulo Mining District, Mali, West Africa: Evidence for Two Distinct Styles of Orogenic Gold Mineralization: *Economic Geology*, v. 108, p. 199-227.

Ledru, P., Pons, J., Milesi, J.P., Feybesse, J.L., and Johan, V., 1991, Transcurrent tectonics and polycyclic evolution in the Lower proterozoic of Senegal-Mali: Precambrian Research, v. 50, p. 337-354.

Liégeois, J.P., Claessens, W., Camara, D., and Klerkx, J., 1991, Short-lived Eburnian orogeny in southern Mali. *Geology, tectonics, U-Pb and Rb-Sr geochronology: Precambrian Research*, v. 50, p. 111-136.

Ludwig, K.R., 2003, Isoplot 3.0; a geochronological toolkit for Microsoft Excel: Berkeley Geochronology Centre Special Publication, v.4, 70 p.

Ludwig, K.R., 2009, Squid 2.50, A User's Manual: Unpublished report by Berkeley Geochronology Centre, California, USA, 95 p.

Masurel, Q., Thébaud, N., Miller, J., Ulrich, S., Hein, K.A.A., Cameron, G., Béziat, D., Bruguier, O., and Davis, J.A., 2015, Sadiola Hill: a world-class carbonate-hosted gold deposit in Mali, West Africa: *Economic Geology*, this volume.

McFarlane, C.R.M., Mavrogenes, J., Lentz, D., King, K., Allibone, A., and Holcombe, R., 2011, Geology and Intrusion-Related Affinity of the Morila Gold Mine, Southeast Mali: *Economic Geology*, v. 106, p. 727-750.

Meinert, L.D., Dipple, G.M., and Nicolescu, S., 2005, World Skarn Deposits: *Economic Geology*, 100th Anniversary Volume, p. 299-336.

Meinert, L.D., 2000, Gold in skarns related to epizonal intrusions: *Reviews in Economic Geology*, v. 13, p. 347-375.

Meinert, L.D., 1992, Skarns and skarn deposits, *Geoscience Canada*, v. 19, p. 145-162.

- Milési, J.P., Ledru, P., Feybesse, J.L., Dommangeat, A., and Marcoux, E., 1992, Early Proterozoic ore deposits and tectonics of the Birimian orogenic belt, West Africa: Precambrian Research, v. 58, p. 305-344.
- Ndiaye, P.M., Dia, A., Viallette, Y., Diallo, D.P., Ngom, P.M., Sylla, M., Wade, S., and Dioh, E., 1997, Données pétrographiques, géochimiques et géochronologiques nouvelles sur les granitoïdes du Paléoprotérozoïque du Supergroupe de Dialé-Daléma (Senegal Oriental): Implications pétrogénétiques et géodynamiques: Journal of African Earth Sciences, v. 25, p. 193-208.
- Oberthür, T., Vetter, U., Davis, D.W., and Amanor, J.A., 1998, Age constraints on gold mineralization and Paleoproterozoic crustal evolution in the Ashanti belt of southern Ghana: Precambrian Research, v. 89, p. 129-143.
- Pawlig, S., Gueye, M., Klischies, R., Schwarz, S., Wemmer, K., and Siegesmund, S., 2006, Geochemical and Sr-Nd isotopic data on the Birimian of the Kedougou-Kenieba Inlier (Eastern Senegal): Implications on the Palaeoproterozoic evolution of the West African Craton: South African Journal of Geology, v. 109, p. 411-427.
- Pouclet, A., Doumbia, S., and Vidal, M., 2006, Geodynamic setting of the Birimian volcanism in central Ivory Coast (western Africa) and its place in the Palaeoproterozoic evolution of the Man Shield: Bulletin de la Société Géologique de France, v. 177, p. 105-121.
- Schwartz, M.O., and Melcher, F., 2004, The Falémé Iron District, Senegal: Economic Geology, v. 99, p. 917-939.
- Seedorff, E., Dilles, J.H., Proffett, J.M., Einaudi, M.T., Zurcher, L., Stavast, W.J.A., Johnson, D. A., and Barton, D., 2005, Porphyry Deposits: Characteristic and Origin of Hypogene Features: Economic Geology 100th Anniversary Volume, p. 251–298.
- Stacey, J.S., and Kramers, J.D, 1975, Approximation of terrestrial lead isotope evolution by a two-stage model: Earth and Planetary Science Letters, v. 26, p. 207–221.
- Stern, R.A., 2001, A new isotopic and trace-element standard for the ion microprobe: preliminary thermal ionization mass spectrometry (TIMS) U-Pb and electron-microprobe data: Geological Survey of Canada, Radiogenic Age and Isotopic Studies, Report 14, Current Research 2001-F1, 11 p.
- Stern, R.A., Bodorkos, S., Kamo, S.L., Hickman, A.H., and Corfu, F., 2009, Measurement of SIMS instrumental mass fractionation of Pb isotopes during zircon dating: Geostandards and Geoanalytical Research, v. 33, p. 145–168.

Sun, S.S., and McDonough, W.F., 1989, Chemical and isotopic systematics of oceanic basalts: implications for mantle composition and processes, *in* Saunders, A. D., and Norry, M.J. (eds), Magmatism in ocean basins: Geological Society Special Publication, v. 42, p. 313-345.

Treloar, P.J., Lawrence, D.M., Senghor, D., Boyce, A., and Harbridge, P., 2014, The Massawa gold deposit, Eastern Senegal, West Africa: an orogenic gold deposit sourced from magmatically derived fluids?: Geological Society, London, Special Publications.

Vidal, M., Gumiaux, C., Cagnard, F., Pouclet, A., Ouattara, G., and Pichon, M., 2009, Evolution of a Paleoproterozoic “weak type” orogeny in the West African Craton (Ivory Coast): Tectonophysics, v. 477, p. 145-159.

Wingate, M.T.D., and Kirkland, C.L., 2013, Introduction to geochronology information: Geological Survey of Western Australia Publication, 5 p.

Yavuz, F., 2013, WinPyrox - a Windows program for pyroxene calculation, classification and thermobarometry: American Mineralogist, v. 98, p. 1338-1359.

11. Supplementary material

11.1. Lithogeochemistry data for igneous rocks of the Alamoutala open pit.

11.2. Sensitive high resolution ion microprobe (SHRIMP) analytical results for the Alamoutala quartz-feldspar-porphyry.

11.3. Representative electron probe micro-analyses of pyroxene in endoskarn.

Lithogeochemistry data for igneous rocks of the Almoutala open pit

Elements	D.L.	Method	quartz-feldspar- porphyry	quartz-feldspar- porphyry	quartz-feldspar- porphyry	quartz-feldspar- porphyry	Early mafic dike	Early mafic dike	Late mafic dike
Major elements (%)									
SiO ₂	0.01	FB1/XRF	67.88	68.3	66.58	68.35	49.54	49.57	51.1
TiO ₂	0.01	FB1/XRF	0.31	0.31	0.29	0.31	0.61	0.64	0.98
Al ₂ O ₃	0.01	FB1/XRF	14.95	15.12	14.46	15.18	11	11.79	16.95
Fe ₂ O ₃	0.01	FB1/XRF	1.91	1.82	1.67	1.74	7.35	8.05	6.28
MnO	0.01	FB1/XRF	0.04	0.03	0.03	0.02	0.18	0.17	0.05
MgO	0.01	FB1/XRF	1.09	1.11	0.86	0.79	7.98	7.82	3.72
CaO	0.01	FB1/XRF	3.32	2.91	4.38	2.98	9	8.08	7.51
Na ₂ O	0.01	FB1/XRF	5.52	6.14	5.51	5.51	0.51	0.49	5.55
K ₂ O	0.01	FB1/XRF	2.02	1.88	1.49	2.02	4.21	4.7	0.68
P ₂ O ₅	0.002	FB1/XRF	0.129	0.126	0.12	0.13	0.17	0.184	0.348
Total	0.01	FB1/XRF	99.66	99.95	99.27	99.91	99.6	99.3	99.37
LOI	0.01	/TGA	2.28	2.02	3.68	2.62	8.75	7.44	6.01
Trace elements (ppm)									
Au	0.01	FA25/AA	0.02	0.02	0.04	1.45	b.d.l.	0.05	0.06
Cr	20	FB6/OE	26	24	23.00	22.00	639	694	24
Co	0.1	4A/MS	5.4	3.7	3.40	4.00	12.9	9.6	27.9
Ni	0.5	4A/OE	15.1	11.6	10.00	10.50	69.2	57.2	17
Cu	0.5	4A/OE	2.9	2.7	18.80	5.20	b.d.l.	1.2	20
Rb	0.1	FB6/MS	49.6	46.2	38.80	50.40	164.8	177.7	12.7
Ba	0.5	FB6/MS	927.7	807.5	1038.60	1676.80	941.7	1138.1	236.2
Th	0.05	FB6/MS	4.93	5.04	4.50	5.20	1.95	2.08	2.59
U	0.05	FB6/MS	2.28	2.4	2.50	1.90	2.04	1.37	2.67
Nb	0.1	FB6/MS	7	7	7.20	7.40	3.8	5.4	12
Ta	0.1	FB6/MS	0.7	0.5	0.60	0.60	0.5	0.3	0.9
La	0.2	FB6/MS	26.1	17.5	19.40	15.50	3.5	8.9	30.5
Ce	0.5	FB6/MS	54.8	41.8	44.10	38.50	7.8	19.4	69.3
Pb	0.5	4A/MS	4.5	3.8	2.80	3.10	3.4	1.1	15.2
Pr	0.05	FB6/MS	6.49	5.17	5.80	5.20	1.03	2.44	8.67
Sr	0.2	FB6/MS	509.8	475.5	304.80	265.60	190.5	340.5	298.5
Nd	0.1	FB6/MS	23.8	22.3	25.00	25.70	4.4	11	33.3
Zr	1	FB6/MS	132	128	126.00	138.00	91	96	171
Hf	0.1	FB6/MS	3.4	3.4	3.40	3.60	2.3	2.5	4.8
Sm	0.05	FB6/MS	4	3.49	4.10	4.00	1.27	2.14	6.23
Eu	0.05	FB6/MS	1.06	0.94	1.00	1.00	0.51	0.81	1.77
Gd	0.05	FB6/MS	2.86	2.88	3.10	2.70	1.92	2.47	5.42
Tb	0.02	FB6/MS	0.36	0.35	0.40	0.30	0.32	0.35	0.75
Dy	0.05	FB6/MS	1.67	1.82	1.70	1.60	2.16	2.31	4.31
Y	0.5	FB6/MS	9.4	9.1	8.10	7.40	14.2	12.7	22.1
Ho	0.02	FB6/MS	0.32	0.32	0.30	0.30	0.47	0.44	0.83
Er	0.05	FB6/MS	0.84	0.87	0.80	0.80	1.4	1.5	2.47
Tm	0.05	FB6/MS	0.16	0.18	0.10	0.10	0.22	0.23	0.34
Yb	0.05	FB6/MS	0.75	0.76	0.90	0.70	1.34	1.39	2.45
Lu	0.02	FB6/MS	0.13	0.1	0.10	0.10	0.2	0.22	0.36
Ag	0.05	4A/MS	0.09	0.06	0.12	0.19	0.07	b.d.l.	0.97
As	0.5	4A/MS	9.6	12.2	5.40	4.80	8.5	8.1	337.5
Bi	0.01	4A/MS	0.07	0.05	0.09	0.20	0.03	0.02	0.35
Cs	0.05	FB6/MS	1.61	0.89	0.80	1.10	5.94	6.45	0.89
Ga	0.1	FB6/MS	26.7	19.1	20.00	21.60	21.4	15.4	26.4
Mo	0.1	4A/MS	0.9	7.6	5.60	1.90	1	0.5	1.2
Sn	1	FB6/MS	1	1	0.50	0.50	1	1	1
V	10	FB6/OE	46	53	38.00	40.00	142	160	189
W	1	FB6/MS	3	3	4.00	6.00	b.d.l.	1	3
Zn	1	4A/OE	25	14	9.00	10.00	104	80	85
Calculated ratios									
Eu/Eu*			0.96	0.91	0.86	0.93	1	1.08	0.93
(La/Yb)N			23.46	15.52	14.53	14.93	1.76	4.32	8.39
ΣREE			116.85	93.31	101.00	91.30	25.51	51.16	158.03
Dy/Yb			2.23	2.39	1.89	2.29	1.61	1.66	1.76

Sensitive high resolution ion microprobe (SHRIMP) analytical results for the Alamoutto quartz-feldspar-porphyry

Spot ID	Ppm U	Ppm Th	232Th /238U	4-corr %com 204Pb 206	204Pb corrected				204Pb corrected				1σ error of mean corrected				
					Total		%	4-corr % 238 err	4-corr % 207* err		4-corr % 206* err		4-corr % 238 err		4-corr % 207* err		
					238	Dis- corr- dant	207	% /206	207*	% /206*	206*	% /206*	238	Dis- corr- dant	207*	% /206*	
Group I zircons (n=4)																	
AL047-13	121.37	77.41	0.66	0.11	2122.49	13.30	1.48	2.60	1.31	0.13	0.68	2.60	1.31	0.38	1.34	0.38	
118.86	67.01	0.58	0.19	0.31	2169.98	16.54	0.92	2.66	1.32	0.13	0.66	2.78	1.23	0.23	1.27	0.85	
AL047-24	199.99	34.87	0.18	-0.01	2075.68	8.61	1.15	2.66	1.05	0.13	0.48	2.66	1.05	0.13	1.09	0.91	
AL047-12	186.23	87.73	0.49	0.05	2135.48	9.90	6.10	2.71	1.11	0.13	0.53	2.71	1.11	0.13	1.29	0.37	
AL047-71	46.99	0.53	0.08	2144.98	14.17	0.43	2.54	1.41	0.13	0.75	2.54	1.41	0.13	0.87	2.24	0.65	
Group II zircons (n=11)																	
AL047_4	313.18	69.20	0.23	0.13	2064.90	8.28	3.41	2.74	0.97	0.13	0.41	2.74	0.97	0.13	0.56	6.42	1.12
93.70	33.02	0.36	0.31	2069.98	16.54	0.92	2.66	1.32	0.13	0.71	2.67	1.33	0.13	0.82	6.62	1.65	
AL047-27	199.99	34.87	0.18	-0.01	2075.68	8.61	1.15	2.66	1.05	0.13	0.48	2.66	1.05	0.13	1.09	0.91	
46.56	0.15	-0.01	2077.39	7.16	3.39	2.72	0.96	0.13	0.40	2.72	0.96	0.13	0.41	6.51	1.09	0.37	
555.20	132.01	0.25	0.03	2081.42	6.21	-0.70	2.61	0.87	0.13	0.34	2.61	0.87	0.13	0.47	6.81	0.99	
195.76	175.40	0.93	0.06	2083.34	9.82	0.67	2.64	1.14	0.13	0.52	2.64	1.14	0.13	0.64	6.74	1.30	
167.87	76.29	0.47	-0.05	2099.14	9.20	-1.84	2.56	6.54	0.13	0.50	2.56	6.54	0.13	0.56	6.97	0.57	
192.15	78.12	0.42	0.29	2095.44	12.72	9.36	2.86	1.11	0.13	0.56	2.87	1.11	0.13	0.79	6.23	1.36	
382.31	90.20	0.24	0.33	2096.21	9.46	3.67	2.69	3.83	0.13	0.37	2.70	3.83	0.13	0.62	6.63	3.88	
281.08	70.72	0.26	0.88	2096.48	14.04	6.93	2.77	1.00	0.14	0.42	2.80	1.00	0.13	0.86	6.41	1.32	
239.82	91.90	0.40	0.13	2096.99	8.42	-0.80	2.58	1.06	0.13	0.42	2.58	1.07	0.13	0.48	6.94	1.17	
Rejected analyses																	
AL047-26	302.34	54.25	0.19	0.08	2046.93	88.04	9.23	2.95	0.96	0.13	4.95	2.95	0.96	0.13	4.98	5.91	
107.92	52.93	0.51	0.24	0.24	2113.27	15.50	11.09	2.89	1.31	0.13	0.71	2.90	1.31	0.13	0.83	6.24	
AL047-17	241.32	111.88	0.48	0.30	2076.00	11.70	11.57	2.97	1.04	0.13	0.50	2.98	1.04	0.13	0.84	5.95	
164.94	95.75	0.60	0.09	2104.05	10.92	12.32	2.95	1.29	0.13	0.57	2.96	1.29	0.13	0.90	6.09		
266.44	35.25	2.14	0.29	2097.06	127.38	-0.86	2.52	4.99	0.15	0.73	2.58	5.10	0.13	0.52	5.11		
222.91	0.82	1.69	2000.49	20.18	-4.67	2.58	12.42	0.14	10.25	2.63	12.42	0.12	11.72	12.43	0.73		
340.07	92.81	0.28	0.24	2082.00	8.89	13.49	3.02	0.95	0.13	0.40	3.03	0.95	0.13	0.59	5.86		
128.41	48.94	0.39	0.16	2088.55	14.25	13.88	3.03	1.21	0.13	0.69	3.03	1.21	0.13	0.87	5.87		
270.54	92.94	0.35	0.22	2068.63	9.36	15.68	3.13	0.99	0.13	0.43	3.13	0.99	0.13	0.88	5.86		
206.45	147.98	0.74	0.37	2160.18	12.76	20.80	3.16	1.06	0.14	0.50	3.17	1.06	0.13	0.82	5.87		
105.21	0.61	2149.19	13.77	24.94	3.35	1.04	0.14	0.48	3.37	1.04	0.13	0.79	5.48	1.34			
343.70	78.46	0.24	1.07	2070.07	14.16	27.81	3.62	0.99	0.14	0.40	3.66	1.00	0.13	0.86	4.82		
420.77	112.31	0.28	2.16	2118.26	191.09	28.83	3.53	9.34	0.15	9.28	3.61	9.34	0.13	9.35	9.35		
127.26	73.48	0.60	0.71	2117.45	21.14	29.04	3.60	1.23	0.14	0.73	3.62	1.23	0.13	1.25	1.27		
264.55	117.73	0.46	1.09	2135.55	116.93	32.79	3.75	1.00	0.14	6.12	3.79	1.01	0.15	6.69	4.83		
383.31	97.87	0.26	1.42	1982.20	133.60	40.57	4.61	12.24	0.13	6.66	4.67	12.24	0.12	7.51	7.59		
805.75	1.05	0.91	1955.49	54.67	43.38	4.94	0.88	0.13	2.80	4.98	0.89	0.12	3.19	0.80			
346.16	275.36	0.82	0.35	2071.61	11.89	46.53	4.92	0.93	0.13	5.0	4.93	0.93	0.13	5.58	1.19		
540.80	172.71	0.33	1.67	1944.20	20.64	56.12	6.37	0.89	0.13	4.67	6.47	0.90	0.12	1.20	2.54		
419.40	333.13	0.82	0.68	2033.29	36.87	56.73	6.19	0.91	0.13	1.86	6.23	0.91	0.10	6.77	1.11		
555.59	142.55	0.27	1.57	2051.35	73.82	57.31	6.15	0.88	0.14	0.41	6.25	1.07	0.12	6.25	1.11		
1141.14	401.72	0.36	3.38	1495.17	33.56	70.57	12.58	0.81	0.12	0.42	13.02	0.83	0.09	1.77	0.98		

Representative electron probe micro-analyses of pyroxene in endoskarn																	
SiO ₂ (wt%)	52.30	53.14	52.36	52.13	52.94	53.08	53.32	52.37	53.21	52.00	52.30	52.61	52.33	52.91	52.21	51.94	52.61
TiO ₂	0.04	0.02	0.08	0.05	0.00	b.d.l.	b.d.l.	b.d.l.	0.03	0.03	b.d.l.	b.d.l.	0.01	b.d.l.	0.01	b.d.l.	b.d.l.
Al ₂ O ₃	0.51	0.63	1.00	1.18	0.66	0.38	0.44	0.43	0.48	0.43	0.36	0.55	0.39	0.61	0.38	0.53	0.52
Cr ₂ O ₃	0.05	b.d.l.	0.01	0.05	b.d.l.	0.04	0.03	b.d.l.	0.02	b.d.l.	0.01	0.04	0.01	0.04	0.02	0.01	b.d.l.
FeO	15.26	14.99	15.90	15.45	15.05	13.86	13.74	14.95	15.14	14.56	14.63	15.09	13.89	15.06	14.28	14.82	15.32
MnO	0.29	0.32	0.27	0.30	0.28	0.31	0.36	0.31	0.31	0.30	0.33	0.29	0.30	0.30	0.28	0.30	0.33
MgO	8.85	9.02	8.06	8.29	8.72	9.49	9.67	8.90	8.90	9.14	9.11	9.06	9.56	8.93	9.41	9.22	8.81
CaO	22.31	21.49	21.69	21.58	22.05	22.77	22.80	22.56	22.23	22.64	22.67	22.62	22.85	22.41	22.71	22.49	22.62
K ₂ O	0.00	b.d.l.	0.00	b.d.l.	0.00	0.00	0.00	0.01	0.00	0.00	0.00	0.00	b.d.l.	0.00	0.00	0.00	0.00
Total	99.63	99.60	99.38	99.01	99.72	99.91	100.31	99.58	100.33	99.11	99.41	100.26	99.65	99.69	100.00	99.57	99.42
Si (atom units)	2.03	2.06	2.05	2.04	2.05	2.04	2.04	2.05	2.05	2.05	2.02	2.03	2.03	2.03	2.04	2.02	2.03
Ti	0.00	0.00	0.00	0.00	0.00	0.00	0.00	0.00	0.00	0.00	0.00	0.00	0.00	0.00	0.00	0.00	0.00
Al	0.02	0.03	0.05	0.05	0.03	0.02	0.02	0.02	0.02	0.02	0.02	0.02	0.02	0.03	0.02	0.02	0.02
Fe _{>3}	0.00	0.00	0.00	0.00	0.00	0.00	0.00	0.00	0.00	0.00	0.00	0.00	0.00	0.00	0.00	0.00	0.00
Cr _{>3}	0.00	0.00	0.00	0.00	0.00	0.00	0.00	0.00	0.00	0.00	0.00	0.00	0.00	0.00	0.00	0.00	0.00
Fe _{<2}	0.50	0.49	0.52	0.51	0.49	0.45	0.44	0.44	0.48	0.49	0.47	0.47	0.49	0.45	0.49	0.46	0.48
Mn	0.01	0.01	0.01	0.01	0.01	0.01	0.01	0.01	0.01	0.01	0.01	0.01	0.01	0.01	0.01	0.01	0.01
Mg	0.51	0.52	0.47	0.48	0.50	0.54	0.55	0.51	0.51	0.53	0.55	0.52	0.55	0.54	0.53	0.51	0.52
Ca	0.93	0.89	0.91	0.90	0.92	0.94	0.94	0.93	0.92	0.94	0.93	0.94	0.93	0.94	0.93	0.93	0.94
K	0.00	0.00	0.00	0.00	0.00	0.00	0.00	0.00	0.00	0.00	0.00	0.00	0.00	0.00	0.00	0.00	0.00
Pyroxene end members																	
MgCa ₂ O ₆	50.35	51.22	47.01	48.45	50.31	54.46	55.09	50.88	50.66	52.29	52.04	51.21	54.56	50.89	53.53	52.08	52.34
FeCaSi ₂ O ₆	48.71	47.75	52.03	50.65	48.71	44.62	43.91	47.95	48.34	46.73	46.89	47.85	44.47	48.14	45.57	46.96	48.85
MnCaSi ₂ O ₆	0.94	1.03	0.96	0.90	0.98	0.91	1.00	1.17	1.00	0.98	1.07	0.93	0.97	0.97	0.90	0.96	1.07

Chapter IV. The Yatela gold deposit in Mali, West Africa: the final product of a long-lived history of hydrothermal alteration and weathering.

Quentin Masurel^{a*}, John Miller^a, Kim A.A. Hein^b, Eric Hanssen^c, Nicolas Thébaud^a, Stanislav Ulrich^d, Jean Kaisin^e, Samuel Tessougue^f

^aCentre for Exploration Targeting, The University of Western Australia, 35 Stirling Highway, Crawley, WA, Australia.

*Corresponding author, Ph: +61864885809, E-mail: qmasurel@hotmail.com

^bUniversity of the Witwatersrand, Johannesburg, South Africa.

^cLegend Gold Corporation, Vancouver, British Columbia.

^dAngloGold Ashanti Australia Limited, Perth, WA.

^eSociété Minière de la Vallée du Fleuve Sénégal.

^fSociété des Mines d'Or du Mali, Sadiola-Yatela gold mines.

Keywords: Kédougou-Kénieba inlier, Yatela, carbonate-hosted gold, auriferous residuum

1. Abstract

The Yatela gold deposit is located in the Kédougou-Kénieba inlier (KKI), a window of ca. 2200-2050 Ma rocks that are exposed in eastern Senegal and western Mali. The geology of the KKI differs from other Paleoproterozoic granite-greenstone belts and sedimentary basins by the abundance of carbonate rocks. The Yatela deposit occurs within 8 km of the regional-scale Senegal-Mali Shear Zone. Country rocks in the Yatela region have been subjected to polycyclic deformation and regional greenschist-facies metamorphism. A syn-kinematic diorite stock has intruded the metasedimentary sequences in the open pit and is associated with a hornblende-hornfels contact aureole. Field relationships and micro-textural data indicate that the primary gold mineralisation is shear-hosted. The similar relative timing and structural setting between the Yatela primary gold mineralisation and other world-class deposits in the region (e.g., Loulo, Lawrence et al., 2013a; Massawa, Treloar et al., 2014; Sadiola Hill, Masurel et al., in

press) suggest that regional orogenic gold mineralisation occurred during a period of transcurrent tectonics, after the cessation of regional compressional deformation. The primary gold mineralisation at Yatela, however, is low-grade and sub-economic. It is hosted by marbles and, to a lesser extent, diorite. The primary ore is pyrite-rich, with abundant chalcopyrite, minor arsenopyrite and accessory Zn-Pb-Sb-Fe-Ag-Co-Ni-bearing mineral species. Post-Birimian surficial dissolution of hydrothermally altered and mineralised host marbles resulted in the creation of troughs, which were draped and infilled with a ferruginous dissolution residue enriched in gold. This auriferous residuum formed the economic resource mined at Yatela until decommissioning in 2013. The Yatela gold deposit is unique with respect to mineralisation types encountered in West Africa because an auriferous residuum of economic interest (>1 Moz) derives from an underlying sub-economic Birimian occurrence. This study provides a new appreciation for the economic interest of Yatela-style orebodies and their prospectivity in other gold provinces of the West African Craton where carbonates are present, such as in the Siguiri basin in Guinea and the Ity region in western Côte d'Ivoire.

2. Introduction

The KKI is the westernmost exposure (~22000 km²) of Paleoproterozoic crust in the West African Craton. It hosts a number of world-class mining districts, which include Loulo-Gounkoto (~14 Moz), Sadiola-Yatela (~10 Moz) and Sabodala-Massawa (~8 Moz). Gold deposits occur in a wide range of host rocks that include mafic volcanics, detrital sedimentary rocks and carbonates, and share a similar structural setting and relative timing to other world-class orogenic gold systems in the West African Craton (e.g., Ashanti, Morila) (Oberthür et al., 1998; Allibone et al., 2002a, b; Feybesse et al., 2006; McFarlane et al., 2011; Lawrence et al., 2013a, b; Treloar et al., 2014; Masurel et al., in press). The Yatela gold deposit, however, is unique in the KKI and, to a larger extent, in the West African Craton because the gold resource is hosted in an auriferous residuum derived from an underlying sub-economic Birimian occurrence (Hanssen et al., 2004). The gold-enriched dissolution residue lined the bottom of deep troughs developed over the carbonates and formed the economic resource until the mine

was decommissioned. A recent study by Hein et al. (in press) examined the geological history of the auriferous residuum through mineralogical, textural and geochronological investigations, and suggested that: 1) the auriferous residuum consists of a mixture of underlying insoluble bedrock fragments (e.g., metagreywacke, marble, metadiorite), blocks and pebbles of Neoproterozoic sandstone, and quartz fragments and pebbles, which are set into a brown-red sandy matrix; 2) the maximum deposition age for the auriferous residuum is constrained in the Neoproterozoic, or during early deposition of the Taoudeni sandstone; 3) the formation of the residuum likely involved a local source that included recycled material based on gold grain morphology and detrital zircon ages; and 4) the creation of a deep weathering profile and supergene enrichment of the auriferous residuum may have taken place during the mid-Cretaceous to early Tertiary. In this study, we summarise the geology, tectonic setting, hydrothermal alteration, and ore mineralogy of the primary gold mineralisation at Yatela with the objective of defining its link to the auriferous residuum, and thus form the basis of an ore genetic model for the deposit.

3. Background

3.1. Regional geology

The geology of the KKI consists of linear volcano-plutonic belts and sedimentary basins, which are separated by the Main Transcurrent Zone (MTZ, Ledru et al., 1991) and the Senegal-Mali Shear Zone (SMSZ, Bassot and Dommange, 1986) (Fig. 1). It differs from other Paleoproterozoic terranes by the abundance of carbonates, with thick sequences (>250 m) in the Dialé-Daléma and Kofi Series representing the most extensive carbonate exposure in the Birimian of West Africa (Fig. 1) (Bosse et al., 1996; Bering et al., 1998). Rocks of the Dialé-Daléma Series (Fig. 1) include volcaniclastics, arenites, wackes, siltstones, argillites, and carbonates with minor intercalations of andesite lavas and rhyolite pyroclastites (Bassot, 1987; Dia, 1988; Hirades and Davis, 2002). Wackes and immature sediments are more widespread towards the margins of the basin (Hirades et al., 2002). Rocks of the Kofi Series (Fig. 1) consist of volcaniclastics, arenites, wackes, carbonates, siltstones, and argillites

(Lawrence et al., 2013a; Masurel et al., in press). The Dialé-Daléma and Kofi have been interpreted to represent syn-deformational foreland basins (e.g., Hirdes and Davis, 2002; Gueye et al., 2008). Four deformation episodes have been identified in the KKI and include early thrusting events associated with crustal thickening (D_1 - D_2), followed by two transcurrent events (D_3 - D_4) accomodating oblique convergence (Ledru et al., 1991; Milési et al., 1992; Dabo and Aïfa, 2010, 2011; Diene et al., 2012). Little is known about the earliest event (D_1) due to pervasive reworking by subsequent deformation. The D_2 and D_3 events mark the principal imprint of the Eburnean orogeny (ca. 2115-2050 Ma) in the eastern part of the KKI and are undoubtedly responsible for the formation of map-scale structures (Lawrence et al., 2013a; Masurel et al., in press). The second event (D_2) is associated with the formation of the SMSZ as a sinistral transpressional fault under NW-SE directed shortening (Lawrence et al., 2013a). Hydrothermal fluid flow and regional orogenic gold mineralisation along the SMSZ (e.g, Loulo, Gounkoto, Sadiola Hill) (Fig. 1) occurred subsequently during the D_3 event, which marked a switch from a dominantly coaxial system to a non-coaxial deformation regime (Lawrence et al., 2013a; Masurel et al., in press). The last deformation event (D_4) has been locally reported in the Loulo deposit area and is correlated with the dextral reactivation of the earlier accretionary structures. Available metamorphic data indicate regional peak metamorphic conditions reached greenschist-facies (e.g., Dia et al., 1997; Hirdes and Davis, 2002; Gueye et al., 2008) with local hornblende-hornfels contact aureoles surrounding Eburnean granitoids (Debat et al., 1984; Pawlig et al., 2006; Masurel et al., in press).

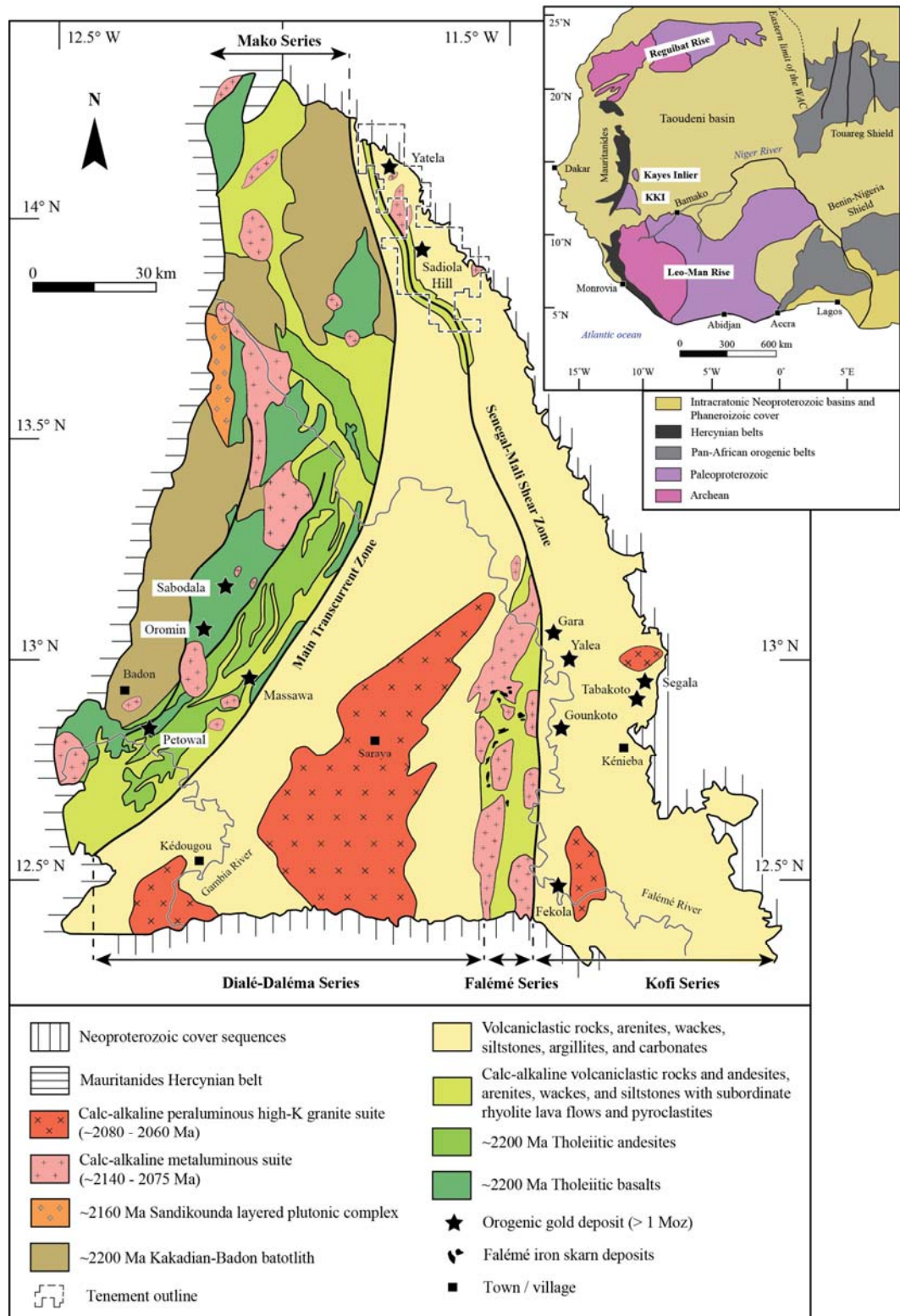


Figure 1. Geologic map of the Birimian Kédougou-Kéniéba Inlier (1:250,000 scale, modified after Gueye et al., 2007; Lawrence et al., 2013a). Geochronological constraints after Dia, 1988; Calvez et al., 1990; Dia et al., 1997; Hirdes and Davis, 2002; Gueye et al., 2007). Inset map shows the geologic setting of the West African Craton (modified after Boher et al., 1992). The Falémé River forms the international border with Senegal to the west and Mali to the east and north.

3.2. Local geology

The geology of the Yatela deposit area is characteristic of the Kofi Series (e.g., Lawrence et al., 2013a) and consists of feldspathic wackes, arkosic arenites, and carbonates with subordinate rhyolite flows and pyroclastites to the west progressing to siltstones and argillites further east (Fig. 2). Chemical and detrital sedimentary rocks transition towards the west into a linear volcano-sedimentary belt that consists of calc-alkaline volcaniclastic rocks and porphyritic andesites with subordinate rhyolite flows and pyroclastites (Masurel et al., *in press*) (Fig. 2). The original lithostratigraphy has been complicated by folding and thrusting during the Eburnean orogeny. A number of syn-kinematic elliptic to oval-shaped plutons have intruded the volcano-sedimentary rocks in the Yatela deposit area. These intrusions have a calc-alkaline affinity and exhibit a differentiated trend from hornblende-monzo-diorite to biotite-granodiorite (Masurel et al., *in press*). Deformed Birimian rocks are unconformably overlain to the east by flat-lying Neoproterozoic cover sequences locally referred to as the Seroukoto sandstone (Fig. 2).

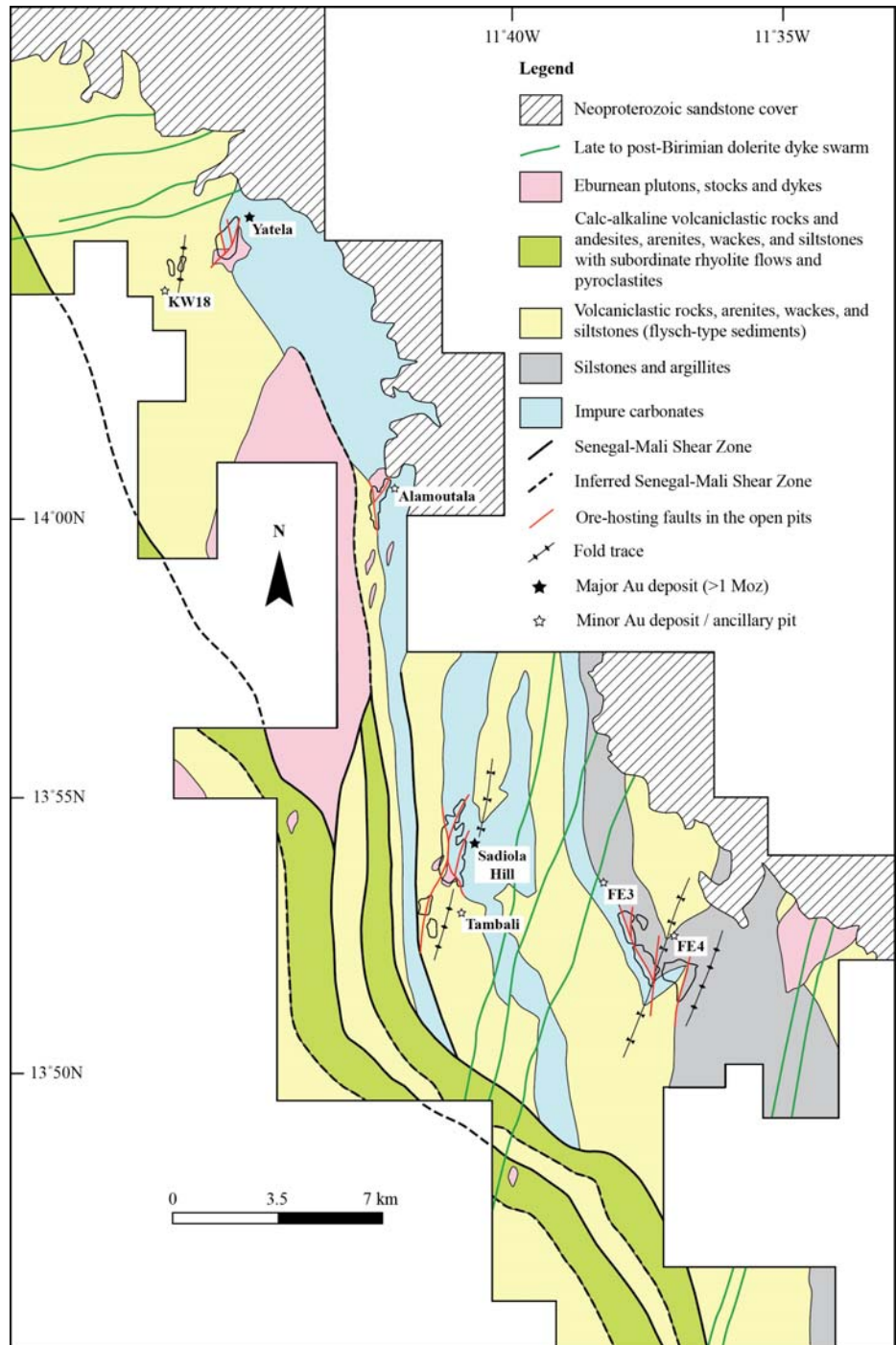


Figure 2. Geology of the Sadiola-Yatela mining and exploration permit based on SEMOS regional map (2014) and field investigation by the authors (scale 1:35,000).

3.3. The Yatela gold resource

The Yatela gold mine is located 25 km north of the world-class Sadiola Hill gold mine in southwest Mali (Fig. 2). Economic mineralisation at Yatela occurs in a saprolitic residuum that lines the bottom of deep troughs (max. depth of 220 m) developed over carbonate rocks (Hein et al., *in press*). The residuum consists of a mixture of underlying insoluble Paleoproterozoic bedrock fragments (e.g., metagreywacke, marble, metadiorite), blocks and pebbles of Neoproterozoic sandstone, quartz fragments and pebbles, and gossanous fragments derived from the primary hypogene mineralisation, which are set into a clay-rich ferruginous matrix (Hanssen et al., 2004). Recent research by Hein et al. (*in press*) presented evidence for two types of gold in the auriferous residuum. The bulk of the ore is associated with 40 to 450 µm long, irregular (e.g., dendritic to wire-like forms), angular gold grains. These grains occur in micro-fractures of angular quartz fragments and partly oxidised pyrite grains, suggesting a proximal source. A minor part of the ore is associated with 275 to 315 µm long, rounded detrital gold grains that exhibit abraded surfaces and Ag-depleted rims (gold fineness 981-1000), suggesting a more distal source. The mine production started in 2001 and as of 2010, the Yatela gold deposit (oxidised and partly oxidised orebody) had total mineral resources of 1.18 million tonnes at average grade of 2.56 g/t Au (public data from AngloGold Ashanti Ltd. mineral resource and ore reserve report 2010). The Yatela mining operations have been managed by the Société des Mines d'Or du Mali (SEMOS), a joint venture between AngloGold Ashanti Limited, IAMGold Corporation and the government of Mali. As of 2012 (near the end of mining of the oxidised and partly oxidised orebody), the primary gold mineralisation was evaluated to be sub-economic and the subsequent drop in the spot price of gold and the reduction of the profit margin led to the closure of the Yatela gold mine (IAMGold news release, September 2013).

4. Methodology

4.1. Pit mapping, drill core logging, sampling and 3D modelling

Systematic face mapping was conducted on all accessible ramps and benches of the Yatela open pit where fresh rocks are exposed. As of 2013, the main open pit is 1,300 m in length, 600 m wide and 220 m deep. Detailed logging was undertaken and included five diamond drill holes chosen to represent the main structural, lithological and mineralogical variations observed in the deposit. Petrographic data reported in this paper investigates primary mineralisation and therefore largely relies on deep diamond drill core samples. All structural readings are given in true north coordinates. Planar features are given in strike/dip/quadrant and linear data is given as plunge and azimuth. In this paper, the “y” subscript indicates that the considered structural event is only valid for the Yatela district, which may differ from regional structural compilations reported for the West African Craton. The trends of ore shoots were evaluated using Leapfrog® three-dimensional rendering of combined grade control and exploration drill hole assay data.

4.2. Petrography and mineral chemistry

Fifty samples were collected from diamond drill core and directly in the Yatela open pit. The considered suite of samples included representative examples of country rocks, alteration facies of varying intensities, and ore. Forty-five polished thin sections were prepared at the University of Western Australia (UWA) and at Vancouver Petrographics Ltd. These were studied using optical microscopy at the Centre for Exploration Targeting in Perth, and scanning electron microscopy at the Centre for Microscopy, Characterisation and Analysis at UWA. Backscattered electron (BSE) imaging and mineral chemistry analyses were obtained using a Tescan Vega3 XM (SEM) equipped with an Oxford instrument X-ACT energy dispersive detector (EDS) and a JEOL JXA-8530F Hyperprobe fitted with 5 wavelength-dispersive spectrometers (WDS). Quantitative microanalyses were performed using proprietary standards. The analytical software used to collect semi-quantitative microanalyses was the Oxford

Instruments® INCA analytical suite on Tescan Vega 3. Operating parameters for the SEM-EDS included an accelerating voltage of 20 kV, a working distance of 15 mm, a beam current of 1.5 nA and a detector process time of 4 s. Operating conditions for WDS analysis were an accelerating voltage of 15 kV, a beam current of 20 nA and a counting time of 20 s on peak for tourmalines. Mean atomic number background and ZAF (i.e. atomic number absorption fluorescence) corrections were performed using the Armstrong (1988) algorithm. Yatela open pit geology

4.3. Host rocks

The Yatela lithostratigraphy, as exposed in the open pit, consists of calcitic and dolomitic marbles overlain by detrital metasedimentary rocks (Fig. 3). Marbles are generally pure but a distinct lithofacies occurs locally and is characterised by thin (0.2 – 2 cm) argillaceous-silty horizons. Detrital metasedimentary rocks are exposed on the western pit walls and consist of alternating sequences of feldspathic wacke, arkosic arenite, siltstone, and shale. Well-preserved way-up indicators such as fining-upwards sequences in wackes and rare cross bedding in arenite indicate upright beds with a younging direction to the west. The marbles and detrital metasedimentary rocks have been intruded by a diorite stock in the south-eastern part of the pit (Fig. 3). The intrusive rock is dark greenish-grey and medium-grained in hand specimen. It has a phaneritic equigranular texture but is locally amphibole-phyric. Under the optical microscope, the least-altered rock specimens are largely composed of plagioclase feldspars (>80% modal vol.), which exhibit characteristic polysynthetic twinning (albite and rare pericline). Plagioclase feldspars are euhedral prismatic, fine-grained (<2mm in size) and are variably altered to carbonate, muscovite, clay and other very fine-grained products. Primary magmatic hornblende generally occurs as a minor phase (<10% modal vol.). Quartz is an accessory phase and occurs in interstitial space (<5% modal vol.). The emplacement of the Yatela diorite resulted in the development of a high temperature-low pressure hornblende-hornfels contact aureole. Marbles adjacent to the contact margin (0-20 m) exhibit porphyroblastic tremolite-actinolite and scapolites minerals.

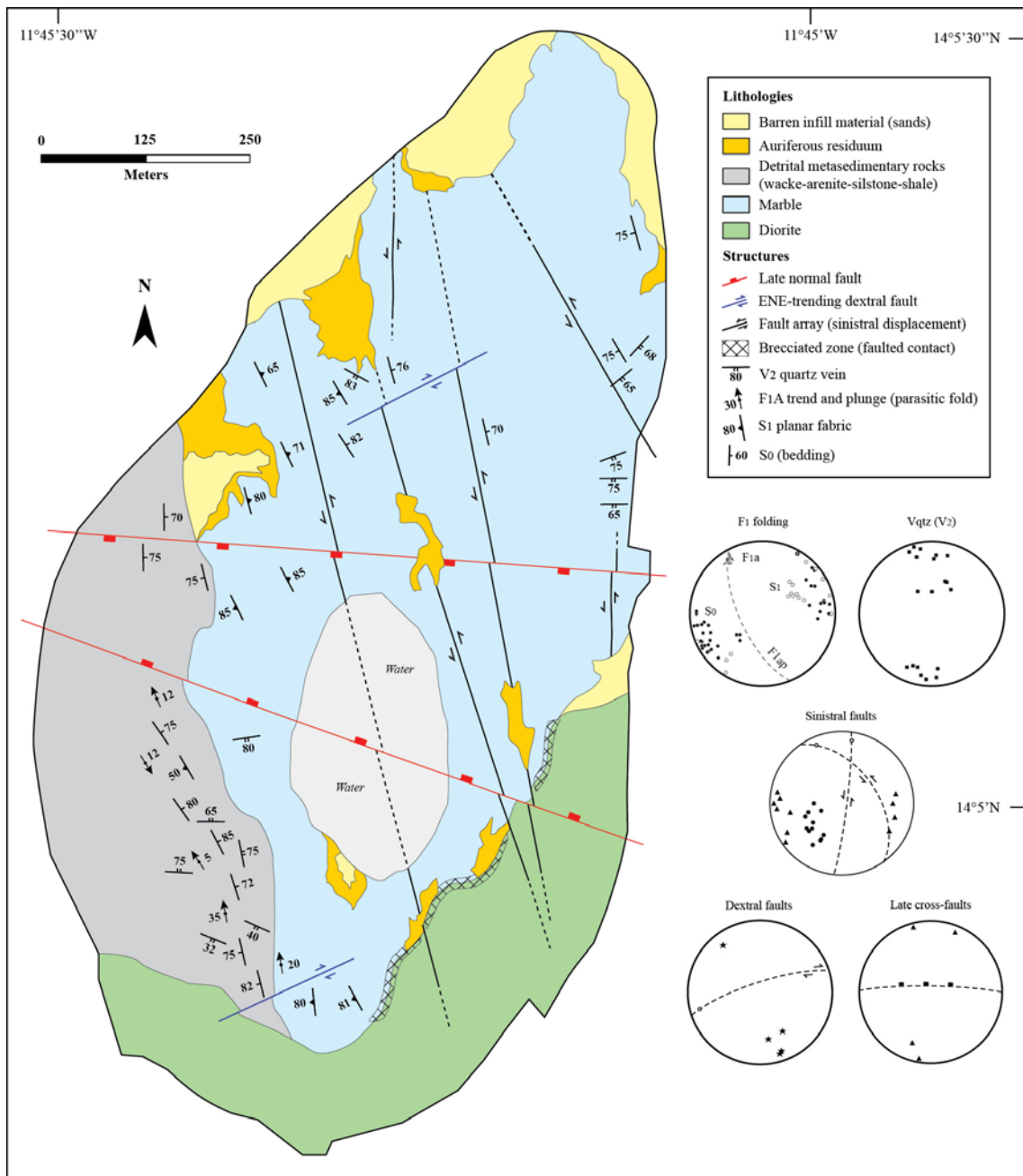


Figure 3. Geological map of the Yatela open pit. Structural data recorded during field mapping is presented as equal area stereonets using the lower hemisphere convention.

4.4. Structural framework

The earliest structural component consists of a strong NW-trending steeply west-dipping planar fabric (S_1), which sub-parallels the main orientation of bedding (S_0) in the open pit (Fig. 3, Fig. 4A). That planar fabric is ubiquitous in the detrital sedimentary rocks on the western pit walls. Numerous parasitic folds associated with that fabric have fold axes (F_1A) and intersection lineations (L_1) plunging gently to the NW. Barren quartz veins (V_1) are locally dismembered and boudinaged along S_1 (Fig. 4B). A second folding episode has been recorded in the two KW18 ancillary pits 1.5 km west of the Yatela deposit (see Fig. 2 for location) and is correlated with the formation of disharmonic, inclined to upright folds (F_2). Fold axes plunge gently (10-30°) to the NNE and are associated with 015°/80E axial-planar cleavage (S_2). Interference patterns associated with the refolding of the early folds (F_1) by the F_2 folds were observed locally. The Yatela diorite crosscut S_1 , however, the timing of its emplacement with respect to the development of S_2 remains unclear due to the absence of clear structural relationships. Numerous steep ENE-trending quartz veins (V_2) have been observed in the open pit (Fig. 3, Fig. 4C). These veins crosscut S_1 and S_2 , range from 5 cm to 30 cm in width, and host accessory pyrite. A number of NNW-trending (325°/50°NE) to NNE-trending (010°/85°E) to faults have been mapped throughout the open pit (Fig. 3, Fig. 4C-D). These faults are preferentially developed within marbles and diorite and crosscut all earlier structural elements including the S_1 and S_2 planar fabrics. Kinematic indicators such as slickenfibres on fault walls and V_2 quartz veins offset indicate sinistral displacement. A steep NNE-trending fault developed along the diorite-marble interface and is correlated with zones (up to 2-m-wide) of hydrothermal-tectonic breccias. This NNE-trending fault, however, displays no reliable kinematic indicators due to the extensive weathering of the rocks. The ENE-trending sub-vertical faults crosscut the NNW-trending fault array and are associated with chlorite slickenfibres indicating dextral displacement (Fig. 3, Fig. 4E). The latest structural component recognised in the field is associated with WNW-trending sub-vertical faults. Kinematic indicators such as drags on fault blocks indicate normal displacement (Fig. 3, 4F). These faults crosscut all Birimian host rocks and previously described structures. Some of these late WNW-trending faults exhibit fault breccia (2-5-cm-wide) filled with iron-

stained sandy material (Fig. 4G). Two of these faults bound the main karst cavity at the Yatela open pit.

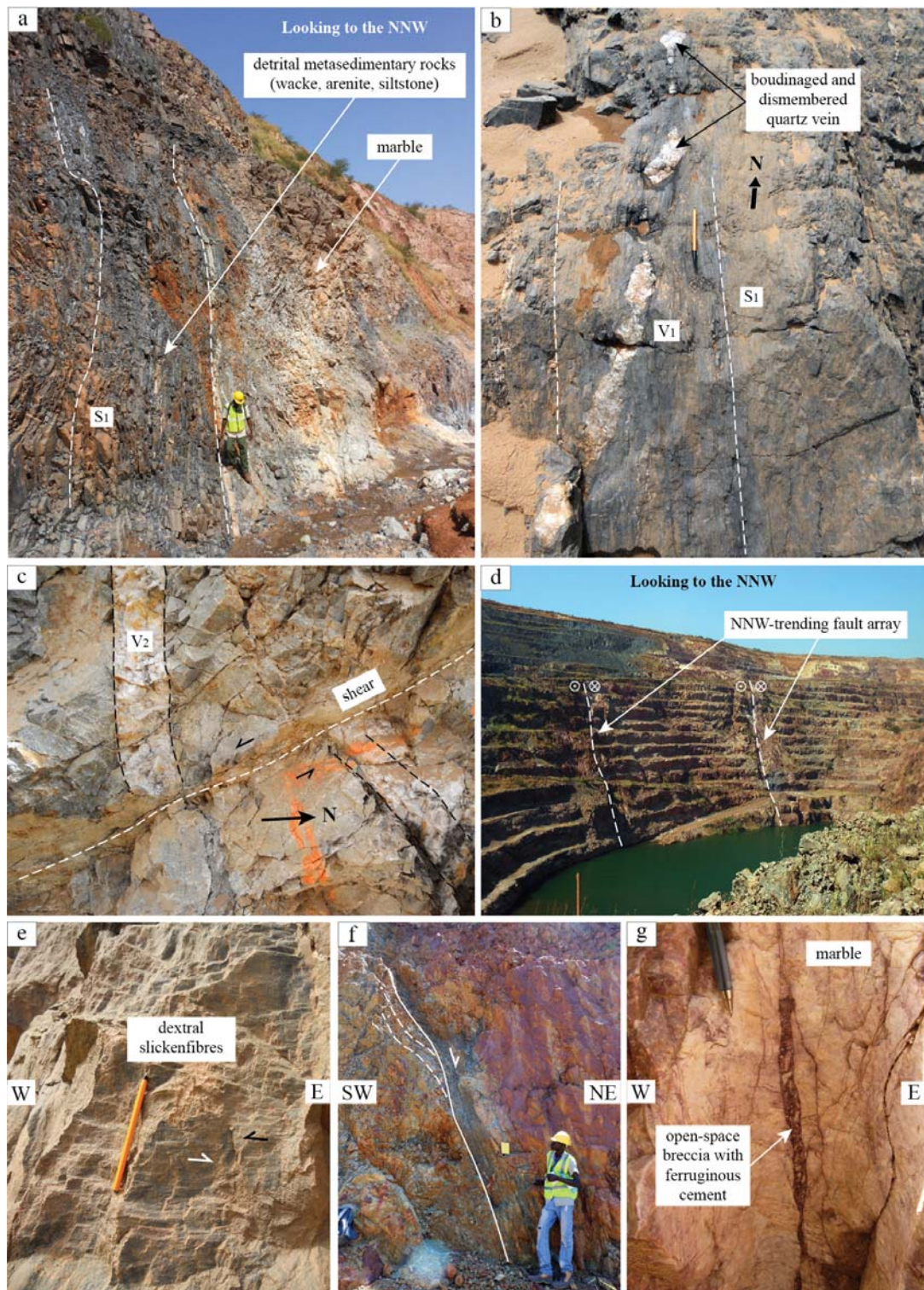


Figure 4. A) Field photograph illustrating the penetrative S_1 planar fabric recorded in metasedimentary rocks. Note the S-shaped asymmetry of the parasitic folds. B) Field photograph showing an early barren quartz vein (V_1) boudinaged and dismembered along S_1 in metasiltstones. C) Field photograph showing an ENE-trending steep quartz vein (V_2) cut and sinistrally offset by a steep NNW-trending fault. D) Panoramic view of Yatela open pit walls looking to the NNW. Note the deep weathering features along the steep NNW-trending fault array. E) Slickenfibres on a sub-vertical ENE-trending fault wall indicate dextral kinematics. Black arrow indicates displacement of the missing block. F) Typical view of a late brittle cross-fault associated with an inferred normal displacement. G) Close-up view of an open breccia associated with the late normal cross-faults.

4.5. Primary gold distribution

The bulk of the primary gold mineralisation occurs in two settings: (1) in the wall-rocks of the NNW-trending fault array and, (2) along the faulted contact between the diorite and marble (Fig. 5A-C). Geochemical and petrographic analysis of the V_1 and V_2 quartz veins indicates they are barren. Mineralised zones are associated with disseminated sulphides and pyrite stringers in wall-rocks, quartz-carbonate stockwork veins, and breccias. Ore minerals are quite diverse but their volumetric proportions are typically low in each rock type (ca. 0.5–3 % sulphides). Sulphide-rich zones in wall rocks and/or in vein are commonly associated with gold grades ranging from 1-2 g/t. The best-mineralised deep drill hole intersect observed was 9m @ 2.12 g/t (weighted average) and correlated with the faulted contact between diorite and marble. As an empirical observation, fabrics displaying a greater degree of deformation are linked to higher sulphide and gold abundance. Gold grades along the NNW-trending fault array tend to decrease with increasing distance away from the main intrusive stock – marble interface (Fig. 5A-C).

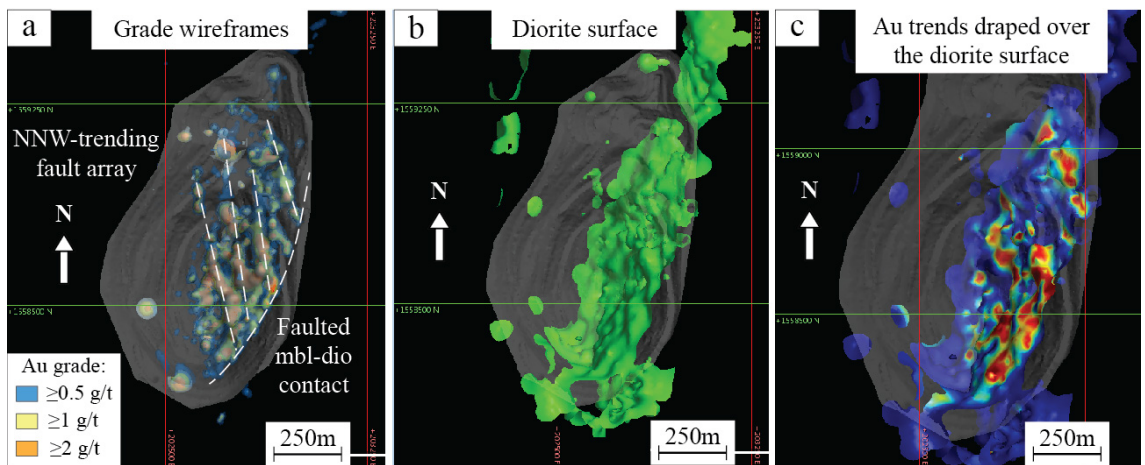


Figure 5. A) Leapfrog® scene illustrating the structural controls on ore shoot geometry. Assay values from combined grade control and exploration drill hole data. B) Wireframe of the diorite surface. C) The scene shows Au trends draped over the diorite surface.

4.6. Hydrothermal alteration

A summary of the ore and alteration paragenesis at Yatela is presented in Figure 6 and is explained in detail hereafter. A syn-tectonic hydrothermal alteration overprints early hornblende-hornfels contact-metamorphic assemblages in host rocks and is typically defined by Fe-dolomite + quartz + biotite \pm tourmaline, muscovite, albite, actinolite-tremolite. Pyrite and a wide range of accessory ore minerals are texturally associated with this hydrothermal alteration phase. Fault breccias in marble typically exhibit silicified angular clasts and pyrite stringers (Fig. 7A). Pyrite in these breccias is present in clasts and in the finer-grained comminuted matrix, suggesting a syn-tectonic timing of formation (Fig. 7B). Rare examples of stylolitic-shaped pyrite veinlets have been observed in drill core (Fig. 7C-D). Grey to milky white quartz-dolomite stockwork veins are common in diorite (Fig. 7E-F). These veins typically contain euhedral to subhedral pyrite crystals and are also associated with fine-grained pyrite disseminated in wall-rocks. Rare actinolite-tourmaline-pyrite veins are also recorded in diorite (Fig. 7G). Biotite typically marks the shear fabric in diorite and is closely associated with pyrite and traces of tourmaline (Fig. 7H). Tourmaline alteration is structurally-controlled and occurs in trace amounts (up to 2 % modal vol.) in vein and/or disseminated in wall-rocks and breccias. Representative electron probe micro-analyses of hydrothermal tourmalines are presented in Appendix A. Micro-analyses indicate that the tourmalines at Yatela belong to the alkali group and the schorl-dravite series, similar to those identified at the Sadiola Hill gold deposit and in the Loulo district (Fig. 8A-B). Syn-mineralisation stage tourmalines at Yatela also plot along the oxydravite-povondraite compositional trend (meta-evaporite tie line proposed by Henry et al., 2008) (Fig. 8B).

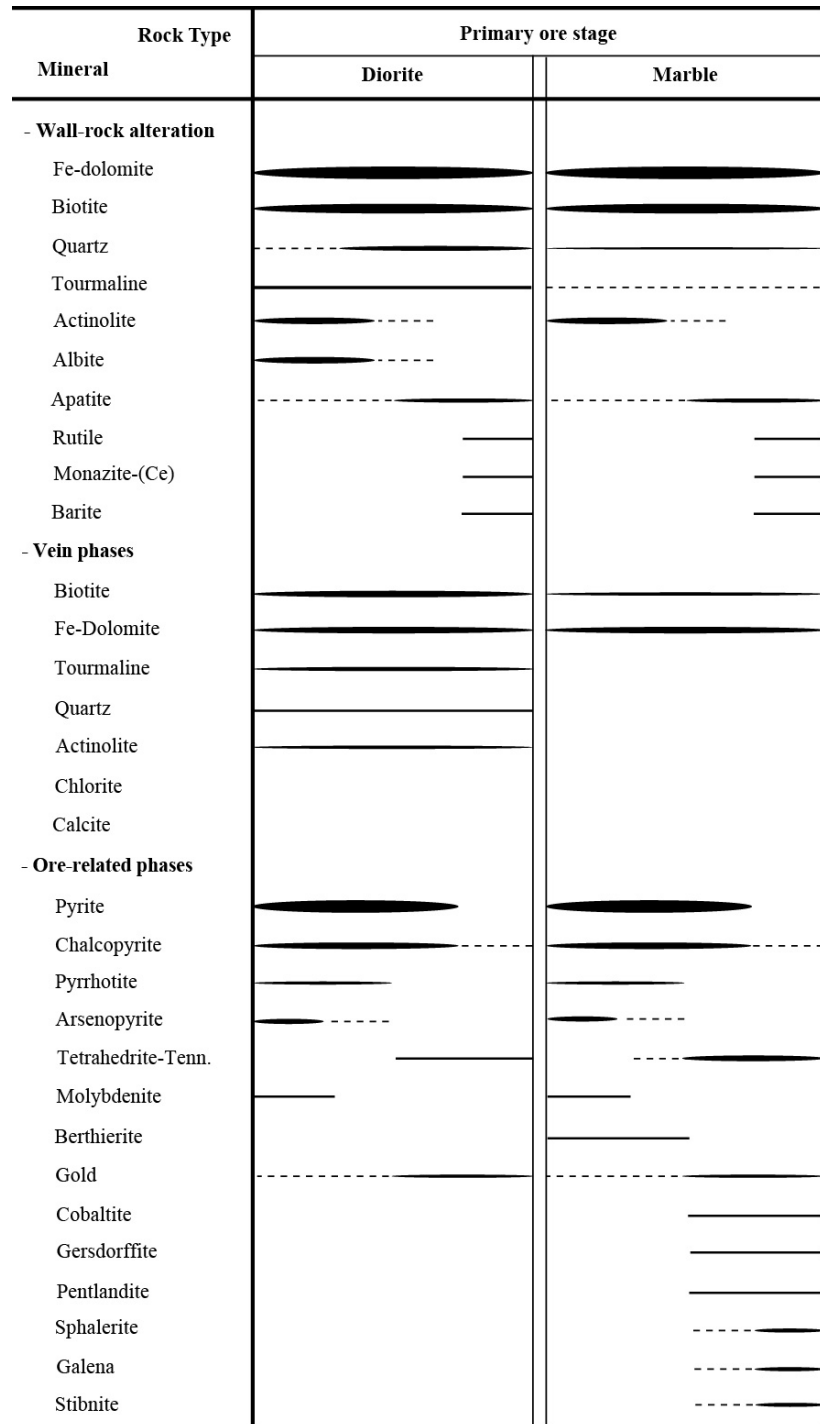


Figure 6. Ore and alteration paragenetic sequence chart for Yatela primary gold mineralisation. The ore-related phases correspond to both the veining style and disseminated style of mineralisation (both styles formed contemporaneously). Accessory mineral formulas: berthierite = FeSb_2S_4 ; tetrahedrite = $(\text{Cu},\text{Fe})_{12}\text{Sb}_4\text{S}_{13}$; tennantite = $(\text{Cu},\text{Fe})_{12}\text{As}_4\text{S}_{13}$; stibnite = Sb_2S_3 ; cobaltite = CoAsS ; pentlandite = $(\text{Fe},\text{Ni})_9\text{S}_8$; gersdorffite = NiAsS .

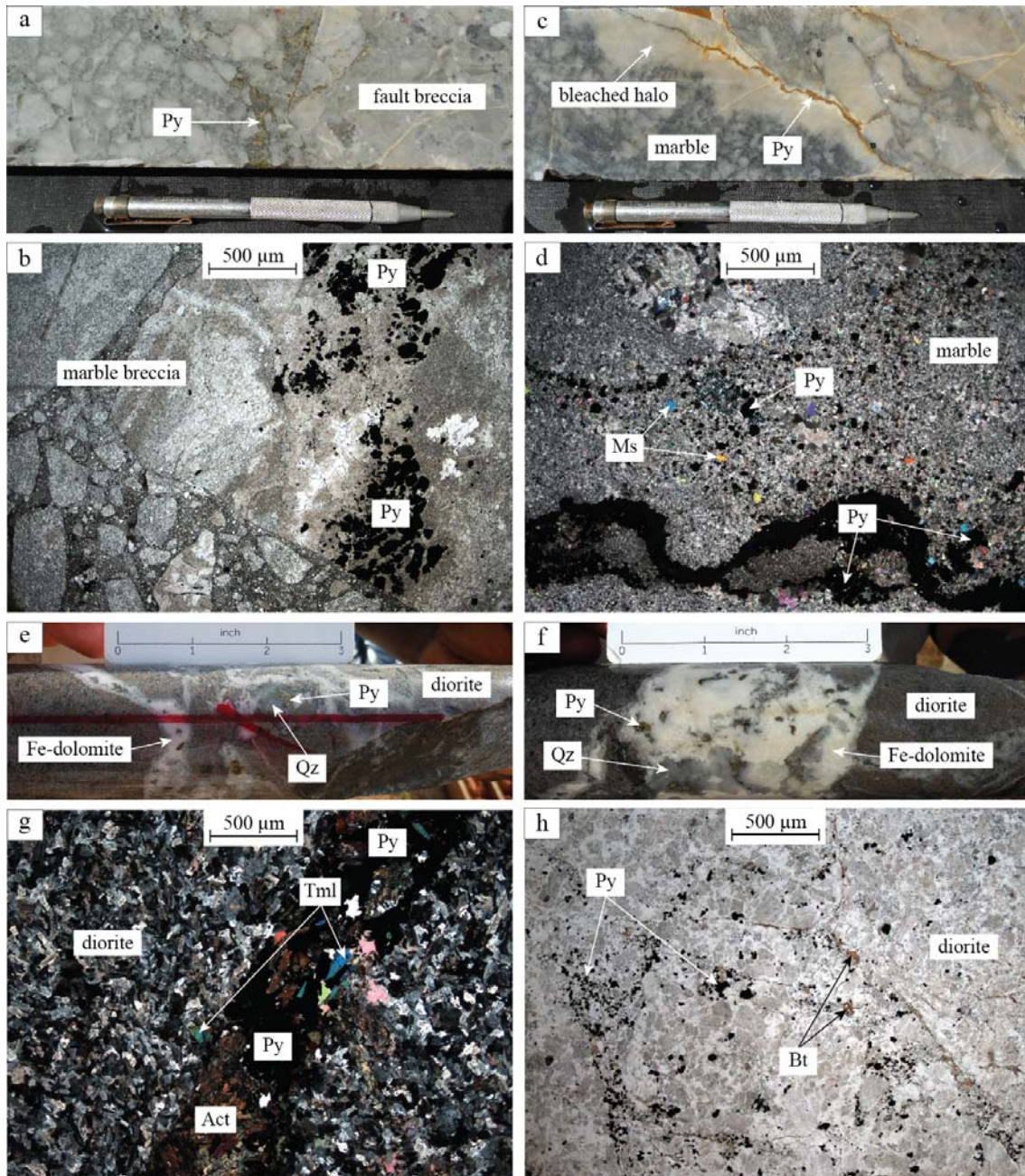


Figure 7. A) Faulted breccia after marble in drill core. B) Fault breccia after marble in thin section. Pyrite occurs in clasts and in the finer-grained comminuted matrix between angular clasts of silicified marble. C) Drill core photograph showing a sylolitic-shaped pyrite veinlet in marble. D) Representative micrograph of the stylolitic-shaped pyrite veinlet. Note the finer-grained pyrite disseminated in wall-rocks. E-F) White quartz-dolomite stockwork veins in diorite. These veins occur in wall-rocks along the fault arrays and typically contain euhedral to subhedral pyrite crystals. G) Representative micrograph of an actinolite-tourmaline-pyrite vein in diorite. H) Micrograph showing micro-fractures marked by biotite and pyrite in diorite.

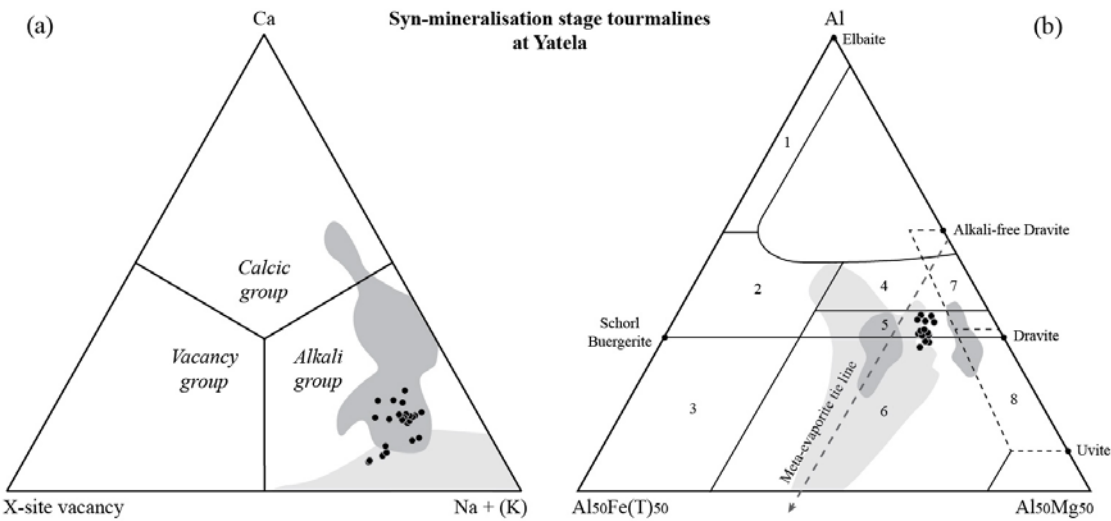


Figure 8. Representative chemical composition of Yatela syn-mineralisation stage hydrothermal tourmalines. Micro-analyses were undertaken using an electron probe and the stoichiometry was calculated using the Winclastour software (Yavuz et al., 2006). Ternary plots show the classification of hydrothermal tourmaline at Yatela. Light shaded areas show the composition of multistage hydrothermal tourmaline from the Loulo deposits (Yalea North, Gara, P-129, P-64 and Gounkoto; data from Lawrence et al., 2013a). Darker shaded areas show the composition of hydrothermal tourmaline from the Sadiola Hill deposit (data from Masurel et al., in press). A) Classification based on the X-site occupancy, using the Ca - X-site vacancy - Na + (K) diagram of Hawthorne and Henry (1999). B) Classification based on Y- and Z-site occupancy, using the Al-Fe-Mg ternary diagram of Henry and Guidotti (1985). Labelled fields: 1. Li-rich granitoid pegmatites and aplites. 2. Li-poor granitoids pegmatites and aplites. 3. Fe³⁺-rich quartz-tourmaline rocks (altered granitoids). 4. Metapelites and metapsammites with Al-saturating phase. 5. Metapelites and metapsammites lacking Al-saturating phase. 6. Fe³⁺-rich quartz-tourmaline rocks, calc-silicate rocks and metapelites. 7. Low Ca meta-ultramafic rocks and Cr-V-rich metasedimentary rocks. 8. Metacarbonates and metapyroxenites. Meta-evaporite tie line after Henry et al. (2008).

4.7. Primary ore mineralogy

The primary mineralisation is pyrite-rich, contains abundant chalcopyrite, minor arsenopyrite, and accessory Zn-Pb-Sb-Ag-Co-Ni-Fe-bearing mineral species. Pyrite is the dominant sulphide phase at Yatela and largely occurs in two forms that include single euhedral to subhedral crystals and crystal aggregates (Fig. 9A). Chalcopyrite and arsenopyrite are also common ore phases. Chalcopyrite occurs as subhedral crystals enclosed in pyrite, crystals intergrown with pyrite, interstitial space infill between pyrite crystals, infill of micro-fractures in pyrite, crystals mantling pyrite faces, and as overgrowths on pyrite (Fig. 9B). Arsenopyrite occurs as fine-grained acicular to prismatic crystals and aggregates, enclosed in pyrite, and intergrown with pyrite. Accessory pyrrhotite occurs as euhedral inclusion in pyrite and single crystals closely associated with pyrite-chalcopyrite. Traces of needle-shaped molybdenite and subhedral berthierite are present as fine-grained inclusions in pyrite and traces of subhedral sphalerite occur intergrown with tetrahedrite-tennantite minerals (Fig. 9C). Accessory galena occurs as infill in pyrite micro-fractures, rarely associated with tetrahedrite and chalcopyrite (Fig. 9D). Traces of stibnite are present as overgrowths on pyrite. Accessory cobaltite and pentlandite are also present in the ore; they were consistently deposited late in the paragenesis.

Native gold particles are present in the ore. Gold is associated with a low silver content (<10 wt. %) and deposited as (1) subhedral to anhedral inclusions and blebs (1-10 μm) within pyrite (Fig. 9E) (G-I); (2) individual particles (5-20 μm) located on pyrite crystal edges (G-II) (Fig. 9F); and rarely as (3) free disseminated anhedral gold particles (2-15 μm) closely associated with pyrite (G-III).

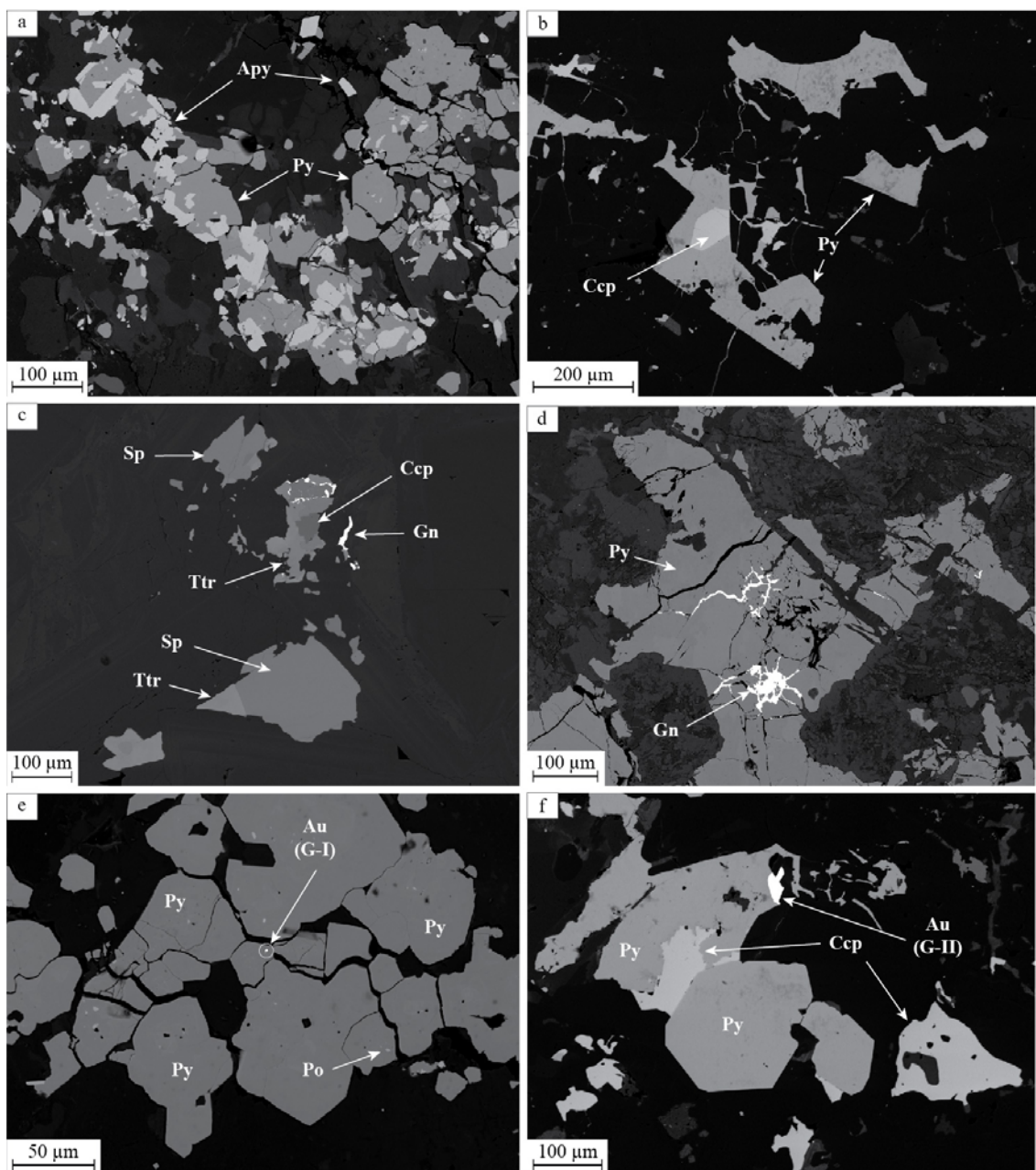


Figure 9. BSE images of ore-related phases at Yatela. A) Minor arsenopyrite is enclosed and/or mantled by pyrite. B) Chalcopyrite is enclosed by and intergrown with pyrite. C) Traces of base metal sulphides consistently occur late in the paragenesis. D) Galena occurring as infill in pyrite micro-fractures. E) Minute gold bleb (~2 μm) enclosed in pyrite (G-I). F) Gold particle (~20 μm) located on pyrite crystal edge (G-II).

4.8. Karst infill stratigraphy

Post-Birimian karstification and the development of a deep weathering profile have modified the original lithostratigraphy in the Yatela deposit area. The dominant geological feature at Yatela is the presence of a complex surficial karst topography characterised by coalescing troughs that are infilled by unconsolidated sandy material. The vertically-extensive trough in the southern part of the open pit is 220 m deep. Drilling and satellite pits targeting oxide ore have allowed this buried karstic topography to be traced northwards up to the Neoproterozoic sandstone escarpment where it thins out. The karst infill shows a simple stratigraphy as follows (Fig. 10): The basal layer of the karst cavity infill comprises the auriferous residuum (i.e. saprolite-hosted gold-enriched dissolution residue). It consists of a mixture of insoluble fragments of underlying bedrock, blocks and pebbles (approx. 1 cm to 20 cm) of saprock after the Seroukoto sandstone, quartz fragments and pebbles (approx. 2 mm up to 10 cm), residual dolomitic marble fragments, and gossanous fragments derived from the primary mineralisation, which are set into a clay-rich ferruginous matrix (Fig. 10, Fig. 11A-B).

The blocky sand unit overlies the residuum (Fig. 10, Fig. 11C-E). The contact between the residuum and the blocky sand unit occurs over less than a metre and is laterally irregular. The blocky sand unit consists of weathered angular blocks (up to several tens of metres wide) of the Seroukoto sandstone supported in a coarse-grained (approx. 0.5-2 mm), silica-rich, sandy matrix. Numerous 2-50-m-long sandstone blocks exposed on the pit walls dip at variable angles towards the depocentre. In some parts of the open pit, the blocky sand unit entirely consists of an accumulation of Seroukoto-derived sandstone blocks. The individual block surfaces locally exhibit slickenfibres suggestive of down-karst slumping and block rotation.

The blocky sand unit shares a gradational contact with a fine sand unit, which consists of fine-grained (approx. 125-250 µm), silica-rich, unconsolidated sands (Fig. 10, Fig. 11D). Bedding in the fine sand unit is defined by layers of transported laterite (i.e. duricrust and pisolithic gravel) of varying thickness (from a few 10's of cm to several metres) (Fig. 10, Fig. 11D). The transported laterite layers show relatively flat bedding at the top of the infill but gradually steepen with depth. This suggests active dissolution

and sagging during infill. Pisolitic layers exhibit sag-induced growth faults and sand dykes (i.e. extensional cracks filled with sand). A 10-15 m thick alluvial unit (complex cycles of alluvial infill) unconformably overlies the blocky and fine sand units, capping the karst infill succession (Fig. 10, Fig. 11E). Each cycle is erosive on the other and fines upwards from basal gravels consisting of pisoliths, angular fragments of duricrust and Seroukoto sandstone, to finer silica-rich sands.

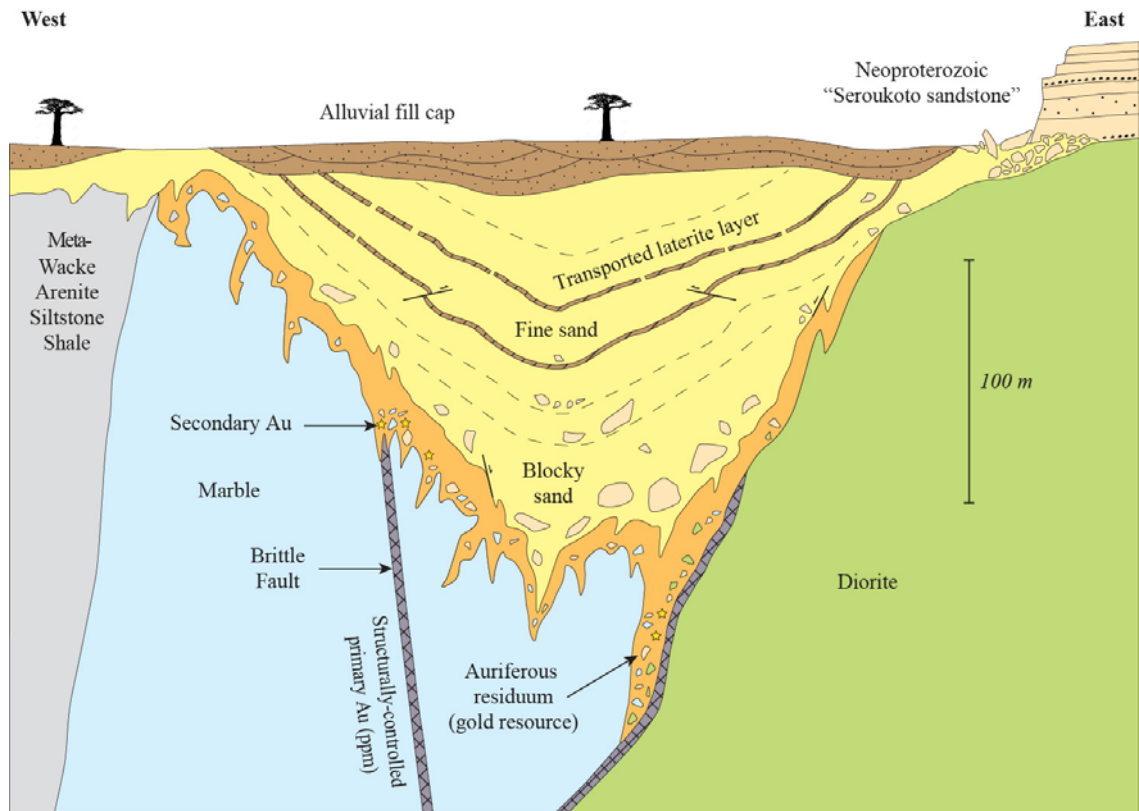


Figure 10. Schematic geological cross-section through the Yatela deposit showing idealised karst infill stratigraphy (modified from Hanssen et al., 2004).

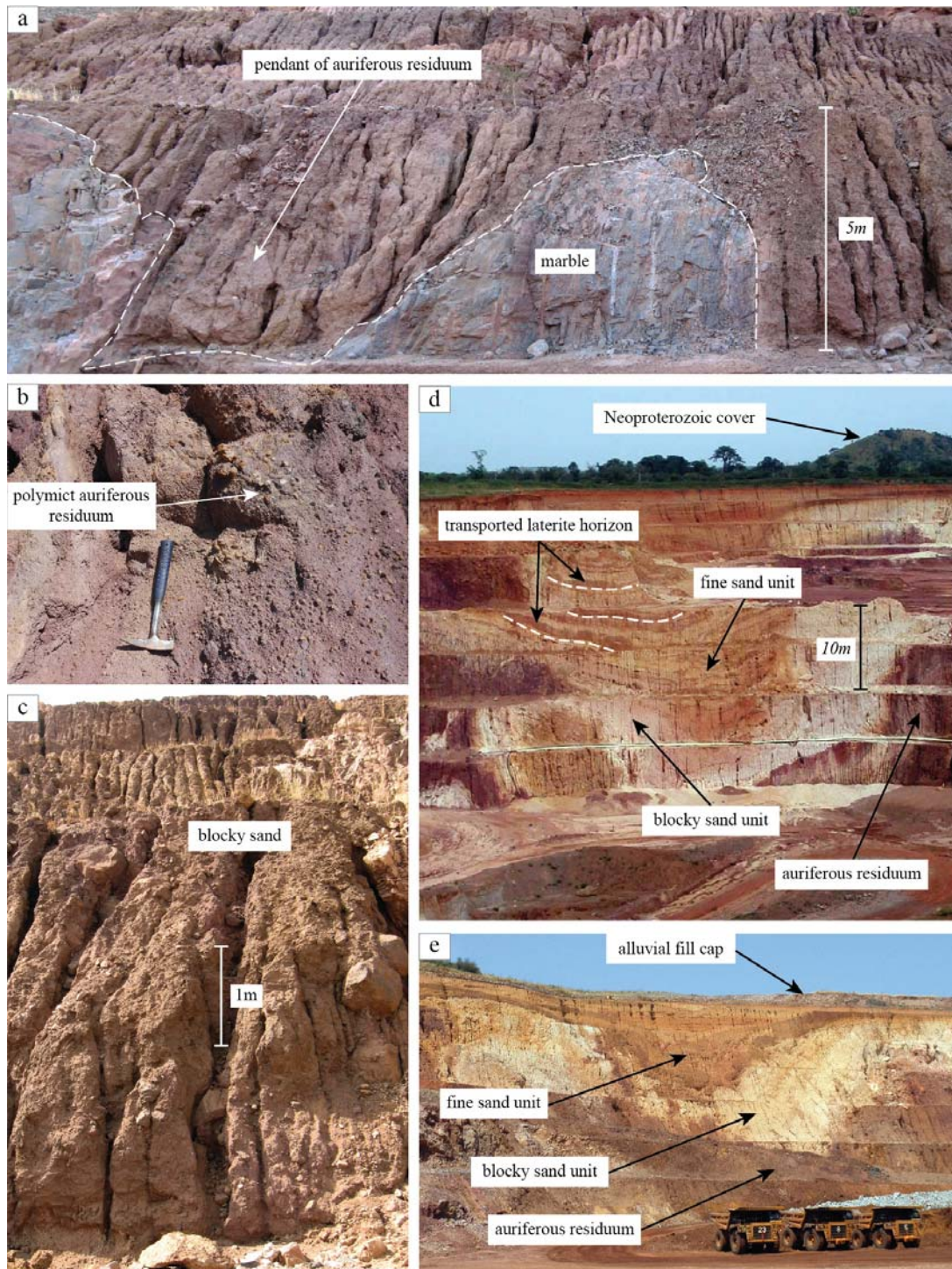


Figure 11. Representative field photographs of the karst infill stratigraphy. A) Pendants of auriferous residuum draped over the irregular karst topography. B) Typical view of the gold-enriched, polymict, ferruginous dissolution residue. C) Typical view of the blocky sand unit. Sandstone boulders of variable size float within a sandy matrix. Each bench is 5m high. D) Panoramic view of the karst infill stratigraphy showing clear sagging of the fine sand unit towards the depocentre. The hill immediately northeast of the open pit consists of Neo-proterozoic sandstone cover. E) Panoramic view of the karst infill unconformably overlain by complex cycles of alluvial material.

4.9. Secondary gold distribution

There is a spatial relationship between the NNW-trending faults in carbonate near the Yatela diorite, the location of hydrothermal alteration and primary mineralisation, and the location of auriferous residuum (Fig. 12A). In contrast, the ENE-trending and WNW-trending sub-vertical fault sets do not appear as dominant controls on development of the auriferous residuum. The steep WNW-trending normal faults, however, bound the main karst cavity in the Yatela open pit and may have played a significant role in the deposition of the blocky sand and fine sand units (Fig. 12B). The sharp increase in thickness of the blocky and fine sand units in the central part of the depocentre does not correlate with an increase in thickness of the residuum (Fig. 12C-D). This suggests that the structural controls on location of the primary mineralisation and auriferous residuum were distinct from those that controlled infill of the depocentre by silica-rich sands (i.e. blocky and fine sand units).

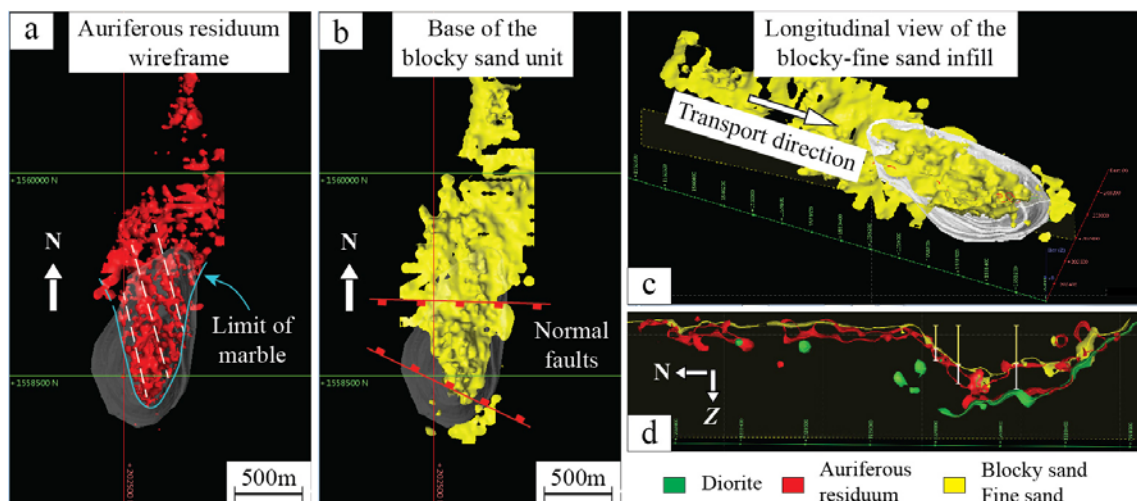


Figure 12. A) Leapfrog® scene illustrating the wireframe of the auriferous residuum. B) The scene shows the modelled base of the blocky sand unit. C) Longitudinal section illustrating the blocky-fine sand infill wireframe. D) Longitudinal section illustrating the auriferous residuum and blocky-fine sand infill wireframes. Note that the increase in thickness of the blocky-fine sand infill does not correlate with an increase in thickness of the auriferous residuum.

5. Discussion

5.1. Integration with regional geology and tectonics

At least two phases of folding have affected the country rocks in the Yatela area. The pervasive steep NW-trending cleavage (S_1) and associated lineation data are consistent with NE-SW directed shortening (D_{1y}). This deformation event is correlated with the folding and thrusting of the lithostratigraphic units in the region. This early event (D_{1y}) has been similarly reported in the Mako volcanic belt where it is correlated with stratigraphic stacking and the formation of a NNW-trending planar fabric (D_1 in Diene et al., 2012; Gueye et al., 2008). The development of NNE-trending upright folds (F_2) and penetrative axial-planar cleavage (S_2) is cryptic at Yatela but represents the dominant structural feature 1.5 km west in the KW18 ancillary pits and 25 km south at the world-class Sadiola Hill gold deposit. Fold geometry and lineation data associated with the second deformation event (D_{2y}) are consistent with NW-SE directed shortening. The D_{2y} event is compatible with a period of fold-and-thrust tectonics responsible for the region-wide structural grain (D_2) (in Ivory Coast, Pouclet et al., 2006; Vidal et al., 2009; in Burkina Faso, Hein, 2010; in Guinea, Lahondère et al., 2002; in Mali, Liégeois et al., 1991; Milési et al., 1992; Dabo and Aïfa, 2010; McFarlane et al., 2011; Diene et al., 2012; Lawrence et al., 2013a; in Senegal, Treloar et al., 2014). Calc-alkaline magmatic suites intruded the Birimian volcano-sedimentary pile at ca. 2100 Ma in the KKI (Ndiaye et al., 1997; Pawlig et al., 2006; Dioh et al., 2006). The Yatela diorite was emplaced during D_{2y} and has been dated at 2106 ± 10 Ma by Hein et al. (in press). The development of the ENE-trending steep vein set is interpreted to represent a post- D_{2y} , short-lived and local episode of extension as no regional correlations could be made. The geometry of the NNW-trending fault array and NNE-trending fault at the diorite-marble interface, and associated kinematic indicators are consistent NW-SE directed shortening (D_{3y}). At the regional scale, D_{3y} is compatible with a period of transcurrent tectonics (D_3) coeval with voluminous calc-alkaline magmatism (in southern Mali, Milési et al., 1992; Olson et al., 1992; McFarlane et al., 2011; in eastern Guinea, Egal et al., 2002; in southern Ghana, Feybesse et al., 2006; in western Burkina Faso, Baratoux et al., 2011). The two local deformation phases D_{2y} and

D_{3y} documented at Yatela relate to the evolution of a regional system accommodating oblique convergence during the Eburnean orogeny (ca. 2115-2060 Ma). The steep ENE-trending sub-vertical faults recorded at Yatela crosscut the ore-hosting structures and hence post-date the primary mineralisation. Fault geometry and associated dextral kinematic indicators are consistent with E-W oriented shortening (D_{4y}). At the regional scale, this D_{4y} deformation phase could correlate with the very late Eburnean (ca. 2060-2050 Ma) dextral reactivation described by Dabo and Aïfa (2011) in the Falémé region. The last local deformation event (D_{5y}) is correlated with the formation of sub-vertical WNW-trending normal faults. These structures cut across all pre-existing structures and post-date primary mineralisation. These faults are interpreted to have formed post-deposition of the Neoproterozoic Seroukoto sandstone and acted as a major control on infill of the karst cavity.

5.2. Towards a genetic model

In what follows we propose an ore genetic model integrating the formation of the primary gold mineralisation with subsequent processes leading to the formation of the gold resource (i.e. auriferous residuum).

The primary gold mineralisation occurred during D_{3y} based on field relationships and micro-textural observations. The equivalent structural setting and relative timing of gold between Yatela and other world-class gold deposits in the KKI (e.g., Loulo, Lawrence et al., 2013a; Massawa, Treloar et al., 2014; Sadiola Hill, Masurel et al., in press) suggests that region-wide gold mineralisation occurred during a period of transcurrent tectonics, after the cessation of regional-scale compressional deformation. Although not diagnostic of a specific fluid source, the chemical composition of syn-mineralisation hydrothermal tourmalines at Yatela is also consistent with that reported for Sadiola Hill (Masurel et al., in press) and for the Loulo-Bambadji district (Lawrence et al., 2013a; Lambert-Smith, 2014). At the district scale, the primary ore paragenesis at Yatela is compatible with the Au-As-Sb \pm Cu-Ag-W-Mo-Bi-Zn-Pb-Te metal signature identified at Sadiola Hill (Masurel et al., in press). The presence of pyrite as principal sulphide phase at Yatela, however, is interpreted to reflect a host-rock dependency, and/or a spatial zoning of metals with increasing distance from the Senegal-Mali Shear Zone,

and/or mineralisation at a distinct crustal level. Thus, the Yatela gold occurrence is interpreted to have formed during a period of region-wide orogenic gold (e.g., Groves et al., 1998; McCuaig and Kerrich, 1998; Ridley and Diamond, 2000; Groves et al., 2003; Goldfarb et al., 2005) mineralisation in the late Eburnean, similarly to world-class and minor gold deposits in the KKI.

The bulk of the resource at Yatela, however, is hosted in the auriferous residuum and is associated with irregular (e.g., dendritic to wire-like forms), angular secondary gold grains (Hein et al., *in press*). Such morphology is interpreted to result from mobilisation (physical and/or chemical) of the locally-sourced primary (hypogene) gold during the creation of a deep weathering profile and associated karstification processes (e.g., Bowell et al., 1996). The creation of a deep weathering profile was initiated in the upper-Cretaceous across West Africa (e.g., Brown et al., 1994; Lavaud et al., 2004). The surficial dissolution of the carbonate host rocks resulted in the creation of troughs that were draped and filled with a ferruginous dissolution residue locally containing secondary gold (e.g., Hein et al., *in press*) and blocks of Neoproterozoic sandstone that are likely to have collapsed into the Yatela depocentre because karstification started beneath the cover sequences (Fig. 13A-B). The term residual is used here rather than “*in-situ*” because the formation of the residuum may have involved minor (5-50 m) lateral displacement as well as vertical collapse (e.g., Anand and Butt, 2010). Physical transport of gold occurred due to profile reduction (e.g., erosion, karstification) and creep of fine-grained material, whereas chemical mobilisation occurred due to dissolution and reprecipitation of the gold by groundwater or near-surface waters (e.g., Williams-Jones et al., 2009). The grade of the auriferous residuum varied locally depending on the initial gold grade carried by the host marble and the abundance of silty-argillaceous horizons in that carbonate rock volume. Progressive karstification and sagging resulted in deposition of the sandy infill material (Fig. 13C). Evidence for sagging is cryptic at surface but abundant at depth. Individual pisolithic layers are locally buckled and affected by low-angle thrusts. Such deformation features are explained by the competency contrast between the fine sand and pisolithic layers. Minor folding occurred in the deeper parts of the dissolution troughs. Within the cavity and along its walls, a set of syn-depositional normal faults facilitated sliding of the infill material downwards towards the centre of dissolution. The presence of the transported laterite layers is also important because lateritic reworking occurred during the Paleocene to

Miocene in West Africa (Beauvais et al., 2008; Beauvais and Chardon, 2013). Lastly, the Yatela karst infill succession was capped by barren alluvial cover (Fig. 13D).

The presence of carbonate host rocks, characteristics of the primary mineralisation, semi-arid climatic conditions, and weathering intensity were probably the major factors that determined residual and supergene gold enrichment at Yatela (e.g., Anand and Butt, 2010). The Yatela-style orebodies represent attractive exploration opportunities as the surficial karst cavities are deep and laterally extensive. The Yatela-style targets, however, represent an exploration challenge. Indeed, the detection of either primary or secondary gold mineralisation using conventional geochemical surveys will be very limited if the karst cavity is covered by barren material. Moreover, the complex geometry of a residuum horizon and irregular karst topography require significant close-spaced drilling for resource estimates.

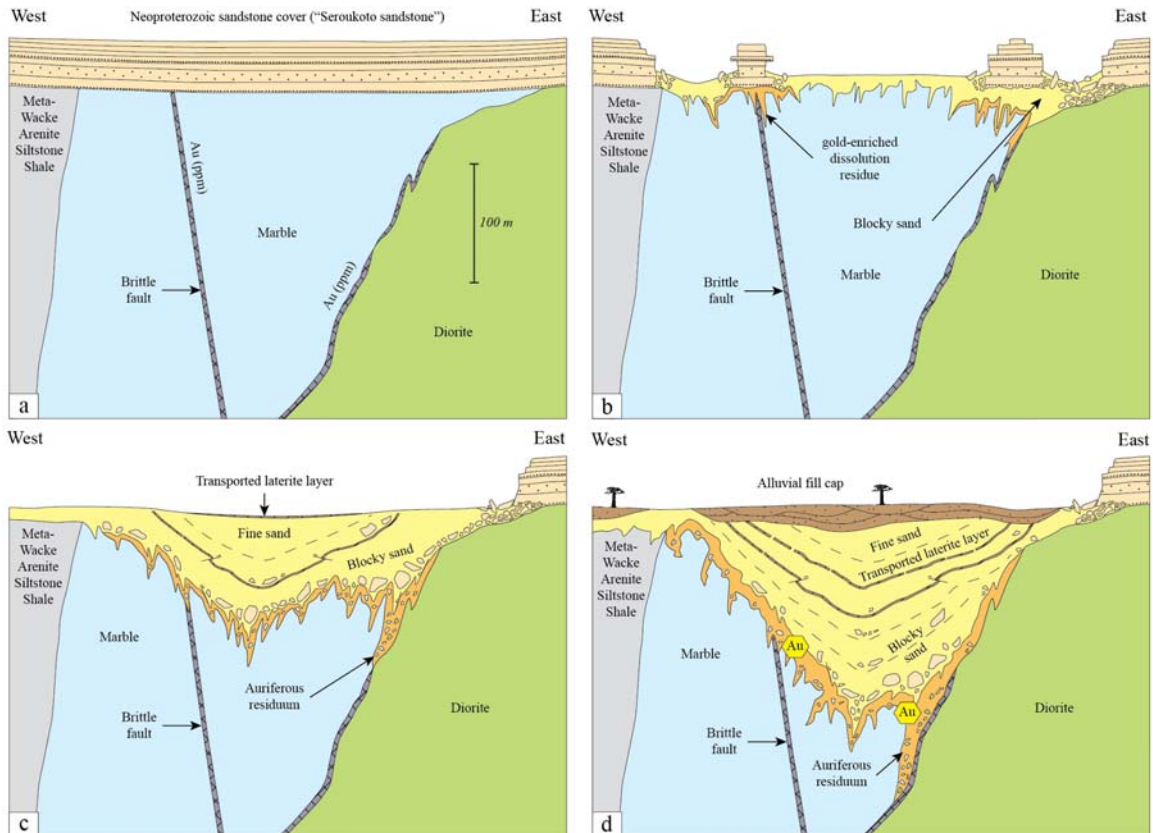


Figure 13. Series of schematic geological cross-sections illustrating a protracted ore-forming process at Yatela. A) Unconformable deposition of Neoproterozoic sandstone cover sequences over Birimian country rocks. The country rocks host a low-grade, primary gold mineralisation. B) Surficial dissolution of marble host rocks results in the formation of troughs that are draped and filled with a ferruginous dissolution residue locally enriched in gold. Blocks of the sandstone collapse into the Yatela depocentre because karstification started beneath the cover sequences. C) Progressive karstification results in sagging and infill of the troughs by the blocky sands and fine sands. The creation of a deep weathering profile results in residual and supergene gold enrichment. D) The Yatela karst infill succession is capped by complex cycles of alluvial material.

6. Conclusions

The presented field and petrographic data indicate that primary orogenic gold mineralisation at Yatela formed during a period of transcurrent tectonics (D_3), after the cessation of compressional deformation in the region. The Yatela primary gold mineralisation shares a similar structural setting and relative timing to that of world-class orogenic gold deposits in the KKI and in the West African Craton (e.g., Ashanti, Loulo, Sadiola Hill). The mined out gold resource, however, consisted of an auriferous residuum that lined the bottom of deep and laterally extensive troughs. The formation of the Yatela gold deposit reflects a lengthy process of residual and supergene gold enrichment by weathering processes and associated karstification. The Yatela deposit is unique with respect to gold mineralisation types encountered in West Africa because an auriferous residuum of economic interest (>1 Moz) derives from an underlying low-grade, sub-economic Birimian occurrence. Yatela-style orebodies offer new exploration opportunities in other gold provinces of the West African Craton where carbonates are present, such as in the Siguiri basin in Guinea and the Ity region in western Côte d'Ivoire.

7. Acknowledgements

This study forms part of a PhD project, which began in February 2012 at the Centre for Exploration Targeting, the University of Western Australia. SEMOS, a joint venture between AngloGold Ashanti, IAMGOLD and the Malian government, is gratefully acknowledged for its financial support. AMIRA International and the industry sponsors are gratefully acknowledged for their support of the WAXI project (P934A). Many thanks to T. Gell (AGA), A. Mason-Apps (AGA), O. Terblanche (AGA) and M. Skwarnecki (AGA) for their enthusiasm for the study and their constructive discussions. Special thanks are extended to D. Traoré, C.O. Sanogo, T. Sogoba, F. Samake, M. Traoré, Y.S. Kone, and to SEMOS managers G. Gushee, H. Eybers, H. Sitshengiso, and P. Herron who assisted with field work and logistics. The authors also acknowledge the Australian Microscopy & Microanalysis Research Facility at the Centre for Microscopy, Characterisation & Analysis (UWA), a facility funded by the University, State and

Commonwealth Governments. Dr. Malcolm Roberts is acknowledged for his excellent help with the electron microprobe. Dr. James-Lambert Smith is thanked for his comprehensive appraisal of the study and constructive reviews.

8. References

- Allibone, A.H., McCuaig, T.C., Harris, D., Etheridge, M.A., Munroe, S., Byrne, D., Amanor, J., and Gyapong, W., 2002a. Structural controls on gold mineralization at the Ashanti gold deposit, Obuasi, Ghana. Society of Economic Geologists Special Publication 9, 65–93.
- Allibone, A.H., Teasdale, J., Cameron, G., Etheridge, M.A., Uttlev, P., Soboh, A., Appiah-Kubi, J., Adanu, A., Arthur, R., Mamphrey, J., Odoom, B., Zuta, J., Tsikata, A., Patave F., Famiyeh, S., and Lamb, E., 2002b. Timing and structural controls on gold mineralization at the Bogoso gold mine, Ghana, West Africa. *Economic Geology* 97, 949–969.
- Anand, R.R., and Butt, C.R.M., 2010. A guide for mineral exploration through the regolith in the Yilgarn Craton, Western Australia. *Australian Journal of Earth Sciences* 57, 1015–1114.
- AngloGold Ashanti, 2010. Mineral resource and ore reserve report. Accessed in March 2015 from <http://www.ag-a-reports.com/10/>.
- Armstrong, J.T., 1988. Quantitative analysis of silicates and oxide minerals: Comparison of Monte-Carlo, ZAF and Phi-Rho-Z procedures. *Microbeam Analysis* 23, 239-246.
- Baratoux, L., Metelka, V., Naba, S., Jessell, M.W., Grégoire, M., and Ganne, J., 2011. Juvenile Paleoproterozoic crust evolution during the Eburnean orogeny (ca. 2.2–2.0 Ga), western Burkina Faso. *Precambrian Research* 191, 18-45.
- Bassot, J.P., 1987. Le complexe volcano-plutonique calco-alcalin de la rivière Daléma (Est Sénégal): discussion de sa signification géodynamique dans le cadre de l'orogénie eburnéenne (Protérozoïque inférieur). *Journal of African Earth Sciences* 6, 505-519.
- Bassot, J.P., and Dommange, A., 1986. Mise en évidence d'un accident majeur affectant le Protérozoïque inférieur des confins sénégal-maliens. *Comptes Rendus Géosciences* 302, 1101–1106.

- Bering, D., Brinckmann, J., Camara, N., Diawara, M., Gast, L., and Kieita, S., 1998. Evaluation de l'inventaire des ressources minérales de Guinée: Hannover, Bundesanstalt für Geowissenschaften und Rohstoffe, 109 p.
- Beauvais, A., and Chardon, D., 2013. Modes, tempo, and spatial variability of Cenozoic denudation: the West African example. *Geochemistry, Geophysics, Geosystems* 14, 1590-1608.
- Beauvais, A., Ruffet, G., Hénocque, O., and Fabrice, C., 2008. Chemical and physical erosion rhythms of the West African Cenozoic morphogenesis: the ^{39}Ar - ^{40}Ar dating of supergne K-Mn oxides. *Journal of Geophysical Research* 113, 15 p.
- Boher, M., Abouchami, W., Michard, A., Albareda, F., and Arndt, N.T., 1992. Crustal Growth in West Africa at 2.1 Ga. *Journal of Geophysical Research* 97, 345-369.
- Bosse, H.R., Gwosdz, W., Lorenz, W., Markwich, H., Roth, W., and Wolff, F., 1996. Limestone and dolomite resources of Africa. *Geologisches Jahrbuch* D102, 3-532.
- Bowell, R.J., Laffoley, N.A., d'Afreh, E.O., Hanssen, E., Abe, S., Yao, R.K., and Pohl, D., 1996. Gold and base metals distribution and exploration in tropical soils: four contrasting case studies from West Africa, *in* Foster, R.P., (eds) *Exploration and Mining in Africa: towards 2000*. Transactions of the Institute of Mining and Metallurgy 105, B12-33.
- Brown, E.T., Bourlès, D.L., Colin, F., Sanfo, Z., Raisbeck, G.M., and Yiou, F., 1994. The development of iron crust lateritic systems in Burkina Faso, West Africa examined with in-situ-produced cosmogenic nuclides. *Earth and Planetary Science Letters* 124, 19-33.
- Calvez, J.Y., Feybesse, J.L., Ledru, P. and Milesi, J.P., 1990. Géochronologie du Proterozoïque inférieur du craton ouest africain (méthode d'évaporation directe de zircons isolés). 13^e Réunion des Sciences de la Terre, Grenoble, France; *in* Milési, J.P., Feybesse, J.L., Ledru, P., Dommangeat, A., Quedraogo, M.F., Marcoux, E., Prost, A., Vinchon, C., Sylvain, J.P., Johan, V., Tegyey, M., Calvez, J.Y., and Lagny, P., 1989. Les minéralisations aurifères de l'Afrique de l'Ouest et leurs relations avec l'évolution lithostructurale au Protérozoïque inférieur. *Chronique de la Recherche Minière* 497, 3-98.
- Dabo, M., and Aïfa, T., 2010. Structural styles and tectonic evolution of the Kolia-Boboti sedimentary Basin, Kédougou-Kéniéba inlier, eastern Senegal. *Comptes Rendus Geoscience* 342, 796-805.

- Dabo, M., and Aïfa, T., 2011. Late Eburnean deformation in the Kolia-Boboti sedimentary basin, Kédougou-Kéniéba Inlier, Senegal. *Journal of African Earth Sciences* 60, 106-116.
- Debat, P., Diallo, D.P., Ngom, P.M., Rollet, M., and Seyler, M., 1984. La série de Mako dans ses parties centrale et méridionale (Sénégal Oriental, Afrique de l'ouest). Précisions sur l'évolution de la série volcanosédimentaire et données géochimiques préliminaires sur les formations magmatiques post-tectoniques. *Journal of African Earth Sciences* 2, 71-79.
- Dia, A., Van Schmus, W.R., and Kröner, A., 1997. Isotopic constraints on the age and formation of a Palaeoproterozoic volcanic arc complex in the Kedougou Inlier, eastern Senegal, West Africa. *Journal of African Earth Sciences* 24, 197-213.
- Dia, A., 1988. Caractères et signification des complexes magmatiques et métamorphiques du secteur de Sandikounda-Laminia (Nord de la boutonnière de Kédougou, Est du Sénégal): un modèle géodynamique du Birimien de l'Afrique de l'Ouest. Unpublished Ph.D. thesis, Sénégal, Université de Dakar, 350 p.
- Diene, M., Gueye, M., Diallo, D.P., and Dia, A., 2012. Structural Evolution of a Precambrian Segment: Example of the Paleoproterozoic Formations of the Mako Belt (Eastern Senegal, West Africa). *International Journal of Geosciences* 3, 153-165.
- Dioh, E., Béziat, D., Debat, P., Grégoire, M., and Ngom, P.M., 2006. Diversity of the Palaeoproterozoic granitoids of the Kédougou inlier (eastern Senegal): Petrographical and geochemical constraints. *Journal of African Earth Sciences* 44, 351-371.
- Egal, E., Thiéblemont, D., Lahondère, D., Guerrot, C., Costea, C.A., Iliescu, D., Delor, C., Goujou, J.C., Lafon, J.M., Tegyey, M., Diaby, S., and Kolié, P., 2002. Late Eburnean granitization and tectonics along the western and northwestern margin of the Archean Kénéma-Man domain (Guinea, West African Craton). *Precambrian Research* 117, 57-84.
- Feybesse, J.L., Billa, M., Guerrot, C., Duguey, E., Lescuyer, J.L., Milesi, J.P., and Bouchot, V., 2006. The paleoproterozoic Ghanaian province: Geodynamic model and ore controls, including regional stress modeling. *Precambrian Research* 149, 149-196.
- Goldfarb, R.J., Baker, T., Dubé, B., Groves, D.I., Hart, C.J.R., and Gosselin, P., 2005. Distribution, character, and genesis of gold deposits in metamorphic terranes. *Economic Geology* 100th Anniversary Volume, 407-450.

- Groves, D.I., Goldfarb, R.J., Robert, F., and Hart, C.J.R., 2003. Gold Deposits in Metamorphic Belts: Overview of Current Understanding, Outstanding Problems, Future Research, and Exploration Significance. *Economic Geology* 98, 1-29.
- Groves, D.I., Goldfarb, R.J., Gebre-Mariam, M., Hagemann, S.G., and Robert, F., 1998. Orogenic gold deposits: A proposed classification in the context of their crustal distribution and relationship to other gold deposit types. *Ore Geology Reviews* 13, 7-27.
- Gueye, M., Siegesmund, S., Wemmer, K., Pawlig, S., Drobe, M., Nolte, N., and Layer, P., 2007. New evidences for an early Birimian evolution in the West African Craton: An example from the Kédougou-Kénieba inlier, southeast Senegal. *South African Journal of Geology* 110, 511-534.
- Gueye, M., Ngom, P.M., Diène, M., Thiam, Y., Siegesmund, S., Wemmer, K., and Pawlig, S., 2008. Intrusive rocks and tectono-metamorphic evolution of the Mako Paleoproterozoic belt (Eastern Senegal, West Africa). *Journal of African Earth Sciences* 50, 88-110.
- Hanssen, E., Kaisin, J., and Tessougue, S., 2004. The Yatela gold mine, Western Mali: Supergene enrichment of lower Proterozoic gold mineralization in a surficial karst. In Conference Proceedings - CIM Annual Meeting, Edmonton.
- Hawthorne, F.C., and Henry, D.J., 1999. Classification of the minerals of the tourmaline group. *European Journal of Mineralogy* 11, 201–215.
- Hein, K.A.A., Matsheka, J.R., Bruguier, O., Masurel, Q., Bosch, D., Renaud, C., and Monié, P., in press. The Yatela gold deposit: 2 billion years in the making. *Journal of African Earth Sciences*.
- Hein, K.A.A., 2010. Succession of structural events in the Goren greenstone belt (Burkina Faso): Implications for West African tectonics. *Journal of African Earth Sciences* 56, 83-94.
- Henry, D.J., Sun, H., Slack, J.F., and Dutrow, B.L., 2008. Tourmaline in meta-evaporites and highly magnesian rocks: perspectives from Namibian tourmalinites. *European Journal of Mineralogy* 20, 889-904.
- Henry, D.J., and Guidotti, C.V., 1985. Tourmaline as a petrogenetic indicator mineral- an example from the staurolite-grade metapelites of NW Maine. *American Mineralogist* 70, 1–15.
- Hirdes, W., and Davis, D.W., 2002. U–Pb Geochronology of Paleoproterozoic Rocks in the Southern Part of the Kédougou-Kénieba Inlier, Senegal, West Africa: Evidence for

Diachronous Accretionary Development of the Eburnean Province. *Precambrian Research* 118, 83-99.

IAMGold, 2013. News release, Yatela closure. Accessed in September 2015 from <http://www.iamgold.com/English/investors>

Lahondère, D., Thiéblemont, D., Tegyey, M., Guerrot, C., and Diabaté, B., 2002. First evidence of early Birimian (2.21 Ga) volcanic activity in Upper Guinea: The volcanics and associated rocks of the Niani suite. *Journal of African Earth Sciences* 35, 417–431.

Lambert-Smith, J., 2014. The geology, structure and metallogenesis of the world class Loulo-Bambadji Au district in Mali and Senegal, West Africa. Ph.D. Thesis, Kingston University, London, 346 p.

Lavaud, T., Beziat, D., Blot, A., Debat, P., and Lombo, M., 2004. Paleo-gossans within the lateritic iron crust: example of the nickeliferous prospect of Bonga, Burkina Faso. *Journal of African Earth Sciences* 39, 465–471.

Lawrence, D.M., Treloar, P.J., Rankin, A.H., Boyce, A., and Harbidge, P., 2013b. A Fluid Inclusion and Stable Isotope Study at the Loulo Mining District, Mali, West Africa: Implications for Multifluid Sources in the Generation of Orogenic Gold Deposits. *Economic Geology* 108, 229-257.

Lawrence, D.M., Treloar, P.J., Rankin, A.H., Harbidge, P., and Holliday, J., 2013a. The Geology and Mineralogy of the Loulo Mining District, Mali, West Africa: Evidence for Two Distinct Styles of Orogenic Gold Mineralization. *Economic Geology* 108, 199-227.

Ledru, P., Pons, J., Milesi, J.P., Feybesse, J.L., and Johan, V., 1991. Transcurrent tectonics and polycyclic evolution in the Lower proterozoic of Senegal-Mali. *Precambrian Research* 50, 337-354.

Liégeois, J.P., Claessens, W., Camara, D., and Klerkx, J., 1991. Short-lived Eburnian orogeny in southern Mali. Geology, tectonics, U-Pb and Rb-Sr geochronology. *Precambrian Research* 50, 111-136.

Masurel, Q., Thébaud, N., Miller, J., Ulrich, S., Hein, K.A.A., Cameron, G., Béziat, D., and Bruguier, O., in press. Sadiola Hill: a world-class gold deposit in Mali, West Africa. *Economic Geology – Special Issue on the West African Craton*.

McCuaig, T. C., and Kerrich, R., 1998. P-T-t-deformation-fluid characteristics of lode gold deposits: evidence from alteration systematics. *Ore Geology Reviews* 12, 381-453.

- McFarlane, C.R.M., Mavrogenes, J., Lentz, D., King, K., Allibone, A., and Holcombe, R., 2011. Geology and Intrusion-Related Affinity of the Morila Gold Mine, Southeast Mali. *Economic Geology* 106, 727-750.
- Milési, J.P., Ledru, P., Feybesse, J.L., Dommangeat, A., and Marcoux, E., 1992. Early Proterozoic ore deposits and tectonics of the Birimian orogenic belt, West Africa. *Precambrian Research* 58, 305-344.
- Ndiaye, P.M., Dia, A., Viallette, Y., Diallo, D.P., Ngom, P.M., Sylla, M., Wade, S., and Dioh, E., 1997. Données pétrographiques, géochimiques et géochronologiques nouvelles sur les granitoïdes du Paléoprotérozoïque du Supergroupe de Dialé-Daléma (Senegal Oriental): Implications pétrogénétiques et géodynamiques. *Journal of African Earth Sciences* 25, 193-208.
- Oberthür, T., Vetter, U., Davis, D.W., and Amanor, J.A., 1998. Age constraints on gold mineralization and Paleoproterozoic crustal evolution in the Ashanti belt of southern Ghana: *Precambrian Research* 89, 129-143.
- Olson, S.F., Diakité, K., Ott, L., Guindo, A., Ford, C.R.B., Winer, N., Hanssen, E., Lay, N., Bradley, R., and Pohl, D., 1992. Regional Setting, Structure, and Descriptive Geology of the Middle Proterozoic Syama Gold Deposit, Mali, West Africa. *Economic Geology* 87, 310-331.
- Pawlig, S., Gueye, M., Klischies, R., Schwarz, S., Wemmer, K., and Siegesmund, S., 2006. Geochemical and Sr-Nd isotopic data on the Birimian of the Kedougou-Kenieba Inlier (Eastern Senegal): Implications on the Palaeoproterozoic evolution of the West African Craton. *South African Journal of Geology* 109, 411-427.
- Pouclet, A., Doumbia, S., and Vidal, M., 2006. Geodynamic setting of the Birimian volcanism in central Ivory Coast (western Africa) and its place in the Palaeoproterozoic evolution of the Man Shield. *Bulletin de la Société Géologique de France* 177, 105-121.
- Ridley, J. R., and Diamond, L. W., 2000. Fluid Chemistry of Orogenic Lode Gold Deposits and Implications for Genetic Models. *SEG Reviews* 2000, 141-162.
- Treloar, P.J., Lawrence, D.M., Senghor, D., Boyce, A., and Harbridge, P., 2014. The Massawa gold deposit, Eastern Senegal, West Africa: an orogenic gold deposit sourced from magmatically derived fluids? *Geological Society London Special Publications* 393, 135-160.

- Vidal, M., Gumiaux, C., Cagnard, F., Pouclet, A., Ouattara, G., and Pichon, M., 2009. Evolution of a Paleoproterozoic “weak type” orogeny in the West African Craton (Ivory Coast). *Tectonophysics* 477, 145-159.
- Williams-Jones, A.E., Bowell, R.J., and Migdisov, A.A., 2009. Gold in solutions. *Elements* 5, 281-287.
- Yavuz, F., Yavuz, V., and Sasmaz, A., 2006. WinClastour - a visual basic program for tourmaline formula calculation and classification. *Computers & Geosciences* 32, 1156-1168.

9. Supplementary material

9.1. Representative chemical composition of syn-mineralisation hydrothermal tourmalines at Yatela.

Representative chemical composition of syn-mineralisation stage hydrothermal tourmalines at Yatela																	
SiO ₂	36.83	36.92	36.97	37.15	37.44	36.83	36.95	36.75	36.48	36.71	36.94	36.80	37.03	36.87	36.77	36.97	
TiO ₂	1.05	0.74	0.62	0.67	0.42	0.16	0.81	0.34	0.74	1.10	0.83	1.14	1.14	0.45	0.52	0.69	0.56
Al ₂ O ₃	30.24	31.37	30.73	31.29	31.38	32.18	30.63	31.80	30.78	29.74	30.45	30.42	30.42	29.66	31.50	31.44	30.76
FeO(T)	4.85	3.62	4.45	3.78	4.46	4.31	4.76	3.85	4.55	4.61	4.75	4.80	4.80	5.34	4.37	4.55	4.57
MnO	0.00	0.00	0.00	0.00	0.00	0.00	0.00	0.00	0.00	0.00	0.00	0.00	0.00	0.00	0.00	0.00	0.00
MgO	9.17	8.87	8.97	9.04	8.73	8.68	8.95	9.05	9.22	9.19	8.73	8.97	9.02	8.78	8.55	8.95	8.74
CaO	1.10	0.91	0.94	0.89	0.55	0.36	0.98	0.44	0.89	1.24	0.94	1.12	1.12	0.62	0.65	0.87	0.37
Na ₂ O	2.12	2.17	2.22	2.18	2.17	2.14	2.27	2.18	2.10	2.07	2.13	1.97	1.97	2.04	2.32	2.34	2.23
K ₂ O	0.00	0.02	0.02	0.01	0.01	0.00	0.01	0.01	0.00	0.01	0.00	0.01	0.01	0.01	0.02	0.01	0.01
H ₂ O*	0.00	0.00	0.00	0.00	0.00	0.00	0.00	0.00	0.00	0.00	0.00	0.00	0.00	0.00	0.00	0.00	0.00
B ₂ O ₃ *	0.00	0.00	0.00	0.00	0.00	0.00	0.00	0.00	0.00	0.00	0.00	0.00	0.00	0.00	0.00	0.00	0.00
Li ₂ O ₂ *	0.00	0.00	0.00	0.00	0.00	0.00	0.00	0.00	0.00	0.00	0.00	0.00	0.00	0.00	0.00	0.00	0.00
Total	99.42	98.57	98.88	98.86	98.90	99.37	99.33	98.65	99.06	98.36	98.47	99.39	99.16	99.16	98.96	99.11	99.26
B	3.00	3.00	3.00	3.00	3.00	3.00	3.00	3.00	3.00	3.00	3.00	3.00	3.00	3.00	3.00	3.00	3.00
Si(T)	6.03	6.04	6.06	6.04	6.07	6.08	6.03	6.04	6.02	6.04	6.05	6.04	6.04	6.05	6.07	6.04	6.07
Al(T)	0.00	0.00	0.00	0.00	0.00	0.00	0.00	0.00	0.00	0.00	0.00	0.00	0.00	0.00	0.00	0.00	0.00
Total(T)	6.03	6.04	6.06	6.04	6.07	6.08	6.03	6.04	6.02	6.04	6.05	6.04	6.04	6.05	6.07	6.04	6.07
Al(Z)	5.84	6.00	5.94	6.00	6.00	5.91	6.00	5.94	5.80	5.92	5.86	5.75	6.00	5.94	6.00	5.91	5.90
Mg(Z)	0.17	0.00	0.06	0.00	0.00	0.09	0.00	0.06	0.20	0.08	0.14	0.14	0.25	0.00	0.06	0.10	0.00
Fe ³⁺ (Z)	0.00	0.00	0.00	0.00	0.00	0.00	0.00	0.00	0.00	0.00	0.00	0.00	0.00	0.00	0.00	0.00	0.00
Z Total	6.00	6.00	6.00	6.00	6.00	6.00	6.00	6.00	6.00	6.00	6.00	6.00	6.00	6.00	6.00	6.00	6.00
Al(Y)	0.00	0.05	0.00	0.02	0.05	0.15	0.00	0.13	0.00	0.00	0.00	0.00	0.06	0.07	0.00	0.13	0.00
Ti(Y)	0.13	0.09	0.08	0.08	0.05	0.02	0.10	0.04	0.09	0.14	0.10	0.14	0.15	0.06	0.09	0.02	0.11
Fe ³⁺ (Y)	0.00	0.00	0.00	0.00	0.00	0.00	0.00	0.00	0.00	0.00	0.00	0.00	0.00	0.00	0.00	0.00	0.00
Fe ²⁺ (Y)	0.66	0.50	0.61	0.52	0.61	0.59	0.65	0.53	0.62	0.64	0.66	0.66	0.74	0.60	0.62	0.63	0.68
Mg(Y)	2.07	2.16	2.14	2.20	2.13	2.10	2.10	2.20	2.19	2.06	2.07	2.05	2.05	2.05	2.14	2.09	2.12
Li(Y)	0.00	0.00	0.00	0.00	0.00	0.00	0.00	0.00	0.00	0.00	0.00	0.00	0.00	0.00	0.00	0.00	0.00
Y Total	2.87	2.80	2.82	2.84	2.84	2.86	2.85	2.90	2.91	2.84	2.82	2.84	2.84	2.85	2.84	2.85	2.87
Ca(X)	0.19	0.16	0.16	0.16	0.10	0.06	0.17	0.08	0.16	0.22	0.17	0.20	0.20	0.11	0.12	0.15	0.17
Na(X)	0.67	0.69	0.71	0.69	0.67	0.72	0.69	0.67	0.66	0.68	0.62	0.65	0.73	0.74	0.71	0.69	0.70
X Total	0.87	0.85	0.87	0.85	0.79	0.74	0.89	0.77	0.82	0.89	0.85	0.82	0.85	0.86	0.84	0.87	0.88
X vacancy	0.13	0.15	0.13	0.15	0.21	0.26	0.11	0.23	0.18	0.12	0.15	0.18	0.18	0.15	0.16	0.14	0.15
Fe(Fe+Mg)	0.23	0.19	0.22	0.19	0.22	0.23	0.19	0.22	0.23	0.23	0.23	0.25	0.25	0.23	0.22	0.24	0.22
Na(Na+Ca)	0.78	0.81	0.82	0.88	0.92	0.81	0.90	0.75	0.80	0.76	0.76	0.77	0.87	0.82	0.81	0.83	0.89
Fe ²⁺ (Fe ²⁺ +Fe ³⁺)	1.00	1.00	1.00	1.00	1.00	1.00	1.00	1.00	1.00	1.00	1.00	1.00	1.00	1.00	1.00	1.00	1.00
Mg(Fe ²⁺ +Fe ³⁺)	3.37	4.37	3.59	4.27	3.49	3.59	3.36	4.19	3.61	3.55	3.28	3.33	3.01	3.58	3.35	3.49	3.60
Al/(Al+Fe+Mg)	0.67	0.70	0.68	0.69	0.70	0.68	0.69	0.67	0.67	0.68	0.67	0.67	0.66	0.69	0.68	0.69	0.69
Mg/(Mg+Al+Fe)	0.26	0.25	0.25	0.24	0.24	0.25	0.25	0.26	0.26	0.25	0.25	0.25	0.24	0.24	0.25	0.25	0.24
Ca(Ca+Fe+Mg)	0.06	0.06	0.05	0.03	0.02	0.06	0.03	0.05	0.07	0.06	0.07	0.06	0.04	0.04	0.05	0.05	0.03
Σ cations	18.76	18.69	18.75	18.71	18.70	18.67	18.78	18.71	18.75	18.74	18.72	18.70	18.75	18.74	18.75	18.72	18.72

Chapter V. The tectono-magmatic evolution of the Kédougou-Kénieba inlier, West Africa: new insights from igneous rock geochemistry and U-Pb geochronology in the Sadiola-Yatela region

Quentin Masurel^{1*}, Nicolas Thébaud¹, John Miller¹, Stanislav Ulrich²

¹Centre for Exploration Targeting, The University of Western Australia, 35 Stirling Highway, Crawley, WA, Australia.

²AngloGold Ashanti Australia Limited, Asset Development - Brownfields, 44 St. Georges Terrace, Perth, WA, Australia.

*Corresponding author, Ph: +61864885809, E-mail: qmasurel@hotmail.com

Keywords: Kédougou-Kénieba inlier; Sadiola; Eburnean orogeny; geochemistry; U-Pb geochronology.

1. Abstract

The Paleoproterozoic terranes of West Africa provide a complete record of crustal growth. The Kédougou-Kénieba inlier is the westernmost exposure of Birimian crust in the West African Craton and a world-class gold province. The bulk of the orogenic gold mineralisation in the inlier has been related to a period of transcurrent tectonics coeval with calc-alkaline magmatism in the late Eburnean (ca. 2090 and 2070 Ma). In this study, the geology, structural framework, geochemistry ($n=28$) and focused geochronology ($n=13$) of representative magmatic rocks from the Sadiola-Yatela region are presented and integrated with published data in order to provide the tectono-magmatic framework to gold mineralisation in the Kédougou-Kénieba inlier.

The granitoids from the Sadiola-Yatela region display a temporal evolution from ca. 2150-2080 Ma calc-alkaline metaluminous plutons (e.g., diorite, hornblende-granodiorite) to ca. 2080-2060 Ma peraluminous high-K granites (e.g., biotite-monzogranite). The least-evolved rocks are associated with flat REE patterns and

correspond to plutons of the ca. 2140 Ma Finman complex and the ca. 2115 Ma Sadiola Hill quartz-feldspar-porphyry. In contrast, the vast majority of the Eburnean (ca. 2115–2060 Ma) granitoids have a calc-alkaline affinity and are characterised by negative Nb-Ta anomalies, marked Pb positive anomalies and high LIL/HFS ratios. These Eburnean magmatic rocks share a close affinity with relatively hydrous, oxidised magmas and source regions. The polycyclic deformation recorded in sedimentary and magmatic rocks of the region includes a period of early convergence (D_{1s}), followed by a period of fold-and-thrust tectonics (D_{2s}), and later transcurrent tectonics (D_{3s} - D_{4s}). The bulk of the gold mineralisation in the region occurred during D_{3s} , with sinistral displacement and hydrothermal fluid circulation along the Senegal-Mali Shear Zone and steep NNE-trending shear zones connected to structural traps in the Kofi basin.

The results of this study, when integrated with published data, indicate that the late Eburnean tectono-thermal event between 2080 and 2060 Ma represented the geodynamic engine that empowered orogenic gold mineralisation in the Kédougou-Kénieba inlier. The new data also further supports the hypothesis that the Eburnean tectono-magmatic activity affected the Baoulé-Mossi domain diachronously from SE to NW.

2. Introduction

Paleoproterozoic supracrustal and intrusive rocks in the West African Craton mark a major episode of juvenile crust growth that lasted ~175 Ma from ca. 2.25 to 2.05 Ga. The geology of the KKI consists of linear greenstone belts and wider sedimentary basins. Available geochronological data indicate that distinct peaks of magmatic activity occurred in the region from ca. 2200 Ma to 2070 Ma (e.g., Boher et al., 1992; Dia et al., 1997; Hirdes and Davis, 2002; Pawlig et al., 2006; Dioh et al., 2006; Gueye et al., 2007, 2008). Intensive studies of the Eburnean granitoids have focused on the western and southern parts of the KKI but limited data exist for the eastern part of the inlier, which hosts the world-class Loulo and Sadiola-Yatela gold districts. Hence, the study of igneous rocks in that exceptionally gold-endowed region appears critical not only to unravel the tectono-thermal evolution of the KKI crust but also in terms of mineral system, whereby gold deposits are viewed as local expressions of orogen-

lithospheric-scale processes (e.g., Bierlein et al., 2006; McCuaig et al., 2010). Recent research in the KKI has highlighted the spatial association between late Eburnean calc-alkaline plutons and gold mineralisation (Lawrence et al., 2013a, b; Treloar et al., 2014; Lambert-Smith, 2014; Masurel et al., in press a, b). The potential role a complex fluid history involving metamorphic and magmatic sources has been proposed in the development of major gold deposits (e.g., Loulo, Lawrence et al., 2013a,b; Massawa, Treloar et al., 2014). The late Eburnean magmatic activity has also been proposed to have participated in the generation of thermal gradients, which produced regional fluid systems capable of transpoting gold (e.g., Masurel et al., in press a,b). Regardless of the variability in gold mineralisation at the deposit-scale, the late Ebrunean tectono-thermal event may represent the geodynamic engine that empowered orogenic gold mineralisation in the KKI. This study aims at (i) documenting the petrographical-geochemical characteristics and absolute timing of representative igneous rocks in the Sadiola-Yatela region and (ii) placing these rocks into a regional geological framework with respect to polycyclic deformation and gold mineralisation. These data will be used to discuss the tectono-magmatic evolution of the KKI and geodynamic implications.

3. Geological setting of the Kédougou-Kénieba inlier

The Kédougou-Kénieba inlier (KKI) is the westernmost exposed part of the Paleoproterozoic Baoulé-Mossi domain in the West African Craton (inset Fig. 1). The inlier is bounded on its western margin by the Hercynian Mauritanides (Villeneuve, 2008). It is unconformably overlain by Neoproterozoic cover (i.e. Taoudeni sandstone) on all other sides (Villeneuve and Cornée, 1994). The KKI terrain is flat at an average elevation of 125 m above the sea level. The region is characterized by a thick subtropical weathering profile that has obscured much of the surface geology. The first-order geological features that characterise the KKI are outlined below.

3.1. Magmatic activity

Several geochronological studies have been carried out in the KKI. Available geochronological data rely on several analytical methods and indicate a polycyclic magmatic activity that lasted from ca. 2200 to 2070 Ma (Table 1).

The oldest peak of magmatic activity recorded in the KKI led to the formation of the Mako volcanic belt, the Sandikounda amphibolite-gneiss plutonic complex, and the Badon granodiorite-granite complex. Rocks of the Mako Series consist of juxtaposed tholeiitic basalts and calc-alkaline andesitic lavas intercalated with minor immature sedimentary rocks, volcaniclastic rocks, and pyroclastic rocks (Fig. 1) (Bassot, 1987; Hirdes and Davis, 2002; Dioh et al., 2006; Gueye et al., 2008). Tholeiitic basalts in the Mako belt have been dated at ca. 2195 ± 11 Ma (Dia, 1988). The best crystallisation age estimates for emplacement of the Sandikounda amphibolite-gneiss plutonic complex and the Badon granodiorite fall within error at ca. 2200 Ma (Fig. 1) (Dia et al., 1997; Gueye et al., 2007). The Sandikounda amphibolite-gneiss plutonic complex has been interpreted to represent the deeper root of the Mako volcanic system (Dia et al., 1997). Altogether, this early phase of magmatism is interpreted to reflect the initial stage of juvenile crustal growth in the region (ME-I) (e.g., Pawlig et al., 2006; Gueye et al., 2007).

The second manifestation of magmatism (ME-II) was associated with the emplacement of the Sandikounda layered plutonic complex, which intruded rocks of the Mako greenstone belt (Fig. 1). The layered plutonic complex is composed of Na-differentiated plutons with varying composition from opx-gabbro to amphibole-biotite-bearing tonalite (Dioh et al., 2006). The best estimate for crystallisation of the layered plutonic complex is 2158 ± 8 Ma (Dia et al., 1997), which provides a minimum age for the Mako volcanic assemblage.

The third peak of magmatic activity (ME-III) occurred between ca. 2140 and 2120 Ma and is associated with the intrusion of the Mako volcanic rocks by the Laminia-Kaourou plutonic complex. The plutonic complex is a large calc-alkaline composite pluton composed of granodiorite, tonalite and granite (Dia et al., 1997) (Fig. 1). The plutonic complex has been dated between 2138 ± 6 Ma and 2127 ± 6 Ma (Dia et al., 1997).

The fourth peak of magmatic activity (ME-IV) occurred during the onset of the Eburnean orogeny between ca. 2115 and 2090 Ma. It is marked by the intrusion of numerous basic to felsic calc-alkaline plutons forming circular to elliptic bodies of various sizes (e.g., Diombalou, Bouroumbourou) (Gueye et al., 2008) (Fig. 1). This time period also represents the best age estimate for the emplacement of pillowed andesitic flows with subordinate rhyolitic lavas and pyroclastites in the Falémé belt (Fig. 1). Geochronological data acquired on a rhyolite flow provides a magmatic age of 2099 ± 4 Ma (Hirdes and Davis, 2002).

The last peak of magmatic activity (ME-V) was associated with the massive emplacement of Eburnean granitoids in the KKI upper crust between ca. 2090 and 2070 Ma (e.g., Dia et al., 1997; Hirdes and Davis, 2002; Gueye et al., 2007). These plutons vary in size (100's of metres to 10's of km) and define a wide compositional spectrum from metaluminous hornblende-biotite-bearing granodiorite (e.g., Mamakono, 2076 ± 3 Ma, Hirdes and Davis, 2002) and pyroxene-bearing granodiorite-tonalite (e.g., Boboti, 2080 ± 1 Ma, Hirdes and Davis, 2002) to peraluminous monzogranites (e.g., Saraya, 2079 ± 2 Ma, Hirdes and Davis, 2002) (Fig. 1).

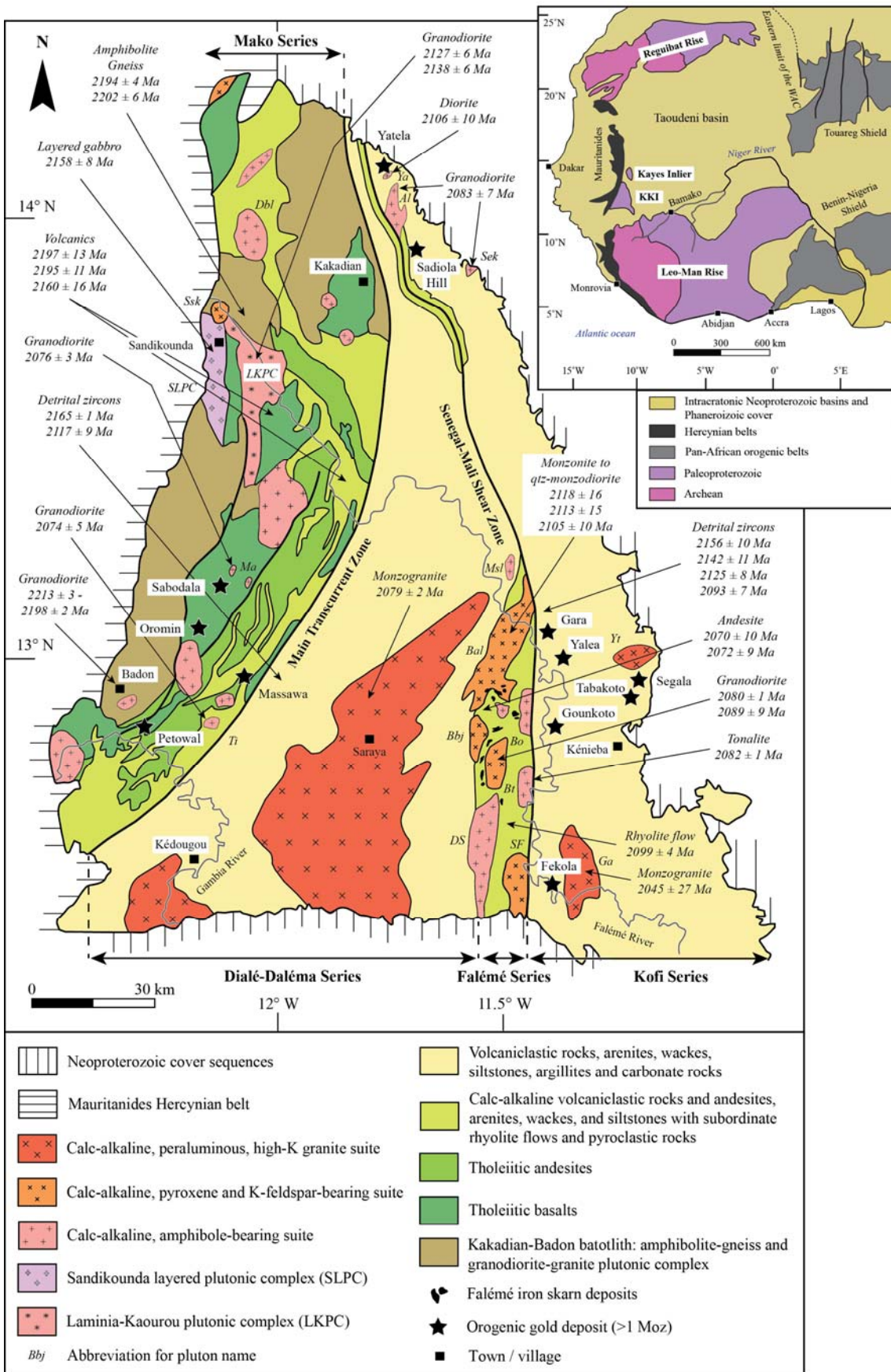


Figure 1. Geologic map of the Kédougou-Kéniéba inlier (1:250,000 scale, modified after Gueye et al., 2007; Lawrence et al., 2013a). Inset map shows the geologic setting of the West African craton (modified after Boher et al., 1992). The Falémé River forms the international border with Senegal to the west and Mali to the east and north. Geochronological data after references given in Table 1. Abbreviations refer to plutons mentioned in the text: (Mako) Ma = Mamakono granodiorite, Ti = Tinkoto granodiorite, Dbl = Diombalou granite, Bbr = Bouroumbourou granodiorite, Ssk = Sanssakhoto monzogranite, LKPC = Laminia-Kaourou plutonic complex, SLPC = Sandikounda layered plutonic complex; (Falémé) Bal = Balangouma tonalite, Bo = Boboti granodiorite, SF = South Falémé granodiorite, DS = Dar Salam granodiorite, Msl = Moussala granodiorite, Bbj = Bambadji granodiorite, Bt = Boto tonalite; (Kofi) Ga = Gamaye monzogranite, Yt = Yatea monzogranite, Al = Alamoutala granodiorite, Ya = Yatela diorite, Sek = Sekekoto granodiorite.

3.2. Sedimentary basins

The Dialé-Daléma and Kofi Series represent the most extensive occurrence of carbonates rocks in the West African Craton (Bessoles, 1977; Bosse, 1996). Sedimentary rocks of the Dialé-Daléma Series include volcaniclastics, arenites, wackes, siltstones, argillites, and carbonates with minor intercalations of andesite flows and felsic pyroclastic rocks (Bassot, 1987; Dia, 1988; Hirdes and Davis, 2002) (Fig. 1). Sedimentary rocks of the Kofi Series consist of volcaniclastic rocks, wackes, arenites, impure carbonates, siltstones and argillites (Lawrence et al., 2013a) (Fig. 1). Hirdes and Davis (2002) proposed that the transitional field relationships between sediments and volcano-plutonic rocks in the KKI imply a proximal derivation of the sediments from eroded rocks in neighbouring volcano-plutonic belts. The diachroneity of magmatic ages in the region is also reflected in the provenance of the sediments based on available detrital zircon data (Table 1). Tarkwian grabens and associated infill material have not yet been detected in the KKI.

Plutonic and supracrustal rocks	Isotope system	Method	Age (Ma)	Reference
<i>Falémé volcano-plutonic belt</i>				
Boboti granodiorite	U-Pb	TIMS (Zircon)	2080 ± 1	Hirdes and Davis (2002)
Boboti quartz-monzdiorite	U-Pb	LA-ICPMS (Zircon)	2089 ± 9	Lambert-Smith et al. (in press)
Boto tonalite	U-Pb	TIMS (Zircon)	2082 ± 1	Hirdes and Davis (2002)
Balangouma quartz-monzonite	U-Pb	LA-ICPMS (Zircon)	2118 ± 16	Lambert-Smith et al. (in press)
Balangouma monzonite	U-Pb	LA-ICPMS (Zircon)	2113 ± 15	Lambert-Smith et al. (in press)
Balangouma quartz-monzdiorite	U-Pb	LA-ICPMS (Zircon)	2105 ± 10	Lambert-Smith et al. (in press)
Flow-banded rhyolite	U-Pb	TIMS (Zircon)	2099 ± 4	Hirdes and Davis (2002)
<i>Laminia-Kaourou plutonic complex</i>				
Kaourou monzogranite	Pb-Pb	Kober single-grain evaporation (Zircon)	2079 ± 6	Dia et al. (1997)
Lamina granodiorite	Pb-Pb	Kober single-grain evaporation (Zircon)	2105 ± 8	Dia et al. (1997)
Lamina quartz-diorite	U-Pb	LA-ICPMS (Zircon)	2127 ± 6	Dia et al. (1997)
Madina Foulbé granodiorite	Pb-Pb	Kober single-grain evaporation (Zircon)	2138 ± 6	Dia et al. (1997)
<i>Sandikounda layered plutonic complex</i>				
Layered gabbro	Pb-Pb	Kober single-grain evaporation (Zircon)	2158 ± 8	Dia et al. (1997)
<i>Mako volcanic-plutonic belt</i>				
Tinkoto granodiorite	Pb-Pb	Kober single-grain evaporation (Zircon)	2074 ± 5	Gueye et al. (2007)
Rhyolite dyke in the Mamakono pluton	Pb-Pb	Kober single-grain evaporation (Zircon)	2067 ± 12	Gueye et al. (2007)
Mamakono granodiorite	U-Pb	TIMS (Zircon)	2076 ± 3	Hirdes and Davis (2002)
Andesite flow	Sm-Nd	Whole rock isochron	2160 ± 16	Boher et al. (1992)
Tholeïtic basalt	Sm-Nd	Whole rock isochron	2197 ± 13	Dia, 1988
Tholeïtic basalt	Pb-Pb	Whole rock isochron	2195 ± 11	Dia, 1988
<i>Sandikounda amphibolite-gneiss plutonic complex</i>				
Sandikounda tonalitic gneiss	U-Pb	TIMS (Zircon)	2205 ± 15	Gueye et al. (2007)
Sandikounda tonalitic gneiss	Pb-Pb	Kober single-grain evaporation (Zircon)	2194 ± 4	Gueye et al. (2007)
Sandikounda dioritic gneiss	Pb-Pb	Kober single-grain evaporation (Zircon)	2202 ± 6	Dia et al. (1997)
<i>Badon plutonic complex</i>				
Badon granodiorite	Pb-Pb	Kober single-grain evaporation (Zircon)	2113 ± 3 - 2198 ± 2	Gueye et al. (2007)
<i>Dialé-Daléma basin</i>				
Pyroclastite	Pb-Pb	Whole rock isochron	2117 ± 9 (n=2)	Calvez et al. (1990)
Quartz-wacke	U-Pb	TIMS (Zircon)	2165 ± 1 (n=6)	Hirdes and Davis (2002)
Saraya biotite-muscovite-bearing monzogranite	U-Pb	TIMS (Zircon)	2079 ± 2	Hirdes and Davis (2002)
<i>Kofi basin</i>				
Gamaye monzogranite	Rb-Sr	Whole rock isochron	2045 ± 27	Bassot and Caen-Vachette (1984)
Sekekoto granodiorite	U-Pb	LA-ICPMS (Zircon)	2083 ± 7	AMIRA International WAXI (2013)
Alamoutala granodiorite	U-Pb	SHRIMP (Zircon)	2083 ± 7	Masurel et al. (in press)
Yatela diorite	U-Pb	SHRIMP (Zircon)	2106 ± 10	Hein et al. (2015)
Andesitic dyke in the Dialé-Daléma basin	Pb-Pb	Kober single-grain evaporation (Zircon)	2070 ± 10	Calvez et al. (1990)
Andesitic dyke in the Dialé-Daléma basin	Pb-Pb	Kober single-grain evaporation (Zircon)	2072 ± 9	Calvez et al. (1990)
Sandstone	U-Pb	LA-ICPMS (Zircon)	2093 ± 7 (n=10)	Boher et al. (1992)
Feldspathic wacke	U/Pb	SHRIMP (Zircon)	2139 ± 6 (n=27) 2180 ± 9 (n=27)	Hein et al. (2015)
Sandstone	Pb-Pb	Kober single-grain evaporation (Zircon)	2096 ± 8 (n=2) 2142 ± 11 (n=1)	Calvez et al. (1990)
Sandstone	Pb-Pb	Kober single-grain evaporation (Zircon)	2125 ± 8 (n=3) 2156 ± 10 (n=3)	Calvez et al. (1990)

Table 1. Compilation of available geochronological data for the Kédougou-Kénieba inlier

3.3. Tectonics

Rocks in the KKI have undergone polycyclic deformation. A summary table presenting structural events reported for different regions of the KKI is given in Table 2. Most authors report an early period of thrusting tectonics responsible for crustal thickening (D_1 - D_2) followed by a period of transcurrent tectonics accommodating oblique convergence (D_3 - D_4) (Diene et al., 2012). The early deformation episode (D_1) was reported in the Mako belt where it is correlated with stratigraphic stacking and the formation of a NNW-trending planar fabric (Dabo and Aïfa, 2010, 2011; Gueye et al., 2008; Diene et al., 2012; Lawrence et al., 2013a; Masurel et al., in press a, b, c). The elongated geometry of the Sandikounda layered plutonic complex (ME-II) and the

Laminia-Kaourou plutonic complex (ME-III), together with local textural variations between magmatic and solid-state fabrics indicate syn-tectonic timing of magma emplacement, which constrain the D₁ event to have occurred between ca. 2160 Ma and 2120 Ma (Gueye et al., 2008). The second (D₂) and third (D₃) deformation events were responsible for the formation of map scale structures and massive magmatic addition (ME-IV, ME-V). These two deformation events mark the principal imprint of the Eburnean orogeny, which occurred between ca. 2115 and 2075 Ma in the KKI (Hirdes and Davis, 2002; Gueye et al., 2008). Folding during D₂ is marked by a locally penetrative NNE-trending cleavage (Dabo and Aïfa, 2010; Lawrence et al., 2013a; Diene et al., 2012; Masurel et al., in press a). Fold and fault geometries, and kinematic indicators are consistent with progressive NW-SE-directed shortening. The following D₃ event is associated with the strike-slip reactivation of early accretionary structures and the formation of steep NNE-trending sinistral shear zones (Diene et al., 2012; Lawrence et al., 2013a; Masurel et al., in press a, b). Fault geometries and kinematic indicators are consistent with NNW-SSE-directed shortening. The D₂ and D₃ events documented in the KKI relate to the evolution of a regional system accommodating oblique convergence during the Eburnean orogeny (Masurel et al., in press a). The Senegal-Mali Shear Zone and the Main Transcurrent Zone are interpreted to have formed during the onset of D₂ as transpressional shear zones (Fig. 1) (Lawrence et al., 2013a; Treloar et al., 2014). The D₃ event has been correlated with hydrothermal fluid flow and gold mineralisation along the Senegal-Mali Shear Zone and the Main Transcurrent Zone (Lawrence et al., 2013a; Treloar et al., 2014; Masurel et al., in press a, b, c). A last deformation event (D₄) has been locally reported for the Loulo region and is correlated with the formation of NW-trending z-shaped folds and the dextral reactivation of the N- to NNE-trending structural corridors (Dabo and Aïfa, 2011). This very late deformation episode occurred between ca. 2075 and 2050 Ma under E-W to NE-SW-directed shortening (Dabo and Aïfa, 2011).

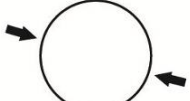
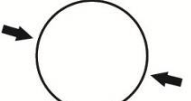
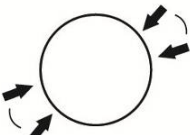
	Mako volcano-plutonic belt (Gueye et al., 2008) (Diene et al., 2012)	Loulo - Falémé region (Dabo and Aïja, 2010, 2011) (Lawrence et al., 2013a)
D4 Very late deformation (ca. 2075-2050 Ma)		 <p>Assymmetric NW-trending z-shaped folds. NW- and NE-trending dextral faults. Dextral reactivation of NNE-trending structural corridors.</p>
D3 Eburnean orogeny (ca. 2115-2075 Ma)	 <p>Sinistral shearing along the MTZ, N-trending and NNE-trending faults.</p>	 <p>Sinistral shearing along the SMSZ, N-trending and NNE-trending faults.</p>
D2 Eburnean orogeny (ca. 2115-2075 Ma)	 <p>Formation of NE-trending folds and SE-verging thrusts responsible for stratigraphic stacking.</p>	 <p>Deformation continuum: early recumbent NNE-trending folds and NW-verging thrusts followed by the formation of upright NNE-trending folds and associated penetrative S2 cleavage.</p>
D1 Early deformation (ca. 2160-2120 Ma)	 <p>Formation of a NNW-trending planar fabric and associated thrusting? Sinistral displacement along ENE-trending high-grade metamorphic foliation.</p>	

Table 2. Compilation of reported tectonic events in the Mako volcano-plutonic belt and Loulo-Falémé region of the KKI. Abbreviations: SMSZ, Senegal-Mali Shear Zone; MTZ, Main Transcurrent Zone.

3.4. Metamorphism

Regional peak metamorphism occurred under regional greenschist-facies conditions during the Eburnean orogeny (Debat et al., 1984; Liégeois et al., 1991; Dia et al., 1997). The reported greenschist-facies assemblages (e.g., biotite, chlorite, muscovite, quartz, K-feldspar) in country rocks of the region may be interpreted as resulting from a pervasive retrogression and hydrothermal overprint of older amphibolite-facies assemblages as proposed in southern Ghana by John et al. (1999). In contrast, amphibolite-facies conditions have been observed locally in contact aureoles surrounding Eburnean granitoids (Debat et al., 1984; Pawlig et al., 2006; Masurel et al., in press).

3.5. Post-Birimian dolerite dykes

Dolerite dykes are abundant across the West African craton and present as magnetic linear features due to their remanent magnetism and high magnetic susceptibility (Perrouty et al., 2012). Two sets of dolerite dyke swarms have been reported in the KKI and consistently present as ENE-WSW and NE-SW-oriented lineaments. Both dyke sets crosscut the Paleoproterozoic basement and show no evidence for deformation and hydrothermal alteration. These dolerite swarms can be correlated with the several generations of Mesoproterozoic to Neoproterozoic dolerite swarms recorded in eastern Senegal and dated at 1500 Ma, 1300 Ma and 1150 Ma (Kalsbeek et al., 2008; Perrouty et al., 2012).

4. Methodology

4.1. Geological mapping and sampling

Geological mapping was conducted in the region with the help a rugged tablet integrating available geological and geophysical data-sets under ArcGIS. Face mapping was conducted on accessible ramps of the open pits in order to provide a robust structural framework for the Sadiola-Yatela region. All structural readings are given in

true north coordinates. Planar features were reported in strike/dip/quadrant and linear data as plunge and azimuth. In this paper, the “s” subscript indicates that the considered structural event is only valid for the Sadiola-Yatela region, which may differ from regional structural compilations reported for the West African Craton.

4.2. Petrography and whole-rock geochemistry

Twenty-eight least-altered samples of representative igneous rocks in the Sadiola-Yatela region were obtained from outcrops, open pits, and diamond drill core. Approximately 1.5 kg of fresh, homogeneous rock was collected per sample. Rust stains were cleaned with abrasives and weathered surfaces were removed. Thin sections were prepared from rock slabs at the University of Western Australia and studied using optical microscopy at the Centre for Exploration Targeting in Perth. Igneous rock classification followed IUGS systematics (Streckeisen, 1974) and was determined using hand specimen description as proxy to rock type and modal composition estimate in thin section. Rock samples were then crushed and chips were pulverized using low chrome-steel vessels. Rock powders were mixed with lithium metaborate/tetraborate and prepared as fusion for lithogeochemistry package LITH-205X analysis at Intertek Genalysis Laboratories in Perth. Major elements were measured by XRF spectrometry. REE, HFSE and trace elements (e.g., Ba, Cr, Cs, Ga, Rb, Sc, Sn, Sr, U, V, W) were analyzed by inductively coupled plasma mass spectrometry (ICP-MS) and inductively coupled plasma optical emission spectrometry (ICP-OES). Other metals were analyzed by the same techniques but prepared with multi-acid digest including hydrofluoric, nitric, perchloric and hydrochloric acids in teflon tubes. Gold content was measured by fire-assay followed by ICP-MS. The Geological Survey of Western Australia Bunbury basalt and Kerba granite standards were analysed during each session to monitor accuracy and instrument stability. The accuracy of the data was typically better than 3 % for the major elements and trace elements were within 6 % of reference values. Raw geochemical data, achieved detection limits, and calculated petrogenetic indicators are listed in the supplementary material. Geochemical data from igneous rocks of the Alamoutala open pit ($n=2$) are included for comparison (Masurel et al., in press b). The location of all samples is illustrated in Figure 2.

4.3. U-Pb geochronology

Focused U-Pb geochronology data was collected from selected igneous rock specimens ($n=13$). Approximately 5 kg of material was collected for each rock sample. After cleaning and removal of weathered surfaces, the rock sample was processed at Geotrack Pty. Ltd. in Australia. The sample was crushed using a mechanical jaw crusher; powdered using a ring mill; and heavy minerals separated using standard heavy liquids and magnetic procedures. Target zircons were handpicked from zircon concentrates under a binocular microscope and mounted in 25 mm epoxy-resin discs with chips of U/Pb zircon standard M257 (561.3 Ma, 840 ppm U; Nasdala et al., 2008) or BR266 (559 Ma, 903 ppm U; Stern, 2001), crystals of reference zircons OGC1 (3465 Ma; Stern et al., 2009) and silicate glass NBS610 at the Minsep Laboratories in Western Australia. Cathodoluminescence and backscattered electron imaging on gold-coated mounts were performed using a Tescan Vega-3 scanned electron microscope at the Centre for Microscopy, Characterization and Analysis of the University of Western Australia in Perth. U–Pb analyses were performed using the sensitive high-resolution ion microprobe (SHRIMP II) at the John de Laeter Centre of Excellence for Mass Spectrometry of Curtin University in Perth. Geochronological data was collected using standard operating procedures similar to those described by Compston et al. (1984) and Wingate and Kirkland (2013). Operating parameters include a 10 keV primary O^{2-} beam focussed to a $\sim 20 \mu m$ diameter spot, a net primary ion current between 1.6 and 3.0 nA and a secondary ion analyser set to a mass of ≥ 5000 . Six data collection cycles (scans) were performed per analysis, and count times (per scan) were 10 s for the ^{204}Pb , ^{206}Pb , and ^{208}Pb mass peaks and background, and 30 s for the ^{207}Pb mass peak. Analyses of unknowns were referenced to multiple analyses of the primary and external standards for U/Pb calibration. Calibration and reproducibility uncertainties are included in the errors of $^{238}U/^{206}Pb$ ratios and age data. Data reduction was carried out using the software SQUID v2.5 and ISOPLOT v3.0 (MS Excel add-ins by Ludwig, 2003, 2009). Corrections for common Pb were based on measured ^{204}Pb , assuming an average crustal composition appropriate to the age of the mineral (Stacey and Kramers, 1975). Analytical cut-offs were used in order to minimise the risk of including zircons with potentially disturbed U-Pb systematics during data interpretation. The reported U-Pb

ages were derived from concordant to near-concordant grains (discordance between -3% and +10%). In addition, analyses that comprised more than 1% of non-radiogenic ^{206}Pb and yielded U concentrations over a 1000 ppm were rejected. All age estimates are reported at 2σ error and include propagated uncertainties in the standard calibrations. Raw geochronological data is provided in the supplementary material

5. Results

5.1. Lithostratigraphy

The local geology presented hereafter is based on the recent field investigation by the authors and is illustrated in Figure 2. The geology of the Kofi basin in the Sadiola-Yatela region consists of carbonate and detrital sedimentary rocks that exhibit KFMASH assemblages (e.g., biotite, chlorite, muscovite, quartz, K-feldspar) indicative of regional greenschist-facies metamorphic conditions. For the purpose of clarity, the prefix “meta” will be omitted in the following section. Carbonate rocks consist of impure limestones in the Sadiola Hill deposit area and are characterised by abundant thin (0.2-2 cm) argillaceous-silty interbeds. Carbonate rocks elsewhere in the region consist of limestones locally interlayered with dolomitic horizons. Meso-scale disharmonic slump folds were mapped in carbonate rocks at the Sadiola Hill and FE3 open pits. The overlying detrital sedimentary rock sequences exhibit way-up indicators such as fining-upwards sequences, scour-and-fill structures, and rare cross-bedding in sandstone, which altogether indicate a younging to the West. These detrital sedimentary rocks consist of feldspathic wackes and arkosic arenites with subordinate rhyolite flows and pyroclastic rocks to the west, progressing to siltstones and argillites further east. A linear to arcuate volcano-sedimentary belt to the west consists of calc-alkaline porphyritic andesites and volcaniclastic rocks interbedded with wackes, arenites, and siltstones. The boundary between rocks of the Kofi Series and rocks of the volcano-sedimentary belt is transitional.

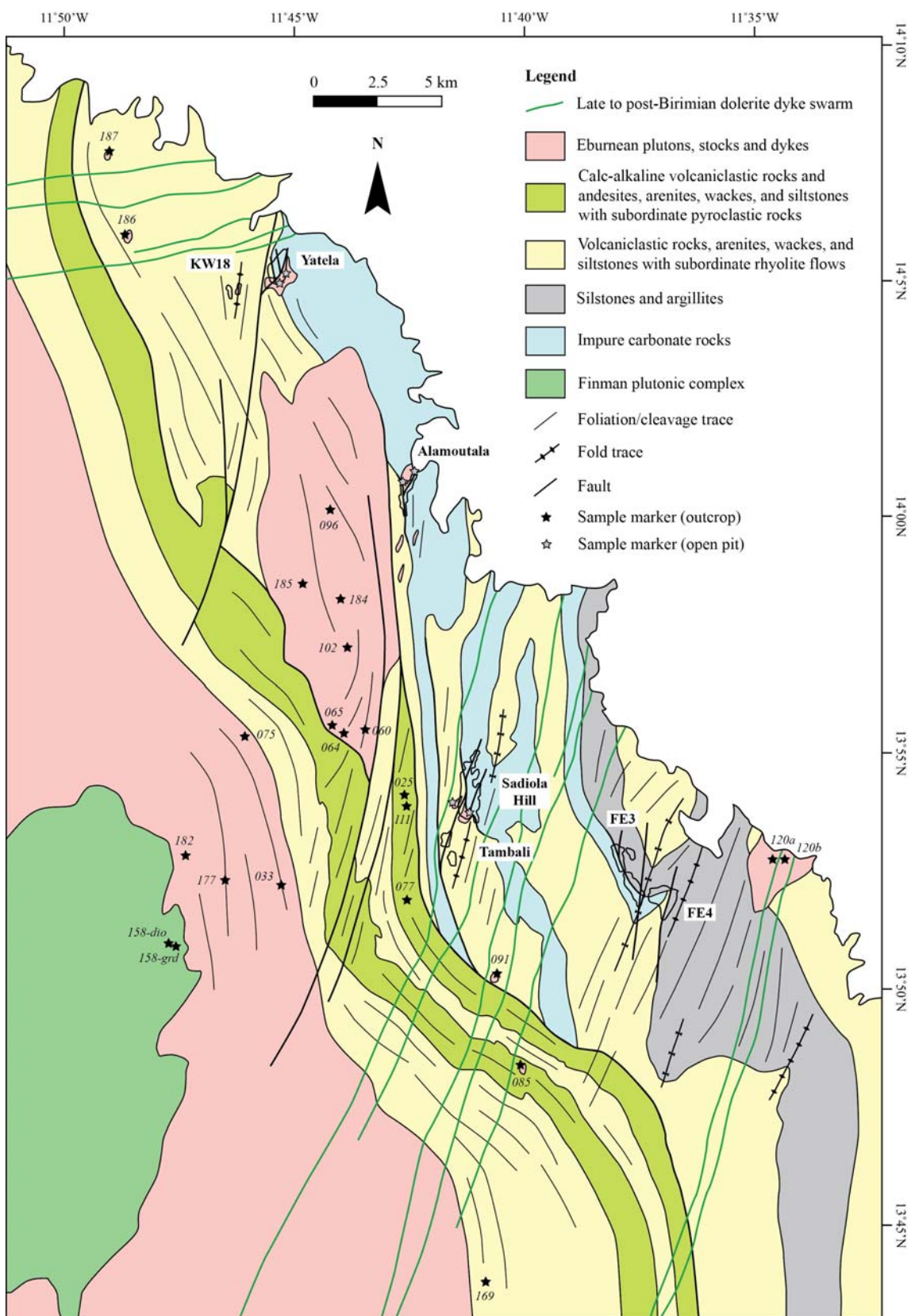


Figure 2. Geology of the Sadiola-Yatela region based on field investigation by the authors and interpretation of SEMOS geophysical data sets.

5.2. Structural framework

The Sadiola Hill, Yatela, and ancillary pits share a similar tectonic evolution (Fig. 2, 3). The data presented hereafter integrates extensive data collected in the open pits with data collected from surface outcrop mapping.

The earliest structural component (D_{1s}) recorded in the region consists of NNW- to N-trending folds. These folds are associated with a weak to strong axial-planar cleavage (S_1) and a gently NNW-plunging intersection lineation (L_1) (Fig. 3). The S_1 planar fabric is sub-parallel to bedding and the general orientation of lithostratigraphic units (see Fig. 2). Fold geometry and lineation data associated with this early deformation event (D_{1s}) are consistent with WSW-ENE-directed shortening. Structural features associated with D_{1s} are better preserved in the Yatela area than further south in the Sadiola area, which is characterised by penetrative reworking of the early fabric by the second episode of folding.

The second structural component (D_{2s}) recorded in the region is correlated with the formation of map-scale NNE-trending structural corridors (see Fig. 2). Early F_1 folds observed in the Sadiola Hill and FE3 open pits have been refolded by F_2 creating interference patterns (Fig. 3, 4A). The F_2 folds are disharmonic with upright to inclined fold hinges. They are associated with a $015^\circ/75^\circ\text{E}$ (e.g. Sadiola Hill, Tambali, Alamoutala) to $035^\circ/75^\circ\text{E}$ (e.g. FE3, FE4) axial-planar cleavage (S_2) indicative of a WNW fold vergence (Fig. 3, 4B-C). Fold axes and intersection lineations plunge gently ($15\text{--}30^\circ$) to the SSW or NNE (Fig. 3, 4D). These F_2 folds are observed from the micro-scale to the map-scale. A large-scale synclinal closure occurs between the FE3 and FE4 open pits (see Fig. 2). A number of NNE-trending thrusts and high-angle reverse faults are closely associated with these F_2 folds. Fold and fault geometry, and lineation data associated with the second deformation event (D_{2s}) are consistent with NW-SE directed shortening.

The following deformation event (D_{3s}) is associated with the strike-slip reactivation of early accretionary structures (e.g., high-angle reverse faults, lithostratigraphic contacts, S_1 , S_2) and the formation of NNE-trending sub-vertical shear zones. The Senegal-Mali Shear Zone consists of alternating high strain and low strain domains mapped along and across the lithological contacts between igneous and sedimentary rocks in the region.

The Sadiola Hill Fracture Zone, the Alamoutala Fracture Zone, and the FE4 Shear Zone (Fig. 3) represent sheared litho-stratigraphic interfaces (see Fig. 2). Such structures are 2-50m wide and are associated with a pinch-and-swell anastomosing geometry that extends both along strike and down dip. These shear zones are discontinuous along strike in contrast to the high-angle NNE-trending shear zones. Steeply-plunging parasitic folds in transposed impure marbles within 25 m of the Sadiola Fracture Zone exhibit an S-shaped asymmetry, indicating of a component of sinistral displacement along the structure (Fig. 3). Sub-horizontal slickenfibres marked by biotite and pyrite on the Alamoutala Fracture Zone indicate sinistral displacement (Fig. 3). Slickenfibres and micro-structural kinematic indicators including strain shadows and mica fish also suggest dominantly sinistral displacement along the NNE-trending high-angle shear zones and reactivated S_2 fabric (Fig. 3). Fault geometries and lineation data associated with the third deformation event (D_{3s}) are consistent with NNW-SSE-directed shortening. Combined channel sampling and three-dimensional rendering of the assay data under Modelling under Leapfrog® shows that the linkage of steep NNE-trending shears with reactivated early accretionary structures (e.g., Sadiola Fracture Zone, Alamoutala Fracture Zone, and FE4 Shear Zone) applied a direct control on ore shoot geometries in the Sadiola Hill, Alamoutala, FE3, and FE4 gold deposits (Fig. 4E-F).

A very late deformation episode (D_{4s}) is associated with a dextral reactivation of earlier accretionary structures. Chlorite-calcite slickenfibres on rare fault walls from the Sadiola Hill and Alamoutala open pits indicate late dextral displacement. Steep NNE-trending faults associated with dextral displacement have been mapped locally in outcrop over the Finman plutonic complex. The apparent dextral offset of the Sadiola volcanics in map scale is tentatively associated with D_{4s} .

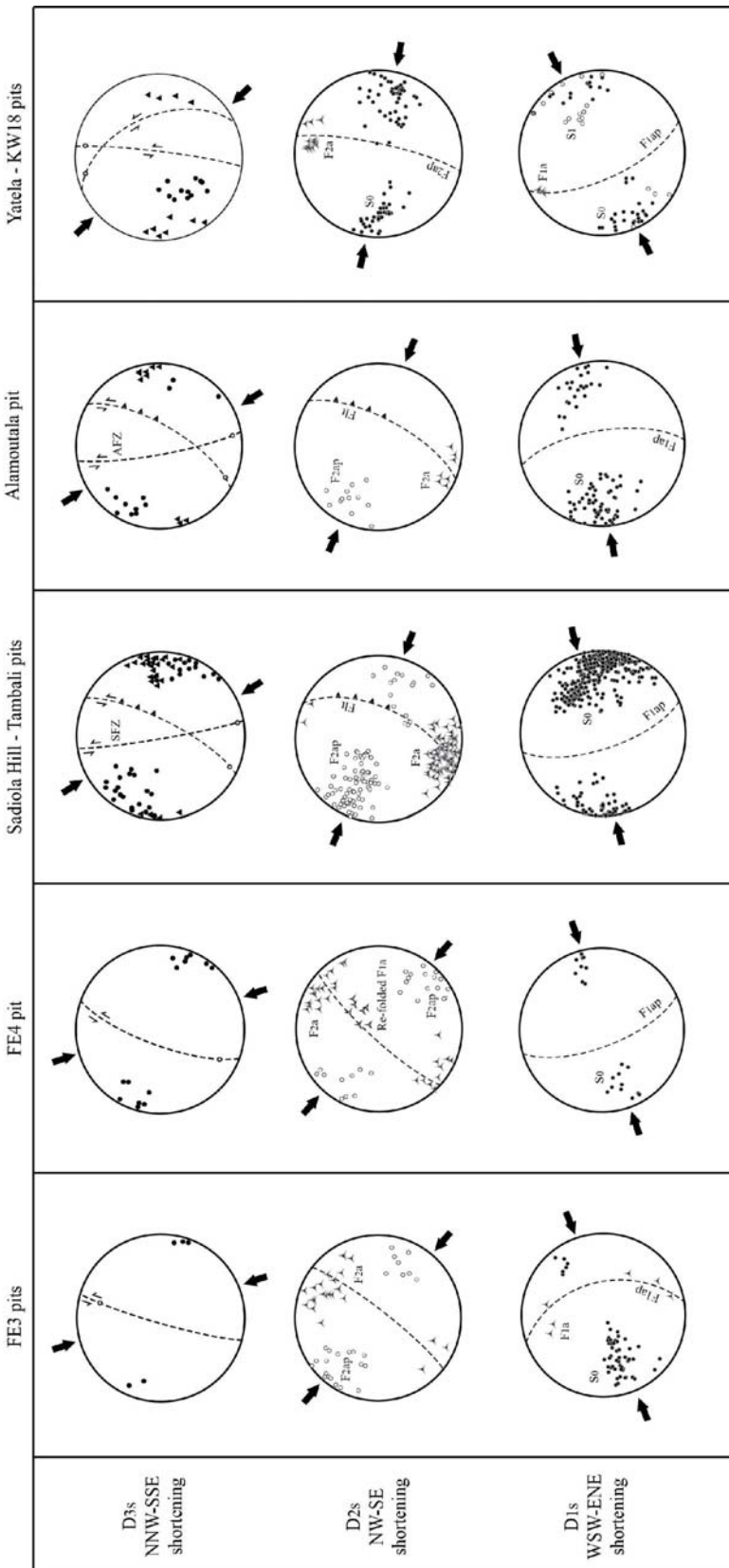


Figure 3. Structural correlation chart including data collected for the Sadiola Hill open pit, the Yatela open pit, and ancillary open pits in the region. SFZ: Sadiola Fracture Zone; AFZ: Alamoutala Fracture Zone.

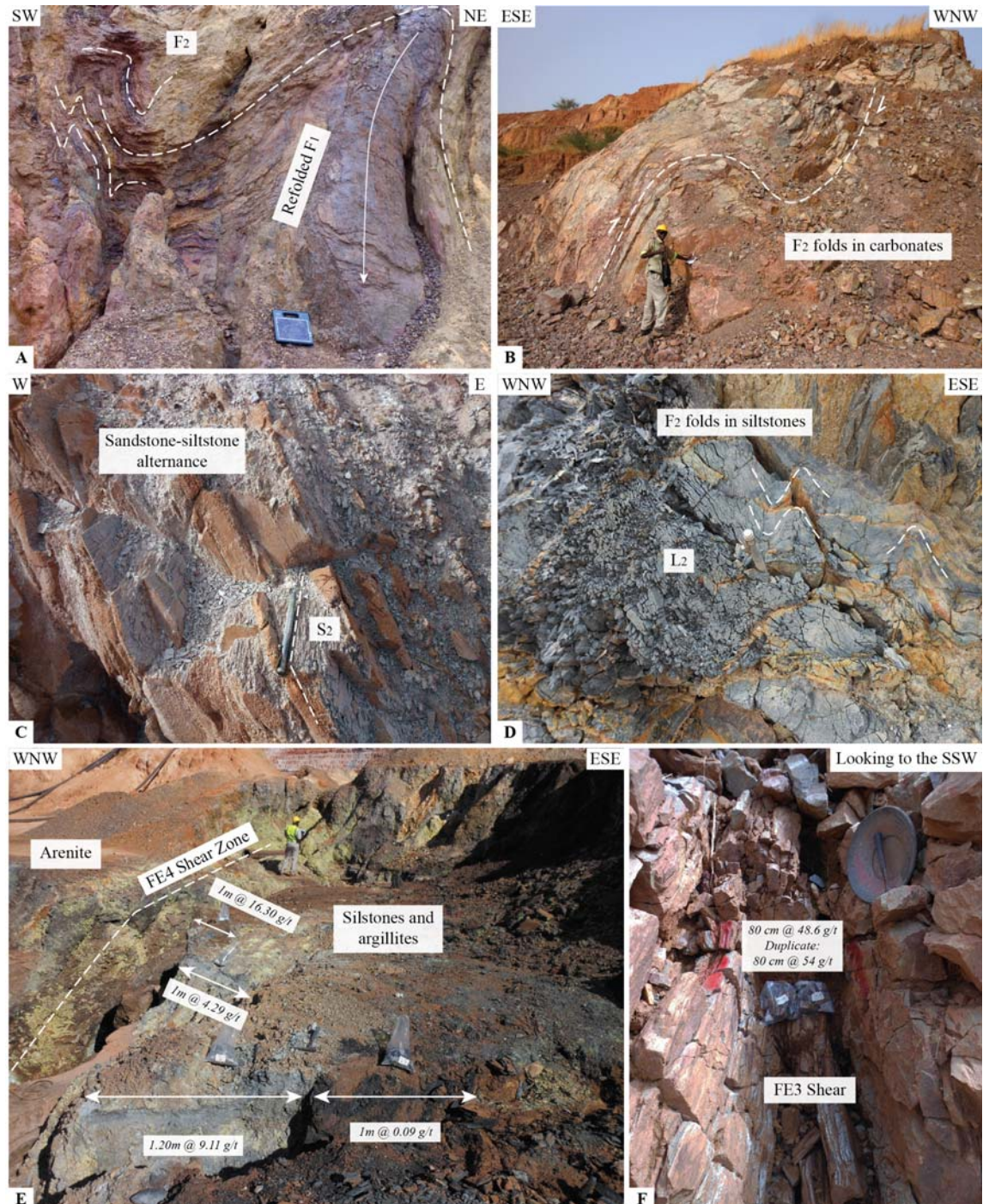


Figure 4. A) Interference pattern resulting from refolding of F_1 by upright F_2 folds in the FE3 open pit. B) Typical F_2 folds show axial-planar cleavage and asymmetry indicative of WNW vergence. C) Refraction of the S_2 cleavage in a sandstone-siltstone alternance. D) Pencil lineation in siltstones. The photograph is looking down stretching lineation, which is indicated by the scribe pen. E) Channel sampling in wall rocks of the mineralised FE4 shear. F) Channel sampling across the mineralised FE3 shear.

5.3. Geochronology

A summary of the determined magmatic crystallisation ages for igneous rocks of the Sadiola-Yatela region is presented in Table 3. The following classification was based on structural evidence recorded in outcrop and absolute timing of magma emplacement. Individual SHRIMP U-Pb geochronology reports (petrographic descriptions, zircon morphology, analytical details, results, interpretation) are provided in the supplementary material.

5.3.1. Pre- to syn- D_{1s} magmatism

SAD-158 β microdiorite and SAD-158grd hornblende-granodiorite:

The outcrop was mapped on a ridge, 12 km west of the Sadiola Hill gold mine. The outcrop is part of the Finman plutonic complex, which is associated with a low U-K-Th signature in the radiometric data. The outcrop consists of microdiorite locally intruded hornblende-granodiorite melts (Fig. 5A-C). The microdiorite is composed of plagioclase feldspars (50% modal vol.) and green hornblende (49% modal vol.) with traces of magnetite (1% modal vol.). The melts are largely composed of quartz (44% modal vol.) and plagioclase feldspars (42% modal vol.) with abundant green hornblende (12% modal vol.) and minor magnetite (up to 2% modal vol.). Both rock types exhibit a solid state planar fabric oriented 342°/83°E. Late cm-wide shear zones oriented 012°/78°E crosscut the latter fabric and dextrally offset the hornblende-granodiorite melts in places (Fig. 5D). Twenty-four near-concordant analyses on magmatic zircons from the microdiorite yield a $^{207}\text{Pb}/^{206}\text{Pb}$ weighted mean date of 2152 ± 7 Ma (MSWD = 1.7) and a Tera-Wasserburg U-Pb Discordia age of 2143 ± 9 Ma (MSWD = 1.16) (Fig. 5E). A Wetherill U-Pb Concordia age could be calculated and yielded a date of 2147 ± 8 (MSWD = 4.6). Twenty-three near-concordant analyses on zircons from the hornblende granodiorite yield a $^{207}\text{Pb}/^{206}\text{Pb}$ weighted mean date of 2142 ± 6 Ma (MSWD = 1.4) and a Tera-Wasserburg U-Pb Discordia age of 2143 ± 8 Ma (MSWD = 1.06) (Fig. 5F). The 2147 ± 8 Ma date is interpreted to represent the magmatic crystallisation age of the microdiorite. The 2142 ± 6 Ma date is interpreted to represent the magmatic crystallisation age of the hornblende-granodiorite.

Sample	Crystallisation age (Ma)	Inheritance (Ma)
SAD-158 β , microdiorite	2147 ± 8 (n=24)	-
SAD-158grd, hornblende-granodiorite	2142 ± 6 (n=23)	-
SAD-077, quartz-feldspar-phyric andesite	2118 ± 9 (n=11)	2249 ± 8 (n=1), 2166 ± 7 (n=20)
SD1071-285m-QFP, quartz-feldspar-porphyry	2108 ± 9 (n=12)	2200 ± 23 (n=3), 2147 ± 12 (n=8)
STA-037, diorite	2114 ± 9 (n=12)	2161.5 ± 7 (n=12)
SAD-096, hornblende-biotite quartz-monzodiorite	2089 ± 7 Ma (n=10)	-
SAD-185, feldspar-phyric biotite-granodiorite	2083 ± 6 (n=22)	2145 ± 25 (n=2)
SAD-102, biotite-bearing quartz-monzonite	2091 ± 8 (n=7)	2142 ± 13 (n=2)
SAD-182, hornblende-biotite granodiorite	2090 ± 9 (n=11)	2188 ± 15 (n=1)
SAD085, quartz-monzonite	2081 ± 3 (n=19)	-
SAD065, biotite-monzogranite	2074 ± 8 Ma (n=13)	2132 ± 9 (n=1)
SAD075, biotite-granite	2071 ± 5 Ma (n=15)	2120 ± 11 (n=2)
SAD033, biotite-granite	2066 ± 8 Ma (n=13)	2131 ± 22 (n=2)

Table 3. Summary U-Pb ages of igneous rocks from the Sadiola-Yatela region

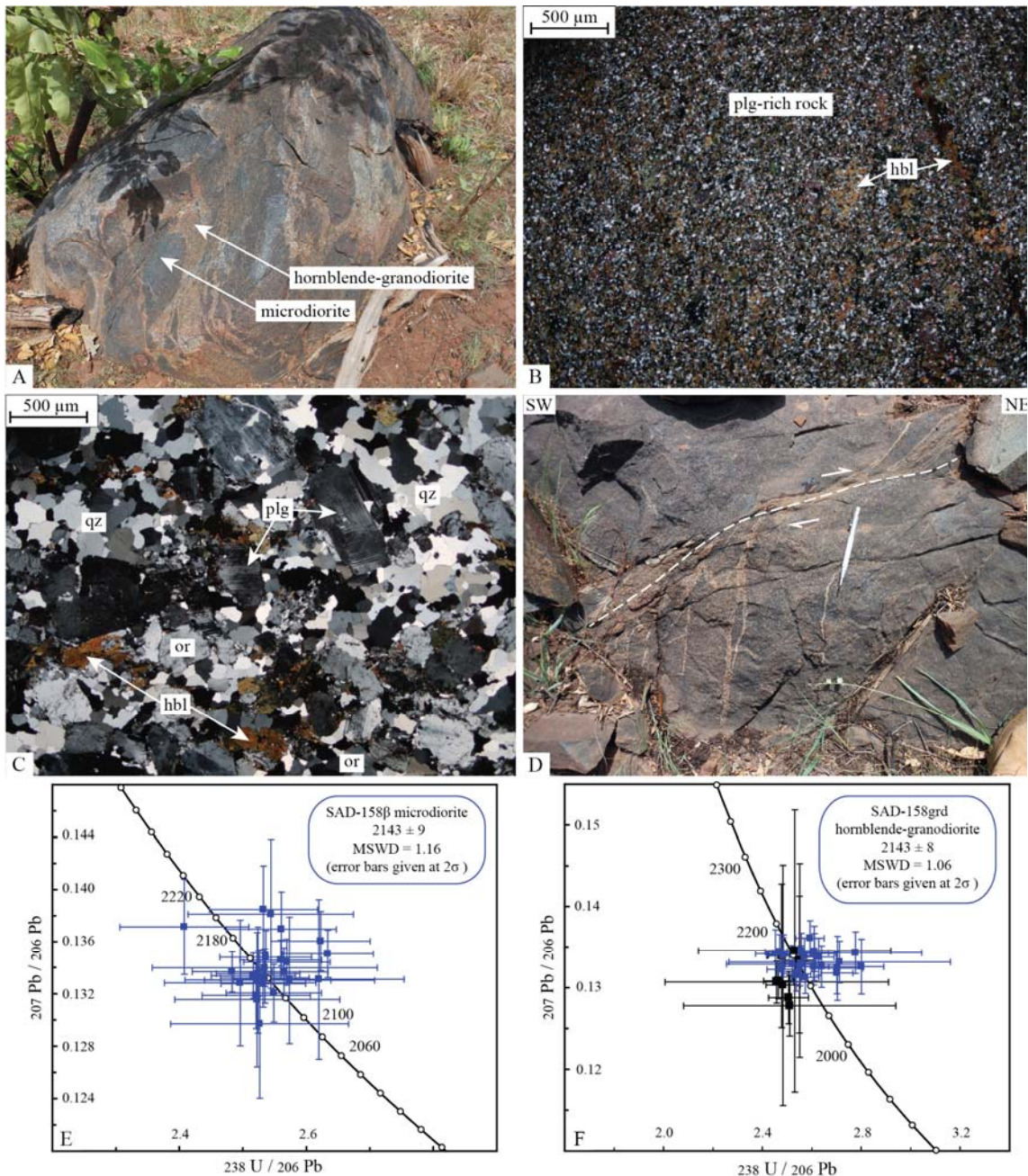


Figure 5. A) Field photograph of the outcrop within the Finman plutonic complex. A microdiorite pluton (SAD-158 β) is locally intruded by hornblende-granodiorite melts (SAD-158grd), which give rocks of the outcrop an apparent breccia texture. B) Representative micrograph of the microdiorite (crossed polars). C) Representative micrograph of the hornblende-granodiorite (crossed polars). D) Dextral cm-wide shear zones offset the hornblende-granodiorite melts in places. E) Tera-Wasserburg U-Pb Discordia plot for zircon analyses from the microdiorite. F) Tera-Wasserburg U-Pb Discordia plot for zircon analyses from the hornblende-granodiorite. *Black squares represent rejected analyses.

5.3.2. *Syn-D_{2s} magmatism*

SAD-077 quartz-feldspar-phyric andesite:

Porphyritic andesites outcrop in and surrounding the Sadiola village (Fig. 6A). Rock samples collected at different locations in the area show no significant mineralogical variations and consist of feldspar (up to 10% modal vol.) and quartz phenocrysts (2% modal vol.) set in a fine-grained (<0.1 mm) to very fine-grained (<0.05 mm) quartz-feldspathic groundmass (80% modal vol.). These rocks exhibit evidence for high strain solid-state deformation including a mylonitic fabric oriented 025°/85°E, strained porphyroclasts with tails, and a sub-horizontal lineation plunging at 5° towards 025° (Fig. 6B). Microtectonic evidence such as symmetrical porphyroclasts and strain shadows indicate dominantly pure shear deformation. The presence of fractured feldspar porphyroclasts and fine grain size of the recrystallised quartz groundmass (<50 µm) together with the abundance of muscovite and biotite along the shear fabric suggest that the mylonites developed at low metamorphic grade (~250-500°C) (e.g., Passchier and Trouw et al., 2005). A least-deformed and least-altered sample of feldspar-quartz-phyric andesite was collected 3 km south from the Sadiola village for geochronology (Fig. 6C). Inheritance proved to be common in that sample based on the $^{207}\text{Pb}/^{206}\text{Pb}$ age distribution. A single zircon analysis yielded a $^{207}\text{Pb}/^{206}\text{Pb}$ date of 2249 ± 8 Ma. Twenty zircon analyses defined a second population associated with a $^{207}\text{Pb}/^{206}\text{Pb}$ weighted mean date of 2166 ± 7 Ma (MSWD = 1.16). Eleven zircon analyses defined a third population associated with a $^{207}\text{Pb}/^{206}\text{Pb}$ weighted mean date of 2118 ± 9 Ma (MSWD = 0.47) and a Tera-Wasserburg U-Pb Discordia date of 2115 ± 11 Ma (MSWD = 0.41) (Fig. 6D). The younger date of 2118 ± 9 Ma is interpreted to represent the magmatic crystallisation age of the porphyritic andesite. The two older dates likely represent inherited zircon components.

SD1071-285m quartz-feldspar-porphyry:

Steep NNE-trending quartz-feldspar-porphyry dykes have been mapped in the Sadiola Hill and Tambali open pits. The quartz-feldspar-porphyritic dykes are generally 1-2 m wide and are spatially associated with NNE-trending faults oriented 020°/75°E. These dykes crosscut an early generation of diorite as well as impure carbonates and detrital sedimentary rocks in the Sadiola Hill open pit. These dykes were locally folded by F₂ and boudinaged. They were also sheared during subsequent D_{3s} deformation and host mineralisation at Sadiola Hill and Tambali. A least-deformed and least-altered sample of quartz-feldspar porphyry was collected from deep diamond drill core at Sadiola Hill. The rock exhibits sub-rounded sparse quartz (5-10% modal vol.) and euhedral prismatic feldspar phenocrysts (5-10% modal vol.) set in a fine-grained (<0.1 mm) to very fine-grained (<0.05 mm) equant quartzo-feldspathic groundmass (80-90% modal vol.). Inheritance also proved to be common in that sample based on the ²⁰⁷Pb/²⁰⁶Pb age distribution. Three zircon analyses yielded a ²⁰⁷Pb/²⁰⁶Pb weighted mean date of 2200 ± 23 Ma. Eight zircon analyses defined a second population associated with a ²⁰⁷Pb/²⁰⁶Pb weighted mean date of 2147 ± 12 Ma (MSWD = 0.67). Twelve zircon analyses defined a third population associated with a ²⁰⁷Pb/²⁰⁶Pb weighted mean date of 2108 ± 9 Ma (MSWD = 0.67) and a Tera-Wasserburg U-Pb Discordia date of 2105 ± 11 Ma (MSWD = 0.89). The younger date of 2108 ± 9 Ma is interpreted to represent the magmatic crystallisation age of the quartz-feldspar-porphyry.

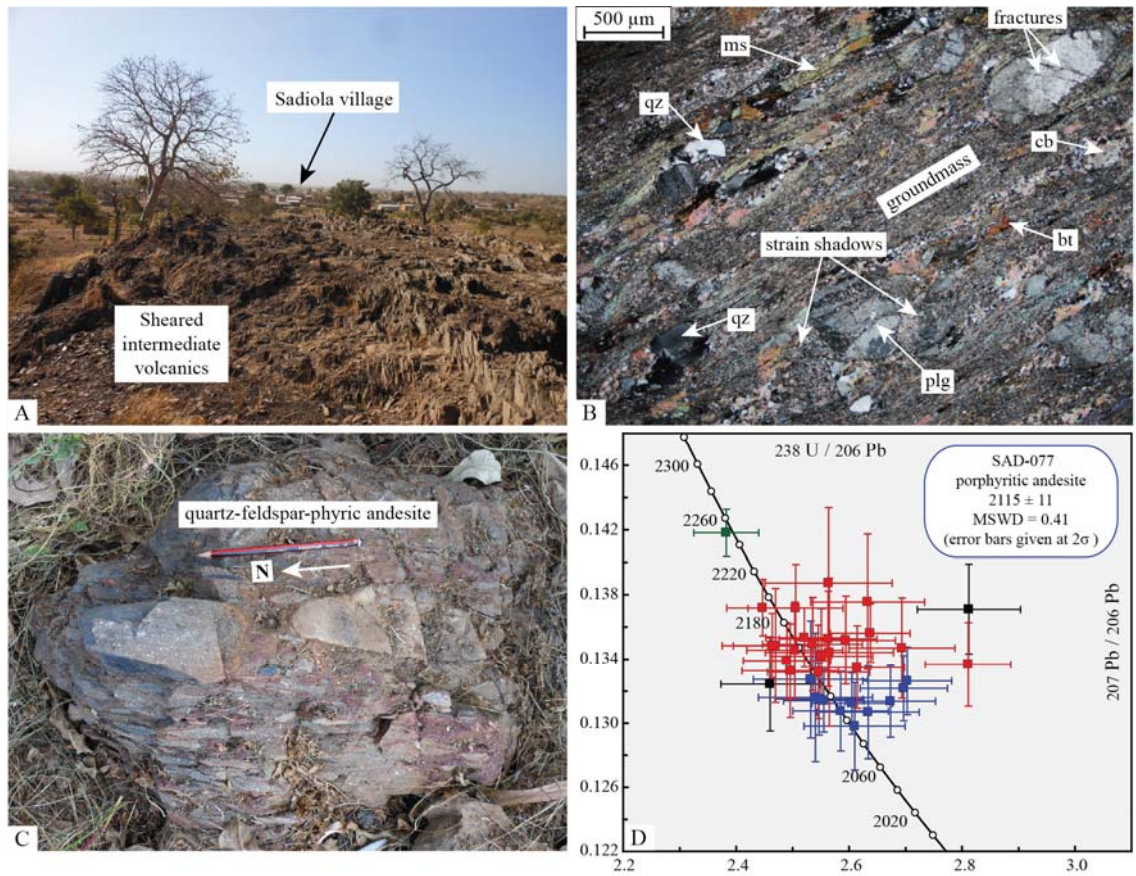


Figure 6. A) Field photograph of deformed intermediate volcanic rocks surrounding the Sadiola village. **B)** Representative micrograph of a mylonite after quartz-feldspar-phyric andesite (crossed polars). **C)** Representative field photograph of the least-deformed and least-altered quartz-feldspar-phyric andesite (SAD-077). **D)** Tera-Wasserburg U-Pb Discordia plot for zircon analyses from SAD-077. *Black squares represent rejected analyses; identified zircon populations are colour-coded.

STA-037 diorite:

A set of NNE-trending diorite dykes (<2 m wide) was identified in the Sadiola Hill and Tambali open pits. Although no direct crosscutting relationships could be observed at Sadiola Hill, these dykes crosscut the quartz-feldspar-porphyry dykes at the Tambali ancillary pits. These diorite dykes are locally affected by F₂ folding and display a well-defined shear foliation marked by aligned sulphides at the Tambali open pits. Despite extensive weathering conditions due to the shallow level of mining activity at the time of fieldwork, a sample was collected from bench walls for geochronology. The rock is essentially composed of plagioclase feldspars (>80% modal vol.) with minor quartz (<10% modal vol.) and green actinolitic hornblende (up to 6% modal vol.). An older population defined by 12 zircons yielded a ²⁰⁷Pb/²⁰⁶Pb weighted mean date of 2161.5 ± 7 Ma (MSWD = 1.2). A younger population defined by 12 zircons yielded a ²⁰⁷Pb/²⁰⁶Pb weighted mean date of 2114 ± 9 Ma (MSWD = 1.17) and a Tera-Wasserburg U-Pb Concordia date of 2119 ± 15 Ma (MSWD = 1.11). The younger date of 2114 ± 9 Ma is interpreted to represent the magmatic crystallisation age of the diorite, which falls within error of that of the intruded quartz-feldspar-porphyry dykes. The older date likely represents an inherited zircon component.

SAD-185 feldspar-phyric biotite-granodiorite:

A feldspar-phyric biotite-granodiorite sample was collected from outcrop 5 km southwest of the Alamoutala open pit (Fig. 7A). The rock is composed of feldspar phenocrysts (up to 30% modal vol.) and minor biotite (5% modal vol.) set in a fine-grained quartzo-feldspathic groundmass (65% modal vol.). Intrusive rocks of the outcrop exhibit a dominant planar fabric oriented 196°/66°NW, which is parallel to S₂. Magmatic biotite and, to a lesser extent, feldspar phenocrysts are stretched along that fabric suggesting deformation occurred at sub-solidus conditions (i.e. magmatic fabric) (Fig. 7B). Two zircon analyses yielded ²⁰⁷Pb/²⁰⁶Pb dates of 2137 ± 21 Ma and 2149 ± 16 Ma. Twenty-two zircon analyses defined a second population associated with a ²⁰⁷Pb/²⁰⁶Pb weighted mean date of 2083 ± 6 Ma (MSWD = 1.5) and a Tera-Wasserburg U-Pb Concordia date of 2083 ± 7 Ma (MSWD = 1.4) (Fig. 7C). The younger date of 2083 ± 6 Ma is interpreted to represent the magmatic crystallisation age of the feldspar-phyric biotite-granodiorite. The two older dates fall within error and likely represent an inherited zircon component.

SAD-085 quartz-monzonite:

A quartz-monzonite sample was collected from outcrop 11 km south of the Sadiola Hill open pit. The small pluton intrudes intermediate volcanics. The intrusive rock consists of quartz phenocrysts (up to 10% modal vol.) set into a fine-grained muscovite-biotite-carbonate-rich groundmass. The intrusive rock exhibits a pervasive planar fabric oriented 122°/74°SW, which is parallel to S₂. The planar fabric is marked by stretched quartz phenocrysts, suggesting deformation occurred at sub-solidus conditions (i.e. magmatic fabric). Such fabric is associated with a well-defined lineation plunging 25° towards 295°. Nineteen near-concordant analyses on zircons yielded a ²⁰⁷Pb/²⁰⁶Pb weighted mean date of 2081 ± 3 Ma (MSWD = 0.99) and a Tera-Wasserburg U-Pb Discordia date of 2082 ± 6 Ma (MSWD = 0.76). The 2081 ± 3 Ma date is interpreted to represent the magmatic crystallisation age of the quartz-monzonite.

SAD-096 hornblende-biotite-bearing quartz-monzodiorite:

A hornblende-biotite-bearing quartz-monzodiorite sample was collected from outcrop 3 km west of the Alamoutala open pit (Fig. 7D). The rock is largely composed of plagioclase feldspars (75% modal vol.) with abundant green hornblende (up to 15% modal vol.), minor biotite (2% modal vol.) and traces of magnetite (up to 2% modal vol.) (Fig. 7E). The plutonic rock does not exhibit any sub-solidus or solid-state fabric. The pluton is associated with a hornblende-hornfels skarn aureole in surrounding detrital meta-sedimentary rocks. Contact-metamorphic mineral assemblages preferentially developed along a planar fabric oriented 150°/60°W in meta-sediments. They consist of hornblende, actinolite, and epidote with traces of pyrite and magnetite. Zircon yield for the hornblende-biotite-bearing quartz-monzodiorite was poor (n=20<). Ten near-concordant analyses on zircons yield a ²⁰⁷Pb/²⁰⁶Pb weighted mean date of 2089 ± 7 Ma (MSWD = 0.47) and a Tera-Wasserburg U-Pb Discordia date of 2092 ± 13 Ma (MSWD = 0.44) (Fig. 7F). The 2089 ± 7 Ma date is interpreted to represent the magmatic crystallisation age of the hornblende-biotite-bearing quartz-monzodiorite. The absolute crystallisation age suggests that it emplaced syn-D_{2s}. The absence of fabric indicates it emplaced in a low strain zone.

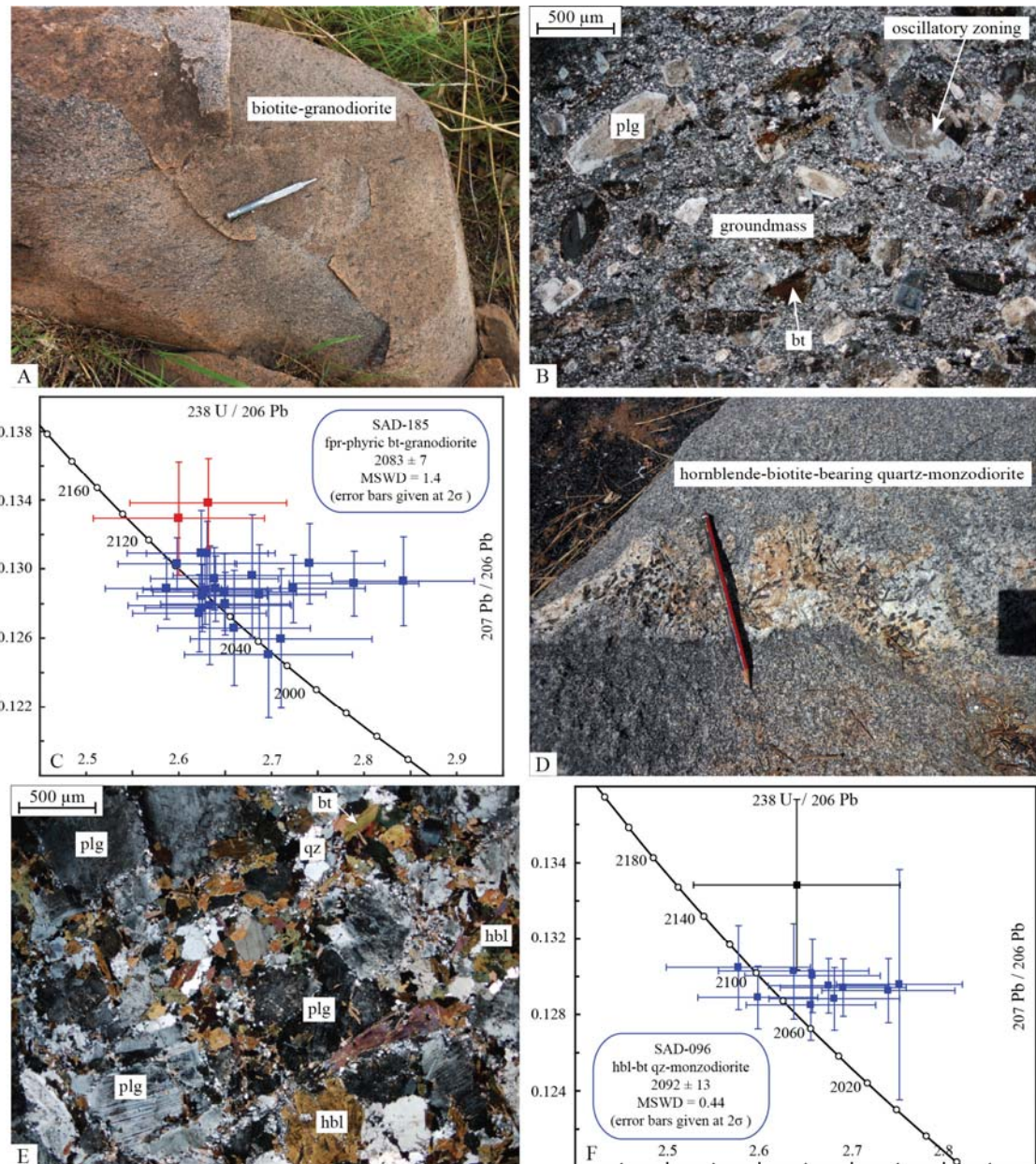


Figure 7. A) Field photograph of the feldspar-phyric biotite-granodiorite (SAD-185). B) Representative micrograph of the pluton (crossed polars). Stretched magmatic feldspar and biotite minerals indicate the syn-tectonic emplacement of the pluton. C) Tera-Wasserburg U-Pb Discordia plot for zircon analyses from SAD-185. D) Field photograph of the hornblende-biotite-bearing quartz-monzonodiorite (SAD-096). E) Representative micrograph of the pluton (crossed polars) showing abundant primary hornblende. F) Tera-Wasserburg U-Pb Discordia plot for zircon analyses from SAD-096. *Black squares represent rejected analyses; identified zircon populations are colour-coded.

SAD-102 biotite-bearing quartz-monzonite:

A biotite-bearing quartz-monzonite sample was collected from outcrop 7 km northwest of the Sadiola Hill open pit on the road to the Alamoutala village. The intrusive rock is light pink and has a weak magnetic response using a magnetic scribe pen. The rock is composed of plagioclase and alkali feldspars (80% modal vol.), quartz (15% modal vol.), minor biotite (5% modal vol.), and traces of magnetite (up to 1% modal vol.). The rock does not exhibit any sub-solidus or solid-state fabric. Zircon yield for the quartz-monzonite was poor ($n=15$). Two zircon analyses yielded $^{207}\text{Pb}/^{206}\text{Pb}$ dates of 2136 ± 10 Ma and 2147 ± 9 Ma. Seven zircon analyses defined a second population associated with a $^{207}\text{Pb}/^{206}\text{Pb}$ weighted mean date of 2091 ± 8 Ma (MSWD = 1.6). The date of 2091 ± 8 Ma is interpreted to represent the magmatic crystallisation age of the biotite-bearing quartz-monzonite. The two older dates fall within error and likely represent an inherited zircon component. The absolute crystallisation age suggests that the biotite-bearing quartz-monzonite emplaced syn-D_{2s}. The absence of fabric indicates it emplaced in a low strain zone.

SAD-182 hornblende-biotite-granodiorite:

A hornblende-biotite-granodiorite sample was collected from outcrop 3 km northwest of the Bembokoto village. The rock is largely composed of plagioclase feldspars (>65% modal vol.) and quartz (25% modal vol.) with minor green hornblende (up to 5% modal vol.) and biotite (3% modal vol.). Rocks of the outcrop are overall undeformed but locally exhibit cm-wide shear zones. These structures are marked by a solid state planar fabric oriented N010/60E and S-C fabrics indicating sinistral displacement. Late barren quartz veins crosscut the intrusion and are oriented N282/85N. A single zircon analysis yielded a $^{207}\text{Pb}/^{206}\text{Pb}$ date of 2188 ± 15 Ma. Eleven zircon analyses defined a second population associated with a $^{207}\text{Pb}/^{206}\text{Pb}$ weighted mean date of 2090 ± 9 Ma (MSWD = 1.5) and a Tera-Wasserburg U-Pb Discordia date of 2103 ± 20 Ma (MSWD = 0.98). The younger date of 2090 ± 9 Ma is interpreted to represent the magmatic crystallisation age of the hornblende-biotite-granodiorite. The older date likely represents an inherited zircon component. The absolute crystallisation age and late cm-wide shear zones suggest that the hornblende-biotite-granodiorite emplaced syn-D_{2s} in a low strain zone.

5.3.3. *Syn-D_{3s} magmatism*

SAD-033 biotite-granite:

A biotite-granite sample was collected from outcrop 1 km east of the Bembokoto village (Fig. 8A). The intrusive rock consists of feldspar phenocrysts (up to 20% modal vol., alkali > plagioclase) and minor biotite (3% modal vol.) set in a finer-grained quartzo-feldspathic groundmass (80% modal vol.) (Fig. 8B). Stretched feldspar minerals and aligned mafic enclaves mark a pronounced planar fabric oriented 341°/82°E. The latter fabric is associated with a sub-horizontal lineation plunging 13° towards 161°. The dominant fabric is locally overprinted by cm-wide D_{3s} shear zones oriented 315°/85°W. These shears sinistrally offset the mafic enclaves in places. Two zircon analysis yielded ²⁰⁷Pb/²⁰⁶Pb dates of 2129 ± 17 Ma and 2132 ± 14 Ma. Thirteen zircon analyses defined a second population associated with a ²⁰⁷Pb/²⁰⁶Pb weighted mean date of 2066 ± 8 Ma (MSWD = 1.19) and a Tera-Wasserburg U-Pb Discordia date of 2069 ± 14 (MSWD = 1.07) (Fig. 8C). The younger date of 2066 ± 8 Ma is interpreted to represent the magmatic crystallisation age of the biotite-granite. The two older dates fall within error and likely represent an inherited zircon component.

SAD-075 biotite-granite:

A biotite-granite sample was collected from outcrop 5 km east of the Kinboukourou village (Fig. 8D). The rock is composed of feldspar phenocrysts (15% modal vol.) and tabular brown biotite (5% modal vol.) set in a medium-grained quartzo-feldspathic groundmass (80% modal vol.) (Fig. 8E). Stretched feldspar phenocrysts mark a planar fabric oriented 135°/65°SW. The biotite-granite is cut by an aplite dyke that exhibits folding axial-planar to that fabric. Two zircon analysis yielded ²⁰⁷Pb/²⁰⁶Pb dates of 2113 ± 10 Ma and 2123 ± 7 Ma. Fifteen zircon analyses defined a second population associated with a ²⁰⁷Pb/²⁰⁶Pb weighted mean date of 2071 ± 5 Ma (MSWD = 1.4) and a Tera-Wasserburg U-Pb Discordia date of 2072 ± 9 Ma (MSWD = 0.91) (Fig. 8F). The younger date of 2071 ± 5 Ma is interpreted to represent the magmatic crystallisation age of the biotite-granite. The two older dates fall within error and likely represent an inherited zircon component.

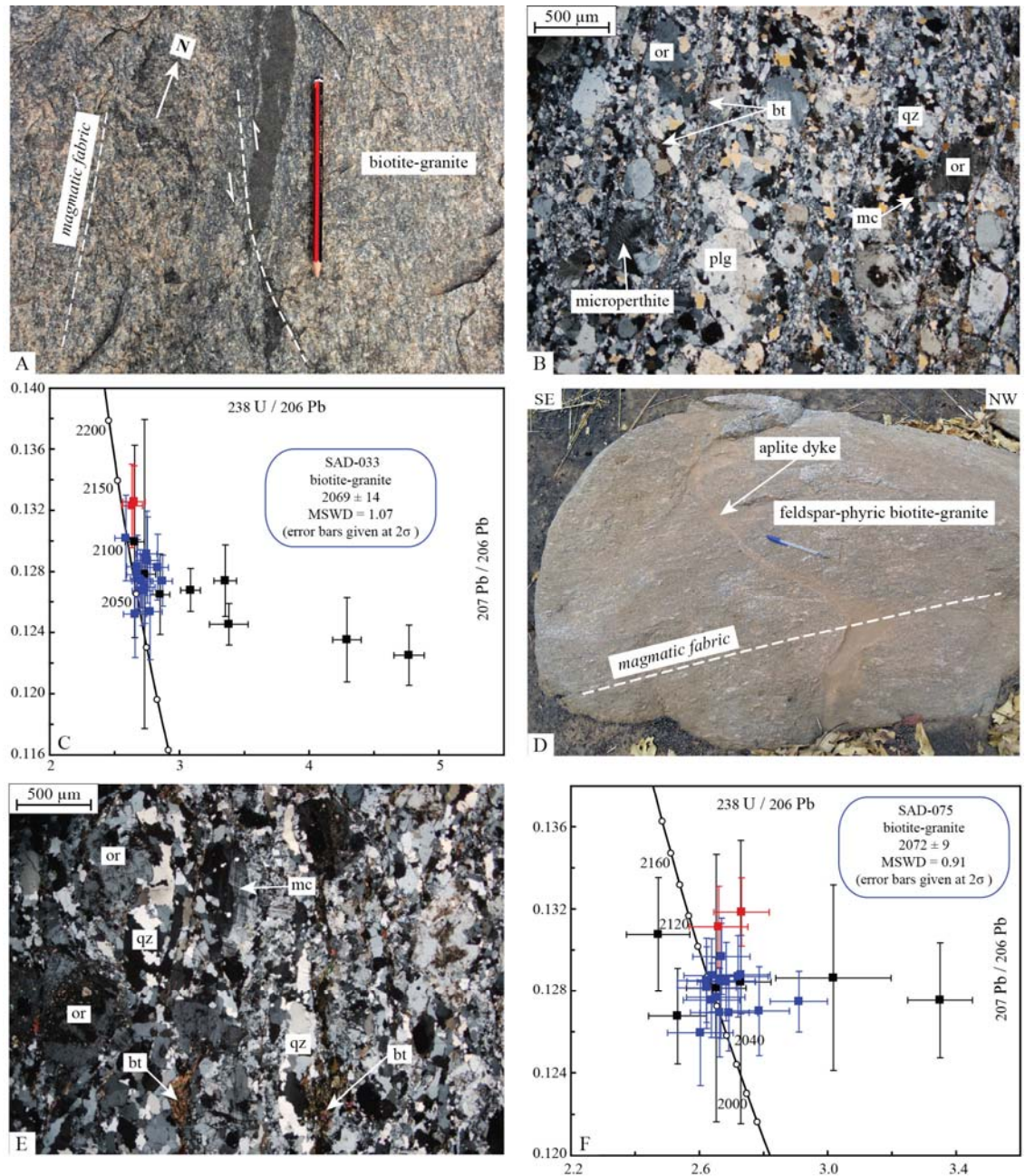


Figure 8 A) Field photograph of the deformed biotite-granite (SAD-033). B) Representative micrograph of the pluton (crossed polars). C) Tera-Wasserburg U-Pb Discordia plot for zircon analyses from SAD-033. D) Field photograph of the deformed biotite-granite (SAD-075). E) Representative micrograph of the pluton (crossed polars). F) Tera-Wasserburg U-Pb Discordia plot for zircon analyses from SAD-075. *Black squares represent rejected analyses; identified zircon populations are colour-coded.

SAD-065 biotite-monzogranite:

A biotite-monzogranite sample was collected from outcrop 4 km northwest of the Neteko village. The intrusive rock is light pink and has a strong magnetic response using a magnetic scribe pen. The rock is largely composed of alkali and plagioclase feldspars (75% modal vol.) and quartz (20% modal vol.) with minor biotite (3% modal vol.) and traces of magnetite (1% modal vol.). A single zircon analysis yielded a $^{207}\text{Pb}/^{206}\text{Pb}$ date of 2132 ± 9 Ma. Thirteen zircon analyses defined a second population associated with a $^{207}\text{Pb}/^{206}\text{Pb}$ weighted mean date of 2074 ± 8 Ma (MSWD = 2.1) and a Tera-Wasserburg U-Pb Discordia date of 2082 ± 13 Ma (MSWD = 1.0). The younger date of 2074 ± 8 Ma is interpreted to represent the magmatic crystallisation age of the biotite-monzogranite. The older date likely represents an inherited zircon component. The absence of any fabric precluded the accurate integration of the pluton with respect to the local structural framework. The absolute crystallisation age and comparable petrographic characteristics with SAD-033 and SAD-075, however, suggest that the biotite-monzogranite emplaced syn-D_{3s} in a low strain zone.

5.4. Whole rock geochemistry

5.4.1. Major elements

The classification scheme adopted in this study is the non-genetic, non-tectonic geochemical classification by Frost et al. (2001). The three-tiered classification uses the $\text{FeO}/(\text{FeO}+\text{MgO})$ ratio (i.e. Fe^*), the modified alkali-lime index (i.e. MALI) and the aluminium saturation index (i.e. ASI). The Fe^* conveys information about the differentiation history of the magma. The MALI conveys information about the magma sources. The ASI conveys information about the magma sources and conditions of melting. Most of the igneous rocks in the Sadiola-Yatela region are magnesian, with only ~25% of the samples plotting in the ferroan field (Fig. 9A). Most of the samples classify as calc-alkalic to alkali-calcic, with only three samples being calcic (Fig. 9B). Evaluation of the ASI index shows that most samples over 66% SiO_2 content are weakly peraluminous whereas all samples below that apparent threshold are metaluminous (Fig. 9C). The evaluation of the samples by relative timing of emplacement suggests a systematic variation from early metaluminous granitoids to peraluminous and younger metaluminous granitoids. The peraluminous samples with silica contents over 75% correspond to a rhyolite flow in the Kofi basin and quartz-feldspar-porphyry dykes from the Sadiola Hill open pit. The relationships between selected major elements (e.g., MgO , Fe_2O_3 , K_2O , and Na_2O) vs. SiO_2 are presented in Figure 10. In the case of $\text{MgO}/\text{Fe}_2\text{O}_3$ vs. SiO_2 (Fig. 10A-B), the samples show a gradual decrease in $\text{MgO}/\text{Fe}_2\text{O}_3$ content with increasing SiO_2 values. In the case of K_2O vs. SiO_2 (Fig. 10C), the general trend indicates successive emplacement of calc-alkaline granitoids gradually enriched in K_2O . The relationship between Na_2O vs. SiO_2 does not show a clear trend (Fig. 10D).

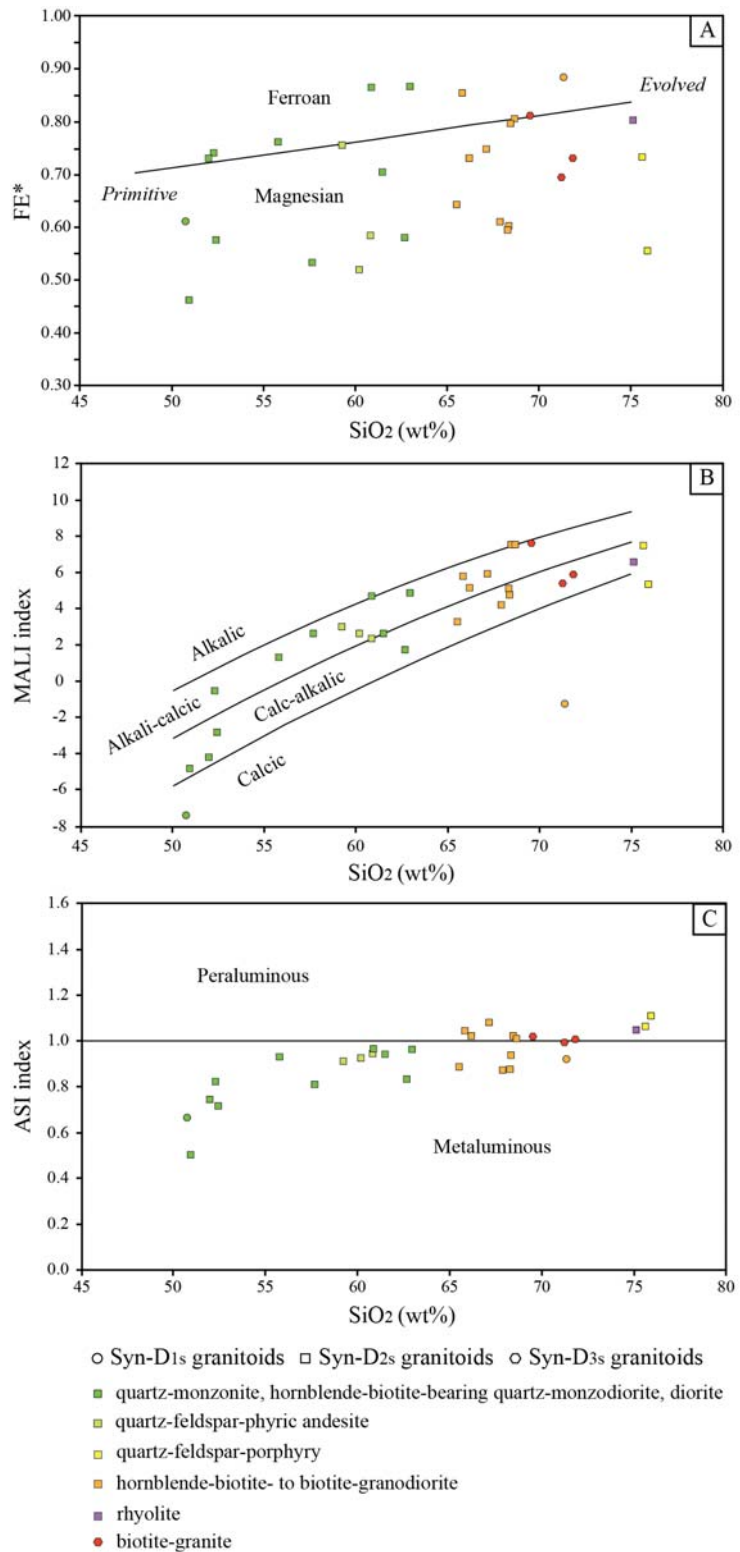


Figure 9. Three-tier classification scheme by Frost et al. (2001) A) Fe* vs. SiO₂ diagram, which conveys information about the differentiation history of the feldspars in the rocks and which is related to the sources of the magmas. B) Modified alkali-lime index vs. SiO₂ diagram, which is related to the sources of the magmas. C) Aluminium saturation index vs. SiO₂ diagram, which is related to the magma sources and the conditions of melting.

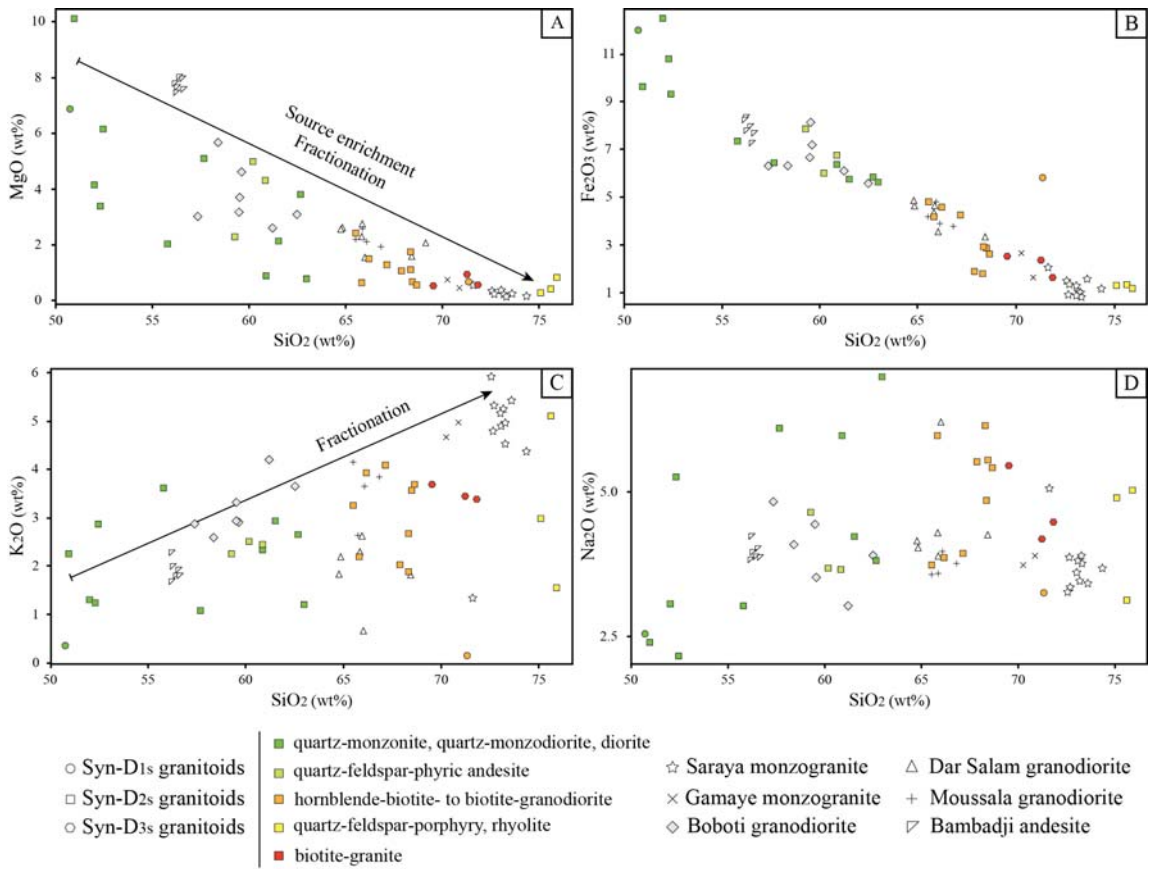


Figure 10. Selected Harker diagrams A) MgO vs. SiO₂ B) Fe₂O₃ vs. SiO₂ C) K₂O vs. SiO₂ D) Na₂O vs. SiO₂. Additional major element igneous chemistry data for the eastern KKI from Ndiaye et al. (1997) and Schwartz and Melcher (2004) are presented for comparison.

5.4.2. Trace elements

Chondrite-normalised REE plots (Sun and McDonough, 1989) associated with syn-D_{1s} plutonic rocks show flat REE patterns, with (La/Yb)_N ratios between 2.35 and 2.99 (Fig. 11A). Spider plots normalised to Primitive mantle (Sun and McDonough, 1989) show a similar trend, with no enrichment of the LREE over the HREE (Fig. 11B). The hornblende-granodiorite shows marked positive Zr and Hf anomalies compared with the diorite pattern. These positive anomalies are likely related to an extensive fluid evolution of the same magma or an enriched source. All syn-D_{2s} Eburnean plutonic and volcanic rocks but quartz-feldspar-porphry from the Sadiola Hill open pit exhibit equivalent REE patterns, suggesting that magmas shared a common parent, process or contaminant. Chondrite-normalised REE plots for the quartz-feldspar-porphry samples show flat patterns, with (La/Yb)_N ratios between 1.08 and 1.83 (Fig. 11C). The patterns are characterised by marked negative Eu anomalies (Eu/Eu* between 0.33 and 0.36).

The patterns also show correlated negative Sr and Eu anomalies. Spider plots normalised to Primitive mantle show patterns enriched in highly incompatible trace elements and show flat HREE patterns, with uniform Dy/Yb ratios between 1.58 and 1.69 (Fig. 11D). The samples display a marked negative Ti anomaly (fractionated or residual). In contrast, chondrite-normalised REE plots for the vast majority of syn- D_{2s} volcanic and plutonic rocks show fractionated REE patterns defined by LREE enrichment over the HREE, with (La/Yb)_N ratios ranging from 3.9 to 52.3 (average of 18.3) (Fig. 11E,G). The less fractionated patterns are associated with the mafic members of the group (e.g., diorite, monzodiorite). The samples do not exhibit marked Eu anomalies (Eu/Eu* range from 0.79 to 1.01). Spider plots normalised to Primitive mantle show patterns enriched in highly incompatible trace elements such as the light rare earth elements and large-ion lithophile elements (e.g. Rb, Sr, Ba, Pb, U), but are depleted in Nb, Ti and Th relative to neighbouring REE. HREE patterns are shallow dipping with relatively uniform Dy/Yb ratios between 1.57 and 3.00 (Fig. 11F,H). The syn-D_{3s} biotite-granites are characterised by similar trace element and REE patterns than that associated with syn-D_{2s} igneous rocks (Fig. 11I-J). Although TTG compositions have been reported in the KKI (e.g., Doh et al., 2006), not a single sample in this study proved to be chemically equivalent to that of TTGs as defined by Moyen and Martin (2012). In contrast, geochemical characteristics of the intrusive rocks show a close resemblance to that of adakites (i.e. Sr-Y-Yb-MgO-Al₂O₃-SiO₂ contents as per definition in Defant and Drummond 1990; Martin et al. 2005).

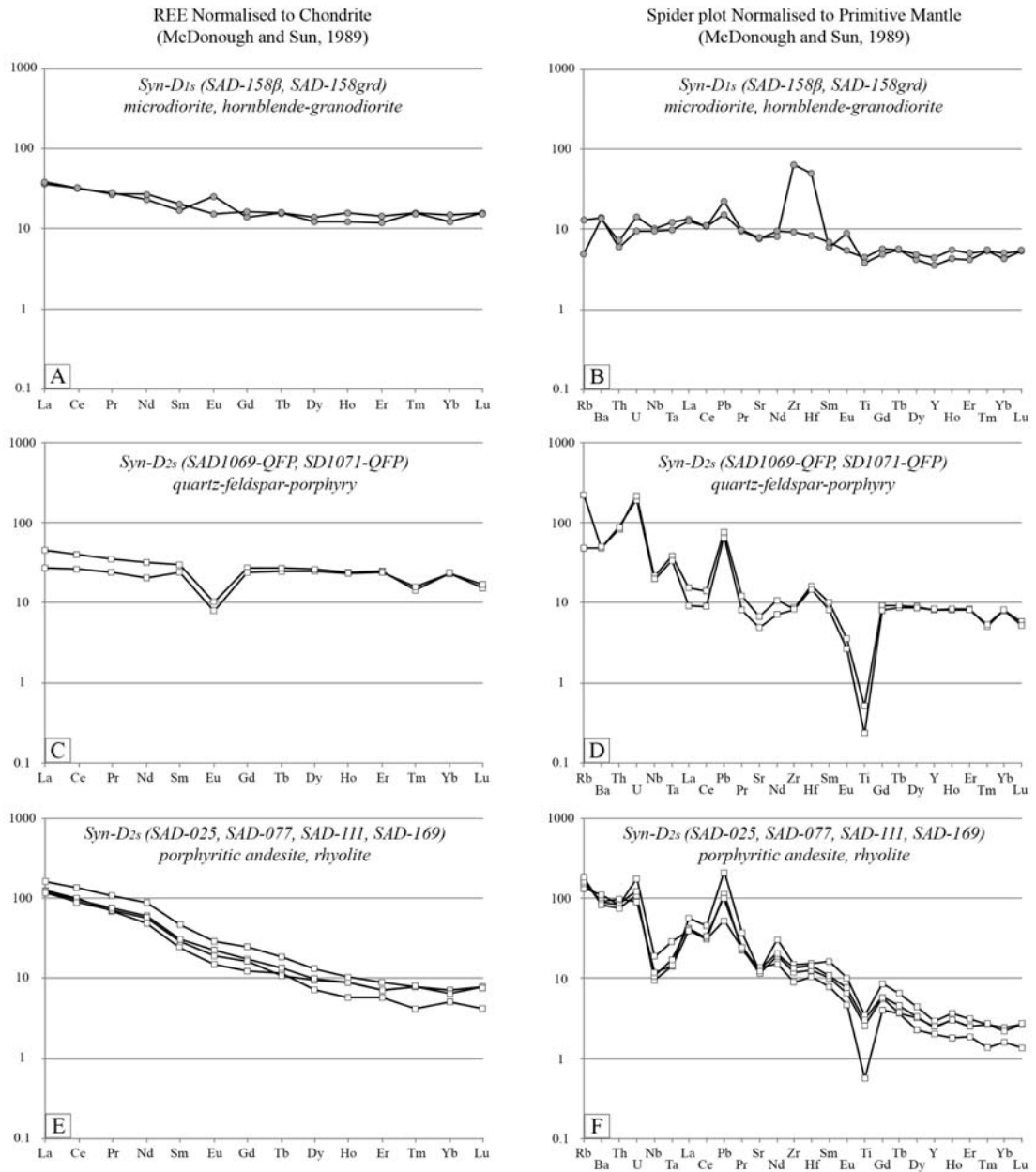


Figure 11a. REE patterns normalised to chondrite and spider plot normalised to primitive mantle (after Sun and McDonough, 1989). A-B) Pre- to syn-D_{1s} granitoids. C-D) Syn-D_{2s} quartz-feldspar porphyry. E-F) Syn-D_{2s} porphyritic andesite.

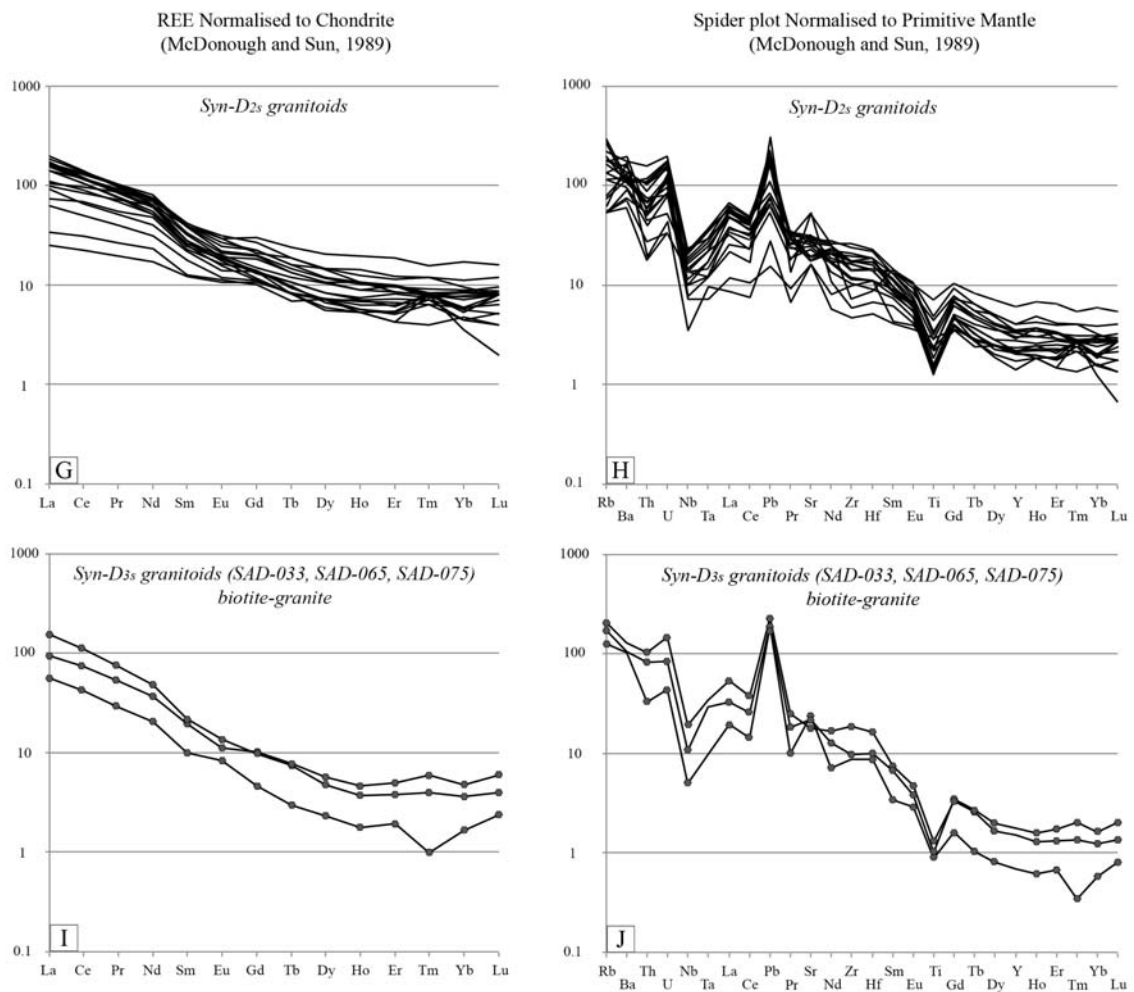


Figure 11b. REE patterns normalised to chondrite and spider plot normalised to primitive mantle (after Sun and McDonough, 1989). G-H) Syn-D_{2s} quartz-monzonite to granodiorite plutons. G-H) Syn-D_{3s} biotite-granites.

6. Discussion

6.1. Geological framework for the Sadiola-Yatela region

6.1.1. Structural evolution

Country rocks have undergone polycyclic deformation, which included early fold-and-thrust tectonics (D_{1s} , D_{2s}) followed by transcurrent tectonics (D_{3s} , D_{4s}). Little is known about D_{1s} but the D_{2s} and D_{3s} events were responsible for the formation of map-scale structures. The D_{2s} and D_{3s} events mark the principal imprint of the Eburnean orogeny in the region and were associated with massive magmatic addition. The bulk of the gold mineralisation in the region occurred during D_{3s} , with sinistral displacement and hydrothermal fluid circulation along the Senegal-Mali Shear Zone and steep NNE-trending shear zones connected to structural traps in the Kofi basin. The Senegal-Mali Shear Zone, however, does not correlate in the field with a continuous crustal-scale structure (e.g., Bassot and Dommange, 1986; Ledru et al., 1991). In contrast, the Senegal-Mali Shear Zone is represented by alternating high strain and low strain domains separating two distinct volcanic and sedimentary lithostratigraphic domains that occur at similar metamorphic grades. Within the high strain domains, microtectonic evidence such as stretched porphyroclasts and symmetrical strain shadows indicate a dominant component of flattening (i.e. pure shear deformation). Such results are consistent with the interpretation that the Senegal-Mali Shear Zone formed as a transpressional fault during the onset of D_{2s} (Lawrence et al., 2013a). It cannot be excluded, however, that the Senegal-Mali Shear Zone represents a tectonic discontinuity operating since the early convergence stage (D_{1s}).

6.1.2. Magmatic evolution

Volcanic and plutonic rocks represent an important part of the exposed crust in the region. The granitoids from the region display a temporal evolution from ca. 2150-2080 Ma calc-alkaline metaluminous plutons to ca. 2080-2060 Ma peraluminous high-K granites. The volcanic and plutonic rocks show distinct variations in their trace and rare

earth element chemistry, which cannot be solely attributed to the respective nature of their host terranes (i.e. volcanic belt-type vs. basin-type plutons). The least-evolved rocks are correlated with plutons of the Finman complex and the Sadiola Hill quartz-feldspar-porphyry. These rocks are associated with relatively flat REE patterns, suggesting derivation from a shallow source. In contrast, the REE patterns associated with other Eburnean volcanic and plutonic rocks suggest derivation from either a metasomatised mantle source with crustal contamination (e.g., Egal et al., 2002) or melting of an enriched lower-crustal garnet-amphibolite source (e.g., Doumbia et al., 1998; Pouclet et al., 2006). These rocks have a calc-alkaline affinity and are characterised by negative Nb-Ta anomalies, marked Pb positive anomalies and high LIL/HFS ratios. Such characteristics are compatible with distinctive features of subduction zone magmatism in modern-day active continental margin context (e.g., Hawkesworth and Kemp, 2006; Moyen and Martin, 2012). The Fe* values associated with magmatic rocks of the Sadiola-Yatela region reflect a close affinity to relatively hydrous, oxidised magmas and source regions (e.g., Frost and Lindsley, 1991), which is compatible with arc magmas (e.g., Richards, 2011). The hydrous nature of these Eburnean magmatic rocks is supported by the abundance of magmatic hornblende and biotite (e.g., Ridolfi et al., 2010). The relatively high magmatic oxidation states are reflected by the stability of titanite in a large number of these volcanic and plutonic rocks (e.g., Foley and Wheller, 1990). It cannot be excluded, however, that these trace element signatures may have been inherited (i.e. remelting of older subduction-related calc-alkaline magmatic rocks or melting of sedimentary rocks derived from such magmatic rocks).

6.2. Integration with regional geology and tectonics

The new magmatic crystallisation ages were integrated with available geochronological data for the KKI into a space-time chart (Figure 12). The synthesis indicates that magmatic activity in the inlier lasted from ca. 2210 Ma to 2060 Ma without evidence for long periods of magmatic quiescence. Inherited zircon ages reported in this study indicate either that early Birimian magmatism occurred in the Kofi basin between ca. 2220 and 2150 Ma, or that sedimentary rocks of the Kofi basin

partly derived from the Mako bimodal volcanic rocks. Eburnean granitoids in the KKI display a similar evolution from calc-alkaline metaluminous diorite-granodiorite plutons to peraluminous high-K granites (e.g., Hirdes and Davis, 2002; Dioh et al., 2006; Gueye et al., 2008). Geochronological data also shows the syn-volcanic nature of Eburnean plutonism. Field relationships and geochronology data indicate that sediment deposition in the Kofi and Dialé-Daléma basins most likely initiated during early convergence (D_1) coeval with the onset of calc-alkaline magmatism. The diachroneity of the recorded magmatic ages is reflected in the provenance of the sediments, which further strengthened the hypothesis that the Kofi and Dialé-Daléma represented syn-deformational basins in a convergent setting. The evolution from fold-and-thrust tectonics to transcurrent tectonics identified in the Sadiola-Yatela region has similarly been proposed for the Mako area (Diene et al., 2012) and the Loulo area (Dabo and Aïfa, 2010; Lawrence et al., 2013a). Available geochronological data suggest that the emplacement of most granitoids took place within a short time span between ca. 2115 and 2060 Ma, which is the best time estimate for the Eburnean orogeny in the KKI. The iron skarns of the Falémé district formed post-peak metamorphism at ca. 2080 Ma and are spatially and genetically associated with syn-kinematic plutons such as the Balangouma monzodiorite and the Boboti clinopyroxene-hornblende-bearing granodiorite (Hirdes and Davis, 2002; Schwartz and Melcher, 2004; Lawrence et al., 2013a; Lambert-Smith, 2014). The similar relative timing and structural setting between gold deposits of the Sadiola-Yatela region and other deposits of the KKI (e.g., Loulo, Lawrence et al., 2013a; Massawa, Treloar et al., 2014) suggests that gold mineralisation occurred subsequently during a period of transcurrent tectonics that outlasted emplacement of the peraluminous high-K granites, after the cessation of regional compressional deformation. It is likely that the late Eburnean magmatic activity participated in the generation of thermal gradients, which produced regional fluid systems capable of transpoting gold (e.g., Masurel et al., a, b). Alternatively, the hydrous nature of the Eburnean magmas in the region could explain the enhanced fertility for the formation of gold magmatic-hydrothermal systems upon shallow crustal emplacement (e.g., Massawa, Treloar et al., 2014).

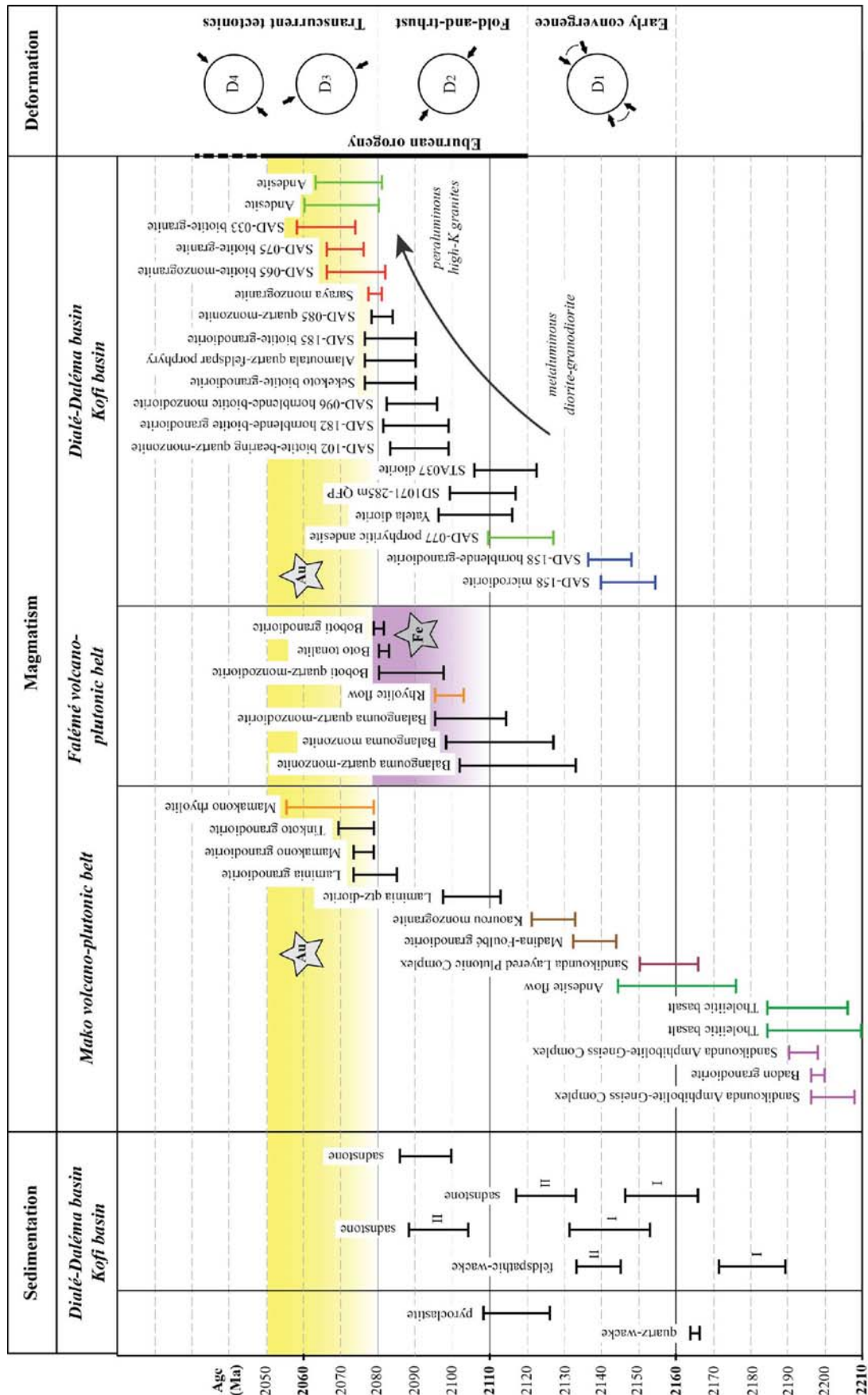


Figure 12. Summary space-time chart integrating new results with available geochronological data for the KKI given in Table 1. The proposed relative timing of iron skarn mineralisation in the Falémé belt is consistent with studies by Schwartz and Melcher (2004), Lawrence et al. (2013a) and Lambert-Smith (2014). The proposed relative timing of gold mineralisation in the KKI is consistent with economic geology studies by Lawrence et al. (2013a, b) for the Loulo district, Treloar et al. (2014) for the Massawa gold deposit, and Masurel et al. (in press a, b, c) for the Sadiola district.

6.3. Implications for the geodynamic evolution of the KKI

The Dy/Dy* vs. Dy/Yb diagram by Davidson et al. (2013) is a powerful tool to represent the shapes of REE patterns and allows to constrain magma sources and petrogenetic processes. A compilation of available data for volcanic and plutonic rocks of the KKI is presented in such diagram in Figure 13. When compared to age data, the compiled geochemical data support the evolution from a volcanic arc environment to an active continental margin. Representative volcanic rocks of the Mako belt likely derived from variably depleted mantle sources (Fig. 13). These volcanic rocks have formed in an immature oceanic plateau (e.g., Abouchami et al., 1990; Boher et al., 1992; Ngom et al., 2009) or in an immature oceanic island arc (e.g., Sylvester and Attoh, 1992; Dia et al., 1997; Diallo, 2001; Pawlig et al., 2006). In contrast, the vast majority of Eburnean volcanic and plutonic rocks overlap with middle and upper continental crust compositions (Fig. 13). The general concave-down pattern from the MORB field to upper continental crust compositions reflects a differentiation trend with amphibole as a major mineral phase control (fractionated or residual). The relative scatter in the field of Eburnean granitoids likely reflects variable incorporation of sedimentary material. This is compatible with the fact that magmas in more mature arcs typically stall at density barriers in the mantle or at one or more levels in the crust, where they undergo wall-rock assimilation and fractionated crystallisation (e.g., De Paolo, 1981), or MASH (melting, assimilation, storage, homogenisation) processes (e.g., Annen et al., 2006). The late Eburnean peraluminous high-K granites (e.g., Saraya, Gamaye) plot to the far right of the diagram, suggesting the presence of garnet in deep residual sources and crustal contamination (Fig. 13). The existence of a thickened lithosphere has been proposed by Lambert-Smith et al. (in press) to allow garnet to become stable in the magma source region for these high-K granites. Although similar in timing, the late peraluminous biotite-granites from the Sadiola-Yatela region are distinct from the

Saraya-type monzogranites. The evolution from metaluminous to peraluminous magmas in the Sadiola-Yatela region was probably related to the fractionation of hydrous melts at increasing pressure without crustal contamination (e.g., Richards, 2011; Loucks, 2014).

The evolution from primitive island arc granitoids to evolved peraluminous granitic melts observed in the KKI is analogous to that of modern active margins (e.g., Gill, 1981). This is supported by findings from Ganne et al. (2011) who recorded evidence for blueschist metamorphism in the ca. 2200-2000 Ma rocks of West Africa, suggesting that subduction was at play in the Paleoproterozoic era.

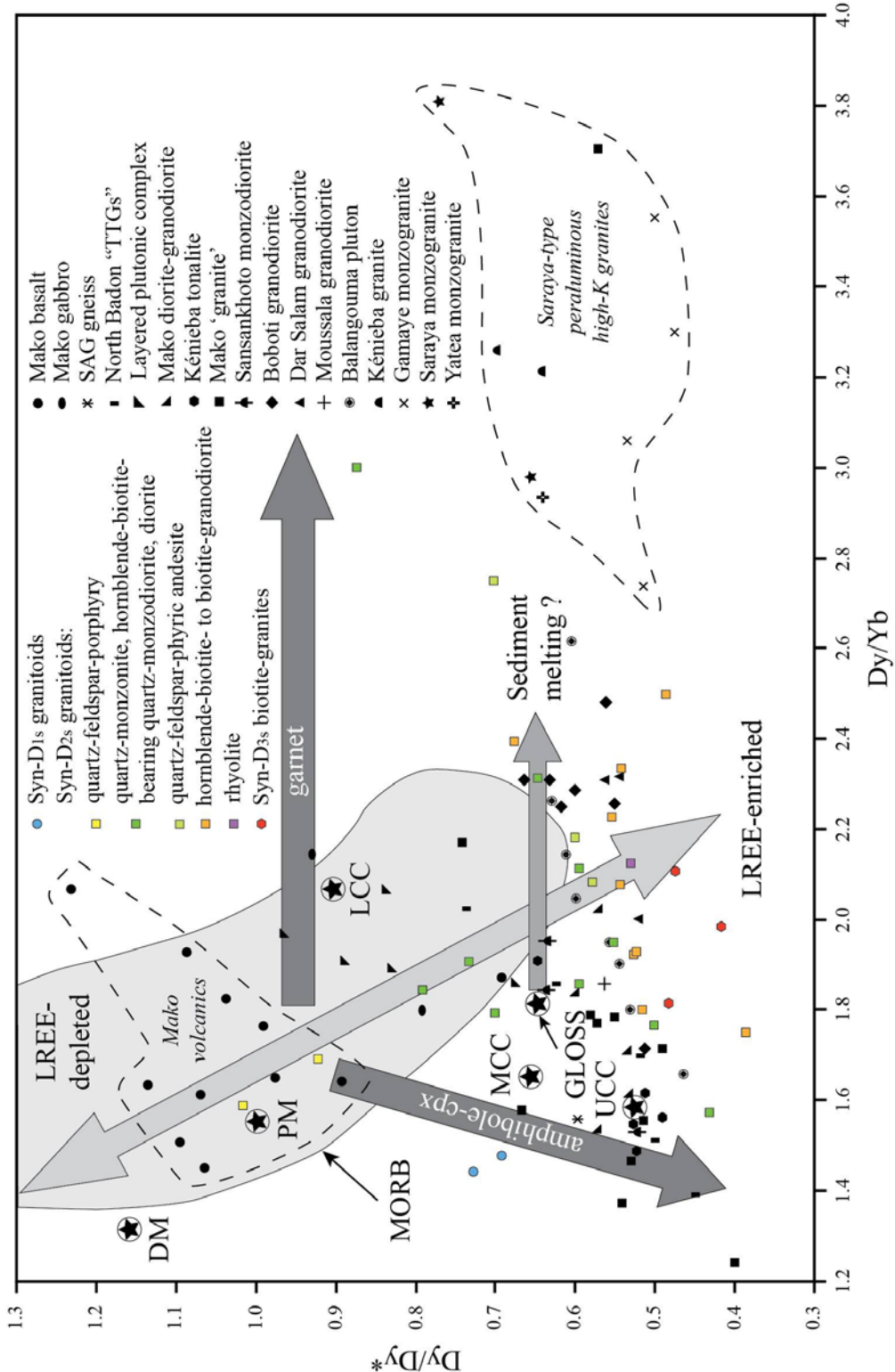


Figure 13. Plot of Dy/Dy^* vs. Dy/Yb (after Davidson et al., 2013). Vectors for mineral control and melting are indicative. PM, primitive mantle; DM, depleted mantle; GLOSS, average global subducting sediment; LCC, lower continental crust; MCC, middle continental crust; UCC, upper continental crust. Additional geochemistry data for the KKI from Ndiaye et al. (1997); Schwartz and Melcher (2004); Pawlig et al. (2006); Dioh et al. (2006) and Lambert-Smith et al. (in press) are presented for comparison.

6.4. Comparison with other Birimian terranes and diachroneity of geological development

The ca. 2110-2070 Ma volcanic rocks exposed in the KKI are younger than volcanic rocks in the Baoulé-Mossi domain. Thus far, ca. 2100 Ma volcanic ages have only been reported in Côte d'Ivoire (Fétékro belt, Leake, 1992; Ouango Fitini belt, Hirdes et al., 1996). In addition, the 2071 ± 5 Ma and 2066 ± 8 Ma magmatic crystallisation ages of the peraluminous biotite-granites in the Kofi basin are the youngest plutonic ages so far reported from the Baoulé-Mossi domain. The polycyclic deformation history recorded in the KKI is similar to that reported at the scale of the West African Craton (In Ivory Coast, Pouclet et al., 2006; Vidal et al., 2009; in Burkina Faso, Hein, 2010; Baratoux et al., 2011; in northern Guinea, Lahondère et al., 2002; in southern Mali, Liégeois et al., 1991; Milési et al., 1992; Olson et al., 1992; McFarlane et al., 2011; in southern Ghana, Allibone et al., 2002a, b). As for the KKI, the bulk of gold mineralisation in the Ashanti belt of Ghana occurred during a period of transcurrent tectonics, after the cessation of regional-scale compressional deformation. The best age estimate for region-wide world-class orogenic gold mineralisation in the Ashanti belt, however, is constrained to 2105 ± 2 Ma (Oberthür et al., 1998). By comparison, regional orogenic gold mineralisation is younger in the KKI and is better correlated with the 2063 ± 9 Ma minor gold phase reported in the Damang area (Pigois et al., 2003) or the 2074 ± 14 Ma gold phase at Morila in southern Mali (McFarlane et al., 2011). Regional peak metamorphism was dated at ca. 2100 Ma in the Ashanti belt of southern Ghana (Oberthür et al., 1998) whereas metamorphic monazite and titanite from west to central Ivory Coast record regional metamorphism at 2080 ± 10 Ma (Kouamelan, 1996). Metamorphic age patterns in the KKI extend from ca. 2070 to 2030 Ma (e.g., Hirdes et al., 2002; Gueye et al., 2007), but largely result from cooling after the late Eburnean tectono-thermal event. Nevertheless, the spatial distribution pattern of metamorphic ages in medium to high-level Birimian rocks suggests diachroneity of the Eburnean tectono-thermal event. The data presented in this study further supports the suggestion that the Eburnean tectono-magmatic activity affected the Baoulé-Mossi domain diachronously from SE to NW as first proposed by Hirdes and Davis (2002).

7. Acknowledgments

This study forms part of a PhD project, which began in February 2012 at the Centre for Exploration Targeting, The University of Western Australia, Perth. We wish to gratefully acknowledge AMIRA International and the industry sponsors for their support of the WAXI Project (P934A). SEMOS, a joint venture between AngloGold Ashanti, IAMGOLD and the Malian government, is gratefully acknowledged for its financial support. Many thanks to T. Gell (AGA), A. Mason-Apps (AGA), O. Terblanche (AGA) and M. Skwarnecki (AGA) for their enthusiasm for the study and their constructive discussions. Special thanks are extended to D. Traoré, C.O. Sanogo, F. Samake, M. Traoré, Y.S. Kone, and to SEMOS managers G. Gushee, H. Eybers, H. Sitshengiso, and S. Tessougue who assisted with field work studies and logistics. The authors acknowledge the John de Laeter Centre of Excellence for Mass Spectrometry, Curtin University (WA). Hao Gao and Cristina Talavera are thanked for their excellent technical assistance on the SHRIMP.

8. References

- Abouchami, W., Boher, M., Michard, A., and Albarede, F., 1990. A major 2.1 Ga event of mafic magmatism in West Africa: an early stage of crustal accretion. *Journal of Geophysical Research* 95, 17605–17629.
- Allibone, A.H., McCuaig, T.C., Harris, D., Etheridge, M.A., Munroe, S., Byrne, D., Amanor, J., and Gyapong, W., 2002a. Structural controls on gold mineralization at the Ashanti gold deposit, Obuasi, Ghana. *Society of Economic Geologists Special Publication* 9, 65–93.
- Allibone, A.H., Teasdale, J., Cameron, G., Etheridge, M.A., Uttlev, P., Soboh, A., Appiah-Kubi, J., Adanu, A., Arthur, R., Mamphey, J., Odoom, B., Zuta, J., Tsikata, A., Patave F., Famiyeh, S., and Lamb, E., 2002b. Timing and structural controls on gold mineralization at the Bogoso gold mine, Ghana, West Africa. *Economic Geology* 97, 949–969.
- Annen, C., Blundy, J.D., and Sparks, R.S.J., 2006. The genesis of intermediate and silicic magmas in deep crustal hot zones. *Journal of Petrology* 47, 505–539.

- Baratoux, L., Metelka, V., Naba, S., Jessell, M.W., Grégoire, M., and Ganne, J., 2011. Juvenile Paleoproterozoic crust evolution during the Eburnean orogeny (ca. 2.2–2.0 Ga), western Burkina Faso. *Precambrian Research* 191, 18-45.
- Bassot, J.P., 1987. Le complexe volcano-plutonique calco-alcalin de la rivière Daléma (Est Sénégal): discussion de sa signification géodynamique dans le cadre de l'orogénie eburnéenne (Protérozoïque inférieur). *Journal of African Earth Sciences* 6, 505-519.
- Bassot, J.P., and Dommange, A., 1986. Mise en évidence d'un accident majeur affectant le Protérozoïque inférieur des confins sénégal-maliens. *Comptes Rendus Géosciences* 302, 1101–1106.
- Bassot, J.P., and Caen-Vachette, M., 1984. Données géochronologiques et géochimiques nouvelles sur les granitoïdes de l'Est du Sénégal: Implications sur l'histoire géologique du Birimien de cette région, *in* Klerkx, J., Michot, J., eds., *African Geology: Belgium, Tervuren*, p. 196-209.
- Bessoles, B., 1977. Géologie de l'Afrique, le craton ouest-africain. Mémoire BRGM 88.
- Bierlein, F.P., Groves, D.I., Goldfarb, R.J., and Dubé, B., 2006. Lithospheric controls on the formation of provinces hosting giant orogenic gold deposits. *Mineralium Deposita* 40, 874-886.
- Boher, M., Abouchami, W., Michard, A., Albarede, F., and Arndt, N.T., 1992. Crustal Growth in West Africa at 2.1 Ga. *Journal of Geophysical Research* 97, 345-369.
- Bosse, H.R., Gwosdz, W., Lorenz, W., Markwich, H., Roth, W., and Wolff, F., 1996. Limestone and dolostone resources of Africa. *Geologisches Jahrbuch* D102, 3-532.
- Calvez, J.Y., Feybesse, J.L., Ledru, P. and Milesi, J.P., 1990. Géochronologie du Protérozoïque inférieur du craton ouest africain (méthode d'évaporation directe de zircons isolés). 13^e Réunion des Sciences de la Terre, Grenoble, France; *in* Milési, J.P., Feybesse, J.L., Ledru, P., Dommange, A., Quedraogo, M.F., Marcoux, E., Prost, A., Vinchon, C., Sylvain, J.P., Johan, V., Tegyey, M., Calvez, J.Y., and Lagny, P., 1989. Les minéralisations aurifères de l'Afrique de l'Ouest et leurs relations avec l'évolution lithostructurale au Protérozoïque inférieur. *Chronique de la Recherche Minière* 497, 3-98.

- Compston, W., Williams, I.S., and Meyer, C., 1984. U–Pb geochronology of zircons from lunar breccia 73217 using a sensitive high mass-resolution ion microprobe. *Journal of Geophysical Research* 89, B252–B534.
- Dabo, M., and Aïfa, T., 2010. Structural styles and tectonic evolution of the Kolia-Boboti sedimentary Basin, Kédougou-Kéniéba inlier, eastern Senegal. *Comptes Rendus Geoscience* 342, 796-805.
- Dabo, M., and Aïfa, T., 2011. Late Eburnean deformation in the Kolia-Boboti sedimentary basin, Kédougou-Kéniéba Inlier, Senegal. *Journal of African Earth Sciences* 60, 106-116.
- Davidson, J., Turner, S., and Plank, T., 2013. Dy/Dy*: Variations arising from mantle sources and petrogenetic processes. *Journal of Petrology* 54, 525-537.
- Debat, P., Diallo, D.P., Ngom, P.M., Rollet, M., and Seyler, M., 1984. La série de Mako dans ses parties centrale et méridionale (Sénégal Oriental, Afrique de l'Ouest). Précisions sur l'évolution de la série volcano-sédimentaire et données géochimiques préliminaires sur les formations magmatiques post-tectoniques. *Journal of African Earth Sciences* 2, 71-79.
- Defant, M.J., and Drummond, M.S., 1990. Derivation of some modern arc magmas by melting of young subducted lithosphere. *Nature* 347, 662-665.
- De Paolo, D.J., 1981. Trace element and isotopic effects of combined wall-rock assimilation and fractional crystallisation. *Earth and Planetary Scienc Letters* 53, p. 189-202.
- Dia, A., Van Schmus, W.R., and Kröner, A., 1997. Isotopic constraints on the age and formation of a Palaeoproterozoic volcanic arc complex in the Kédougou Inlier, eastern Senegal, West Africa. *Journal of African Earth Sciences* 24, 197-213.
- Dia, A., 1988. Caractères et signification des complexes magmatiques et métamorphiques du secteur de Sandikounda-Laminia (Nord de la boutonnière de Kédougou, Est du Sénégal): un modèle géodynamique du Birimien de l'Afrique de l'Ouest. Unpublished Ph.D. Thesis, Université de Dakar, Sénégal, 350 p.
- Diallo, D.P., 2001. Paleovolcanism in the western border of the Paleoproterozoic Kédougou inlier, eastern Senegal: geodynamic implications. *Journal of African Earth Sciences* 32, 919-940.
- Diene, M., Gueye, M., Diallo, D.P., and Dia, A., 2012. Structural evolution of a Precambrian Segment: example of the Paleoproterozoic formations of the Mako

- belt (eastern Senegal, West Africa). International Journal of Geosciences 3, 153-165.
- Dioh, E., Béziat, D., Debat, P., Grégoire, M., and Ngom, P.M., 2006. Diversity of the Palaeoproterozoic granitoids of the Kédougou inlier (eastern Senegal): Petrographical and geochemical constraints. Journal of African Earth Sciences 44, 351-371.
- Doumbia, S., Pouclet, A., Kouamelan, A., Peucat, J.J., Vidal, M., and Delor, C., 1998. Petrogenesis of juvenile-type Birimian (Paleoproterozoic) granitoids in Central Côte-d'Ivoire, West Africa: geochemistry and geochronology. Precambrian Research 87, 33-63.
- Egal, E., Thiéblemont, D., Lahondère, D., Guerrot, C., Costea, C.A., Iliescu, D., Delor, C., Goujou, J.C., Lafon, J.M., Tegyey, M., Diaby, S., and Kolié, P., 2002. Late Eburnean granitization and tectonics along the western and northwestern margin of the Archean Kénéma-Man domain (Guinea, West African Craton). Precambrian Research 117, 57-84.
- Foley, S.F., and Wheller, G.E., 1990. Parallels in the origin of the geochemical signatures of island arc volcanics and continental potassic igneous rocks: the role of residual titanites. Chemical Geology 85, p. 1-18.
- Frost, B.R., Barnes, C.G., Collins, W.J., Arculus, R.J., Ellis, D.J., and Frost, C.D., 2001. A geochemical classification for granitic rocks. Journal of Petrology 42, 2033-2048.
- Frost, B.R., and Lindsley, D.H., 1991. Occurrence of iron-titanium oxides in igneous rocks. Reviews in mineralogy and geochemistry 25, 433-468.
- Ganne, J., De Andrade, V., Weinberg, R.F., Vidal, O., Dubacq, B., Kagambega, N., Naba, S., Baratoux, L., Jessell, M., and Allibon, J., 2011. Modern-style plate subduction preserved in the Palaeoproterozoic West African craton. Nature geoscience 5, 60-65.
- Gill, J.B., 1981. Orogenic andesites and plate tectonics. Springer, Berlin, 390 p.
- Gueye, M., Ngom, P.M., Diène, M., Thiam, Y., Siegesmund, S., Wemmer, K., and Pawlig, S., 2008. Intrusive rocks and tectono-metamorphic evolution of the Mako Paleoproterozoic belt (Eastern Senegal, West Africa). Journal of African Earth Sciences 50, 88-110.

- Gueye, M., Siegesmund, S., Wemmer, K., Pawlig, S., Drobe, M., Nolte, N., and Layer, P., 2007. New evidence for an early Birimian evolution in the West African Craton: An example from the Kédougou-Kénieba inlier, southeast Senegal. *South African Journal of Geology* 110, 511-534.
- Hawkesworth, C.J., and Kemp, A.I.S., 2006. The differentiation and rates of generation of the continental crust. *Chemical Geology* 226, 134-143.
- Hein, K.A.A., Matsheka, I.R., Bruguier, O., Masurel, Q., Bosch, D., Caby, R., and Monié, P., 2015. The Yatela gold deposit: 2 billion years in the making. *Journal of African Earth Sciences*, doi: 10.1016/j.jafrearsci.2015.07.017
- Hein, K.A.A., 2010. Succession of structural events in the Goren greenstone belt (Burkina Faso): Implications for West African tectonics. *Journal of African Earth Sciences* 56, 83-94.
- Hirdes, W., and Davis, D.W., 2002. U-Pb Geochronology of Paleoproterozoic Rocks in the Southern Part of the Kédougou-Kénieba Inlier, Senegal, West Africa: Evidence for Diachronous Accretionary Development of the Eburnean Province. *Precambrian Research* 118, 83-99.
- John, T., Klemd, R., Hirdes, W., and Loh, G., 1999. The metamorphic evolution of the Paleoproterozoic (Birimian) volcanic Ashanti belt (Ghana West Africa). *Precambrian Research* 98, 11–30.
- Kalsbeek, F., Frei, D., and Affaton, P., 2008. Constraints on provenance, stratigraphic correlation and structural context of the Volta basin, Ghana, from detrital zircon geochronology: an Amazonian connection? *Sedimentary Geology* 212, 86-95
- Kouamelan, A.N., Delor, C., and Peucat, J.J., 1996. Geochronological evidence for reworking of Archean terrains during the early Proterozoic (2.1 Ga) in the western Côte d'Ivoire (Man Rise, West African Craton). *Precambrian Research* 86, 177–199.
- Lahondère, D., Thiéblemont, D., Tegyey, M., Guerrot, C., and Diabaté, B., 2002. First evidence of early Birimian (2.21 Ga) volcanic activity in Upper Guinea: The volcanics and associated rocks of the Niani suite. *Journal of African Earth Sciences* 35, 417–431.
- Lambert-Smith, J., Lawrence, D.M., Müller, W., Treloar, P.J., in press. Paleotectonic setting of the eastern Kédougou-Kénieba inlier, West Africa: new insights from

- igneous trace element geochemistry and U-Pb zircon ages. *Precambrian Research*.
- Lambert-Smith, J., 2014, The geology, structure and metallogenesis of the world class Loulo-Bambadjii Au district in Mali and Senegal, West Africa. Ph.D. Thesis, Kingston University London, U.K., 346 p.
- Lawrence, D.M., Treloar, P.J., Rankin, A.H., Boyce, A., and Harbidge, P., 2013b. A Fluid Inclusion and Stable Isotope Study at the Loulo Mining District, Mali, West Africa: Implications for Multifluid Sources in the Generation of Orogenic Gold Deposits. *Economic Geology* 108, 229-257.
- Lawrence, D.M., Treloar, P.J., Rankin, A.H., Harbidge, P., and Holliday, J., 2013a. The Geology and Mineralogy of the Loulo Mining District, Mali, West Africa: Evidence for Two Distinct Styles of Orogenic Gold Mineralization. *Economic Geology* 108, 199-227.
- Leake, M.H., 1992. The petrogenesis and structural evolution of the early Proterozoic Fettekro greenstone belt, Dabakala region, NE Côte d'Ivoire. Unpublished Ph.D. Thesis, Portsmouth, U.K., 315 p.
- Ledru, P., Pons, J., Milesi, J.P., Feybesse, J.L., and Johan, V., 1991. Transcurrent tectonics and polycyclic evolution in the Lower proterozoic of Senegal-Mali. *Precambrian Research* 50, 337-354.
- Liégeois, J.P., Claessens, W., Camara, D., and Klerkx, J., 1991. Short-lived Eburnian orogeny in southern Mali. Geology, tectonics, U-Pb and Rb-Sr geochronology. *Precambrian Research* 50, 111-136.
- Loucks, 2014. Distinctive composition of copper-forming arc magmas. *Australian Journal of Earth Sciences: an international geoscience journal of the geological society of Australia* 61, 5-16.
- Ludwig, K.R., 2009. Squid 2.50, A User's Manual: Unpublished report by Berkeley Geochronology Centre, California, USA, 95 p.
- Ludwig, K.R., 2003. Isoplot 3.0; a geochronological toolkit for Microsoft Excel: Berkeley Geochronology Centre Special Publication 4, 70 p.
- Martin, H., Smithies, R.H., Rapp, R., Moyen, J.F., and Champion, D., 2005. An overview of adakite, tonalite-trondhjemite-granodiorite (TTG) and sanukitoid: relationships and some implications for crustal evolution. *Lithos* 79, 1-24.

- Masurel, Q., Thébaud, N., Miller, J., Ulrich, S., Hein, K.A.A., Cameron, G., Béziat, D., Bruguier, O., and Davis, J.A., in press a. Sadiola Hill: a world-class gold deposit in Mali, West Africa. *Economic Geology – Special Issue on the West African Craton*.
- Masurel, Q., Thébaud, N., Miller, J., Ulrich, S., Roberts, M.P., and Béziat, D., in press b. The Alamoutala carbonate-hosted gold deposit, Kédougou-Kénieba inlier, West Africa. *Economic Geology – Special Issue on the West African Craton*.
- Masurel, Q., Miller, J., Hein, K.A.A., Hanssen, E., Thébaud, N., Ulrich, S., Kaisin, J., and Tessougue, S., in press c. The Yatela gold deposit in Mali: the final product of a long-lived history of hydrothermal alteration and weathering. *Journal of African Earth Sciences*.
- McCuaig, T.C., Beresford, S., and Hronsky, J., 2010. Translating the mineral systems approach into an effective exploration targeting system. *Ore Geology reviews* 38, 128-138.
- McFarlane, C.R.M., Mavrogenes, J., Lentz, D., King, K., Allibone, A., and Holcombe, R., 2011. Geology and Intrusion-Related Affinity of the Morila Gold Mine, Southeast Mali. *Economic Geology* 106, 727-750.
- Moyen, J.F., and Martin, H., 2012. Forty years of TTG research. *Lithos* 148, 312-336.
- Milési, J.P., Ledru, P., Feybesse, J.L., Dommanget, A., and Marcoux, E., 1992. Early Proterozoic ore deposits and tectonics of the Birimian orogenic belt, West Africa. *Precambrian Research* 58, 305-344.
- Nasdala, L., Hofmeister, W., Norberg, N., Martinson, J. M., Corfu, F., Dörr, W., Kamo, S.L., Kennedy, A.K., Kronz, A., Reiners, P.W., Frei, D., Kosler, J., Wan, Y., Götze, J., Häger, T., Kröner, A., and Valley, J. W., 2008. Zircon M257 a Homogeneous Natural Reference Material for the Ion Microprobe U-Pb Analysis of Zircon. *Geostandards and Geoanalytical Research* 32, 247-265.
- Ndiaye, P.M., Dia, A., Viallette, Y., Diallo, D.P., Ngom, P.M., Sylla, M., Wade, S., and Dioh, E., 1997. Données pétrographiques, géochimiques et géochronologiques nouvelles sur les granitoïdes du Paléoprotérozoïque du Supergroupe de Dialé-Daléma (Senegal Oriental): Implications pétrogénétiques et géodynamiques. *Journal of African Earth Sciences* 25, 193-208.
- Ngom, P.M., Cordani, U.G., Teixeira, W., and Janasi, V.A., 2009. Sr and Nd isotopic geochemistry of the early ultramafic–mafic rocks of the Mako bimodal volcanic

- belt of the Kedougou-Kéniéba Inlier (Senegal), *Arabian Journal of Geosciences* 3, 49-57.
- Oberthür, T., Vetter, U., Davis, D.W., and Amanor, J.A., 1998. Age constraints on gold mineralization and Paleoproterozoic crustal evolution in the Ashanti belt of southern Ghana: *Precambrian Research* 89, 129-143.
- Olson, S.F., Diakité, K., Ott, L., Guindo, A., Ford, C.R.B., Winer, N., Hanssen, E., Lay, N., Bradley, R., and Pohl, D., 1992. Regional setting, structure, and descriptive geology of the middle Proterozoic Syama gold deposit, Mali, West Africa. *Economic Geology* 87, 310-331.
- Passchier, C.W., and Trouw, R.A.J., 2005. *Microtectonics*. Springer, 2d edition, p. 118-123.
- Pawlig, S., Gueye, M., Klischies, R., Schwarz, S., Wemmer, K., Siegesmund, S., 2006. Geochemical and Sr-Nd isotopic data on the Birimian of the Kedougou-Kenieba Inlier (Eastern Senegal): Implications on the Palaeoproterozoic evolution of the West African Craton. *South African Journal of Geology* 109, 411-427.
- Perrouty, S., Aillères, L., Jessel, M.W., Baratoux, L., Bourassa, Y., and Crawford, B., 2012. Revised Eburnean geodynamic evolution of the gold-rich Ashanti belt, Ghana, with new field and geophysical evidence of pre-Tarkwaian deformations. *Precambrian Research* 204-205, 12-39.
- Pigois, J.P., Groves, D.I., Fletcher, I.R., McNaughton, N.J., and Snee, L.W., 2003. Age constraints on Tarkwaian paleoplacer and lode-gold formation in the Tarkwa-Damang district, SW Ghana. *Mineralium Deposita* 38, 695-714.
- Pouclet, A., Doumbia, S., and Vidal, M., 2006. Geodynamic setting of the Birimian volcanism in central Ivory Coast (western Africa) and its place in the Palaeoproterozoic evolution of the Man Shield. *Bulletin de la Société Géologique de France* 177, 105-121.
- Richards, J.P., 2011. Magmatic to hydrothermal metal fluxes in convergent and collided margins. *Ore Geology Reviews* 40, p. 1-26.
- Ridolfi, F., Renzulli, A., and Puerini, M., 2010. Stability and chemical equilibrium of amphibole in calc-alkaline magmas: an overview, new thermo-barometric formulations and application to subduction-related volcanoes. *Contributions to Mineralogy and Petrology* 160, p.45-66.

- Stacey, J.S., and Kramers, J.D, 1975. Approximation of terrestrial lead isotope evolution by a two-stage model. *Earth and Planetary Science Letters* 26, 207–221.
- Stern, R.A., Bodorkos, S., Kamo, S.L., Hickman, A.H., and Corfu, F., 2009. Measurement of SIMS instrumental mass fractionation of Pb isotopes during zircon dating: *Geostandards and Geoanalytical Research* 33, 145–168.
- Stern, R.A., 2001. A new isotopic and trace-element standard for the ion microprobe: preliminary thermal ionization mass spectrometry (TIMS) U–Pb and electron-microprobe data. *Geological Survey of Canada, Radiogenic Age and Isotopic Studies, Report 14, Current Research 2001-F1*, 11 p.
- Streckeisen, A., 1974. Classification and nomenclature of plutonic rocks, recommendations of the IUGS subcommission on the systematics of igneous rocks. *Geologische Rundschau* 63, 773–786.
- Schwartz, M.O., and Melcher, F., 2004. The Falémé Iron District, Senegal. *Economic Geology* 99, 917–939.
- Sun, S.S., and McDonough, W.F., 1989. Chemical and isotopic systematics of oceanic basalts: implications for mantle composition and processes; *in* Saunders AD, Norry MJ. *Magmatism in ocean basins: Geological Society Special Publication* 42, 313–345.
- Sylvester, P.J., and Attoh, K., 1992. Lithostratigraphy and composition of the 2.1 Ga greenstone belts of the West African Craton and their bearing on crustal evolution and the Archean-Proterozoic boundary. *The Journal of Geology* 100, 377–393.
- Treloar, P.J., Lawrence, D.M., Senghor, D., Boyce, A., and Harbidge, P., 2014. The Massawa gold deposit, Eastern Senegal, West Africa: an orogenic gold deposit sourced from magmatically derived fluids? *Geological Society London Special Publications* 393, 135–160.
- Vidal, M., Gumiäux, C., Cagnard, F., Pouclet, A., Ouattara, G., and Pichon, M., 2009. Evolution of a Paleoproterozoic “weak type” orogeny in the West African Craton (Ivory Coast). *Tectonophysics* 477, 145–159.
- Villeneuve, M., 2008. Review of the orogenic belts on the western side of the West African Craton: the Bassarides, Rokelides and Mauritanides; *in* Ennih, N., and

- Liégeois, J.P., eds., The boundaries of the West African Craton. Geological Society of London Special Publication 297, 169-201.
- Villeneuve, M., and Cornée, J. J., 1994. Structure, evolution and palaeogeography of the West African Craton and bordering belts during the Neoproterozoic. *Precambrian Research* 69, 307-326.
- AMIRA International, 2013. P934A - West African Exploration Initiative – Stage II, Final Report, p. 438-439.
- Wingate, M.T.D., and Kirkland, C.L., 2013. Introduction to geochronology information. Geological Survey of Western Australia Publication, 5 p.

Chapter VI. Conclusions

1. Key research outcomes

The concept of this multi-scale and multidisciplinary study was to understand the underpinning factors that allow integration of the observed variability in gold mineralisation (e.g., structural setting, host rocks, ore and alteration paragenesis) at both the deposit- and camp-scale into a single coherent framework of value to exploration. The key research outcomes are summarised hereafter.

1.1. Lithostratigraphy

The Birimian lithostratigraphy in the region consisted of carbonates overlain by younger sequences of detrital sedimentary rocks (e.g., wackes, arenites, siltstones, argillites) based on way-up indicators such as fining-upwards sequences in wackes, and rare cross-bedding and scour-and-fill structures in arenites. The Dialé-Daléma and Kofi Series represent the most extensive occurrence of carbonates rocks in the West African Craton (Bosse, 1996). The carbonates are locally impure and characterised by abundant thin (0.2-2 cm) argillaceous-silty interbeds. Evidence for slump folding has been observed in the Sadiola Hill and FE3 open pits. In contrast, there is a lack of evidence for stromatolitic facies in carbonates of the region, which would reflect shallow water conditions. Thus, the deposition of thick carbonate sequences probably occurred in the slope and plain of a syn-deformational basin in a convergent setting. Sedimentary rock deposition resulted from a combination of abundant periplatform and hemipelagic sedimentation and rapid basinal subsidence (e.g., Sami and James, 1994). Available detrital zircon data from the KKI indicate that the diachroneity of magmatic ages is reflected in the provenance of the sediments. In the Sadiola-Yatela district, the minimum deposition age for sedimentary rocks of the Kofi Series correlates with the emplacement of the Alamoutala plutonic complex at c. 2100 Ma. The prevalence of this Bririmian-aged detritus in locally-derived sediments in the district and the KKI suggests

that these older rocks must have been uplifted, eroded and transported before the late Eburnean tectono-thermal event (ca. 2090-2060 Ma). The change in sedimentary rock facies deposition from carbonate sequences to flysch-type detrital sedimentary rocks in the Kofi basin may reflect the onset of the Eburnean orogeny (i.e. advanced convergence).

1.2. Deformation

The Sadiola Hill gold deposit, the Yatela gold deposit and all ancillary open pits share a similar structural evolution. The identified deformation history is consistent with available structural data for the KKI (e.g., Gueye et al., 2008; Dabo and Aïfa, 2010; Diene et al, 2012; Lawrence et al., 2013a; Treloar et al., 2014). At least two episodes of folding have been identified in the Sadiola-Yatela region. Early F_1 folds are disharmonic with recumbent to inclined fold hinges. These folds are NNW- to N-trending, gently south-dipping (10° - 30°), and associated with a weak to strong axial-planar cleavage (S_1). Fold geometry and lineation data associated with this early deformation event (D_{1s}) are consistent with WSW-ENE-directed to E-W-directed shortening. These early F_1 folds are refolded by F_2 disharmonic folds associated with upright to inclined fold hinges. The F_2 folds are associated with a 015° / 75° E (e.g. Sadiola Hill, Tambali, Alamoutala) to 035° / 75° E (e.g. FE3, FE4) axial-planar cleavage (S_2) indicative of a WNW fold vergence. Fold axes and intersection lineations plunge gently (15 - 30°) to the SSW or NNE. A number of NNE-trending thrusts and high-angle reverse faults are closely associated with these F_2 folds. Fold and fault geometry, and lineation data associated with this second deformation event (D_{2s}) are consistent with NW-SE directed shortening. The following deformation increment (D_{3s}) marks a switch from a coaxial to a non-coaxial deformation regime and is associated with the strike-slip reactivation of early accretionary structures (e.g., lithostratigraphic interfaces, S_1 , Sadiola Fracture Zone) and the formation and/or reactivation of NNE-trending sub-vertical shear zones. Fault geometries and lineation data associated with the third deformation event (D_{3s}) are consistent with NNW-SSE-directed shortening. The D_{2s} and D_{3s} events mark the principal imprint of the Eburnean orogeny in the region and were responsible for the formation of map-scale structures. The D_{2s} and D_{3s} events may relate

to the evolution of a regional system accommodating oblique convergence (i.e. transpressive regime) during the Eburnean orogeny (ca. 2115-2060 Ma). The Senegal-Mali Shear Zone is an anastomosing fault network that is interpreted to have formed during D₂ as a transpressional fault.

1.3. Metamorphism

No evidence for large-scale amphibolite-facies metamorphic conditions could be identified in the region. In contrast, the country rocks exhibit regional greenschist-facies mineral assemblages (e.g., biotite, chlorite, muscovite, quartz, K-feldspar). Amphibolite-facies metamorphic conditions (e.g., garnet-pyroxene-actinolite-tremolite mineral assemblage) are restricted to contact aureoles surrounding Eburnean granitoids. All gold deposits of the district are unmetamorphosed. Regional peak metamorphism pre-dated the late Eburnean tectono-magmatic event that occurred between 2090 and 2060 Ma.

1.4. Magmatism

The emplacement of most exposed granitoids in the Sadiola-Yatela region took place within a short time span between ca. 2115 and 2060 Ma, which is the best time estimate for the Eburnean orogeny in the KKI. The evolution from calc-alkaline metaluminous hornblende-granodiorite plutons (ca. 2120-2080 Ma) to evolved peraluminous monzogranites (ca. 2080-2060 Ma) is similar to that reported for Eburnean granitoids elsewhere in the KKI (e.g., Hirdes and Davis, 2002; Dioh et al., 2006; Gueye et al., 2008). The Sadiola volcanic rocks formed at 2118 ± 9 Ma and are significantly younger than bimodal volcanic rocks in the Mako belt (dated between 2195 ± 11 and 2158 ± 8 Ma, Dia, 1988, Dia et al., 1997). The 2071 ± 5 Ma and 2066 ± 8 Ma ages for magmatic crystallisation of the peraluminous biotite-granites in the Sadiola Hill deposit area are the youngest plutonic ages so far reported from the Baoulé-Mossi domain. These young ages support the hypothesis that the Eburnean tectono-thermal event affected the Baoulé-Mossi domain diachronously from SE to NW (e.g., Hirdes and Davis, 2002).

1.5. Gold mineralisation

Gold mineralisation is largely hosted by metacarbonates in the district (e.g., Sadiola Hill, Alamoutala, Yatela, FE3) but also occurs in detrital metasedimentary rocks (e.g., Tambali, FE4, KW18) and plutonic rocks (e.g., Alamoutala, Sadiola Hill). The late-Eburnean sinistral reactivation of early accretionary structures (e.g., lithostratigraphic interfaces, S_1 , Sadiola Fracture Zone) and coupling/linkage with steep NNE-trending shears was critical to ore location and geometry. Lithological contacts with contrasting competency properties and low mean stress areas surrounding rigid granitoid bodies were critical to hydrothermal fluid flow focussing. The similar relative timing and structural setting between gold deposits of the Sadiola-Yatela district and other deposits of the KKI (e.g., Loulo, Lawrence et al., 2013a; Massawa, Treloar et al., 2014) indicates that gold mineralisation in the region occurred during a period of transcurrent tectonics (D_3), after the cessation of regional contractional deformation (D_1-D_2). Orogenic gold mineralisation in the Sadiola-Yatela region is constrained to have occurred younger than 2083 ± 7 Ma. For comparison, the orogenic overprint at the Morila gold deposit in southern Mali is constrained to have occurred at 2074 ± 14 Ma (hydrothermal titanite, McFarlane et al., 2011). In addition to primary orogenic gold mineralisation, prospectivity in the region is increased due to the exploration potential for Yatela-style orebodies. Such orebodies formed by residual and supergene gold enrichment processes associated with the development of a deep weathering profile over carbonate host rocks.

1.6. Hydrothermal alteration

Although gold deposits of the district share equivalent structural setting and relative gold timing, the diversity in ore paragenesis, nature and chemistry of wall-rock alteration recognised over the camp points toward three distinct styles of mineralisation typified by the Sadiola Hill, the Alamoutala, and the Yatela gold deposits (Table 1). The typical gold-related hydrothermal alteration assemblage in the district is defined as biotite + calcite-dolomite + quartz \pm actinolite-tremolite \pm muscovite \pm tourmaline \pm pyrite-arsenopyrite-pyrrhotite. One difficulty in interpreting gold deposits of the district

is to reconcile the thermal disequilibrium between country rocks at regional greenschist-facies conditions and the higher temperature of the ore-related hydrothermal alteration paragenesis with characteristics of orogenic gold deposits (e.g., Groves et al., 1998; Goldfarb et al., 2001; Groves et al., 2003; Goldfarb et al., 2005). Such geological feature alone is not diagnostic of a magmatic fluid source because it can reflect the interaction of a fluid from any source with reactive country rocks (i.e. impure limestone) at a temperature high enough to stabilise biotite (e.g., Meinert et al., 2005). The identified thermal disequilibrium is suggested to represent a transient thermal effect associated with syn-kinematic igneous activity in the region at the time of mineralisation (i.e. late Eburnean tectono-thermal event). The contrasted primary ore paragenesis identified in the various gold deposits of the district may reflect host rock dependency, and/or a spatial zoning with respect to the Senegal-Mali Shear Zone, and/or ore deposition at distinct crustal levels.

Table 1. Deposit classification for the Sadiola-Yatela gold camp

Characteristics	Sadiola Hill-style	Alamoutala-style	Yatela-style
Examples	Sadiola Hill, Tambali	Alamoutala	Yatela, FE3, FE4, KW18
Host rocks	marble ± diorite ± wacke-arenite-siltstone ± quartz-feldspar porphyry	marble + porphyritic granodiorite ± wacke-arenite-siltstone	marble + diorite ± wacke-arenite-siltstone-argillite
Structural controls on ore geometry	Sinistral displacement along N-trending Sadiola Fracture Zone and NNE-trending shear array	Sinistral displacement along NNW-trending Alamoutala Fracture Zone and NE-trending shear	Sinistral displacement along faulted NNE-trending diorite-marble interface and NNW-trending shear array
Relative timing of gold mineralisation	D3s NNW-SSE shortening	Late D2s NW-SE shortening - D3s NNW-SSE shortening	D3s NNW-SSE shortening
Ore mineralogy			
Mineralisation styles	Shear-hosted	Shear-hosted, breccia-hosted, disseminated	
Major sulfides	Arsenopyrite, Pyrrhotite		
Minor sulfides	Pyrite, chalcopyrite	Pyrite	
Minor / trace ore minerals	scheelite + molybdenite + berthierite + stilbite + tetrahedrite ± sphalerite ± galena ± jamesonite ± gersdorffite ± gedmannite ± ullmannite ± rutile	Chalcopyrite arsenopyrite ± monazite-(Ce) ± scheelite ± molybdenite ± sphalerite ± galena ± tetrahedrite-tennantite ± berthierite ± gedmannite ± ullmannite ± gersdorffite ± cobaltite ± petlandite ± synchisite ± horobetsuite ± millerite ± hessite ± tellurobismuthite ± coloradoite ± gerdosorfite	
Oxide		Traces to minor magnetite	Traces magnetite
Metal association	Au-As-Sb ± Cu-W-Mo-Ag-Bi-Zn-Pb-Tc	Au-Cu ± Ag-As-Sb-Bi-Mo-Zn-Pb-W-P-REE-Ni-Co-U	Au-Cu ± As-Zn-Pb-Fc-Sb-Ag-Ni-Co
Gold phases	Ag-poor gold, aurostibite, traces maldonite	native gold, electrum	native gold, electrum
Gold sites	free gold, enclosed in arsenopyrite crystals, locally remobilised along micro-fractures in sulphides, lattice-bound in arsenopyrite	enclosed in pyrite ± in tetrahedrite-tennantite crystals, locally remobilised along micro-fractures in pyrite	(1) disseminated free gold, gold enclosed in pyrite crystals and gold blebs locally remobilised along micro-fractures in pyrite
Hydrothermal alteration			
Alteration types	Calc-silicate (1) and potassic (2)	Potassic (1)	Carbonate (1) and potassic (2)
Alteration assemblage	(1) Pophyroblastic actinolite-tremolite (2) Biotite + calcite ± tourmaline ± K-feldspar ± quartz actinolite-tremolite ± apatite	(1) Fe-dolomite (2) Biotite ± tourmaline + quartz ± actinolite-tremolite ± apatite	

2. Implications for exploration

In November 2013, John Miller, Nicolas Thébaud, and the candidate conducted a targeting workshop on the Sadiola mine site with SEMOS personnel and AngloGold Ashanti brownfield exploration group. The targeting session used a mineral system approach (e.g., McCuaig and Beresford, 2009; McCuaig et al., 2010; McCuaig and Hronsky, 2014) in order to identify and rank targets based on research data and extensive in-house knowledge. The mineral system approach relies on the breakup of the mineralising process into a series of base critical processes that can be treated as independent variables. These range from a primary fluid source region, an active fluid pathway, and at the deposit-scale a fluid sink related to a physical throttle and/or a chemical trap. This approach presents significant advantages over the deposit model approach or empirical exploration approaches, which are traditionally used. These advantages are that it has a basis in probability theory and is permissive enough to allow for the discovery of a new style of deposit, rather than just analogues of what have already been found. During that exercise, a refined regional geological map that used available geophysical data sets (e.g., geophysics, soil/termite geochemistry, outcrop mapping data) was produced. In addition, a total of 31 targets were generated including some unexplored and untested to date. The considered information and status of follow-up investigations remain confidential to date.

3. Future work

Despite the work undertaken by the candidate, a number of questions remain unanswered, some of which are directly relevant to exploration targeting:

3.1. Source of fluids and metals

Recent research suggests that the diversity in mineralisation styles and ore paragenesis expressed in the KKI result from a dynamic hydrothermal system that sourced fluids and metals from both metamorphic and magmatic reservoirs (Lawrence et al., 2013a, b; Treloar et al., 2014). The collection and interpretation of fluid inclusion and stable isotope data is critical to establishing an ore genetic model for the gold deposits of the Sadiola-Yatela district. It would also be interesting to see how well the orogenic gold paradigm (Groves et al., 1998; Goldfarb et al., 2001; Groves et al., 2003; Goldfarb et al., 2005) translate to accretionary terranes of the West African Craton.

3.2. Timing of regional orogenic gold mineralisation

The relative timing of gold mineralisation is well constrained with respect to the structural evolution of the KKI. No absolute ages for the region-wide orogenic gold mineralisation, however, have yet been reported. Such data would allow regional correlations to be made, which in turn could provide critical information in terms of geological development of the West African Craton. The 2028 ± 10 Ma age for gold mineralisation at Gara in the Loulo district reported by Vielreicher (U-Pb on xenotime and monazite, 2006) is incompatible with the proposed tectonic evolution of the KKI. Such young age may relate to cooling paths after the late Eburnean tectono-thermal event.

3.3. Metamorphic data

There is a lack of metamorphic data for the KKI. A study by Ganne et al. (2014) in the Baoulé-Mossi domain indicates that a moderate apparent geothermal gradient (M2: 20-30°C/km) produced greenschist- to amphibolites-facies metamorphic assemblages during the Eburnean orogeny and is superimposed on an early thermal regime (M1: <10-15°C/km) that produced high-*P* greenschist- to blueschist-facies metamorphic assemblages. The determination of *P-T* time paths in country rocks of the region would help to better understand the tectono-thermal evolution of the Kédougou-Kénieba crust.

3.4. Lu-Hf isotopic studies

In situ U-Pb analyses on magmatic zircons have allowed the determination of crystallisation ages of representative magmatic rocks in the region but using the Lu-Hf isotopic system would provide relevant information to the source rocks, distinguishing between a juvenile mantle-derived input and crustal reworking. The combination of U-Pb and Lu-Hf isotopic data would provide better picture of the crustal evolution in the region (e.g., Griffin et al., 2007; O'Reilly et al., 2008).

4. References

- Bosse, H.R., Gwosdz, W., Lorenz, W., Markwich, H., Roth, W., and Wolff, F., 1996, Limestone and dolomite resources of Africa. Geologisches Jahrbuch D102, 3-532.
- Dabo, M., and Aïfa, T., 2010, Structural styles and tectonic evolution of the Kolia-Boboti sedimentary Basin, Kédougou-Kénieba inlier, eastern Senegal: Comptes Rendus Geoscience, v. 342, p. 796-805.
- Dia, A., 1988, Caractères et signification des complexes magmatiques et métamorphiques du secteur de Sandikounda-Laminia (Nord de la boutonnière de Kédougou, Est du Sénégal): un modèle géodynamique du Birimien de l'Afrique de l'Ouest: Unpublished Ph.D. thesis, Sénégal, Université de Dakar, 350 p.

- Dia, A., Van Schmus, W.R., and Kröner, A., 1997, Isotopic constraints on the age and formation of a Palaeoproterozoic volcanic arc complex in the Kedougou Inlier, eastern Senegal, West Africa: *Journal of African Earth Sciences*, v. 24, p. 197-213.
- Diene, M., Gueye, M., Diallo, D.P., and Dia, A., 2012, Structural Evolution of a Precambrian Segment: Example of the Paleoproterozoic Formations of the Mako Belt (Eastern Senegal, West Africa): *International Journal of Geosciences*, v. 03, p. 153-165.
- Dioh, E., Béziat, D., Debat, P., Grégoire, M., and Ngom, P.M., 2006, Diversity of the Palaeoproterozoic granitoids of the Kédougou inlier (eastern Sénégal): Petrographical and geochemical constraints: *Journal of African Earth Sciences*, v. 44, p. 351-371.
- Ganne, J., Gerbault, M., and Block, S., 2014, Thermo-mechanical modeling of lower crust exhumation – Constraints from the metamorphic record of the Paleoproterozoic Eburnean orogeny, West African Craton: *Precambrian Research*, v. 243, p. 88-109.
- Goldfarb, R.J., Baker, T., Dubé, B., Groves, D.I., Hart, C.J.R., and Gosselin, P., 2005, Distribution, character, and genesis of gold deposits in metamorphic terranes: *Economic Geology*, 100th Anniversary Volume, p. 407-450.
- Goldfarb, R.J., Groves, D.I., Gardoll, S., 2001, Orogenic gold and geologic time: a global synthesis: *Ore Geology Reviews*, v. 18, p. 1-75.
- Griffin, W.L., Belousova, E., and O'Reilly, S.Y., 2007, Crustal History and Metallogenic fertility: Terrane-scale assessment with detrital zircons: *Proceedings of Exploration*, p. 311- 315.
- Groves, D.I., Goldfarb, R.J., Robert, F., and Hart, C.J.R., 2003, Gold Deposits in Metamorphic Belts: Overview of Current Understanding, Outstanding Problems, Future Research, and Exploration Significance: *Economic Geology*, v. 98, p. 1-29.
- Groves, D.I., Goldfarb, R.J., Gebre-Mariam, M., Hagemann, S.G., and Robert, F., 1998, Orogenic gold deposits: A proposed classification in the context of their crustal distribution and relationship to other gold deposit types: *Ore Geology Reviews*, v. 13, p. 7-27.
- Gueye, M., Ngom, P.M., Diene, M., Thiam, Y., Siegesmund, S., Wemmer, K., and Pawlig, S., 2008, Intrusive rocks and tectono-metamorphic evolution of the Mako

- Paleoproterozoic belt (Eastern Senegal, West Africa): *Journal of African Earth Sciences*, v. 50, p. 88-110.
- Hirdes, W., and Davis, D.W., 2002, U-Pb Geochronology of Paleoproterozoic Rocks in the Southern Part of the Kedougou-Kéniéba Inlier, Senegal, West Africa: Evidence for Diachronous Accretionary Development of the Eburnean Province: *Precambrian Research*, v. 118, p. 83-99.
- Lawrence, D.M., Treloar, P.J., Rankin, A.H., Harbridge, P., and Holliday, J., 2013a, The Geology and Mineralogy of the Loulo Mining District, Mali, West Africa: Evidence for Two Distinct Styles of Orogenic Gold Mineralization: *Economic Geology*, v. 108, p. 199-227.
- Lawrence, D.M., Treloar, P. J., Rankin, A.H., Boyce, A., and Harbridge, P., 2013b, A Fluid Inclusion and Stable Isotope Study at the Loulo Mining District, Mali, West Africa: Implications for Multifluid Sources in the Generation of Orogenic Gold Deposits: *Economic Geology*, v. 108, p. 229-257.
- McCuaig, T.C., and Hronsky, J.M.A., 2014, The Mineral System Concept: The Key to Exploration Targeting: *Society of Economic Geologists Special Publication*, v. 18, p. 153-175.
- McCuaig, T.C., Beresford, S., and Hronsky, J.M.A., 2010, Translating the mineral systems approach into an effective exploration targeting system: *Ore Geology Reviews*, v. 38, p. 128-138.
- McCuaig, T.C., and Beresford, S.W., 2009, The scale dependency of targeting criteria based on recent advances in understanding mineral systems; *in* Proceedings of the 10th Biennial Meeting of the Society for Geology Applied to Mineral Deposits, Townsville, Australia, p. 123-125.
- Meinert, L.D., Dipple, G.M., and Nicolescu, S., 2005, World Skarn Deposits: *Economic Geology*, 100th Anniversary Volume, p. 299-336.
- McFarlane, C.R.M., Mavrogenes, J., Lentz, D., King, K., Allibone, A., and Holcombe, R., 2011, Geology and Intrusion-Related Affinity of the Morila Gold Mine, Southeast Mali: *Economic Geology*, v. 106, p. 727-750.
- O'Reilly, S.Y., Griffin, W. L., Pearson, N. J., Jackson, S. E., Belousova, E. A., Alard, O., and Saeed, A., 2008, Taking the pulse of the Earth: linking crustal and mantle events: *Australian Journal of Earth Sciences*, v. 55, p. 983-995.

Sami, T.T., and James, N.P., 1994, Peritidal carbonate platform growth and cyclicity in an early Proterozoic foreland basin, upper Pethei Group, northwest Canada, v. B64, p. 111-131.

Treloar, P.J., Lawrence, D.M., Senghor, D., Boyce, A., and Harbridge, P., 2014, The Massawa gold deposit, Eastern Senegal, West Africa: an orogenic gold deposit sourced from magmatically derived fluids?: Geological Society, London, Special Publications, v. 393, p. 135-160.

Vielreicher, N.M., 2006, Reconnaissance SHRIMP xenotime and monazite geochronology on mineralised samples from Loulo 0 gold deposit, Kédougou-Kéniéba Inlier, western Mali: Randgold Resources Ltd, internal report, 13 p.

Electronic Appendices

Appendix A.

Accepted co-authored manuscript: Hein, K.A.A., Matsheka, I.R., Bruguier, O., Masurel, Q., Bosch, D., Caby, R., Monié, P., The Yatela gold deposit: 2 Billion years in the making, *Journal of African Earth Sciences* (2015), doi: 10.1016/j.jafrearsci.2015.07.017.

Appendix B.

Geochemical data for representative igneous rocks from the Sadiola-Yatela region.

Appendix C.

Sensitive high resolution ion microprobe (SHRIMP) analytical results for selected igneous rocks from the Sadiola-Yatela region.

Appendix D.

Individual U-Pb geochronology reports.

Appendix E.

Outcrop, hand specimen, and petrographic descriptions for representative igneous rocks from the Sadiola-Yatela region.